The Dissertation Committee for Jesús Mauricio Salazar Luna Certifies that this is the approved version of the following dissertation:

Simulation and Inversion of Borehole Electromagnetic Measurements for the Estimation of Petrophysical Properties in the Presence of Mud-Filtrate Invasion

Committee:

Carlos Torres-Verdín, Supervisor

Ekwere J. Peters

Steven L. Bryant

Clark R. Wilson

James D. Klein

Simulation and Inversion of Borehole Electromagnetic Measurements for the Estimation of Petrophysical Properties in the Presence of Mud-Filtrate Invasion

by

Jesús Mauricio Salazar Luna, B.S.; M.S.

Dissertation

Presented to the Faculty of the Graduate School of
The University of Texas at Austin
in Partial Fulfillment
of the Requirements
for the Degree of

Doctor of Philosophy

The University of Texas at Austin
May, 2008

Dedication

I dedicate this dissertation to my homeland Venezuela

Acknowledgements

First and foremost I would like to thanks my parents Erasmo and Maximiliana for giving me life, moral values, and teaching me that education come first. I thank my three brothers and four sisters for giving me their support and taking care of my folks during these years away from home.

I would like to express my gratitude to my supervising professor Dr. Carlos Torres-Verdín for his continuous guidance, support, and encouragement during all these years at The University of Texas at Austin. I also thank my former fellow graduate student Dr. F. Omer Alpak for his great mentoring in the area of inversion and numerical simulation of fluid-flow. The contribution of Dr. Gong Li Wang (UT) in the coding of SP and Resistivity modeling and inversion was invaluable to accomplish the objective of this work. To him goes my sincerest appreciation. I am also grateful to Dr. James D. Klein (ConocoPhillips) for his help on the interpretation of field measurements and for being part of my dissertation committee. I would like to extend my most sincere appreciation to the members of my dissertation committee professors Dr. Ekwere J. Peters, Dr. Steven L. Bryant, and Dr. Clark R. Wilson for taking the time to review my dissertation. A note of gratitude is also extended to Dr. Barbara Anderson, Dr. Tom Barber, and Dr. Tarek M. Habashy of Schlumberger for their constructive comments on array-induction measurements acquisition, processing, and simulation.

Special thanks go to my friends and fellow graduate students Hee Jae Lee and Mayank Malik for their help with the simulations of water-base and oil-base mud-filtrate invasion, respectively and also to Alberto Mendoza, Renzo Angeles, Robert Mallan, and Nathan Vrubel for their technical comments and suggestion either using commercial software packages, programming, or any other topic. But overall, I thank them all for being supportive and good friends during these years together at the Formation Evaluation Group. Roger Terzian, for keeping my computer up-to-date, and Reynaldo Casanova, for being in charge of the paperwork of my appointments, also deserve my appreciation. I also thank the support and camaraderie of my friends in the department Maylín Carrizalez, Silvia Solano, Thaimar Ramírez, Elif Altinay, Crystal Duan, Tobi Odumoso, Chez Uzoh, Crystal Duan, Tatyana Torskaya, L. Javier Miranda, Ben Voss, Malek Lemkecher, Jorge Sánchez, those friends I made at JP's Java (my second office), my only Venezuelan friends when I first arrived in Austin, Paulina Galavís, Jean C. Pérez, and Armando Sena, and many others that I may have forgotten to mention.

I would like to express my gratitude to ConocoPhillips and Occidental Oil and Gas Corporation for giving me the opportunity to expand my experience in the industry through summer internships as well as to the foundation of the Society of Petrophysicist and Well Log Analyst and the UT Cockrell School of Engineering for bestowing me with generous scholarships. The work reported in this dissertation was funded by the University of Texas at Austin's Research Consortium on Formation Evaluation, jointly sponsored by Anadarko, Aramco, Baker Atlas, BHP Billiton, BP, British Gas, ConocoPhillips, Chevron, ENI E&P, ExxonMobil, Halliburton Energy Services, Hydro, Marathon Oil Corporation, Mexican Institute for Petroleum, Occidental Petroleum Corporation, Petrobras, Schlumberger, Shell International E&P, Statoil, TOTAL, and Weatherford. A note of special gratitude goes to ConocoPhillips, Kerr-McGee (now Anadarko), and the Andrew Field Partner Group for providing the data sets used in the field studies.

Simulation and Inversion of Borehole Electromagnetic Measurements for the Estimation of Petrophysical Properties in the Presence of Mud-Filtrate Invasion

Publication No._____________

Jesús Mauricio Salazar Luna, Ph.D.
The University of Texas at Austin, 2008

Supervisor: Carlos Torres-Verdín

Acoustic, electromagnetic (EM), and nuclear open-hole measurements are affected by fluids saturating near-wellbore porous and permeable rock formations, including hydrocarbons, water, and mud filtrate. Fluid invasion effects can be quantified and advantageously used to estimate petrophysical properties of the invaded rock formations. This dissertation incorporates the physics of water-base mud- (WBM) and oil-base mud- (OBM) filtrate invasion to the simulation and inversion of borehole EM measurements.

We assume vertical boreholes penetrating clastic hydrocarbon- or water-bearing formations subject to either WBM- or OBM-filtrate invasion. The simulation of EM measurements in the presence of mud-filtrate invasion considers three different approaches: (1) piston-like invasion profiles, where we solely consider invaded- (flushed) and virgin- (uncontaminated) zones, (2) two-phase immiscible displacement and salt mixing between the invading WBM filtrate and connate water, and (3) invasion of single-

or multi-component OBM-filtrate into a formation saturated with multiple hydrocarbon components wherein the individual components are first-contact miscible. The last two approaches honor the physics of mudcake growth as well as the petrophysical properties that govern the process of multi-phase, multi-component fluid-flow displacement and include the presence of irreducible, capillary-bound and movable water. Electromagnetic measurements are simulated from spatial distributions of electrical resistivity calculated from the simulations of mud-filtrate invasion using clean- or shaly-sand water-saturation-resistivity models. Inversion of petrophysical properties is posed as the nonlinear minimization of quadratic objective functions that quantify the misfit between EM measurements and their simulations.

In the case of WBM piston-like invasion profiles in water-bearing formations, combined inversion of array-induction resistivity and spontaneous potential (SP) measurements yields connate water electrical resistivity and Archie's cementation exponent. Permeability is calculated from the inversion of array-induction resistivity measurements assuming immiscible fluid-flow displacement of WBM into hydrocarbon-bearing formations. Accurate reconstructions of layer-by-layer permeability are primarily constrained by the availability of *a-priori* information about time of invasion, rate of mud-filtrate invasion, overbalance pressure, capillary pressure, and relative permeability.

This dissertation also quantifies the influence of petrophysical and fluid properties on borehole resistivity measurements acquired in the presence of compositional mixing of OBM filtrate invading partially hydrocarbon-saturated rock formations. Numerical simulations of OBM-filtrate invasion are performed with an adaptive-implicit compositional formulation that allows one to quantify the effects of additional components of mud-filtrate and native fluids on EM measurements. Perturbations of petrophysical and fluid properties enable the quantification of rock wettability changes

due to OBM-filtrate invasion and their effect on the simulated induction resistivity measurements. Finally, simulations of induction resistivity measurements in the presence of OBM are compared to the corresponding measurements in the presence of WBM-filtrate invasion. The latter analysis allows us to estimate a realistic flow rate of OBM-filtrate invasion that is responsible for the variation of induction resistivity measurements as a function of their radial length of response. The combined simulation of the physics of mud-filtrate invasion and EM measurements provides reliable estimates of true formation resistivity and hence of water saturation, thereby improving the assessment of in-place hydrocarbons reserves.

Table of Contents

List of Tables

List of Figures

Chapter 1: Introduction

1.1 BACKGROUND

Initial water saturation of hydrocarbon reservoirs has an enormous impact on the calculation and production of original oil in place. When laboratory measurements of Archie's parameters (a, m, and n) and connate water resistivity (R_w) are available, this petrophysical property is properly constrained. However, such measurements are not always available, and if they are, their reliability may be questionable. Therefore, there is a strong need for alternative methods to estimate Archie's parameters and R_w prior to calculating initial water saturation.

Likewise, in the history of formation evaluation, absolute permeability has been one of the most difficult petrophysical properties to assess from well log measurements. Empirical methods have been traditionally used to estimate permeability from porosity, irreducible water saturation (Balan *et al.*, 1995), and pore-throat aperture size (Pittman, 1992). However, these methods rely on the availability of core measurements, which is rarely the case, do not necessarily honor the scales of spatial resolution and length of investigation of the different measurements involved in the estimation, and none considers the effect of mud-filtrate invasion on well logs used to estimate porosity and water saturation.

Mud-filtrate invasion takes place while drilling a borehole in a porous and permeable formation due to mechanical overbalance and mud circulation. Invasion depends on the chemical properties of the mud, pressure of the mud column, and rock properties, such as permeability, porosity, initial water saturation, capillary pressure, and relative permeability (Wu *et al.*, 2005). Depending on the drilling environment, water-base mud (WBM) or oil-base mud (OBM) are alternatively used in the process of drilling a wellbore. Such fluids have different effects on the response of wireline measurements. Acoustic, EM, and nuclear open-hole measurements alike are affected by the fluids saturating the near-wellbore, including native hydrocarbons, formation water, and mud filtrate invading the formation. Such effects can be advantageously used to estimate petrophysical properties of the invaded rock formations.

Resistivity and spontaneous potential (SP) are the most common and oldest wireline measurements available in most drilled wells and both are highly affected by mud-filtrate invasion. In this dissertation, we show how the combined inversion of induction-resistivity and spontaneous potential measurements in the presence of invasion yields the parameters needed to estimate water saturation. The physics of mud-filtrate invasion is applied to the simulation and inversion of induction resistivity measurements. Such a process allows us to assess absolute permeability in rock formations drilled with water-base muds. By simulating array-induction resistivity measurements in the presence of oil-base and water-base mud-filtrate invasion, we are able to estimate a more realistic value of true formation resistivity that enables the accurate assessment of water saturation and hydrocarbon in place.

1.2 PROBLEM STATEMENT

Simulation of borehole EM measurements, particularly resistivity, is commonly carried out assuming piston-like invasion profiles. A realistic way of modeling resistivity measurements consists of using the physics of fluid-flow mud-filtrate invasion. At the onset of this dissertation we use the first approach to introduce a new inversion method to estimate connate water resistivity (R_w) and Archie's (1942) cementation exponent (m) from the combined use of borehole spontaneous potential and raw array-induction resistivity measurements acquired in water-bearing depth intervals.

In the following stage, the effect of invasion is used as a motivation to integrate the physics of mud-filtrate invasion with inversion and simulation of array-induction resistivity measurements to assess permeability and water saturation in rock formations drilled with WBM.

Subsequently, we study the effect of OBM-filtrate invasion on resistivity measurements. Perturbations of formation petrophysical properties allow us to assess the effect of OBM invasion on EM measurements and assess their impact on the estimation of true formation resistivity. The presence of surfactants emulsified in the OBM and alterations of rock wettability are analyzed via perturbations of capillary pressure and relative permeability. The final goal is to quantitatively compare the processes of WBM- and OBM-filtrate invasion and their effect on borehole resistivity measurements. In so doing, we calculate a time-dependent flow rate of OBM-filtrate invasion that includes the dynamically coupled effects of mudcake growth and multi-phase filtrate invasion.

1.3 RESEARCH OBJECTIVES

This dissertation focuses on the integration of borehole EM, geological, and laboratory (fluid and rock-core samples) measurements to estimate in-situ petrophysical properties. The following list summarizes global objectives pursued by the dissertation:

- Develop a method to compute true formation resistivity, connate water resistivity, and Archie's cementation exponent in water-saturated rocks via inversion of raw array-induction resistivity and SP measurements assuming piston-like WBM-filtrate invasion fronts.
- Apply nonlinear inversion to estimate absolute permeability in geologically complex rocks from induction resistivity measurements using the physics of fluid-flow WBM-filtrate invasion.

- Develop a method to simulate array-induction resistivity measurements from spatial distributions of water saturation in the presence of multi-component OBM-filtrate invasion.
- Study the effect of OBM-filtrate invasion on the near wellbore zone by performing multiple sensitivity analyses of resistivity measurements to fluid and rock properties. This includes the assessment of variations of rock wettability when oil invades water-wet rock formations, the effect of surfactant on water saturation, and wettability alterations on capillary pressure and relative permeability.
- Perform a quantitative comparison of the processes of WBM- and OBM-filtrate invasion and their corresponding effects on borehole resistivity measurements.

1.4 METHOD AND APPROACH OVERVIEW

The first stage of this dissertation uses a finite-element algorithm to simulate SP measurements using vector and scalar potential theory (Zhang and Wang, 1997; Zhang and Wang, 1999). Simulation of resistivity measurements is performed with the Numerical-Mode Matching Method (Chew *et al*., 1984; Zhang *et al*., 1999). We use raw borehole-corrected array-induction resistivity measurements and consider the effect of both invasion and layer thickness on both resistivity and SP. Our objective is to calculate connate water resistivity (R_w) and Archie's cementation exponent (m) for a field data set acquired in a water-bearing clastic formation based on the combined inversion of SP and raw array-induction measurements. The estimation method is based on quantitative simulations and interpretation of the measurements with realistic physical assumptions and not on qualitative interpretations.

The next stage of the dissertation considers a tight-gas sand formation where rock-core measurements are used to synthesize a petrophysical model necessary to simulate the physics of mud-filtrate invasion. Such a model is “calibrated” against the existing suite of wireline logs, especially array-induction logs. Flow sub-units defined from porosity and an initial guess of absolute permeability are taken as horizontal layers to simulate the process of mud-filtrate invasion with a two-dimensional chemical flow simulator that includes the effect of salt mixing between mud filtrate and connate water. We generate spatial distributions of electrical resistivity from the simulated cross-sections of water saturation and salt concentration using Archie’s equation. In turn, these spatial distributions are used to simulate array-induction resistivity measurements acquired across the formation. The estimation of permeability for each layer is posed as a nonlinear minimization problem. We consider limiting values of rock and fluid properties to quantify the impact of the spatial distributions of water saturation and salt concentration on array-induction measurements.

We also quantify the influence of petrophysical properties on field array-induction resistivity measurements acquired in clastic formations in the presence of OBM-filtrate invasion. First, we consider a simple two-component formulation for the oil phase (OBM and reservoir oil) wherein the components are first-contact miscible. A second approach consists of adding water and surfactant to a multi-component OBM invading a formation saturated with multiple hydrocarbon components. Simulations also include presence of irreducible, capillary-bound, and movable water. The dynamic process of OBM invasion causes component concentrations to vary with space and time. In addition, the relative mobility of the oil phase varies during the process of invasion because oil viscosity and oil density are both dependent on component concentrations. This behavior in turn conditions the spatial distribution of electrical resistivity, hence the associated borehole array-induction measurements. Presence of surfactants in the OBM is simulated with a commercial adaptive-implicit compositional formulation that models the flow of three-phase multi-component fluids in porous media.

The final stage of the dissertation quantitatively compares the effect of the processes of WBM- and OBM-filtrate invasion on borehole resistivity measurements. In so doing, we simulate the process of mud-filtrate invasion into a porous and permeable rock formation assuming one-dimensional (1D) radial distributions of fluid saturation and fluid properties while porosity, permeability, capillary pressure, and relative permeability remain constant.

In this dissertation we have developed an efficient framework to perform simulations that consider the fluid distribution near the wellbore as conditioned by OBM- and WBM-filtrate invasion. Results can be used to improve the petrophysical interpretation of other logging measurements, including those acquired with nuclear and sonic tools.

1.5 OUTLINE OF THE DISSERTATION

Following the introductory chapter, this dissertation consists of six additional chapters. Chapter 2 describes a new inversion method to estimate connate water resistivity and Archie's cementation exponent based on the combined use of borehole SP and raw array-induction resistivity measurements acquired in a water-bearing sandstone formation.

Chapter 3 elaborates on the successful application of a new petrophysical inversion algorithm to estimate permeability from borehole array-induction measurements. We consider measurements acquired in a North Louisiana tight-gas sand formation subject to WBM-filtrate invasion. Moreover, the invasion model honors the physics of mudcake growth as well as the petrophysical properties that govern the process of two-phase, three-component flow.

Chapter 4 quantifies the influence of petrophysical properties on array-induction resistivity measurements acquired in the presence of OBM-filtrate invasion. In this chapter, the simulation of OBM-filtrate invasion considers a simple two-component formulation for the oil phase (OBM and reservoir oil) wherein the components are first-contact miscible. Simulation of induction resistivity measurements in the presence of OBM are compared against the corresponding measurements acquired in the presence of water-base mud (WBM) using field measurements acquired in a deepwater Gulf-of-Mexico reservoir.

Chapter 5 studies the influence of oil-base mud-filtrate invasion and formation fluid properties on the spatial distribution of fluid saturation and electrical resistivity in the near-wellbore region. We approach the simulation of OBM-filtrate invasion by adding water and surfactant to a multi-component OBM filtrate invading a formation saturated with multiple hydrocarbon components. Presence of surfactants in the OBM is simulated with a commercial adaptive-implicit compositional formulation that models the flow of three-phase multi-component fluids in porous and permeable media. The resulting two-dimensional spatial distributions of water saturation are transformed into spatial distributions of electrical resistivity and used as input to simulate the corresponding array-induction resistivity measurements assuming axial-symmetric variations of electrical resistivity.

Chapter 6 introduces a comparative study of the processes of WBM- and OBM-filtrate invasion into a porous and permeable rock formation assuming 1D radial distributions of fluid saturation. To model OBM-filtrate invasion, we develop an algorithm to calculate the time-dependent flow rate of OBM-filtrate invasion by adapting the available formulation of the physics of WBM-filtrate invasion. This chapter shows that, in general, flow rates of WBM-filtrate invasion are higher than those of OBM-filtrate invasion due to viscosity contrasts between OBM-filtrate and native fluids, which slow down the process of invasion. Such a conclusion is validated by the marginal variability of array-induction resistivity measurements observed in the simulations of OBM invasion compared to those of WBM invasion. Finally, Chapter 7 summarizes the concluding remarks and recommendations stemming from this dissertation.

1.6 LIST OF PUBLICATIONS

Several journal and conference papers have been published or submitted for review as a result of the research work developed in this dissertation:

- **Refereed Journal Publications**

Salazar, J.M., Wang, G.L., Torres-Verdín, C., and Lee, H.J., 2008, "Combined simulation and inversion of SP and resistivity logs for the estimation of connate water resistivity and Archie's cementation exponent," *Geophysics* (in press).

Malik, M., Salazar, J.M., Torres-Verdín, C., Wang, G.L., Lee, H.J., and Sepehrnoori, K., 2008, "Effects of petrophysical properties on array-induction measurements acquired in the presence of oil-base mud-filtrate invasion," *Petrophysics*, v. 49, no. 1, pp. 74-92.

Salazar J.M., Malik, M., Torres-Verdín, C., Wang G.L., and Duan H., 2007, "Fluid density and viscosity effects on borehole resistivity measurements acquired in the presence of oil-based mud and emulsified surfactants," *SPE Journal* (submitted for review).

Salazar, J.M., Torres-Verdín, C., Alpak, F.O., Habashy, T.M., and Klein, J.D., 2006, "Estimation of permeability from borehole array induction measurements: application to the petrophysical appraisal of tight-gas sands," *Petrophysics*, v. 47, no. 6, pp. 527-544.

- **Refereed Conference Proceedings**

Salazar J.M., Malik, M., Torres-Verdín, C., Wang G.L., and Duan H., 2007, "Fluid density and viscosity effects on borehole resistivity measurements acquired in the presence of oil-based mud and emulsified surfactants," paper SPE 109946 presented at the SPE Annual Technical Conference and Exhibition, Anaheim, California, November 11-14, 16 p.

Malik, M., Salazar, J.M., Torres-Verdín, C., Wang, G.L., Lee, H.J., and Sepehrnoori, K., 2007, "Influence of petrophysical and fluid properties on array-induction measurements acquired in the presence of oil-base mud-filtrate invasion," paper AAA presented at the 48th Annual Logging Symposium: Society of Petrophysicist and Well Log Analysts, Austin, TX, June 3-6, 16 p.

Salazar, J.M., Wang, G.L., Torres-Verdín, C., and Lee, H.J., 2007, "Combined simulation and inversion of SP and resistivity logs for the estimation of connate water resistivity and Archie's cementation exponent," paper H presented at the 48th Annual Logging Symposium: Society of Petrophysicist and Well Log Analysts, Austin, TX, June 3-6, 16 p.

Salazar, J.M., Alpak, F.O., Torres-Verdín, C., Habashy, T.M., and Klein, J.D., 2005, "Automatic estimation of permeability from array induction measurements: applications to field data," paper FF presented at the 46th Annual Logging Symposium: Society of Petrophysicist and Well Log Analysts, New Orleans, LA, June 26-29, 16 p.

Chapter 2: Combined Simulation and Inversion of SP and Resistivity Logs for the Estimation of Connate Water Resistivity and Archie's Cementation Exponent

Knowledge of initial water saturation is necessary to estimate original hydrocarbon in place. Reliable assessment of this petrophysical property is possible when rock-core measurements of Archie's parameters, such as saturation exponent (n) and cementation exponent (m), are available. In addition, chemical analysis of formation water is necessary to measure connate water resistivity (R_w). Such measurements are seldom available in most applications, and if they are, their reliability may be questionable. This chapter describes a new inversion method to estimate connate water resistivity and Archie's cementation exponent from the combined use of borehole spontaneous potential (SP) and raw array-induction resistivity measurements acquired in water-bearing depth intervals.

2.1 INTRODUCTION

Initial water saturation in hydrocarbon reservoirs has an enormous impact on the calculation and production of original oil in place. When laboratory measurements (core, water analysis, etc.) are available, this variable is properly constrained. However, such measurements are not always available, and if they are, their reliability may be questionable. Therefore, there is a strong need for alternative methods to estimate thee parameters prior to calculating initial water saturation.

Two of the main parameters needed to calculate water saturation are R_w and m, which can be obtained from connate water analysis and special core analysis, respectively. Core measurements are often expensive because they involve the cost of extracting the core sample and subsequent laboratory work. Moreover, measurements of water resistivity are difficult due to the need to acquire connate water samples when wells are already in production and water-injection/steam-flood have been applied to enhance production. Fluid samples taken by fluid acquisition tools are often contaminated with mud-filtrate and/or hydrocarbon.

In the early days of formation evaluation, SP and resistivity measurements were the only borehole measurements available to log analysts or petrophysicists (Doll, 1949). One of the first physical models of SP was developed using a resistor network (Segesman, 1962), where dipole layers were simulated using voltage sources. Zhang and Wang (1997 and 1999) developed a finite-element algorithm to simulate SP measurements using the vector and scalar potential theory. Their algorithm successfully reproduced the resistor model developed by Segesman.

In this chapter, we simulate SP measurements using Zhang and Wang's algorithm and resistivity measurements with the Numerical-Mode Matching Method (Chew *et al*., 1984; Zhang *et al*., 1999). We use raw borehole-corrected array-induction resistivity (AIT[1]) measurements and consider the effect of invasion and layer thickness on both resistivity and SP. Our objective is to calculate R_w and m for a field data set acquired in a water-bearing clastic formation based on the combined inversion of SP and raw array-induction measurements. The estimation method is based on quantitative simulations and interpretation of the measurements with realistic physical assumptions and not on qualitative interpretations. Additionally, in order to benchmark the technique, values of R_w obtained with this method are compared to those obtained with Pickett's plots (Pickett, 1966). Finally, we give a summary of the possible applications of the interpretation method developed in this chapter.

---

[1] Mark of Schlumberger

2.2 RESISTIVITY MODELING AND INVERSION

The purpose of resistivity modeling (forward modeling) and inversion is to estimate the invaded-zone (R_{xo}) and virgin-zone (R_t) resistivities and the radius of invasion (r_{inv}) from raw array-induction conductivity (inverse of resistivity) measurements. Figure 2.1 shows the subsurface model assumed in the simulations. Initially, we assume a single-layer model and a piston-like radial profile of invasion. The system is bounded at the top and bottom by shale beds (shoulders) with resistivities equal to R_{shtop} and R_{shbot}, respectively. Also, the model is radially bounded by a borehole with fluid resistivity equal to R_m and the virgin zone whose resistivity is one of the main inputs necessary to estimate water saturation.

2.2.1 Forward Model

Induction tools measure formation conductivity (σ) by inducing low-frequency electric currents into the formation surrounding the borehole. In this chapter, we adopt a 2D axial-symmetric model. In such a model, current loop sources reside at the center of borehole with a magnetic moment pointing upward; the conductivity is invariant in the azimuthal direction. Sedimentary rocks are generally non-magnetic, hence the magnetic permeability (μ) is assumed equal to the vacuum magnetic permeability (μ_0). As a result, the electric field comprises only the azimuthal component (E_φ) and varies only in the meridian plane. Assuming that there is only one source current loop, with radius r_s and vertical position z_s, the governing equation in cylindrical coordinates (r,z) for E_φ is given by

$$\left[\frac{\partial}{\partial r}\frac{1}{r}\frac{\partial}{\partial r}r+\frac{\partial^2}{\partial z^2}+k^2\right]E_\varphi\left(r,z;r_s,z_s\right)=-i\omega\mu_0 I\delta\left(r-r_s\right)\delta\left(z-z_s\right), \qquad (2.1)$$

where I is the electric-current intensity, δ is Dirac's delta function, ω is angular frequency, $k^2 = i\omega\mu_0\sigma$, $i = \sqrt{-1}$, and the time convention $e^{-i\omega t}$ is assumed, where t is time. The boundary condition is $E_\varphi(r,z)|_{\partial\Omega} = 0$, where $\Omega = \{(r,z)|0 \le r < \infty, -\infty < z < \infty\}$.

We assume a piecewise-constant spatial distribution of electrical conductivity, i.e.,

$$\sigma(r,z) = \sigma_0(r)H(z_1 - z) + \sigma_M(r)H(z - z_M) + \sum_{m=1}^{M-1} \sigma_m(r)\left[H(z - z_m) - H(z - z_{m+1})\right], \quad (2.2)$$

where $H(z)$ is the Heaviside function and σ_0 and σ_M are the conductivities of the first and last layers, respectively. There is a total of $M+1$ horizontal layers with boundaries z_1, z_2, …, z_M, and layer conductivities given by

$$\sigma_m(r) = \sigma_{mud}H(r_w - r) + \sigma_{t,m}H(r - r_{inv,m}) + \sigma_{xo,m}(r)\left[H(r - r_w) - H(r - r_{inv,m})\right],$$

$$m = 0,1,...,M \;,$$

where r_{inv} is the radial length of invasion, r_w is the borehole radius, σ_{mud} is the borehole conductivity, and σ_{xo} and σ_t are the invaded- and virgin-zone conductivities, respectively.

We make use of the Numerical-Mode Matching Method (NMM) to solve the above 2D simulation problem (Chew *et al.*, 1984; Zhang *et al.*, 1999). This algorithm combines a 1D finite-element solution in the radial direction with an analytical solution in the vertical direction. When augmented by amplitude and slope[2] basis functions (Zhang *et al.*, 1999), the NMM is hundreds of times more computer efficient than either 2D finite-element or finite-difference methods.

---

[2] One function describes the amplitude and the remaining function describes the slope of the basis function at nodal points.

2.2.2 Inversion

Inversion of array-induction resistivity measurements is posed as the minimization of a quadratic cost function that comprises an additive term that weighs the data residuals and one additive term introduced to stabilize the inversion in the presence of noisy and sparsely sampled measurements. In this chapter, we adopt the quadratic cost function given by

$$C\left(\bar{\mathbf{x}}\right)=\frac{1}{2}\left\{\left\|\bar{\mathbf{e}}\left(\bar{\mathbf{x}}\right)\right\|^2+\lambda^2\left\|\bar{\mathbf{x}}\right\|^2\right\}, \tag{2.3}$$

where $\bar{\mathbf{x}}$ includes the unknown model parameters (layer-by-layer values of R_{xo}, R_t, and r_{inv}), λ^2 is the regularization (stabilization) parameter, and $\bar{\mathbf{e}}$ is the vector of data residuals given by

$$\bar{\mathbf{e}}\left(\bar{\mathbf{x}}\right)=\bar{\mathbf{d}}\left(\bar{\mathbf{x}}\right)-\bar{\mathbf{d}}^o .$$

In the above expressions, $\bar{\mathbf{d}}\left(\bar{\mathbf{x}}\right)$ contains the indexed numerically simulated measurements and $\bar{\mathbf{d}}^o$ contains the corresponding indexed field measurements (raw AIT conductivities). For the estimation of layer resistivities we assume that layer boundaries are known *a priori*.

We approach the minimization of the quadratic cost function given by equation (2.3) using the distorted Born iterative method (DBIM) (Chew and Liu, 1994). The computation of sensitivities (entries of the Jacobian matrix) is crucial to the solution of the nonlinear minimization problem by iterative linear steps. We now describe the procedure adopted in this chapter for the calculation of sensitivities.

Consider a generic single-transmitter single-receiver induction system. Let r_T be the radius and z_T be the vertical location of the transmitter. Likewise, let r_R and z_R be the radius and vertical location of the receiver, respectively. When applying a perturbation to the background conductivity (σ^0), the corresponding perturbation of apparent conductivity (σ_a) is given by (Zhang, 1984)

$$\Delta\sigma_a = \int_0^{\infty}\int_{-\infty}^{\infty} drdz\ g(r,z)\Delta\sigma(r,z), \tag{2.4}$$

where $g(r,z) = \mathrm{Re}\left\{-\frac{2\pi\omega^2\mu_0^2 I}{\mathrm{K}} rG(r,z;r_R,z_R)G(r,z;r_T,z_T)\right\}$, K is the tool constant, $G(r,z;r_s,z_s)$ is the Green's function that satisfies equation (2.1) with the right-hand side replaced with $-\delta(r-r_s)\delta(z-z_s)$, and $\Delta\sigma = \sigma - \sigma^0$ is a perturbation of the background conductivity. Substitution of equation (2.2) into equation (2.4) yields

$$\begin{aligned}
\frac{\partial\sigma_a(r,z)}{\partial\sigma_{xo,m}} &= \int_{r_w}^{r_{inv,m}}\int_{z_m}^{z_{m+1}} drdz\ g(r,z), \\
\frac{\partial\sigma_a(r,z)}{\partial\sigma_{t,m}} &= \int_{r_w}^{\infty}\int_{z_m}^{z_{m+1}} drdz\ g(r,z), \text{ and} \\
\frac{\partial\sigma_a(r,z)}{\partial r_{inv,m}} &= \left(\sigma_{xo,m} - \sigma_{t,m}\right)\int_{z_m}^{z_{m+1}} dz\ g\left(r_{inv,m}, z\right),
\end{aligned} \tag{2.5}$$

where $\sigma_{xo,m}$ and $\sigma_{t,m}$ are invaded- and virgin-zone layer conductivities, respectively, and $r_{inv,m}$ is the radius of invasion for each layer.

In the above equations, we assume that the formation boundary z_{m} is known. Initially in the DBIM, the Jacobian matrix, whose entries are given by equation (2.5), is re-calculated after updating the conductivity distribution (Chew and Liu, 1994). Since the induction problem is quasi-linear (Zhang, 1984), the Green's function is approximated with that of a homogeneous medium penetrated by a borehole and fixed for all iteration steps. Consequently, at each step the Jacobian matrix is reset by evaluating only the three integrals given by equation (2.5). This approach represents a highly cost-effective process because the repeated evaluation of $g(r,z)$ is not necessary. For the inversion, we assume that σ_{mud} and r_w are known and that the conductivity of the homogeneous medium is equal to 0.01 S/m. The above strategy greatly reduces the computer cost required by the calculation of derivatives.

We invoke the multiplicative regularization technique described by Habashy and Abubakar (2004) to calculate the regularization parameter included in the quadratic cost function (equation 2.3) with the relationship

$$\lambda^2 = \frac{\left\| \bar{\mathbf{e}}\left(\bar{\mathbf{x}}\right) \right\|^2}{\beta},$$

where β is a constant that can be determined with numerical experiments and in our case is equal to 2.0. In thick formations (over hundreds of feet thick) containing many layers, the inversion process acts as a depth window sliding over the data set layer-by-layer. This is possible because induction is primarily a localized measurement, namely, apparent conductivity is mostly affected by layers close to the measurement point whereas the effect of layers far from the measurement point is comparatively small.

2.3 MODEL OF SPONTANEOUS POTENTIAL

The SP has four main components (Hallemburg, 1971): the diffusion potential, the membrane or Nernst potential (both diffusion and membrane are known as the electrochemical potentials), the electro-kinetic or streaming potential, and the oxidation/reduction potential (redox). Electro-kinetic and redox potentials are negligible in borehole applications compared to the electrochemical potentials. In this chapter, we assume that the total potential measured by a borehole SP tool is solely the sum of the membrane and diffusion potentials (Wyllie and Southwick, 1954).

In a permeable zone at borehole conditions, the maximum differential potential (in absolute value) is known as the static SP (*SSP*). The *SSP* at borehole conditions is measured with respect to the shale baseline (Pirson, 1963) and in mV units is given by

$$SSP \cong -70.7 \cdot \left(\frac{460 + T_F}{537} \right) \log \left(\frac{R_{mfe}}{R_{we}} \right), \tag{2.6}$$

where R_{we} designates the equivalent water resistivity, R_{mfe} is the equivalent mud-filtrate resistivity, and T_F is the formation temperature in ^{o}F. We use equation (2.6) to estimate R_{we} via the combined inversion of SP and resistivity measurements.

2.3.1 Modeling and Inversion of SP

The *SSP* is an electromotive force due to electric dipole layers distributed along the borehole wall, invasion fronts, and formation boundaries. In this study, vector potential theory (Zhang and Wang, 1997 and 1999) is used to compute SP in a water-base mud-filled borehole. Accordingly, electric dipole layers that could extend to infinity are replaced by magnetic current rings located at the intersection points of the borehole wall, invasion fronts, and formation boundaries. In cylindrical coordinates (*r,z*), the governing equation is given by

$$\frac{1}{2\pi} \left[\frac{\partial}{\partial r} \frac{1}{r\sigma} \frac{\partial V}{\partial r} + \frac{\partial}{\partial z} \frac{1}{r\sigma} \frac{\partial V}{\partial z} \right] = -\varepsilon_{SSP} \delta\left(r - r_s\right) \delta\left(z - z_s\right), \tag{2.7}$$

where V is the current potential (Zhang and Wang, 1997 and 1999), σ is the electrical conductivity of the formation, ε_{SSP} is the total potential difference across dipole layers, and r_s and z_s are the radius and vertical position, respectively, of a source in the meridian plane representing a magnetic current ring in 3D space. We use the 2D finite-element method to solve equation (2.7) with a frontal solver to expedite the solution of the resulting linear system of equations.

Results from resistivity inversion are directly used in the inversion of SP measurements. In addition, we assume that mud resistivity, borehole radius, and layer boundary location are *a priori* information determined from other measurements.

Therefore, in the SP inversion, we only invert for the magnitudes of *SSP*. From equation (2.7), we realize that (a) the SP response is linear with respect to the source magnitude and (b) when there are many sources, the total SP response is the superposition of SP responses originating separately from all sources. Thus, one can write the equation for SP (SP_n) as

$$SP_n = \sum_{m=1}^{M} \varepsilon_{SSP,m} SP_{nm}, \tag{2.8}$$

$$n = 1, 2, \ldots, N,$$

where N is the total number of SP measurements, M is the total number of SP sources, $\varepsilon_{SSP,m}$ is the magnitude of the potential difference for the m-th SP source, and SP_{nm} is the response to a unit SP source with radius $r_{s,m}$ and vertical position $z_{s,m}$, which is obtained by solving equation (2.7). Equation (2.8) can be written in matrix notation as

$$\overline{\overline{\mathbf{C}}}\,\overline{\mathbf{y}} = \overline{\mathbf{b}}, \tag{2.9}$$

where $\overline{\overline{\mathbf{C}}} = \left(SP_{nm}\right)^{N\times M}$, $\overline{\mathbf{y}} = \left(\varepsilon_{SSP,m}\right)^{M\times 1}$, and $\overline{\mathbf{b}} = \left(SP_n\right)^{N\times 1}$. Because the coefficient matrix $\overline{\overline{\mathbf{C}}}$ is rectangular, we use the generalized singular value decomposition (SVD) method to solve equation (2.9). Accordingly, the solution of the eigenvalue problem is given by

$$\overline{\mathbf{y}} = \overline{\overline{\mathbf{V}}}\,\overline{\overline{\mathbf{\Sigma}}}^{-1}\,\overline{\overline{\mathbf{U}}}^{T}\,\overline{\mathbf{b}},$$

where $\overline{\overline{\mathbf{U}}} \in R^{N\times M}$ and $\overline{\overline{\mathbf{V}}} \in R^{M\times M}$ are two unitary matrices formed by eigenvectors, $\overline{\overline{\mathbf{\Sigma}}} \in R^{M\times M}$ is a diagonal matrix that consists of singular values obtained from the SVD, and the superscript T designates the transpose of a matrix. We assume that SP sources are far from each other, thereby no truncation on the spectrum of singular values is necessary, whereupon matrix $\overline{\overline{\mathbf{C}}}$ is invertible.

Figure 2.2 shows a multi-layer subsurface model (heterogeneous formation) that includes three invaded layers with different radii of invasion and resistivities for each cylindrical and vertical layer. The resistivity of each radial block (R_{xo} and R_t), the radius of invasion, and the *SSP* at each layer boundary are the properties estimated with the combined inversion of SP and resistivity measurements.

2.3.2 Comments on the Assumptions and Limitations of the Simulation of SP Measurements

The SP sources assumed in our algorithm are exactly the same ones used to construct the SP-3 Schlumberger's chart (Schlumberger, 1991). That is to say, they are dipole layers that could extend to infinity from the borehole wall or from invasion fronts. Under the theory of current potential, these dipole layers are equivalent to many infinitesimal rings centered on the borehole axis. Physically, they are static magnetic current rings which drive the flow of electric current in both the borehole and the formation. Such infinitesimal current rings and dipole layers are mathematically equivalent to each other. However, infinitesimal current rings are more amenable to numerical simulation. The dipole-layer assumption for SP sources has been commonly used in log interpretation. Such an approach will continuously be used until a better assumption is introduced in the SP theory, which should be more physically complete, and numerically easier to implement than the current one.

In modern induction tools, the reliability of SP measurements can be compromised due to the short distance that exists between the SP electrode and the grounded metal. However, the effect of that distance becomes appreciable only when formations are highly resistive (above 100 Ω·m). The field case that we consider in this chapter corresponds to a very conductive formation. The resistivity is generally less than 20 Ω·m, whereby the effect of short distance between the SP electrode and the grounded metal is negligible. Considering that the favorable measurement condition for induction tools is generally low-resistivity formations, it is reasonable to assume that the effect of short distance between the SP electrode and the grounded metal is always negligible as long as this condition is satisfied.

2.4 ESTIMATION OF CONNATE WATER RESISTIVITY AND ARCHIE'S CEMENTATION EXPONENT

Field SP and raw AIT measurements, borehole, and mud properties are used as inputs to the combined SP-Resistivity inversion. Resistivity-inverted results are input to the SP inversion. In order to estimate connate water resistivity, the inversion is carried out in a wet sand interval. Once the *SSP* is calculated at each layer boundary from the inverted SP, the corresponding equivalent water resistivity is calculated with the maximum negative *SSP* via equation (2.6). Subsequently, an empirical correlation from log interpretation charts (Schlumberger, 1991; Bigelow, 1992) is used to estimate R_w, namely,

$$R_w = \frac{R_{we} + 0.131 \cdot 10^{\left[\frac{1}{\log(T_F/19.9)} - 2\right]}}{-0.5 \cdot R_{we} + 10^{\left[\frac{0.0426}{\log(T_F/50.8)}\right]}}. \tag{2.10}$$

In our method, we assume that formation water is a solution of NaCl. Therefore, equation (2.10) is not valid for all types of formation water or waters with very high salt concentration (above 220,000 ppm). Additional transformations are needed for the case of water with ion components other than those of NaCl (Bigelow, 1992).

For the estimation of the cementation exponent, we initially assume a clean (shale-free) 100% water-saturated clastic rock. Archie's equation (Archie, 1942) is used to compute the cementation exponent without specific adjustments for the presence of shale, as follows:

$$m = \frac{1}{\log(\phi)} \log\left(\frac{R_w}{R_t}\right), \tag{2.11}$$

where ϕ is the non-shale porosity taken as an average in the interval of analysis and the tortuosity factor a (not shown in equation 2.11) is assumed equal to 1. On the other hand, when the presence of clay is considered, we use the dual-water model for shaly sands (Clavier *et al.*, 1984) since several of its governing parameters can be calculated from well logs (Dewan, 1983), namely,

$$m = \frac{1}{\log(\phi)} \log\left(\frac{R_w}{R_t}\left[1 - S_b\left(1 - \frac{R_w}{R_b}\right)\right]^{-1}\right), \tag{2.12}$$

where S_b and R_b are bound-water saturation and bound-water resistivity (a function of shale resistivity), respectively. Equation (2.12) is valid in wet sands and reduces to equation (2.11) in clean sands (where $S_b = 0$). Figure 2.3 is a flow diagram that summarizes the steps used to estimate connate water resistivity and cementation exponent via the combined inversion of resistivity and SP measurements.

2.5 FIELD CASE OF STUDY

We select a formation with a water-bearing depth zone to test the developed method on field measurements. The case under analysis corresponds to a North Louisiana (U.S.) fairly clean clastic formation. The reservoir is 100% water-saturated with moderately high salt concentration (>100,000 ppm). Table 2.1 is a summary of the thickness and average petrophysical properties of the formation. Figure 2.4 displays the well logs and estimated porosity and permeability for the formation under analysis. Well logs include gamma ray (GR), SP, and AIT resistivity (2-foot vertical resolution). Porosity is calculated from density-neutron logs via a non-linear dual-mineral (shale-quartz) model and permeability from porosity and irreducible water saturation using a modified Timur-Tixier equation (Balan *et al*., 1995). Water saturation (S_w) is not shown here since the formation is completely water-saturated ($S_w=100\%$).

2.5.1 Combined Inversion

We make use of raw borehole-corrected AIT measurements to perform the combined inversion method. The formation under analysis was divided into three petrophysical layers or flow sub-units. Layer selection was based upon main resistivity changes and petrophysical properties (porosity-permeability). For resistivity inversion, inputs are layer boundaries, borehole radius and conductivity, and raw AIT conductivity data. Inversion results are values of R_{xo}, R_t, and r_{inv} for each layer, which are additional inputs to the SP inversion. Once the inversion is finished, we obtain values of *SSP* for each layer boundary. Table 2.2 summarizes the inversion results for resistivity and radius of invasion. Figure 2.5 shows the results of resistivity inversion together with the comparison of field and simulated SP measurements at the conclusion of the inversion. Figure 2.6 compares field to simulated apparent array-induction resistivity measurements calculated with the inverted values of r_{inv}, R_{xo}, and R_t.

2.5.2 Assessment of *m* and R_w

Equivalent water resistivity is obtained from the inverted *SSP* via equation (2.6). Subsequently, connate water resistivity is computed at reservoir temperature using equation (2.10). Archie's (equation 3.11, for clean sands) and Dual-Water (equation 3.12, for shaly-sands) models yield *m* using the updated values of R_w and R_t obtained from inversion and porosity from logs. Table 2.3 summarizes the inverted values of R_w and *m*.

When comparing the values of *m* obtained with Archie's equation to the one obtained with the Dual-Water equation, we see a reduction in the cementation exponent. The resulting value of *m*, decreasing with increasing shaliness in the Dual-Water model, depends on the ratio between bound-water resistivity and true-formation resistivity (R_b/R_t). Figure 2.8 in Clavier *et al.* (1984) shows no clear tendency of the variations of m as a function of shale content; measurements are scattered between $m = 1.5$ and $m = 2.5$ for a volumetric shale concentration between 0 and 0.50. Therefore, values of m with opposite behavior to the one observed in this chapter are feasible.

2.5.3 Appraisal of R_w

In order to cross-validate the inverted value of connate water resistivity we constructed a traditional Pickett plot (Pickett, 1966). The latter is a plot of $\log(R_t)$ vs. $\log(\phi)$ which yields a straight line whose slope is equal to $-m$ and the ordinate at $\log(\phi)=0$ yields $\log(R_w)$ (assuming $a = 1$). Figure 2.7 displays the corresponding Pickett plot for the formation under analysis. The value of R_w obtained from the Pickett plot was 0.037 Ω·m at 61 ^{o}C. Such result represents a difference of 12% with respect to the value obtained from inversion. The relatively small difference between the Pickett plot calculation and the inversion result lends credence to the reliability of the combined inversion method developed in this chapter.

2.5.4 Applications of Inversion Results

Ideally, in a reservoir penetrating a water zone, the objective is to use the results of inversion (R_w and m) to estimate water saturation in the upper hydrocarbon zone within the same geological formation. The method, parameters, and simulation approach used to compute water saturation, porosity, and initial guess of permeability are described by Salazar *et al.* (2006). Either resistivity matching or inversion (Salazar *et al.*, 2005; Salazar *et al.*, 2006) using the physics of mud-filtrate invasion (Alpak *et al.*, 2003; Wu *et al.*, 2005) are alternative methods for estimating permeability. Values obtained from inversion provide a starting point to accurately estimate water saturation and layer-by-layer permeability. Correct assessment of water saturation leads to reliable estimation of in-place hydrocarbon saturation. Moreover, accurate estimation of permeability is necessary to select perforation intervals, layers for fluid injection, and to forecast production.

2.6 CONCLUSIONS

The combined inversion of resistivity and SP measurements is a reliable method to estimate R_w and m in water-bearing formations. Results obtained from the inversion were consistent with those obtained from Pickett's plots. The difference between the estimates obtained with the two methods was of the order of 10%.

The combined inversion method is highly recommended in zones where NaCl is the most abundant solution component and where connate salt concentration does not change in short depth intervals. This method of inversion works very well in high-permeability, thick formations and when connate water exhibits medium to high concentration of NaCl.

In depth zones where the most abundant salt components are different from NaCl (e.g., $CaCl_2$, KCl, etc.) equation (2.6) is not valid. In addition, when the salt concentration of mud-filtrate and connate water are similar, the deflection of the SP curve is marginal and, therefore, the inversion method is not recommended. In low-permeability formations ($k < 5$ md) the electrokinetic components of the SP may become important for the total contribution to *SSP* and hence could be needed in the formulation before applying the inversion method introduced in this chapter.

In the absence of water zones, resistivity inversion can still be used to estimate R_{xo} and R_t for the refined calculation of initial water saturation. This calculation method can be useful in the petrophysical assessment of exploratory and appraisal wells that are normally devoid of core samples and laboratory measurements.

The fact that service companies do not charge for the acquisition of SP measurements contributes to the fact that neither service companies nor clients pay the attention that the SP deserves. Commonly, SP measurements consist of extremely smooth and low quality curves that make their interpretation more challenging and hence may have an erroneous impact on the application of the inversion method described in this chapter.

Table 2.1: Summary of average petrophysical properties assumed for the case of study.

Property	**Units**	**Values**
Thickness	ft	58
Interconnected porosity	fraction	0.30
Water saturation	fraction	1.0
Volumetric shale concentration	fraction	0.02-0.10
Permeability	md	100-2000

Table 2.2: Summary of inversion results for the case of study.

Thickness	R_{xo}	R_t	r_{inv}	***SSP***
ft	Ω·m	Ω·m	ft	mV
shoulder	3.7586	3.7586	0	56.4128
12	1.8938	0.5425	1.1519	-6.5244
19	1.1665	0.4849	1.2395	-1.7396
27	1.0916	0.3387	1.7618	-49.3705
shoulder	4.2012	4.2012	0	-

Table 2.3: Calculated values of connate water resistivity and Archie's cementation exponent.

Property	Units	Value
R_w	Ω·m	0.042
Temperature	°F	142
[NaCl]	ppm	105,000
m – Archie	-	1.74
m – Dual-Water	-	1.69
Volumetric shale concentration	fraction	0.10

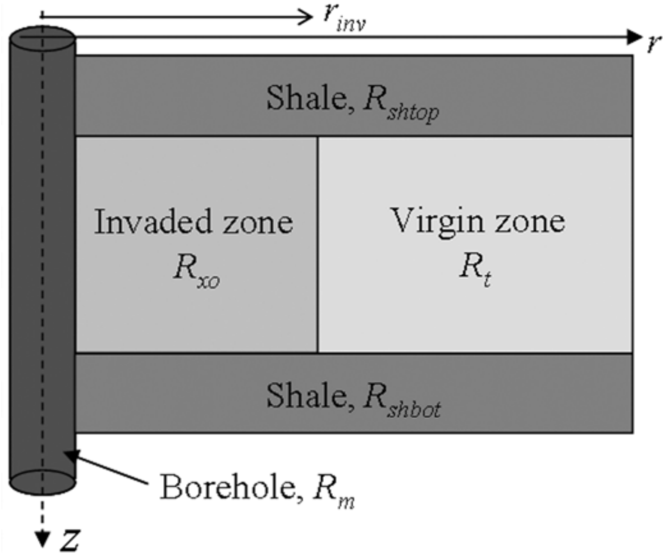

Figure 2.1: Single-layer subsurface model assumed in the simulation and inversion of borehole resistivity measurements. The model assumes a piston-like invasion front.

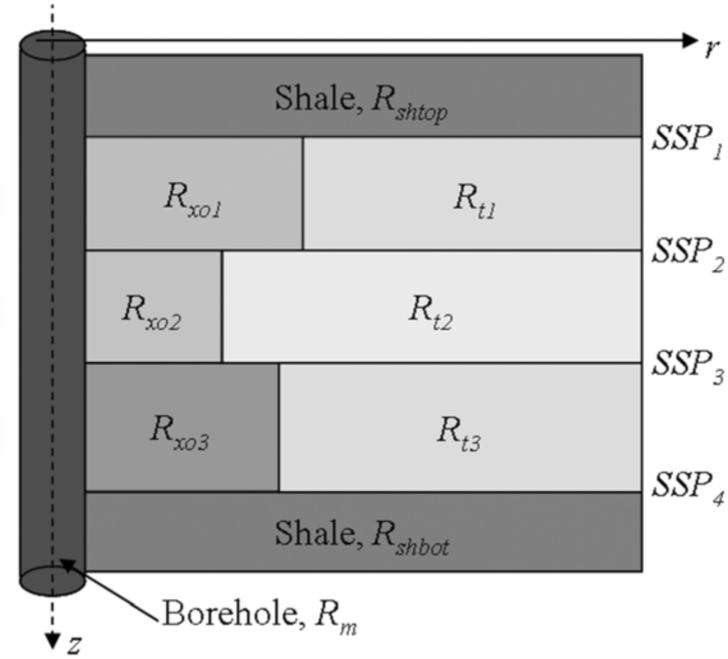

Figure 2.2: Multi-layer subsurface model assumed in the combined simulation and inversion of resistivity and SP measurements.

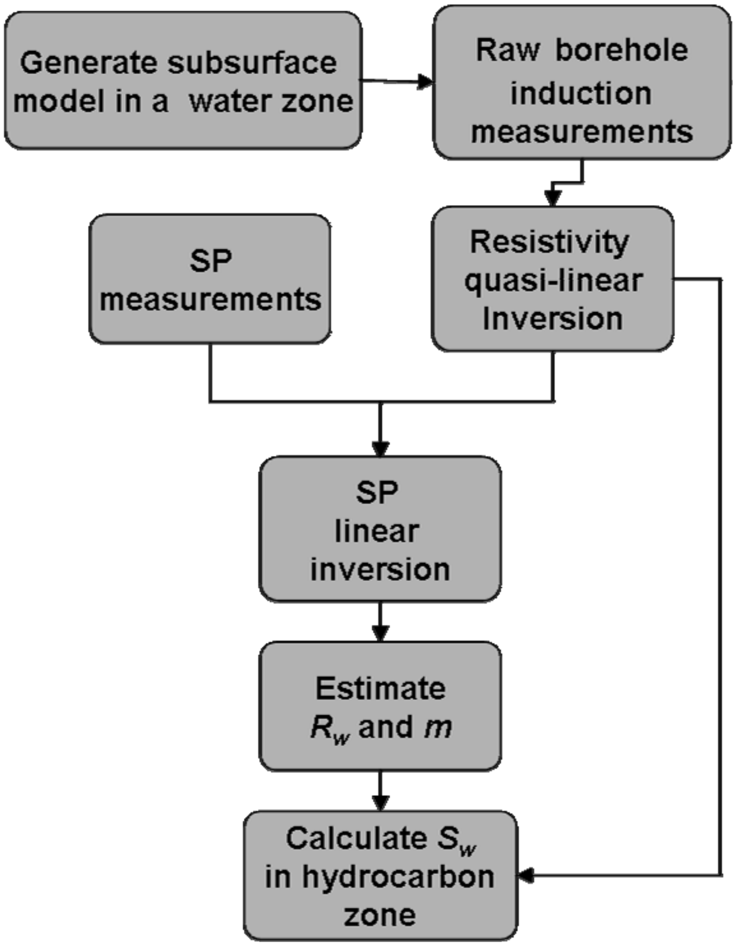

Figure 2.3: Flow chart describing the algorithmic steps included in the combined simulation and inversion of resistivity and SP measurements to estimate R_w and m, and to calculate water saturation in hydrocarbon-bearing zones.

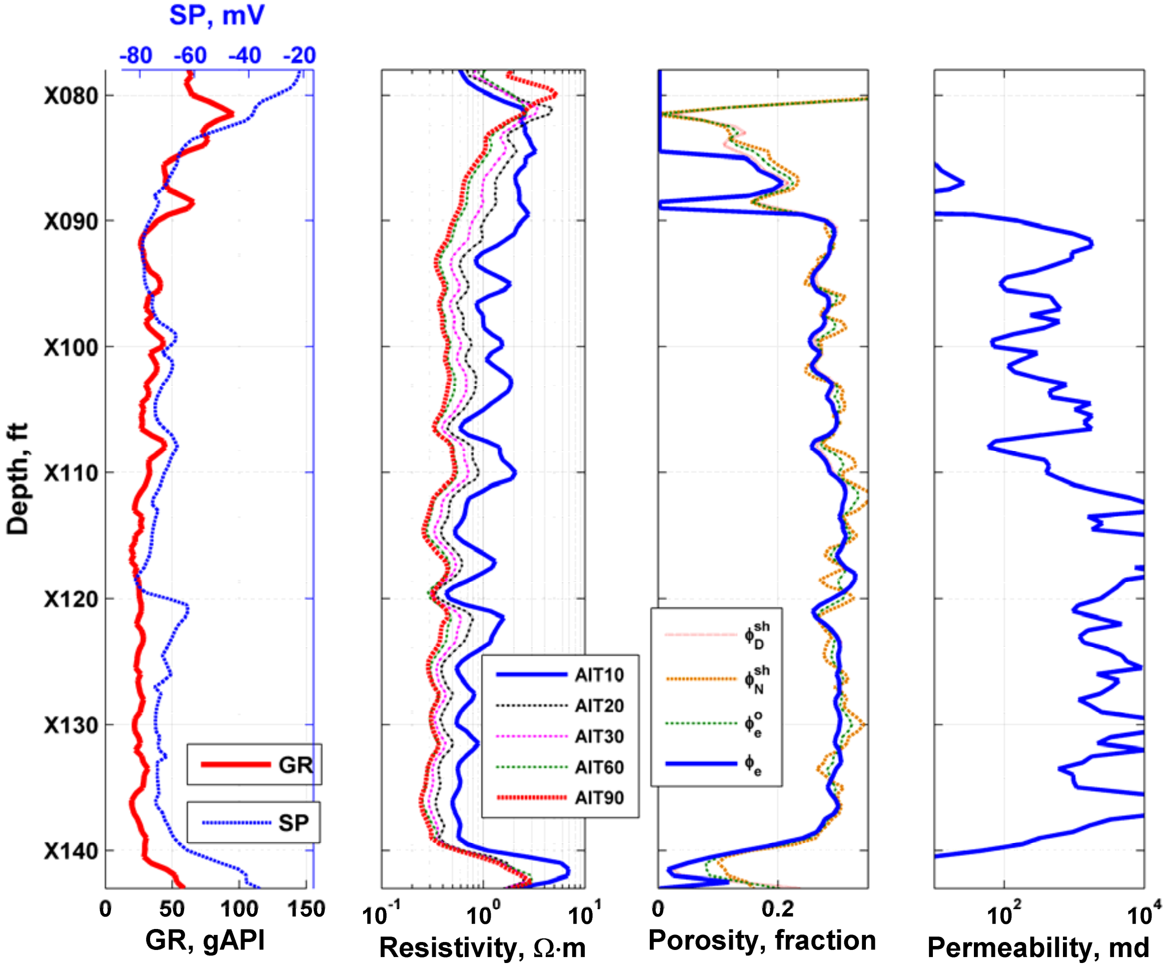

Figure 2.4: Well logs and petrophysical properties for the case of study. Separation of AIT resistivity curves indicates invasion of mud filtrate into the water-bearing sand. The porosity track shows shale-corrected density and neutron porosity (ϕ_D^{sh} and ϕ_N^{sh}), effective initial-guess porosity (ϕ_e^o), and non-shale porosity (ϕ_e) obtained with a nonlinear model that relates density with resistivity.

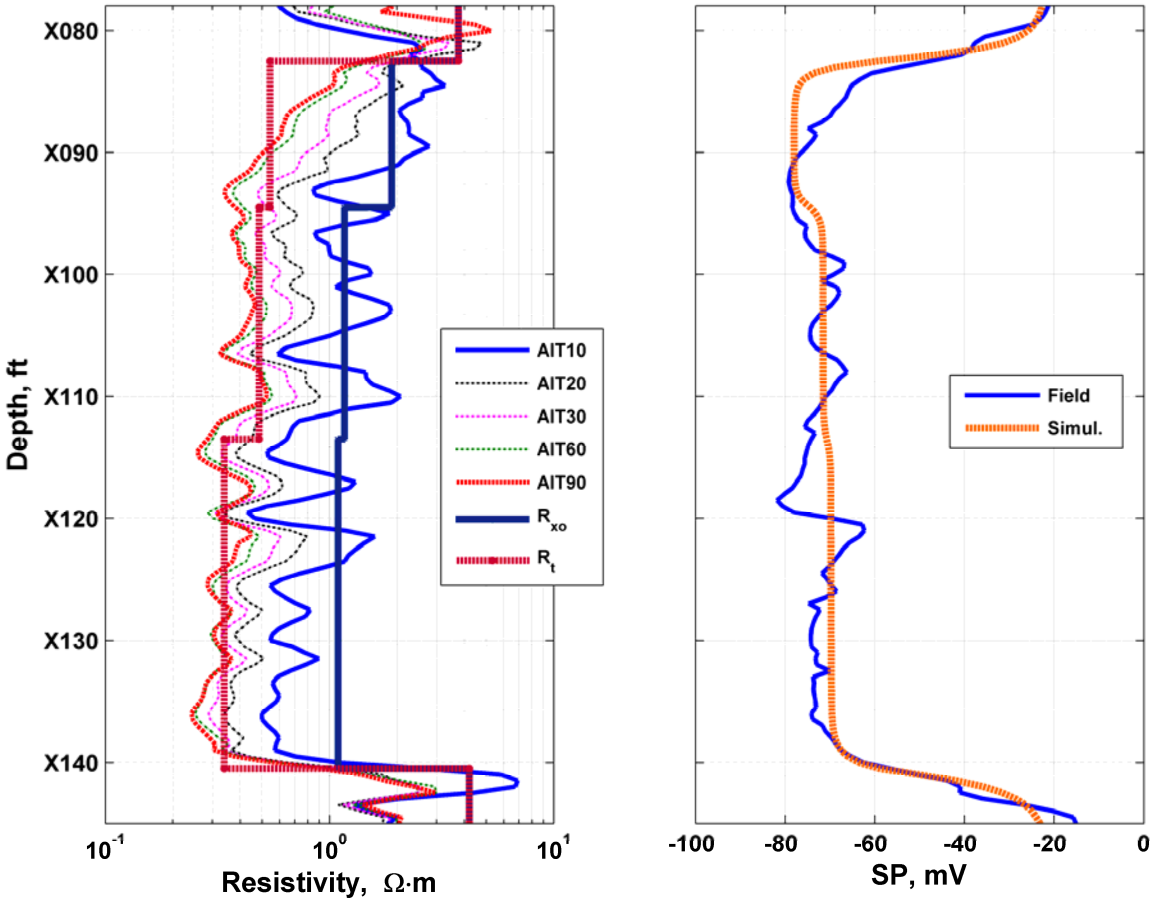

Figure 2.5: Results of the combined inversion of resistivity and SP. The right-hand panel compares inverted R_{xo} and R_t to field AIT (2-foot vertical resolution) measurements and the left-hand panel compares the simulated SP obtained from the inverted *SSP* from field SP measurements.

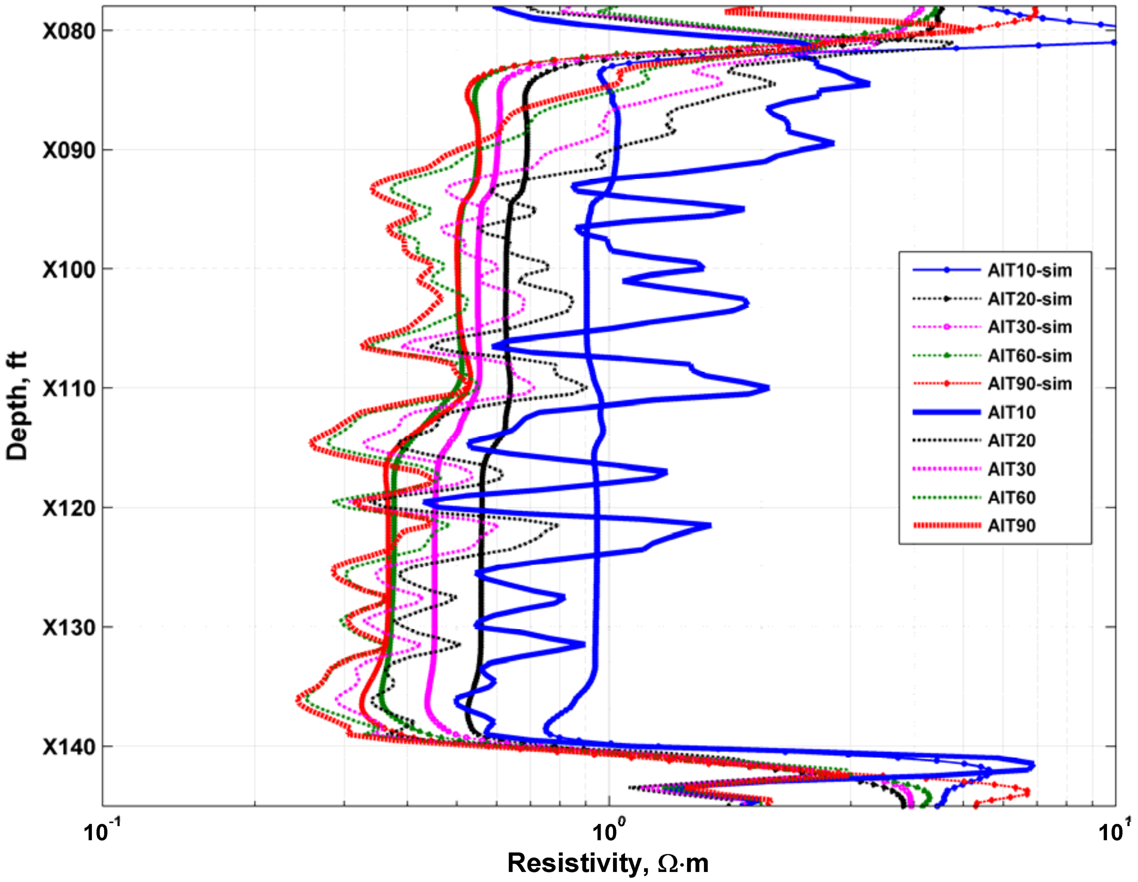

Figure 2.6: Comparison of measured and simulated array-induction logs (2-foot vertical resolution) yielded by the inversion of r_{inv}, R_{xo}, and R_t. The relative separation of the simulated curves agrees well with field data. Because the objective of the inversion was to estimate m and R_w only three petrophysical layers were considered for the inversion, which in turn reduced the accuracy of the match between simulations and field measurements.

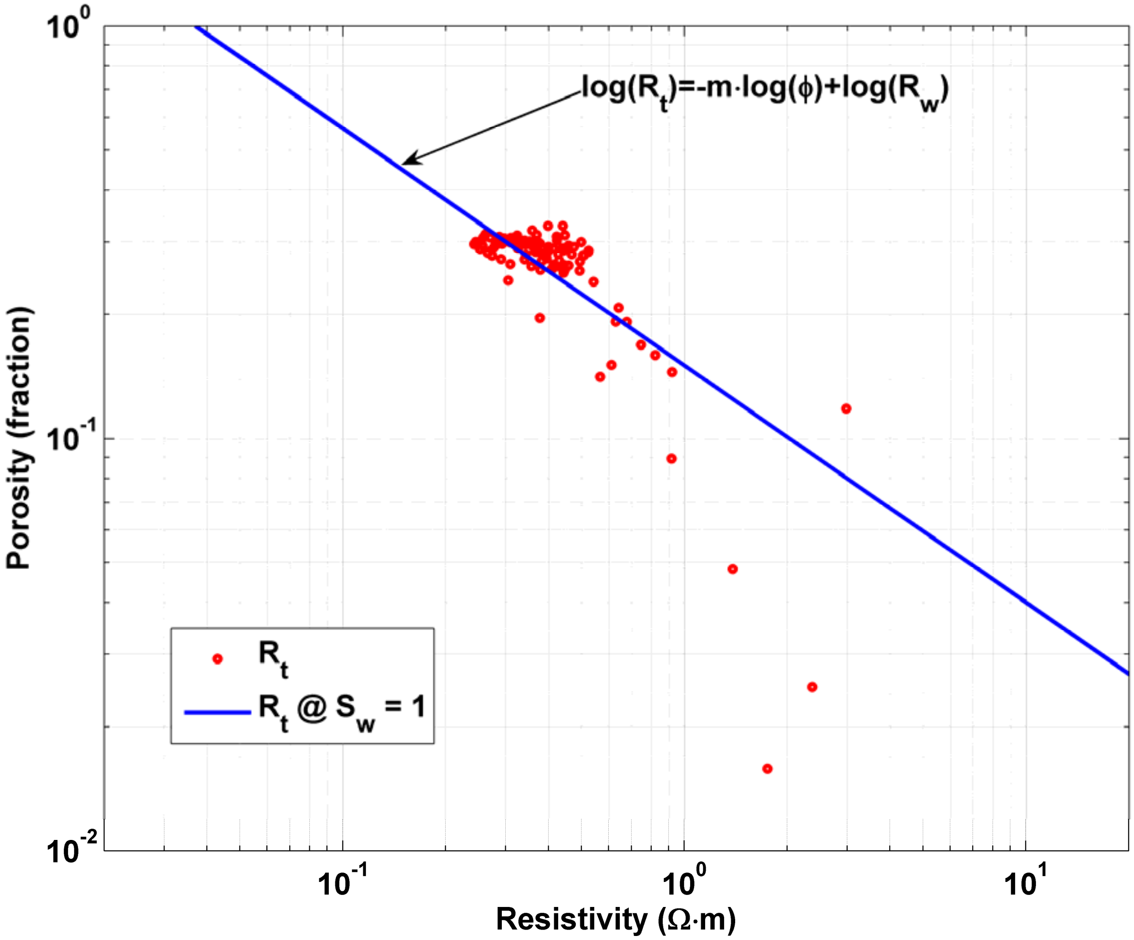

Figure 2.7: Pickett plot used to cross-validate the calculation of connate water resistivity.

Chapter 3: Estimation of Permeability from Borehole Array-Induction Measurements: Application to the Petrophysical Appraisal of Tight-Gas Sands

This chapter describes the successful application of a new petrophysical inversion method to estimate permeability from borehole array-induction measurements. We consider measurements acquired in a North Louisiana tight-gas sand formation subject to water-base mud-filtrate invasion. The inversion methodology incorporates the physics of two-phase immiscible displacement and salt mixing between the invading water-base mud-filtrate and connate water. Moreover, the invasion model honors the physics of mudcake growth as well as the petrophysical properties that govern the process of two-phase three-component flow. The outcome of the inversion is the absolute permeability for each flow sub-unit within a gas-bearing production zone.

3.1 INTRODUCTION

Tight sands comprise important accumulations of natural gas. Similar to conventional oil- and gas-bearing formations, tight-gas sands are associated with complex geological and petrophysical systems that include heterogeneities at all spatial scales. However, unlike conventional oil and gas reservoirs, tight-gas sands usually exhibit unique gas storage and production characteristics. Effective production of these resources is only possible with an accurate description of key reservoir parameters, particularly permeability, capillary pressure, relative permeability, and water saturation (Newsham and Rushing, 2002). The rock formations considered in this chapter correspond to North Louisiana low-permeability tight-gas sand units subject to water-base mud-filtrate invasion.

The main goal of the study is to estimate absolute permeability by quantifying the influence of mud-filtrate invasion on borehole array-induction logs. This process requires the availability of well logs, fluid properties, and rock-core measurements. Rock-core laboratory data are not available for the formation under analysis. Instead, we make use of laboratory measurements from nearby fields penetrating the same geological interval to calibrate the petrophysical properties calculated from well logs and other empirical relationships (S.A. Holditch Associates, 1988 and Luffel *et al*., 1991).

Rock-core measurements are used to synthesize the petrophysical model necessary to simulate the physics of mud-filtrate invasion. Such a model is “calibrated” against the existing suite of wireline logs, especially array-induction logs. Flow sub-units defined from porosity and the initial guess of absolute permeability are taken as horizontal layers to simulate the process of mud-filtrate invasion with a two-dimensional chemical flow simulator that includes the effect of salt mixing between mud filtrate and connate water. We generate spatial distributions of electrical resistivity from the simulated cross-sections of water saturation and salt concentration using Archie’s equation. In turn, these spatial distributions are used to simulate array-induction imager tool (AIT™) measurements acquired across the formation.

Numerical simulation of mud-filtrate invasion has been previously attempted to simulate borehole electromagnetic measurements and to estimate petrophysical properties. Semmelbeck and Holditch (1988) modeled conventional induction resistivity tools in synthetic low-permeability homogeneous formations. Tobola and Holditch (1991) and Yao and Holditch (1996) used a history matching approach to estimate permeability based on the one-dimensional (radial) simulation of time-lapse array-induction resistivity logs for water-base mud invading a gas-saturated low-permeability formation. Salazar *et al*. (2005) estimated permeability in several field examples using the concept of petrophysical flow-units and resistivity matching of a vertically heterogeneous tight-gas sand formation under the effect of water-base mud-filtrate invasion. Non-linear inversion of borehole induction resistivity measurements has been successfully applied using the physics of water-base mud-filtrate invasion for the estimation of permeability from one-dimensional (radial) fractional flow distributions (Ramakrishnan and Wilkinson, 1999), as well as for the estimation of porosity and permeability in two-dimensional axi-symmetric rock formations (Alpak *et al*., 2006 and Torres-Verdín *et al*., 2006) .

In this chapter, we estimate absolute permeability using the inversion algorithm developed by Alpak *et al*. (2006), where estimation of permeability for each layer in a two-dimensional rock formation is posed as a nonlinear minimization problem. We consider limiting values of rock and fluid properties to quantify the impact of the spatial distributions of water saturation and salt concentration on array-induction measurements. Sensitivity analyses are also performed to assess the impact of the assumptions made on mud properties, mudcake growth, time of invasion, capillary pressure, relative permeability, and fluid viscosity on the estimated values of permeability.

The first stage of the study consists of defining rock types by relating geological framework, lithofacies, and petrology to porosity and permeability. The second stage of the work integrates the rock type model with formation evaluation data to define reservoir compartments and flow units (Salazar *et al*., 2005). We integrate logs and rock-core measurements to extend the rock-type model, and to compute continuous storage and flow capacity specific to a given production unit.

The third stage of the work quantifies the influence of mud-filtrate invasion on the spatial distribution of fluids in permeable rocks around the wellbore. Overbalance pressure along with the low porosity of the rock contributes to deep invasion of mud filtrate. In-situ gas saturation of the formation ranges from 40 to 60%, with the remaining pore space occupied by irreducible water saturation. Salinity of mud filtrate is between

1,500 to 3,800 ppm, whereas the salinity of connate water is approximately 160,000 ppm. After 5 days of invasion, spatial distributions of electrical resistivity are calculated from the simulated spatial distributions of water saturation and salt concentration. Subsequently, we simulate array-induction measurements and compare them against actual field measurements.

Simulations of mud-filtrate invasion continue with the only free parameter being average absolute permeability per flow unit. All the remaining petrophysical parameters required by the simulation are either calculated from well logs or extrapolated from the rock-core measurements. We use a modified Timur-Tixier permeability equation (Balan *et al*., 1995) to compute initial values of absolute permeability. These initial permeability values are progressively adjusted in the simulation of mud-filtrate invasion until an acceptable match is reached between the measured and simulated array-induction curves. In the final stage, we perform automatic inversion of permeability from the AIT™ apparent resistivity curves using as starting model the results obtained from manual adjustment of layer permeability values.

3.2 GEOLOGICAL DESCRIPTION

The North Louisiana tight-gas sand formation under analysis consists of very fine- to fine-grained sandstone, shale, and some sandy, fossiliferous oolitic limestone (Finley, 1984). Primary sediments originated from a major influx of terrigenous clastic deposits during the Early Cretaceous. Fluvial deposition by at least two major rivers was responsible for sediment accumulation. The rocks in this formation are texturally mature quartz-arenites and sub-arkose sands (McGowen and Harris, 1984). Interpretation of a large area of the formation suggests global sediment deposition by a system of coalescing deltas prograding from the west, northwest, and north (Finley, 1984). In general, geological cross-sections through the formation show a thick, sand-dominated wedge of sediments mainly consisting of braided stream deposits. Such braided stream facies were reworked by marine transgression when the deltas entered the marine environment (Finley, 1984).

3.3 ASSESSMENT OF WATER SATURATION AND EFFECTIVE POROSITY

We focus the petrophysical analysis to a 20.5-feet thick interval. The formation consists of a relatively clean gas-saturated clastic sequence with connate water salt concentration in the order of 160,000 ppm. Therefore, we use Archie's (1942) equation to compute water saturation without specific adjustments for the presence of shale. Water saturation is given by

$$S_w{}^n = \frac{R_w}{R_t}\frac{a}{\phi^m}, \tag{3.1}$$

where ϕ is effective porosity, R_w is connate water resistivity, R_t is true formation resistivity, a is the tortuosity factor, and m and n are the cementation (lithology) and saturation exponents, respectively. Effective porosity is computed using a dual-fluid dual-mineral nonlinear model given by

$$\hat{\rho}_b = \phi\left[\sqrt[n]{\frac{R_{wxo}a}{\phi^m R_{xo}}}(\rho_1 - \rho_2) + \rho_2\right] + (1 - \phi - C_{sh})\rho_{ma} + C_{sh}\rho_{sh}, \tag{3.2}$$

where $\hat{\rho}_b$ is bulk density, ρ_{ma} is matrix (quartz) density, ρ_{sh} is shale density, ρ_1 is mud-filtrate (fresh water) density, ρ_2 is the density of the gas-mud-filtrate mixture estimated from log interpretation charts (Schlumberger, 1991), R_{wxo} is the invaded zone water resistivity, R_{xo} is the invaded zone resistivity, and C_{sh} is volumetric shale concentration calculated with a linear transformation of the gamma-ray log.

Application of Thomas and Stieber's (1975) methodology to log-computed volumetric shale concentration and porosity indicated that the dominant distribution of clay in the formation was in the form of dispersed shale. We computed an initial guess of effective porosity (ϕ_o) from shale-corrected neutron and density porosity via the formula

$$\phi_o = \sqrt{\frac{1}{2}\left[\left(\phi_N{}^{sh}\right)^2 + \left(\phi_D{}^{sh}\right)^2\right]}, \qquad (3.3)$$

where ϕ_N^{sh} and ϕ_D^{sh} are shale-corrected neutron and density porosity, respectively. Equation (3.2) is solved by minimizing the difference between measured bulk density (ρ_b) and bulk density computed with the initial guess of porosity, i.e.,

$$\min_{(\phi_i)} \sum\left(\rho_{bi} - \hat{\rho}_{bi}\right)^2, \qquad \phi \in [0,1]. \qquad (3.4)$$

The minimum of equation (3.4) yields the best estimate of effective porosity. Water saturation is computed with equation (3.1). Table 3.1 describes the petrophysical and fluid parameters used to apply this methodology. Appendix A describes in more detail the methodology for the assessment of petrophysical properties. In order to assess the value of true formation resistivity devoid of invasion and shoulder-bed effects, we simulated the AIT apparent resistivity measurements assuming a horizontal layer undergoing piston-like invasion. The simulated AIT measurements were compared to field measurements and the values of formation electrical resistivity adjusted until reaching a good match between simulations and measurements. This strategy yielded reliable values of initial water saturation (S_w). Figure 3.1 is a plot of lithology, resistivity, and porosity logs across the depth interval under analysis. Figure 3.2 shows the log of water saturation computed with Archie's equation and resistivity values obtained with forward modeling of AIT apparent resistivity measurements. We believe that the relatively high values of calculated S_w (40%-60%) are due to irreducible water saturation in the formation that could be due to presence of clay and microporosity. Fluid production in the well is mainly gas, hence confirming that the values of computed water saturation correspond to irreducible fluid.

3.4 INITIAL MODEL FOR ABSOLUTE PERMEABILITY

A permeability value (initial guess) is necessary to initialize the simulation of the process of mud-filtrate invasion. Rock-core measurements were only available from nearby gas fields that penetrated the same formation. Such measurements were used to construct the initial guess of permeability. Several approaches were considered to calculate the best initial estimate of permeability (Balan *et al.*, 1995; Haro, 2004). Sensitivity analysis indicated that the generalized Timur-Tixier equation properly reproduced the interplay between porosity, permeability, and irreducible water saturation of rock-core measurements. Accordingly, the relationship between permeability (md), porosity (ϕ, fraction), and irreducible water saturation (S_{wir}, fraction) is given by

$$k = A\frac{\phi^B}{S_{wir}{}^C}, \tag{3.5}$$

where A, B, and C are constants to be determined from a multilinear regression analysis.

Klinkenberg-corrected permeability and porosity were obtained from the available rock-core measurements at 2,000 psi of overburden pressure. We used gas-water capillary pressure curves obtained from the same rock-core measurements to estimate irreducible water saturation. This procedure yielded the following equation for permeability:

$$k = 0.04\frac{\phi^{1.83}}{S_{wir}{}^{2.3}}. \tag{3.6}$$

The degree of confidence for this equation is in the order of 60% based on the correlation coefficient of the multilinear regression. We applied equation (3.6) to well logs using porosity from equation (3.2) and irreducible water saturation[3] computed from (Dewan, 1983)

$$S_{wir} = C_{sh} \frac{\phi_{tsh}}{\phi_t}, \tag{3.7}$$

where ϕ_t is total porosity and ϕ_{tsh} is total shale porosity. An alternative way to estimate S_{wir} is via the general relationship $S_{wir} = \beta C_{sh} + \gamma / \phi_t$, where β and γ are constants to be determined. We used equation (3.7) since it does not require knowledge of additional empirical constants and S_{wir} can be obtained directly from well logs. Moreover, the objective of equation (3.6) is to obtain only an estimate of permeability that will be used as an initial guess for the inversion algorithm. Table 3.2 is a summary of the average petrophysical properties calculated for the interval under study. Figure 3.2 displays the results of the petrophysical analysis with the main curves rendered by the methodology explained above. Finally, Figure 3.3 is a semilog cross-plot of permeability vs. porosity, indicating that the estimated permeability in the well under consideration exhibits a correlation with porosity similar to that of rock-core measurements only in the low-porosity zone.

3.5 SIMULATION OF MUD-FILTRATE INVASION

We use a multiphase chemical flow simulator to calculate the flow rate of mud-filtrate invasion in a manner similar to that of a water injection process. The software used is a modified version of the code UTCHEM developed by The University of Texas at Austin (Delshad *et al*., 1996). This software is a finite-difference simulator referred to as INVADE (Wu *et al*., 2004 and Wu *et al*., 2005) that was specifically developed to

---

[3] Equation (3.7) is only used as an input of equation (3.6) to compute the initial guess of permeability. Based on the explanation given in the previous section, initial water saturation is considered equal to irreducible water saturation. Therefore, the remainder of our analysis is carried out assuming such a saturation condition.

solve the partial differential equations and boundary conditions of immiscible cylindrical flow coupled with mudcake growth.

3.5.1 Radial Grid and Vertical Flow Units

Simulation of mud-filtrate invasion is performed assuming cylindrical flow and permeability isotropy. A two-dimensional finite-difference grid is constructed with 106 logarithmically spaced radial nodes that include shorter radial steps in the near wellbore region. Rock properties are considered constant in the radial direction. In a single-layer case, the vertical grid consists of thin numerical layers to ensure high accuracy in the estimation of the flow rate of mud-filtrate invading the formation.

We make use of a Lorenz plot (Gunter *et al*., 1997) to identify individual flow units in the formation under analysis. Figure 3.4 shows one such plot, describing the relationship between cumulative porosity and cumulative permeability as a function of reservoir thickness. The variable nature of this plot indicates presence of several individual flow sub-units within the formation. Specifically, each segment with a constant slope in the plot identifies an individual flow sub-unit with constant petrophysical properties. Steep slopes in the same plot are associated with high values of flow capacity. Figure 3.5 is an example of the finite-difference grid used in the simulation of mud-filtrate invasion.

3.5.2 Capillary Pressure and Relative Permeability

We use Brooks-Corey (Corey, 1994) two-phase equations to assign water-gas capillary pressure curves to each petrophysical layer. Accordingly, the first imbibition cycle of the capillary pressure curve is given by

$$P_c = P_c^{\,o}\sqrt{\frac{\phi}{k}}\left(1 - S_N\right)^{e_p}, \tag{3.8}$$

where P_c is capillary pressure, P_c^o is the coefficient for capillary pressure, e_p is the pore-size distribution exponent, ϕ is porosity, k is permeability, and S_N is the normalized wetting phase saturation, given by

$$S_N = \frac{S_w - S_{wr}}{1 - S_{wr} - S_{nwr}}, \tag{3.9}$$

where S_{wr} and S_{nwr} are the residual wetting and non-wetting phase saturations, respectively. Water-gas relative permeability curves in the saturated zone are also estimated via Brooks-Corey's equations, namely,

$$k_{rw} = k_{rw}^0 S_N^{\,e_w}, \tag{3.10}$$

and

$$k_{rnw} = k_{rnw}^0 (1 - S_N)^{e_{nw}}, \tag{3.11}$$

where k_{rw} and k_{rnw} are wetting and non-wetting relative permeabilities, k_{rw}^0 and k_{rnw}^0 are relative permeability end points, and e_w and e_{nw} are empirical exponents for each fluid phase. We estimated the three parameters included in Brooks-Corey's equation (exponents, coefficients and end points) from rock-core measurements acquired in a nearby field from the same rock formation. Figure 3.6 is a graphical representation of capillary pressure and relative permeability curves calculated with the equations described above.

3.5.3 INVADE Results

At the outset, the simulation of mud-filtrate invasion is performed assuming a homogeneous flow unit. Petrophysical properties of this flow unit are described in Table 3.2, whereas Table 3.3 describes the corresponding mud-filtrate, mud-cake and formation fluids properties. The simulation of the process of mud-filtrate invasion requires accurate knowledge of the time during which the well was exposed to invasion. According to field reports, the well under analysis was exposed between 3 to 6 days to invasion before the acquisition of resistivity logs.

Several simulation cases for 3, 4, 5, and 6 days of invasion were considered to obtain the best estimate of the rate of mud-filtrate invasion. Figure 3.7 describes the transient behavior of the flow rate of mud-filtrate, mudcake thickness, and pressure across mudcake. The flow rate decays monotonically with time before reaching its steady-state value. In low permeability rock formations (~ 1 - 5 md), laboratory experiments (Dewan and Chenevert, 2001) and numerical simulations (Wu *et al*., 2005) have proved that despite the fact that the flow rate is relatively high at the onset of the invasion, it quickly tends to steady-state behavior after the mudcake is completely formed. The maximum mudcake thickness is approximately reached 15 hours after the onset of invasion. Once the mudcake is completely formed, the overbalance pressure stabilizes at approximately 800 psi and the flow rate becomes constant.

The computed flow rate is averaged over the entire simulation time and input as a time-constant value to simulate the process of invasion. For the case of a vertically heterogeneous flow unit the flow rate is estimated separately for each individual flow sub-unit (petrophysical layer). Five days were chosen as the optimum time of invasion after studying simulation results for different time intervals. For a long time of invasion (more than three days), mudcake is already formed and the average flow rate is dominated by its early time behavior (less than 15 hours after the onset of invasion). Therefore, the error in the estimation of flow rate for extended invasion times is negligible.

3.6 FORWARD MODELING AND INVERSION ALGORITHMS

The forward problem consists of simulating the process of two-phase flow of water-base mud filtrate invading a partially gas-saturated formation. This problem is modeled as convective transport of aqueous and hydrocarbon phases, and components of water, hydrocarbon, and salt concentration (Alpak *et al.*, 2003). Isothermal convective miscible transport is assumed for the salt component while diffusion between mud-filtrate and connate water is neglected. Upper, lower, and external boundaries of the formation impose no-flow conditions. A constant flow rate, obtained as the time average of the flow rate yielded by INVADE (this is the constant line shown in the upper panel of Figure 3.7), is imposed at the borehole wall for each numerical layer as a fixed source condition. Modeling of multi-phase and multi-component fluid-flow is performed with the ECLIPSE®[4] commercial finite-difference reservoir simulator. Appendix B provides a description of the physics of immiscible multi-phase fluid-flow applied in this dissertation.

Petrophysical properties such as porosity, initial water saturation, and initial estimate of permeability obtained from the petrophysical assessment, along with core-calibrated Brooks-Corey capillary pressure and relative permeability curves are the main rock properties input to the simulations (Table 3.2). In addition, mudcake properties, hydrostatic and formation pressure, and fluid properties are input to model the process of mud-filtrate invasion. Table 3.3 summarizes the formation, fluid, and mudcake properties used in the numerical simulations described in this chapter.

The main outputs of the simulation are the spatial distributions of water saturation and salt concentration. Water saturation is transformed into electrical resistivity via Archie's equation. On the other hand, the spatial distribution of salt concentration is used

---

[4] Mark of Schlumberger

to compute equivalent values of water resistivity (R_w) using the equation documented by Bigelow (1992) and Hallemburg (1998) with the corresponding Arps' (1953) temperature conversion factor, namely,

$$R_w = \left(0.0123 + \frac{3647.5}{\left[NaCl\right]^{0.955}} \right) \left(\frac{81.77}{T + 6.77} \right), \tag{3.12}$$

where T is reservoir temperature in ^oF, and *[NaCl]* is salt concentration in ppm. Equation (3.12) is an average approximation of the three equations documented by Worthington *et al*. (1990). They used least-squares regression to fit the values given on tables of brine conductivities as a function of specific values of *NaCl*-brine concentration. Equation (3.12) matches the three resistivity zones defined in Worthington *et al*.'s work with an error below 2% for salinity between 500 and 100,000 ppm. For salt concentration between 100,000 to 230,000 ppm the error is 2-10%. Therefore, we adopted equation (3.12) to convert salt concentration to water resistivity. In the reservoir under consideration, salt concentration ranges between 1,500 and 160,000 ppm.

3.6.1 Array-induction Resistivity Modeling

The next stage is the forward modeling of array-induction measurements from the spatial distribution of formation resistivity. This requires the frequency-domain solution of Maxwell's equations. We performed the numerical simulation with the SLDMINV finite-difference algorithm advanced by Druskin *et al*. (1999). This software provides multi-frequency simulations of array-induction measurements via the Spectral Lanczos Decomposition Method (Alpak *et al*., 2003).

3.6.2 Inversion Method for the Estimation of Permeability

Inversion of permeability from array-induction measurements is posed as the minimization of a quadratic objective function subject to model constraints (Alpak *et al.*, 2006). In this chapter, we adopt the quadratic objective function

$$C(\bar{\mathbf{x}}) = \frac{1}{2}\left[\ \mu\left\{\left\|\bar{\mathbf{e}}(\bar{\mathbf{x}})\right\|^2 - \chi^2\right\} + \left\|\,(\bar{\mathbf{x}} - \bar{\mathbf{x}}_p)\,\right\|^2\right]\ , \qquad (3.13)$$

where χ^2 is the target data misfit, and $\bar{\mathbf{e}}(\bar{\mathbf{x}})$ is the vector of data residuals constructed as the normalized difference between the measurements and their simulations, i.e.,

$$\left\|\bar{\mathbf{e}}(\bar{\mathbf{x}})\right\|^2 = \sum_{j=1}^{M}\left|\frac{S_j(\bar{\mathbf{x}})}{m_j} - 1\right|^2 . \qquad (3.14)$$

In the above expressions, M is the number of measurements, m_j denotes the j-th measurement, and S_j is the corresponding simulated measurement for the vector of unknown model parameters, $\bar{\mathbf{x}}$. The latter vector is given by

$$\bar{\mathbf{x}} = \left[x_1, \ldots, x_N\right]^T , \qquad (3.15)$$

where N is the number of unknown parameters, in this case layer-by-layer values of absolute permeability. In equation (3.13), the positive scalar factor μ is used as stabilization parameter (also called a Lagrange multiplier) to assign relative importance to the two additive terms of the objective function. Finally, the vector $\bar{\mathbf{x}}_p$ contains reference values of layer permeability used to bias the search for the minimum of the quadratic objective function. In our case, vector $\bar{\mathbf{x}}_p$ is constructed with the initial guess of layer permeability values rendered by log analysis (equation 3.6).

In this chapter, the measurement vector consists of values of AIT apparent resistivity sampled at 0.25-foot intervals. There are five apparent resistivities per sampling depth and a total of 277 sampling points in the depth interval from -25.75 ft to +43.25 ft. Consequently, the total number of input measurements is 1385 including measurements above and below the flow unit shown in Figure 3.1 (0 - 20.5 ft). Based on measurement noise considerations, the target misfit in equation (3.13) is set to 0.01.

We assume that the locations of layer boundaries are known from the previously described modified Lorenz plots. Moreover, the inverted model parameters are constrained to remain within their physical bounds using a nonlinear transformation (Habashy and Abubakar, 2004). Minimization of the objective function is performed with a Gauss-Newton method that enforces a backtracking line search algorithm along the descent direction. This minimization strategy guarantees a monotonic reduction of the data misfit from iteration to iteration. The choice of the Lagrange multiplier is adaptively linked to the condition number of the Hessian matrix of the quadratic objective function (Alpak *et al*., 2004).

3.7 ESTIMATION OF PERMEABILITY: FIELD EXAMPLE

We consider the field example described in Figure 3.1 to test our inversion methodology. A homogeneous single-layer case was used as initial model to calibrate the simulation of mud-filtrate invasion and the resistivity inversion. Sensitivity analysis was performed to assess the influence of several petrophysical properties on the inverted permeability until obtaining the best forward model representing the formation. Subsequently, a heterogeneous multi-layer case was considered to estimate layer-by-layer permeabilities within the fluid production unit.

3.7.1 Base Case: Homogeneous Production Unit

Initially, we perform the simulation assuming that the fluid production unit is a homogeneous and isotropic single-layer formation. To this end, initial water saturation was obtained from Archie's equation, porosity from a nonlinear two-fluid two-mineral model, and the initial permeability guess from the modified Timur-Tixier equation. The coefficient for capillary pressure, P_c^o, is set to 1.1 psi.darcy$^{1/2}$, and the exponent for capillary pressure, e_p, is equal to 1.8. On the other hand, the water end-point for relative permeability, k_{rw}^o, is set to 0.9 and for gas, k_{rnw}^o, is set to 0.3. Finally, the water exponent, e_w, is set to 2.0 and for gas, e_{nw}, is equal to 2.5. Figure 3.6 displays the water-gas capillary pressure and relative permeability curves. As observed from the relative permeability curves of Figure 3.6, critical water saturation[5], S_{wcr}, is in the order of 58% for this homogeneous-formation case.

Figure 3.8 shows spatial distributions (radial and vertical directions) of water saturation, salt concentration, and electrical resistivity within the rock formation yielded by the simulation of mud-filtrate invasion. The assumed time of invasion is five days. Invasion reaches a radial distance of approximately 7 ft from the wellbore. Such a relatively deep invasion substantially influences the array-induction measurements. The cross-sections shown in Figure 3.8 are input to SLDMINV to simulate array-induction imager tool (AIT) measurements with an initial guess of absolute permeability equal to 1.5 md. Simulation of AIT measurements is performed at every 0.25 ft vertically along the borehole. Results of such a simulation are shown in Figure 3.9 along with the gamma ray log. On average, the simulated deep apparent resistivity (AIT 90) follows a similar trend to that of the field data. Conversely, the shallowest apparent resistivity curve (AIT 10) follows the trend of the field data only along the cleanest interval of the reservoir (4-12 ft) which is also the one that exhibits the largest resistivity values. Intermediate apparent resistivity curves (AIT 20, AIT 30, and AIT 60) on average do not follow the same trend of the field data. A radially smoother spatial distribution of electrical

---

[5] Critical saturation is here defined as the value of water saturation when relative permeability of wetting phase is equal to that of the non-wetting phase.

resistivity is necessary to match the intermediate AIT apparent resistivity curves. Two of the most important parameters that control the shape of the radial profile of invasion are capillary pressure and relative permeability. Consequently, a sensitivity analysis is necessary to assess the influence of those two formation parameters on the simulated spatial distributions of electrical resistivity.

3.7.1.1 Sensitivity of Array-Induction Measurements to Capillary Pressure and Relative Permeability

We performed simulations of array-induction measurements after enforcing small perturbations to the water-gas capillary pressure and relative permeability curves. Small perturbations (±10%) were performed to the capillary pressure coefficient, P_c^o, as well as to the wetting phase exponent, e_w, for relative permeability. No significant changes were observed in either the spatial distributions of electrical resistivity or the simulated array-induction measurements resulting from these perturbations. Thus, we proceeded to enforce yet larger perturbations (approximately, -70% and +300%) of the same parameters. Figure 3.10 shows the simulated array-induction measurements obtained for the cases when P_c^o = 0.35 psi.darcy$^{1/2}$ (low capillary pressure) and P_c^o = 3.7 psi.darcy$^{1/2}$ (high capillary pressure). Although such changes in capillarity are rather high, they scarcely affect the simulated apparent resistivity curves.

One of the best ways to observe the effect of changes in relative permeability is by modifying the critical water saturation (S_{wcr}). Figure 3.11 shows the simulated array-induction curves for the cases when $e_w = 20.0$ ($S_{wcr} \approx 80\%$) and $e_w = 2.0$ ($S_{wcr} \approx 35\%$), in that order. In the second case ($S_{wcr} \approx 35\%$), it was necessary to change the values of irreducible and initial water saturation to achieve such an extreme shape in the relative permeability curves. For high values of critical water saturation we observe less splitting of the intermediate apparent resistivity curves. This observation indicates that the invasion front is relatively sharp and, therefore, does not entail a good agreement between the measured and simulated array-induction apparent resistivities. A more pronounced splitting of the simulated apparent resistivity curves is observed for the case of low critical water saturation, thereby resulting in a better agreement between the measured and simulated array-induction curves. However, we remark that for a gas-saturated reservoir such as the one considered in this chapter, it is unlikely to encounter relative permeability curves with such a low value of S_{wcr}. Therefore, the base case value ($e_w = 2.0$, $S_{wcr} \approx 58\%$) was used to perform the inversion.

One important observation from this analysis is that large variations of relative permeability cause appreciable changes in the shape of the spatial distribution of electrical resistivity. Capillary pressure is also an important factor to be considered in the analysis. However, our sensitivity analysis shows that the effect of capillary pressure on the shape of the invasion profile is negligible compared to that of relative permeability. It is also pertinent to mention that neither of these two properties affects the radial length of invasion or the electrical resistivity in the near-borehole and virgin zones. Only the transition zone remains influenced by the changes of relative permeability and capillary pressure.

3.7.1.2 Sensitivity of Array-induction Measurements to Permeability, Porosity, Archie's Parameters, and Initial Water Saturation

We performed sensitivity analyses to the initial guess of absolute permeability (k = 1.5 md) to assess its influence on the AIT apparent resistivity curves. Figure 3.12 and 13 show simulated apparent resistivity curves for the cases of 1 (base case, k = 1.5 md), 10, 0.1, and 100 times the initial guess of permeability. We observe a significant influence of small values of absolute permeability on the simulated resistivity curves. Specifically, the shallow apparent resistivity (AIT 10) increases with high values of permeability while the deep apparent resistivity (AIT 90) slightly decreases. A larger splitting of the intermediate apparent resistivity curves is also observed for high values of permeability. Figures 3.12 and 3.13 also indicate that the shallow apparent resistivity curves remain the most sensitive to changes of absolute permeability. Therefore, we conclude that absolute permeability strongly affects the spatial distribution of electrical resistivity. This observation applies not only to the electrical resistivity of the transition zone, but also to the radial length of invasion.

Perturbations of porosity and Archie's parameters produce a uniform parallel shift of the five simulated apparent resistivity curves when plotted on a logarithmic scale. This effect contrasts with that due to perturbations of permeability, where the shift of the simulated apparent resistivity was not uniform for all the AIT curves. For low values of cementation exponent (m), the simulated values of apparent resistivity uniformly decrease with respect to those of the base case. A similar situation occurs either with a decrease of the saturation exponent (n) or with an increase of porosity. For the problem at hand, we found that the simulated AIT apparent resistivity curves exhibited higher sensitivity to m than to either n or porosity. However, when the perturbations of m, n, and porosity were below 10% with respect to the values assumed for the base case, we observed no appreciable differences on the simulated apparent resistivity curves.

Similar to the case of Archie's parameters, changes in initial water saturation entail an uniform parallel shift of the simulated AIT apparent resistivity curves. As expected from Archie's equation, low values of initial water saturation yielded high values of resistivity and high values of initial water saturation yielded low values of resistivity. For changes below 10% of initial water saturation the simulated AIT apparent resistivity curves did not appreciable change with respect to those of the base case. Based on this analysis, we conclude that large variations of initial water saturation (>10%) have an important influence on the shape of the radial profile of invasion. Furthermore, the influence of initial water saturation on the radial shape of invasion is the largest in the virgin zone.

3.7.1.3 Sensitivity of the Estimated Permeability to Mudcake Properties and Time of Invasion

We performed additional sensitivity analyses to study the influence of various mudcake parameters on the estimated permeability. Variations of mudcake properties entail variations in the flow rate of mud-filtrate invasion. Mudcake permeability, maximum mudcake thickness, and mudcake compressibility exponent are the three parameters that primarily govern the flow rate of invasion. These parameters affect both, the shape of the invasion profile and the radial length of invasion. The higher the mudcake permeability the higher the flow rate; the lower the mudcake thickness and compressibility exponent the higher the flow rate. Figure 3.14 describes the influence of mudcake permeability on the flow rate of invasion. We observed that variations above 20% in these properties entailed variations over 15% of the flow rate of invasion. In turn, these variations of flow rate entailed variations of one order of magnitude or less of the inverted values of formation permeability. Figure 3.15 displays the simulated AIT apparent resistivity curves for the base case assuming two values of mudcake permeability. Perturbations in other invasion parameters such as mudcake porosity, mud solid fraction, and mudcake exponent multiplier scarcely affected the calculated flow rate of mud-filtrate invasion.

Time of invasion was another important parameter considered in our sensitivity analysis. We found that the effect of time of invasion on the estimated values of permeability was similar to that associated with variations of mudcake permeability assuming a constant time of invasion. For differences of time of invasion of one day or less we observed variations of half and order of magnitude of the estimated permeability. Variations of the estimated values of permeability remain marginal for variations of the time of invasion of six hours or less.

3.7.1.4 Base-Case Permeability Inversion

We first consider the base formation model. All petrophysical properties are assumed known with the exception of absolute permeability. The initial permeability guess (k = 1.5 md) entered to the inversion was obtained from the modified Timur-Tixier equation. Five Gauss-Newton iterations were necessary to achieve convergence of the minimization process, thereby yielding a value of absolute permeability equal to 55.4 md. Figure 3.16 shows the simulated array-induction measurements associated with the inverted value of absolute permeability. The simulated AIT apparent resistivity curves follow a trend similar to that of the measurements. A clear splitting of the intermediate curves is also noticeable. We observe a better agreement between the measured and simulated AIT apparent resistivity curves as a result of the inversion. The next stage of the analysis consists of improving the vertical agreement between the measured and simulated AIT apparent resistivity curves by progressively increasing the number of flow sub-units in the rock formation. This procedure yields layer-by-layer estimates of absolute permeability.

3.7.2 General Case: Vertically Heterogeneous Flow Unit

In order to account for vertical heterogeneities in the flow unit, we subdivided it into multiple horizontal layers. The modified stratigraphic Lorenz plot shown in Figure 3.4 was used to identify layer boundaries. This plot indicated that the maximum number of flow units was eight. Simulations of mud-filtrate invasion and array-induction measurements were performed for cases with 2, 3, 4, 5, 6, 7, and 8 layers. However, in this chapter we report inversion results only for the case of highest vertical resolution (8 layers).

Initial values of porosity, water saturation, and permeability were calculated in similar fashion to the base formation case and averaged across each flow sub-unit. Table 3.4 describes the thickness and petrophysical properties of each layer used in the description of the formation. Mudcake and mud-filtrate properties remained the same as in the base case. However, flow rates of mud-filtrate invasion were computed specifically for each flow unit. The rate of mud-filtrate invasion is largely controlled by rock properties in low permeability formations (Wu *et al*, 2005). Because capillary pressure remains a function of irreducible water saturation, porosity, and permeability, the flow rate of mud-filtrate invasion is slightly different for each flow unit. Relative permeability, on the other hand, depends on irreducible water saturation and Brooks-Corey's parameters. Therefore, we assumed the same shape of relative permeability curves for all the layers but included layer-dependent variations of critical water saturation.

Figure 3.17 describes the spatial distributions of water saturation, salt concentration, and electrical resistivity resulting from the simulation of mud-filtrate invasion. The invasion front reaches radially deeper zones in the formation when permeability is high. Figure 3.18 compares the corresponding simulated AIT apparent resistivity curves with the measured curves. We simulated the AIT apparent resistivity curves shown in Figure 3.18 using the initial permeability guess. As observed, the match between measured and simulated AIT apparent resistivity curves is not acceptable. The latter observation indicates that the best estimate of absolute permeability has not been reached from forward modeling. Additional changes of permeability for each layer are needed to reach a better agreement between simulated and measured apparent resistivity curves.

3.7.2.1 Estimation of Layer-by-Layer Permeabilities

We proceed to adjust the layer permeability values to improve the match between simulated and measured AIT apparent resistivity curves. This adjustment is guided by vertical variations of the resistivity curves. Simulation of mud-filtrate invasion is performed after each manual change followed by numerical simulation of array-induction measurements. The process is repeated as many times as needed to reach an acceptable match between the simulated and measured AIT apparent resistivity curves. Figure 3.19 describes the spatial distributions of water saturation, salt concentration, and electrical resistivity simulated after several multiple changes of layer permeabilities.

Figure 3.20 compares the simulated and measured AIT apparent resistivity curves. We observe that the simulated deepest (AIT90) and shallowest (AIT10) apparent resistivity curves agree well with the corresponding measured curves. However, the agreement between the intermediate apparent resistivity curves is not acceptable. We conclude that automatic permeability inversion is needed to improve the agreement between simulations and measurements.

3.7.3 General Case of Permeability Inversion

We implemented the inversion of layer permeabilities using as initial guess the permeability values rendered by the manual adjustment process described in the previous section. The inversion was conducted in two steps: Initially, the permeability yielded by the manual resistivity matching was taken as the starting guess. Eight Gauss-Newton iterations were necessary to achieve convergence of the inversion. Permeability values obtained from this inversion were used to re-compute the flow rate of mud filtrate with INVADE and then used as the new initial guess for the subsequent inversion. Table 3.5 describes the values of layer permeability yielded by the second step of the inversion after 8 iterations along with the corresponding percentage change when compared to the

Timur-Tixier permeability values. The deviation of the inverted permeabilities with respect to the initial guess is as low as one-half order of magnitude and as high as four orders of magnitude. Table 3.5 gives a qualitative indication of the level of uncertainty of each estimated value of permeability (right-most column) based on the sensitivity of the simulated apparent resistivity curves to a small perturbation of permeability.

Figure 3.21 shows the spatial distribution of electrical resistivity yielded by the inversion, whereas Figure 3.22 compares the simulated and measured apparent resistivity curves. Even though most of the simulated AIT apparent resistivity curves (in several layers) agree well with the field curves, additional work is needed to assess more realistic values of absolute permeability for those layers that exhibit moderate to high levels of uncertainty. We remark that layers close to the top and base of the fluid production unit are highly influenced by shoulder-bed effects. Some of the differences between simulated and measured apparent resistivity curves could be due to azimuthal variations of electrical resistivity neglected by the simulation model.

3.7.4 Uncertainty Analysis

Sensitivity analyses were carried out to assess the uncertainty of the estimated flow rate of mud-filtrate invasion. The inverted absolute permeability decreased by two orders of magnitude when the average flow rate was made equal to twice the value of the flow rate for the initial case. However, for 5 and 10 times the value of the initial flow rate, the inverted values of permeability remained the same as those obtained for the case of 2 times the initial flow rate. For the case at hand, it is very unlikely that such large errors be made in the estimation of flow rate as the latter is mainly conditioned by formation permeability. We observed that changes in the permeability of a layer entailed changes of the corresponding flow rate only for invasion times shorter than 0.5 days.

Therefore, we conclude that changes of flow rate in the order of 10% scarcely affect the estimated values of permeability.

3.8 SUMMARY AND CONCLUSIONS

Using a challenging field example of tight-gas sands, this chapter considered the estimation of absolute permeabilities of rock formations from borehole array-induction measurements. The estimation was based on the simulation of the process of mud-filtrate invasion. This approach required detailed knowledge of borehole environmental variables, including overbalance pressure, temperature, mud properties, and time of invasion. Accurate simulation of the process of mud-filtrate invasion also required knowledge of fluid and rock-fluid properties such as porosity, permeability, relative permeability, capillary pressure, initial water saturation, salt concentration of connate water, and hydrocarbon density and viscosity, among others. Some of these properties were available from rock-core laboratory measurements, while others were estimated from basic petrophysical analysis of well logs. To estimate permeability from array-induction logs it is imperative that, except for permeability, all of the borehole environmental variables and rock-fluid properties be known with a good level of certainty. Uncertain knowledge of some of these properties requires that their influence on the estimation of permeability be quantified in a systematic manner.

The field study considered in this chapter was approached with a thorough analysis of the role played by several borehole and rock-fluid properties on the time evolution of the process of mud-filtrate invasion. We found that, for the tight-gas sand reservoir under analysis, salt mixing between mud-filtrate and connate water, and relative permeability had the largest influence on the spatial distribution of electrical resistivity resulting from invasion. Rocks with high critical water saturation (strongly water wet) were associated with piston-like invasion fronts and hence did not entail appreciable variations of the intermediate induction apparent resistivity curves. On the other hand, rocks with low critical water saturation were associated with spatially smooth spatial distributions of electrical resistivity. Such variations on the shape of the spatial distribution of electrical resistivity only occurred with a substantial change of relative permeability. Therefore, one can safely conclude that array-induction measurements are not sensitive to small variations of relative permeability and capillary pressure. Conversely, the sensitivity analyses considered in this chapter did indicate that absolute permeability had the largest effect on the measured array resistivity curves, especially on the shallow-reading curves. This observation provided a solid physical background for the estimation of permeability.

We approached the estimation of permeability from induction logs by progressively increasing the number of individual flow sub-units within a single production zone. Such a strategy allowed us to further refine the assumed values of porosity, capillary pressure and relative permeability by assessing their impact on the simulated array-induction measurements, especially the average values and separation of the five AIT apparent resistivity curves.

Permeability values yielded by the inversion of array-induction measurements were higher than those calculated with standard petrophysical formulas (see Table 3.5). However, as observed in Figure 3.3, these results were in the same range of rock-core permeabilities for porosity values larger than 10%.

We remark that the methodology tested in this chapter to estimate permeability was based on the use of apparent resistivity curves yielded by the processing of AIT induction measurements. It is likely that the resolution and accuracy of the estimated values of permeability would improve with the use of “raw” voltages instead of processed apparent resistivity curves. Likewise, it is possible that the resolution and accuracy of the estimated values of permeability would improve with the use of micro-resistivity measurements in addition to AIT measurements.

Table 3.1: Summary of Archie's parameters and rock and fluid properties used to estimate water saturation and porosity.

Variable	**Units**	**Value**
Archie's tortuosity factor *a*	-	1.00
Archie's cementation exponent *m*	-	1.95
Archie's saturation exponent *n*	-	1.75
Connate water resistivity @ 210 °F	Ω·m	0.02
Invasion water resistiv. @ 210 °F	Ω·m	0.56
Matrix density	g/cm^3	2.65
Shale density	g/cm^3	2.68
Water density	g/cm^3	1.00
Water-hydrocarbon density (mix.)	g/cm^3	0.50

Table 3.2: Summary of average petrophysical properties for the single-layer case.

Variable	**Units**	**Value**
Thickness	ft	20.5
Effective porosity	fraction	0.143
Water saturation	fraction	0.410
Shale concentration	fraction	0.132
Absolute Permeability	md	1.502

Table 3.3: Summary of mudcake, fluid, and formation properties used in the simulation of the process of mud-filtrate invasion.

Variable	**Units**	**Value**
Mudcake reference permeability	md	0.03
Mudcake maximum thickness	cm	1.02
Mudcake reference porosity	fraction	0.30
Mud Solid Fraction	fraction	0.06
Mudcake compressibility exponent	fraction	0.40
Mudcake exponent multiplier	fraction	0.10
Mud hydrostatic pressure	psi	5,825
Initial formation pressure	psi	5,000
Mud-filtrate viscosity	cp	1.00
Gas viscosity	cp	0.02
Mud-filtrate density	g/cm^3	1.00
Gas density	g/cm^3	0.0016
Mud-filtrate salt concentration	ppm	3,600
Connate water salt concentration	ppm	160,000
Wellbore radius	cm	10.26
Maximum invasion time	days	5.00
Formation Temperature	^oF	210
Formation outer boundary	m	262
Residual water saturation	fraction	0.40
Residual gas saturation	fraction	0.10

Table 3.4: Summary of average petrophysical properties for the case of a multi-layer formation.

Thickness	ϕ	S_w	k_o
ft	fraction	fraction	md
1.5	0.084	0.980	0.067
3.0	0.156	0.477	1.016
2.0	0.126	0.449	0.827
3.5	0.157	0.417	5.697
3.0	0.169	0.440	0.600
2.5	0.153	0.552	0.134
2.0	0.129	0.571	0.192
3.0	0.075	0.980	0.042

Table 3.5: Summary of permeability values inverted from array-induction measurements for the case of a multi-layer formation. Different columns describe the percent change of permeability with respect to that of the initial guess.

Permeability Resistivity Matching (md)	**% of change**	**Permeability Inversion (md)**	**% of change**	**Uncertainty**
0.031	-54	1.23	1733	Low
0.757	-25	18.63	1734	Low
1.340	62	22.16	2580	Low
2.295	-60	22.20	290	Low
2.482	314	16.90	2719	Low
0.124	-8	7.53	5502	Moderate
0.106	-45	2471.51	1285309	Very High
0.021	-50	82.90	197281	High

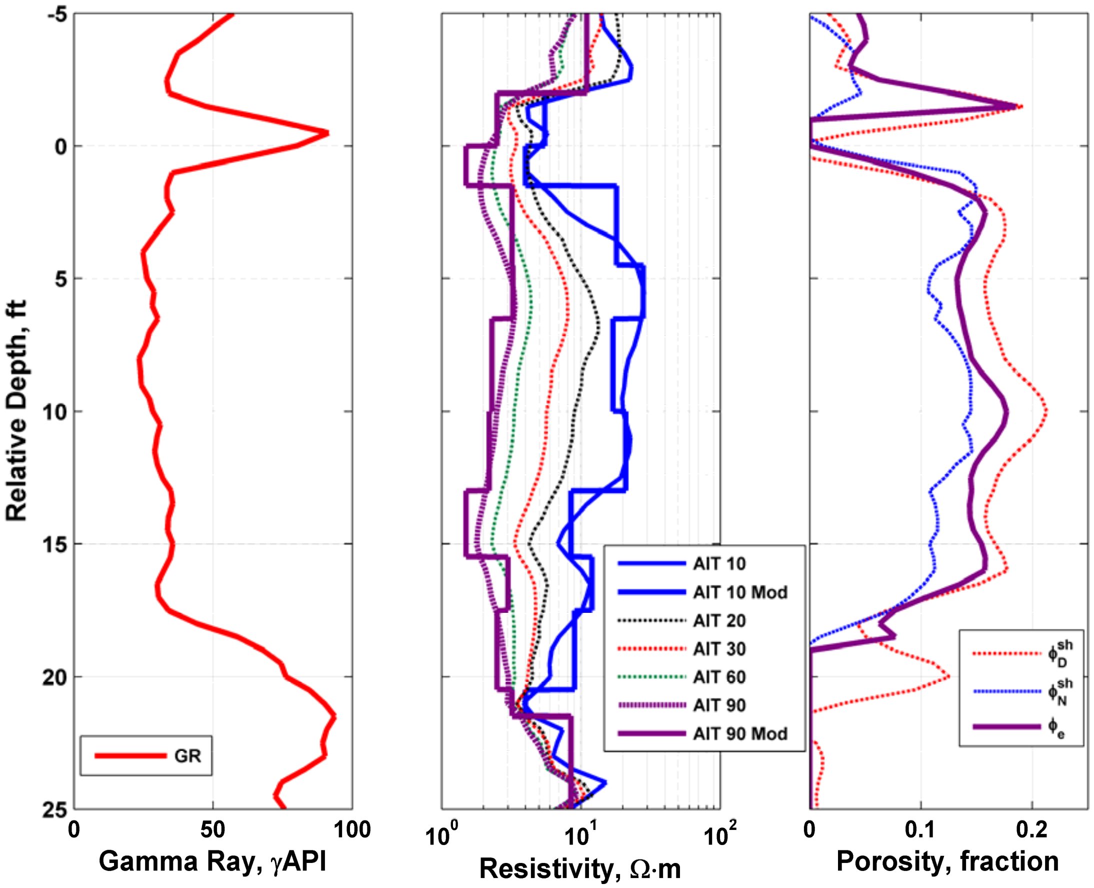

Figure 3.1: Well logs available for petrophysical assessment. The top of the interval under analysis is at 0 ft and the base at 20.5 ft. The left-hand track describes the gamma-ray log indicating a clean sand interval, the middle track shows the AIT apparent resistivity measurements along with the simulated apparent resistivity curves (AIT10 and AIT90), and the right-hand track displays porosity from neutron and bulk density logs with the continuous magenta curve describing effective porosity rendered by the two-fluid two-mineral nonlinear model.

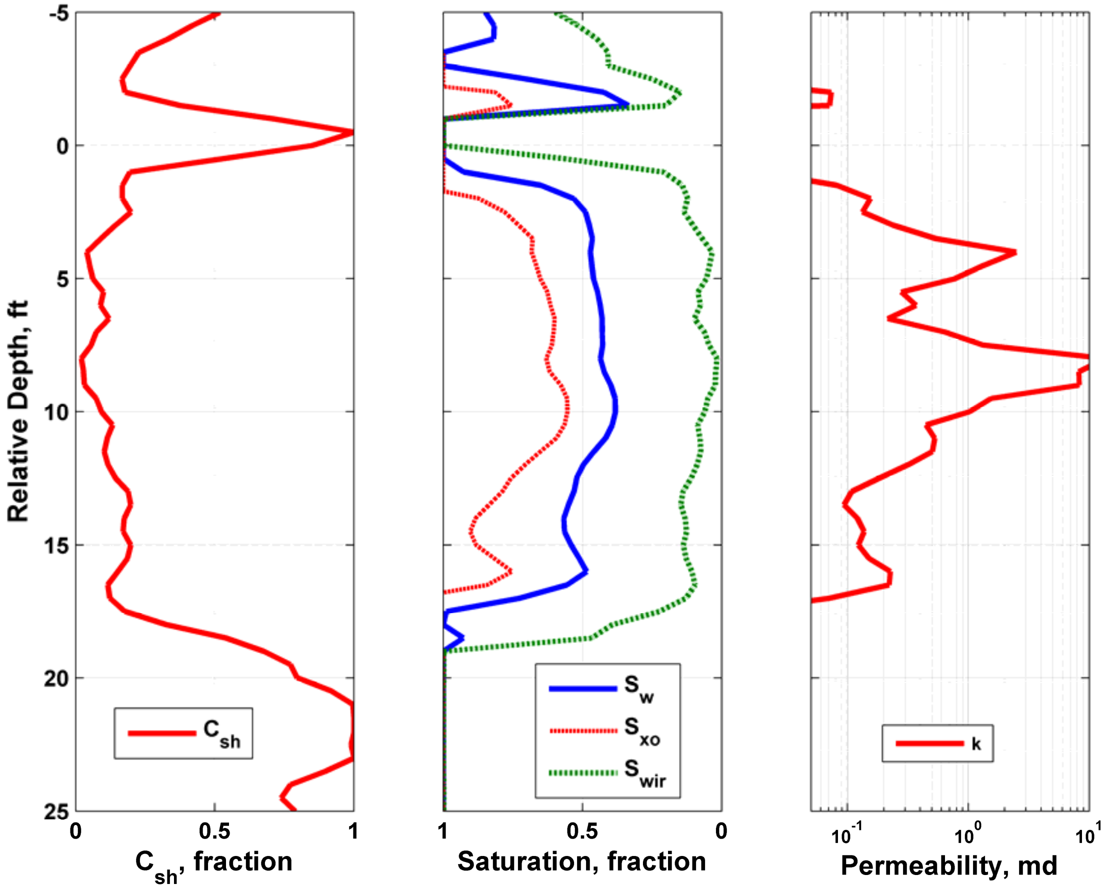

Figure 3.2: Synthesized petrophysical logs. The left-hand track describes the computed shale concentration, the middle track describes water saturation in the flushed and virgin zones along with an estimate of irreducible water saturation (calculated via Dewan's (1983) methodology, and only used to compute an initial guess of permeability), and the right-hand track shows the initial guess of permeability obtained from a modified Timur-Tixier model.

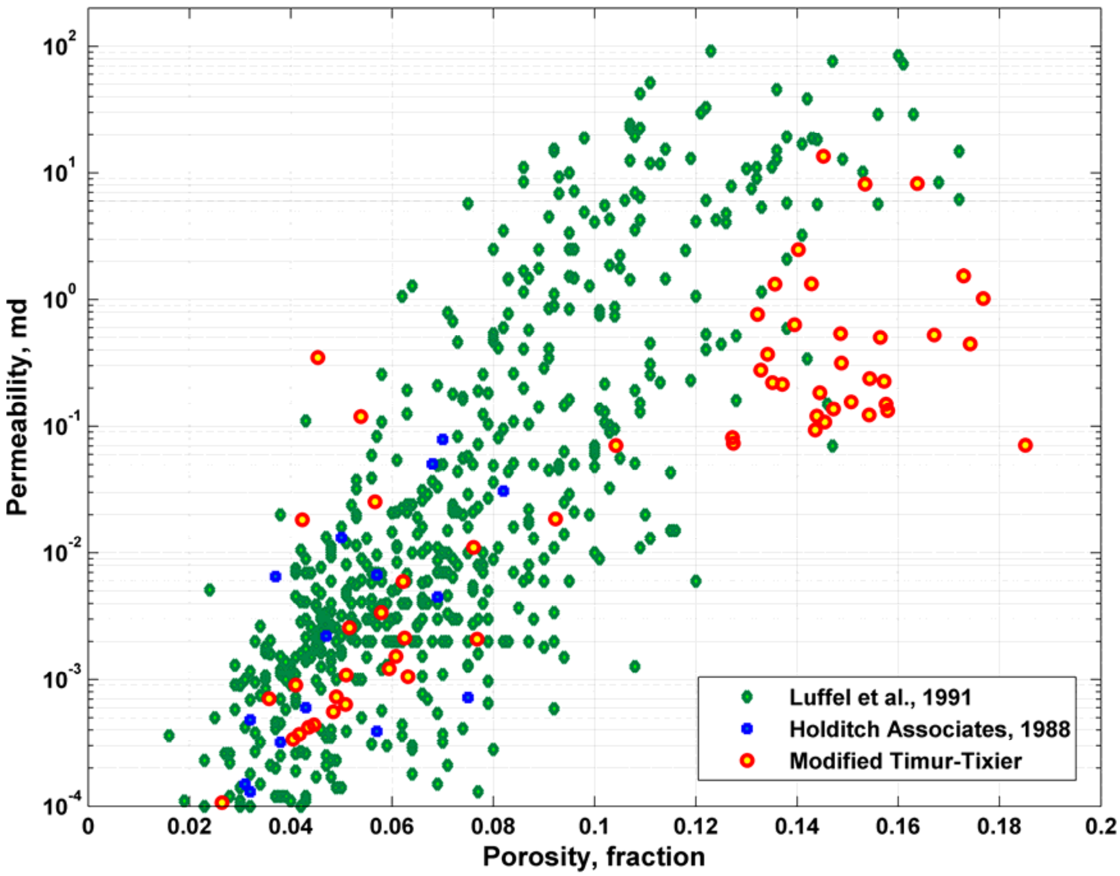

Figure 3.3: Graphical comparison of the initial guess of permeability (Timur-Tixier) and the permeability of rock-core samples acquired from two different wells in the same formation.

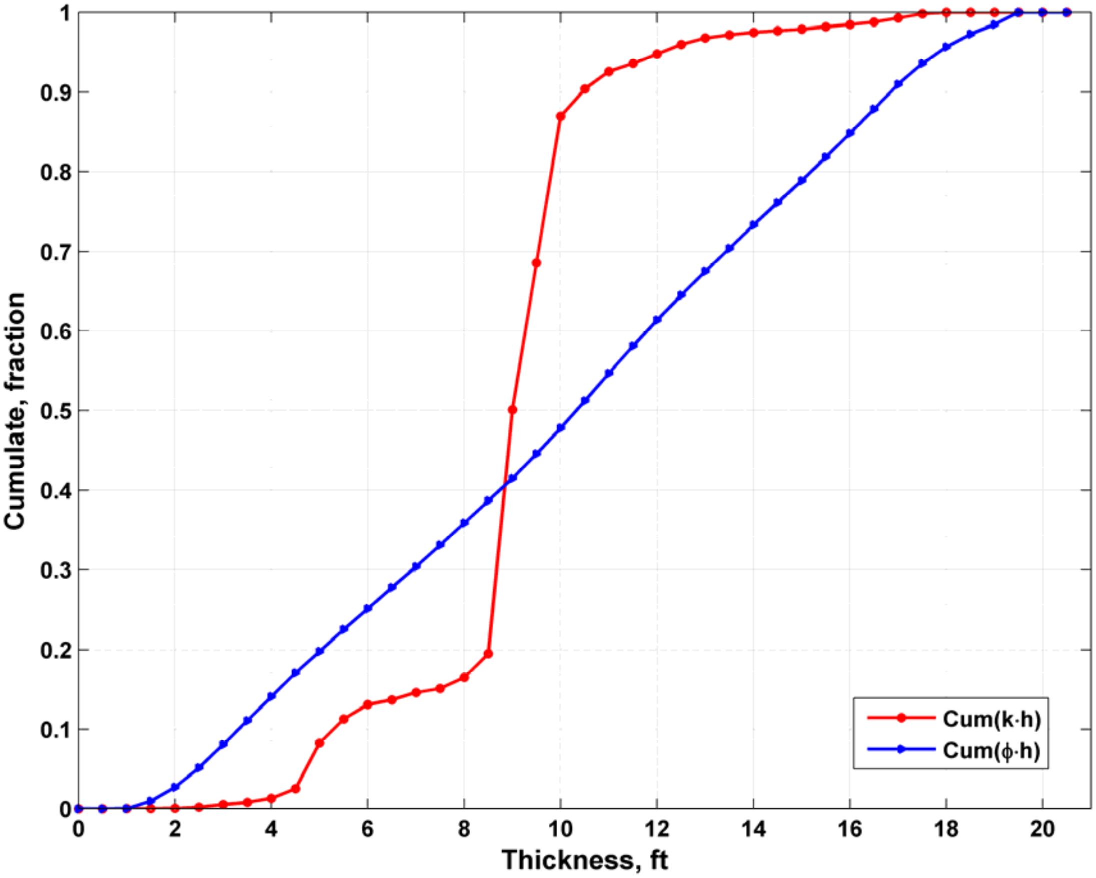

Figure 3.4: Modified Lorenz plot used to identify individual flow sub-units. The storage capacity curve [Cum(ϕh)] does not exhibit significant changes. However, the flow capacity curve [Cum(kh)] displays abrupt changes in slope thereby indicating the presence of individual flow sub-units within the same production interval.

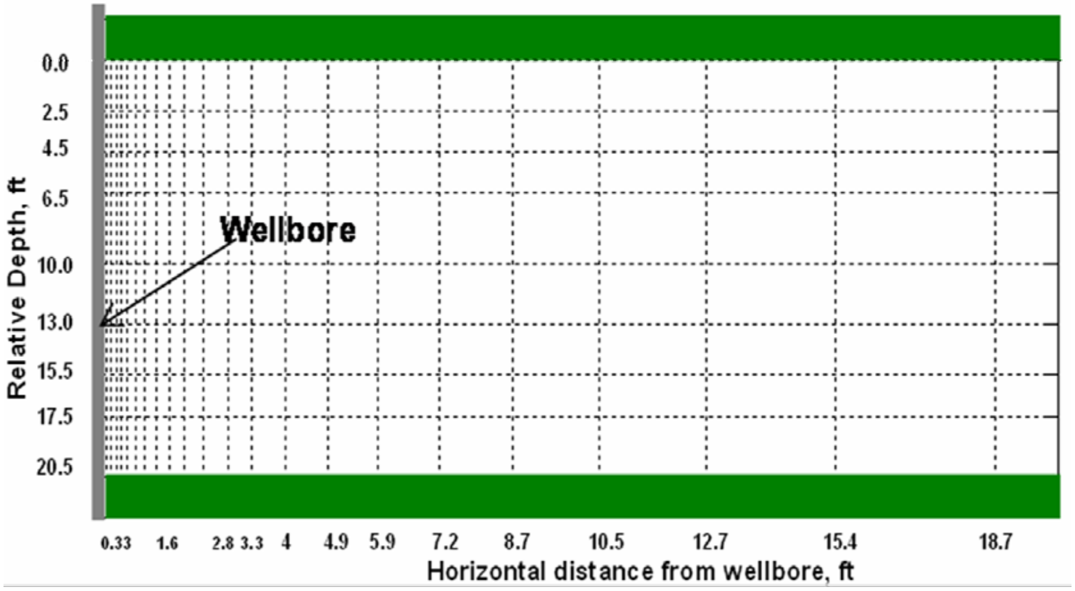

Figure 3.5: Graphical description of the finite-difference grid used in the simulation of mud-filtrate invasion and array-induction measurements.

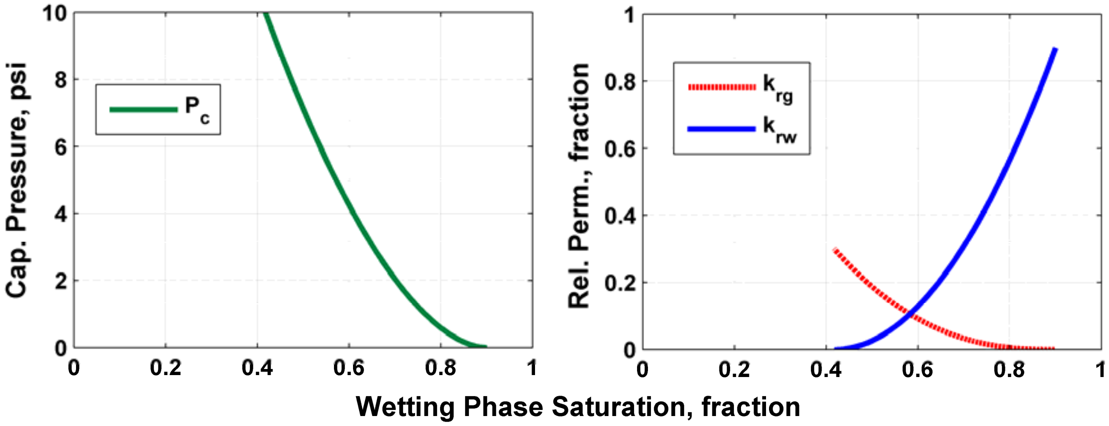

Figure 3.6: Graphical description of the Brooks-Corey water-gas relative permeability and capillary pressure curves used to perform the simulation of mud-filtrate invasion.

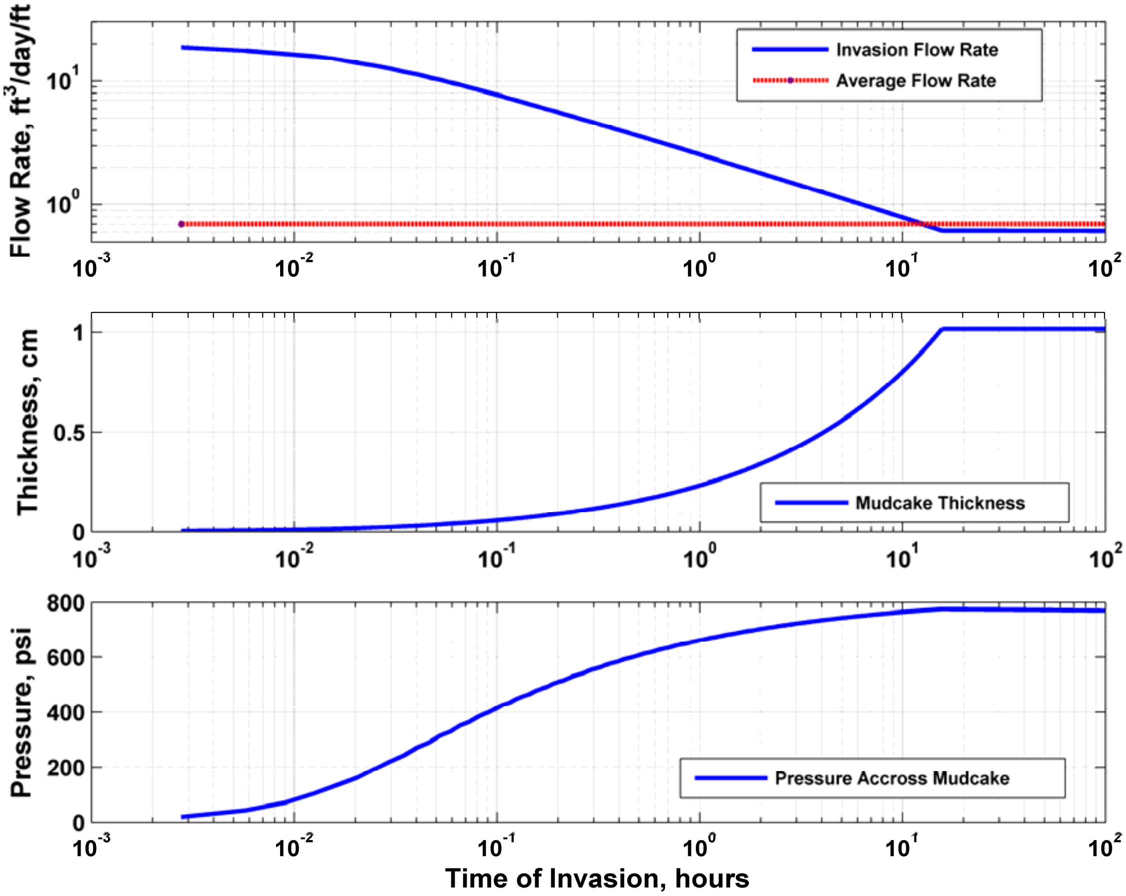

Figure 3.7: Time evolution of (a) flow rate of mud-filtrate invasion, (b) mudcake thickness, and (c) pressure across the mudcake.

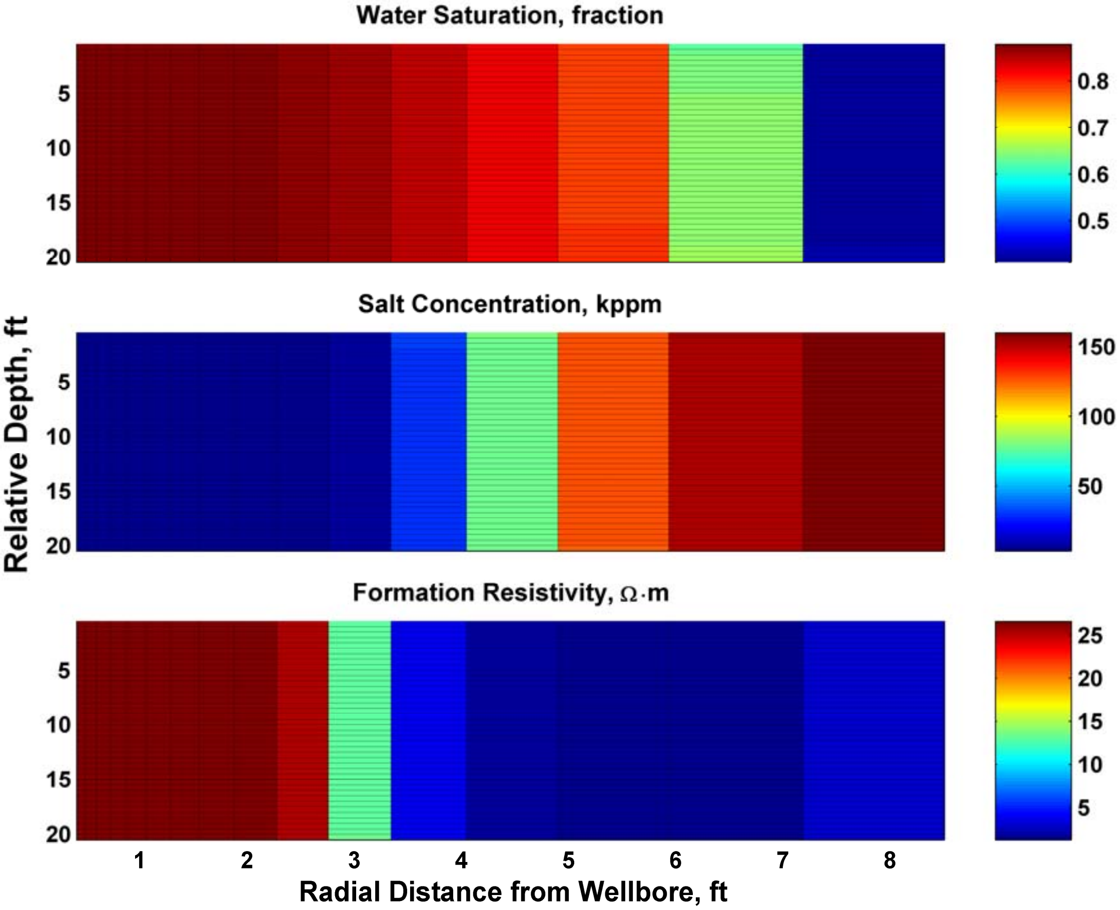

Figure 3.8: Results of the simulation of mud-filtrate invasion at 5 days after the onset of invasion. The cross-sections describe water saturation, salt concentration, and formation resistivity for the case of a vertically homogeneous fluid production unit.

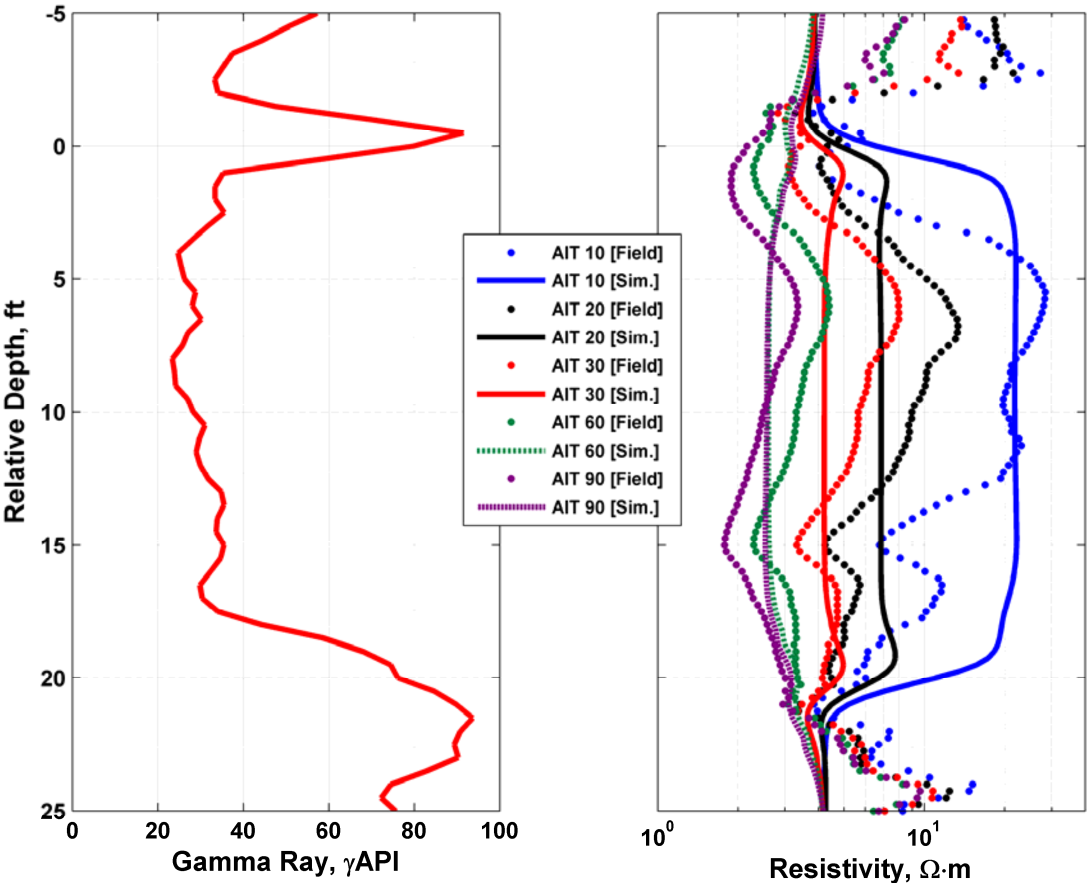

Figure 3.9: Comparison of the simulated and measured array-induction apparent resistivities (right-hand panel) for the base case. The left-hand panel shows the gamma-ray log.

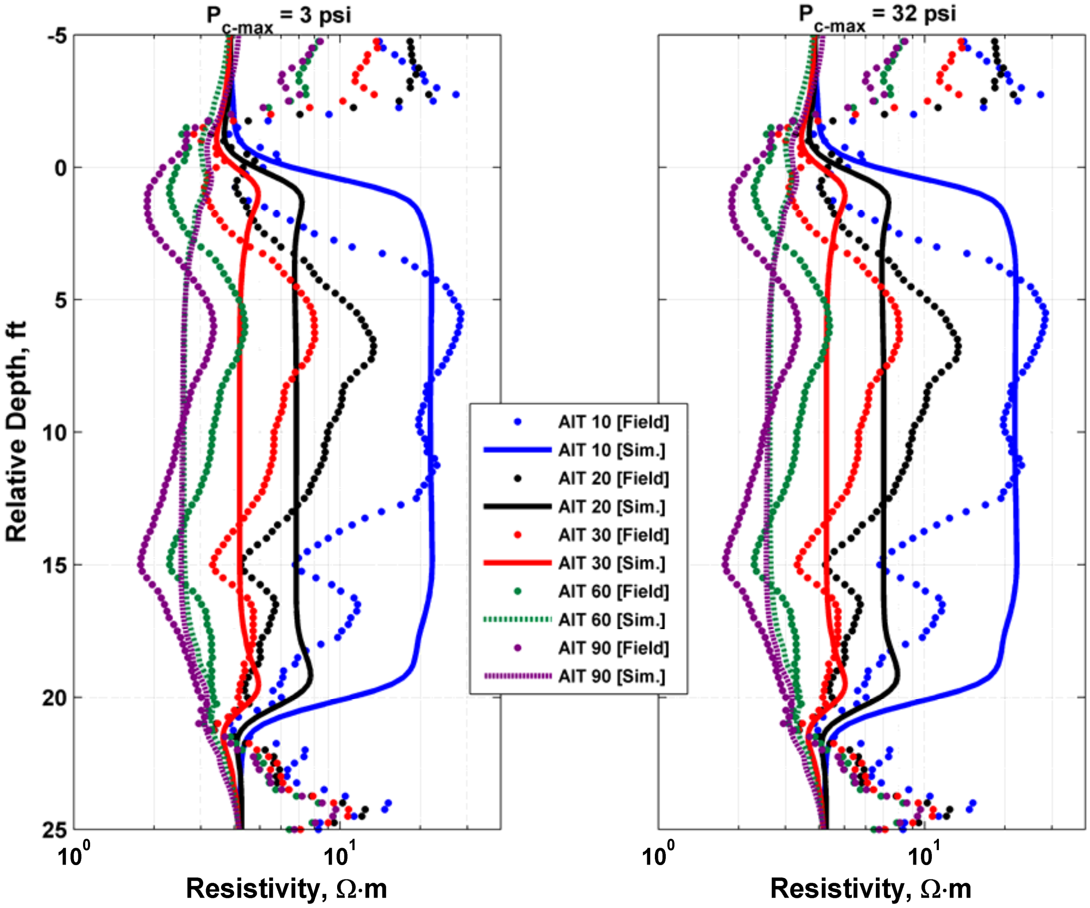

Figure 3.10: Numerical simulation of array-induction measurements: sensitivity to capillary pressure. The left-hand panel shows simulation results obtained for the case of a rock formation whose capillary pressure is 70% lower than that of the base case. The right-hand panel shows simulation results obtained for the case of a rock formation whose capillary pressure is 300% higher than that of the base case.

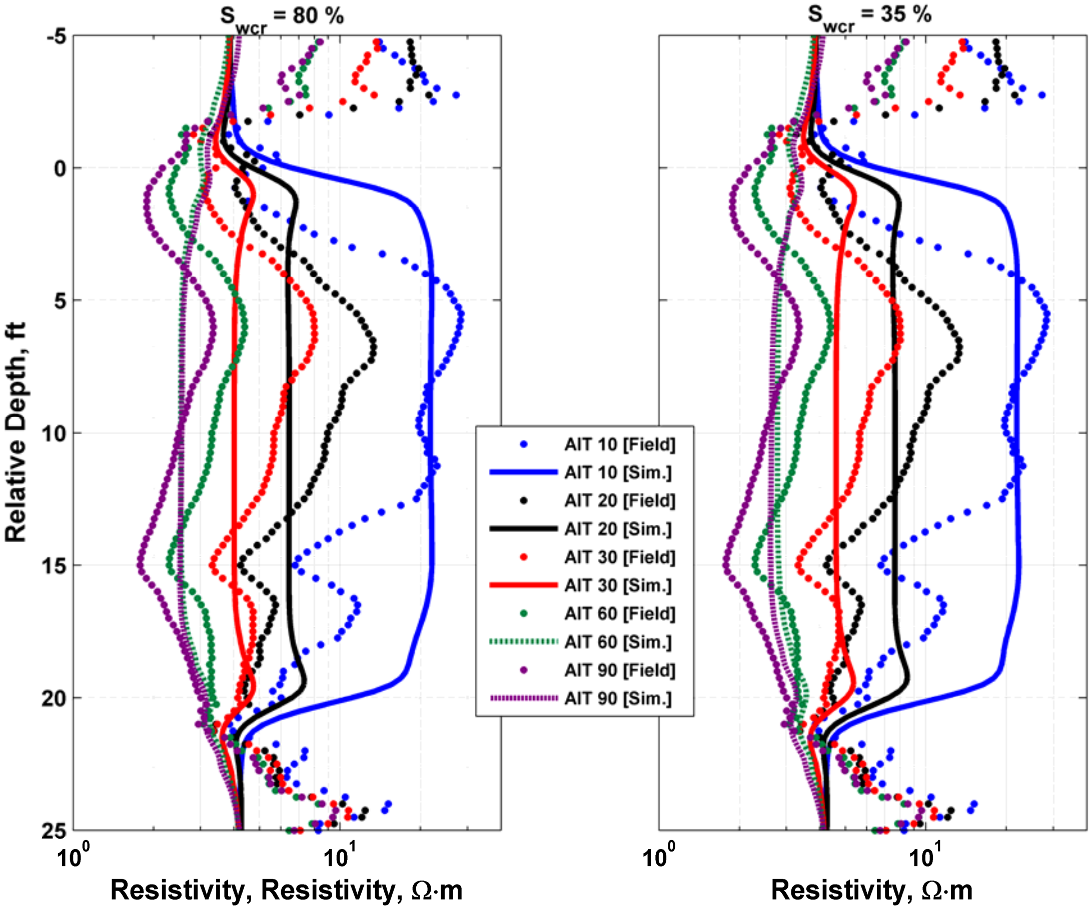

Figure 3.11: Numerical simulation of array-induction measurements: sensitivity to relative permeability. The left-hand panel describes simulations performed for a strongly water-wet sand with critical water saturation 45% higher than that of the base case. The right-hand panel shows simulation results obtained for the case of critical water saturation 35% lower than that of the base case.

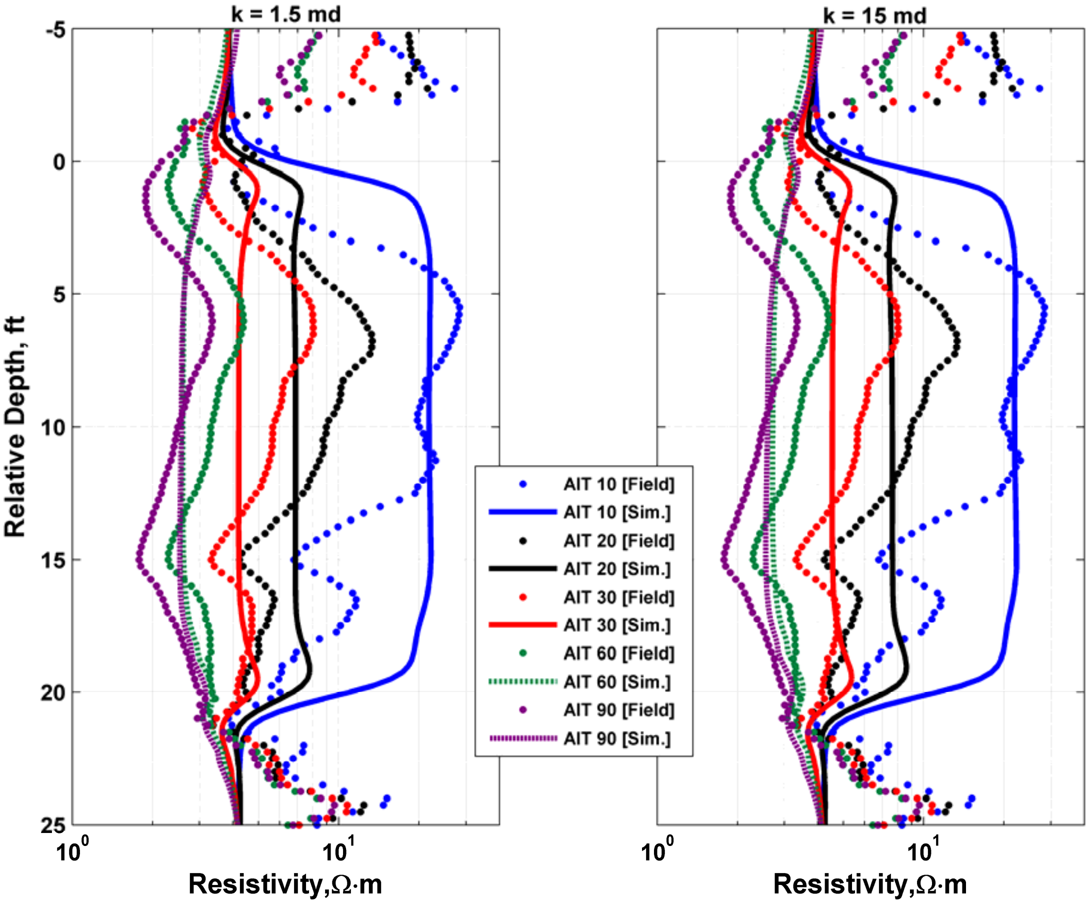

Figure 3.12: Numerical simulation of array-induction measurements: sensitivity to the initial guess of permeability. The left- and right-hand panels describe apparent resistivity curves simulated for the cases of 1 and 10 times the permeability of the base case, respectively.

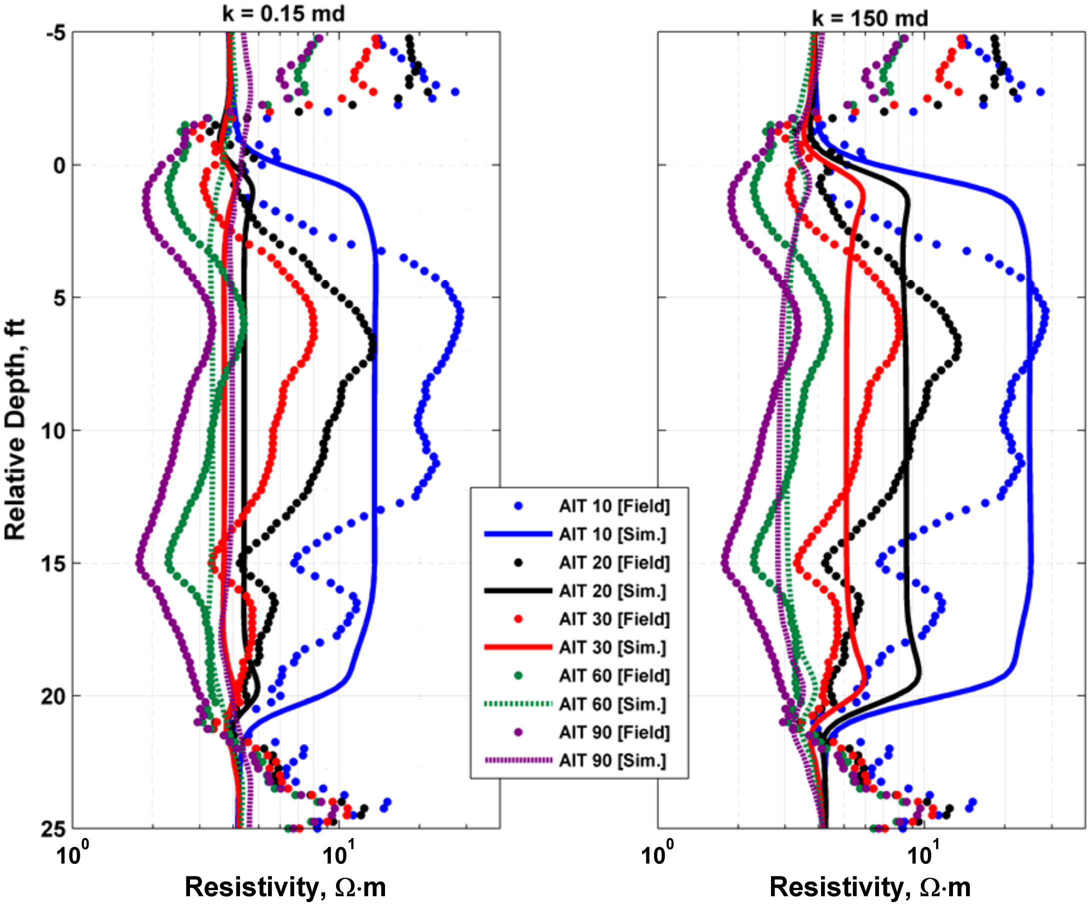

Figure 3.13: Numerical simulation of array-induction measurements: sensitivity to the initial guess of permeability. The left- and right-hand panels describe apparent resistivity curves simulated for the cases of 0.1 and 100 times the permeability of the base case, respectively.

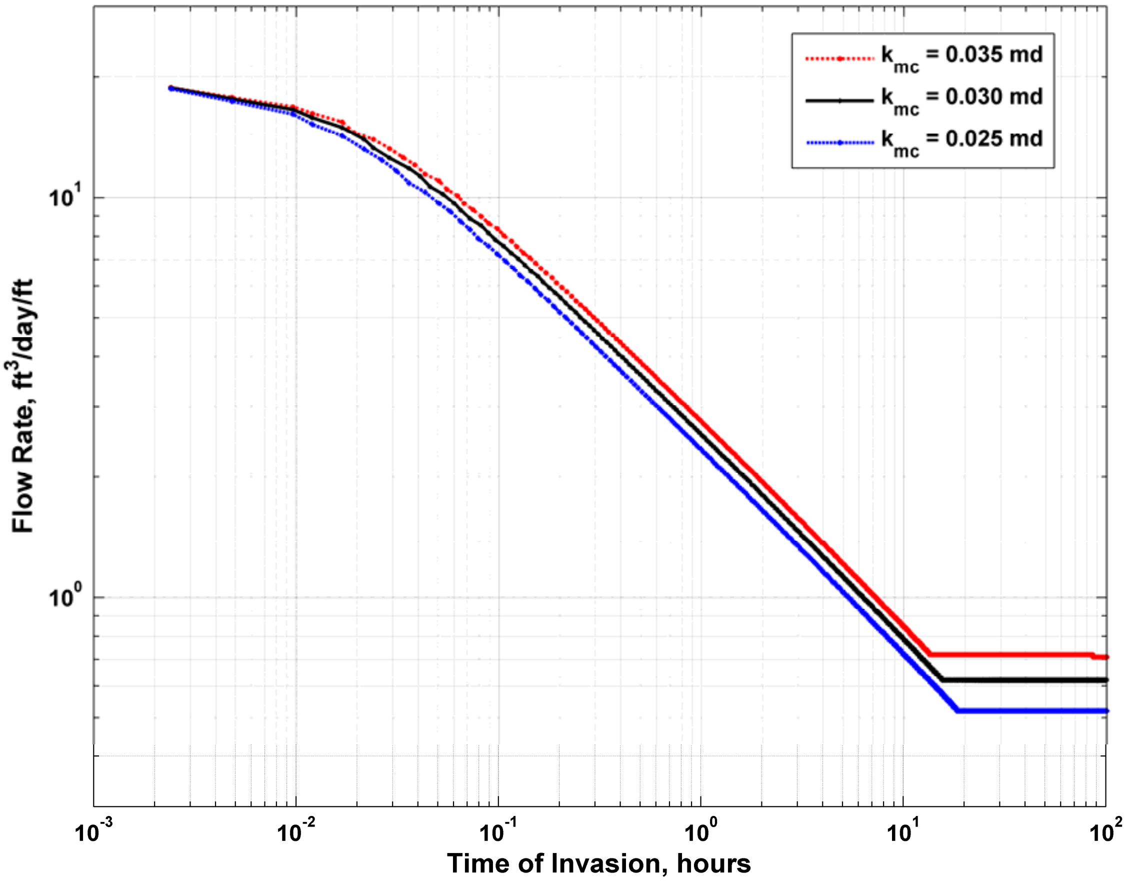

Figure 3.14: Time evolution of the flow rate of mud-filtrate invasion for three values of mudcake permeability. The base case corresponds to k_{mc} = 0.030 md. In general, variations of k_{mc} lower than 20% do not entail appreciable variations of flow rate.

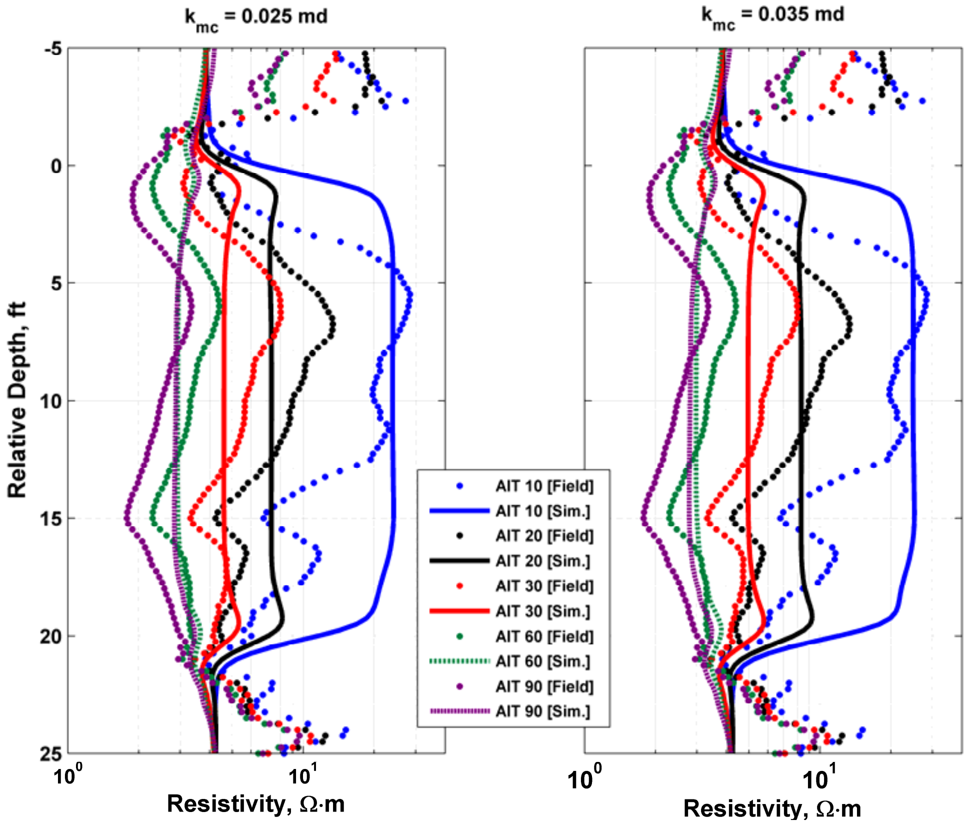

Figure 3.15: Numerical simulation of array-induction measurements: sensitivity to mudcake permeability. The left- and right-hand panels describe apparent resistivity curves simulated for the cases of variations of -17% and +17% the k_{mc} of the base case, respectively.

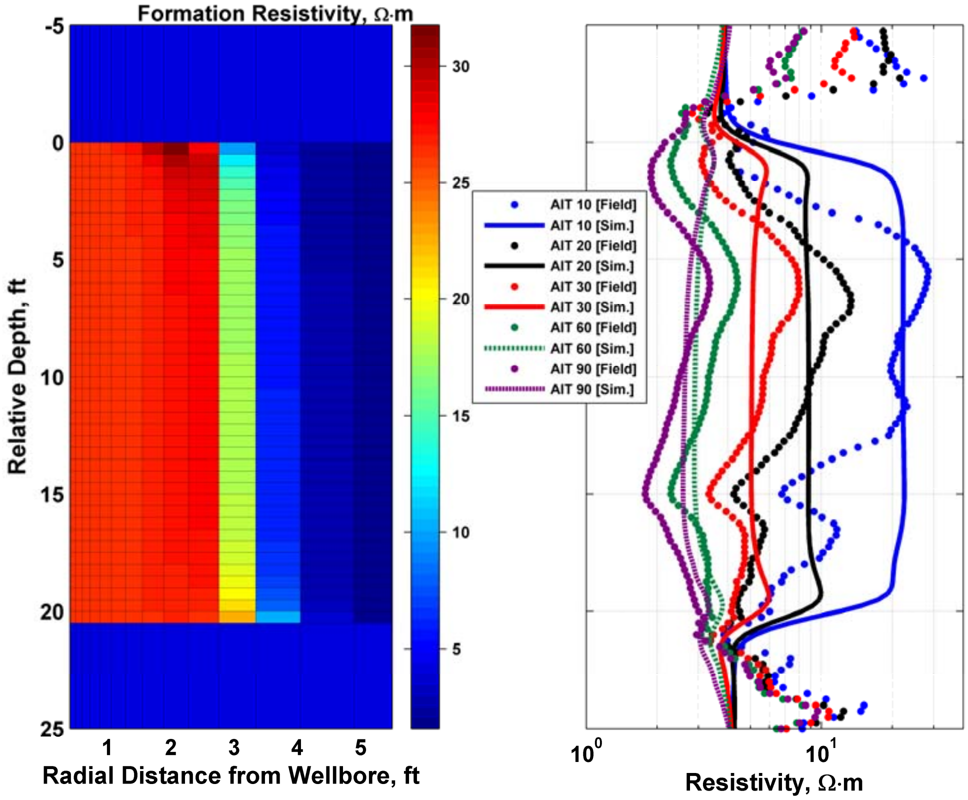

Figure 3.16: Numerical simulation of array-induction measurements yielded by the inversion of absolute permeability. The left-hand panel is a cross-section of electrical resistivity and the right-hand panel compares the simulated and measured AIT apparent resistivity logs.

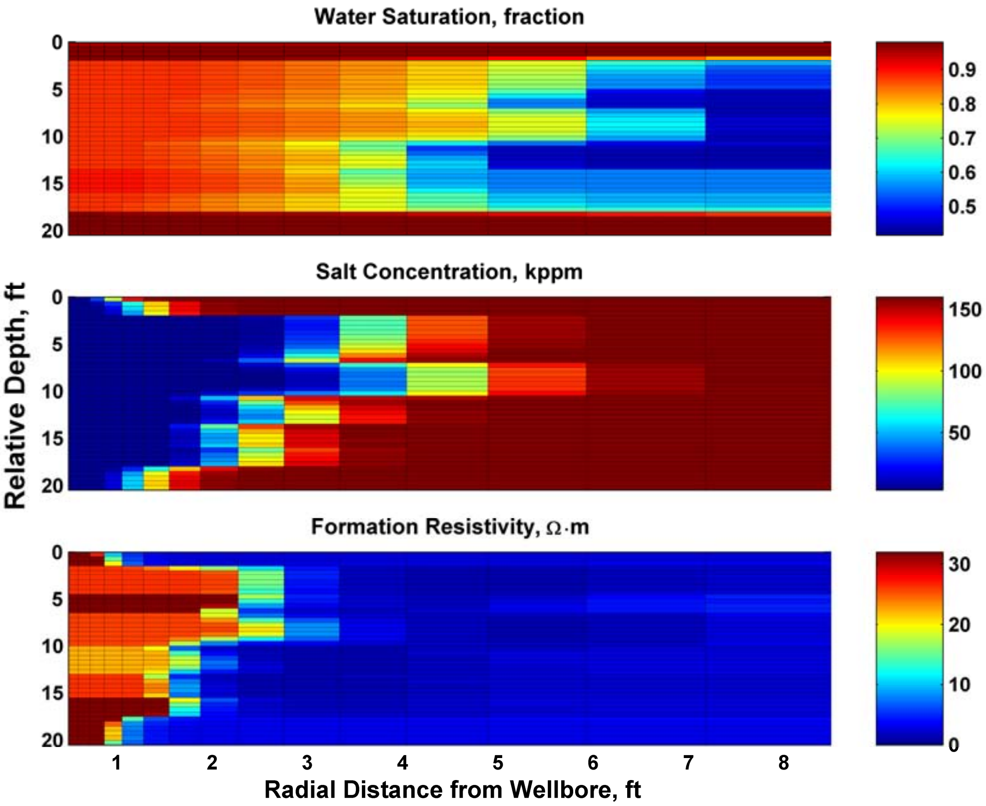

Figure 3.17: Cross-sections of water saturation, salt concentration, and electrical resistivity simulated for the case of a vertically heterogeneous flow unit. The time of invasion is five days. Layer permeabilities were assigned using initial permeability values obtained from petrophysical analysis (starting guess).

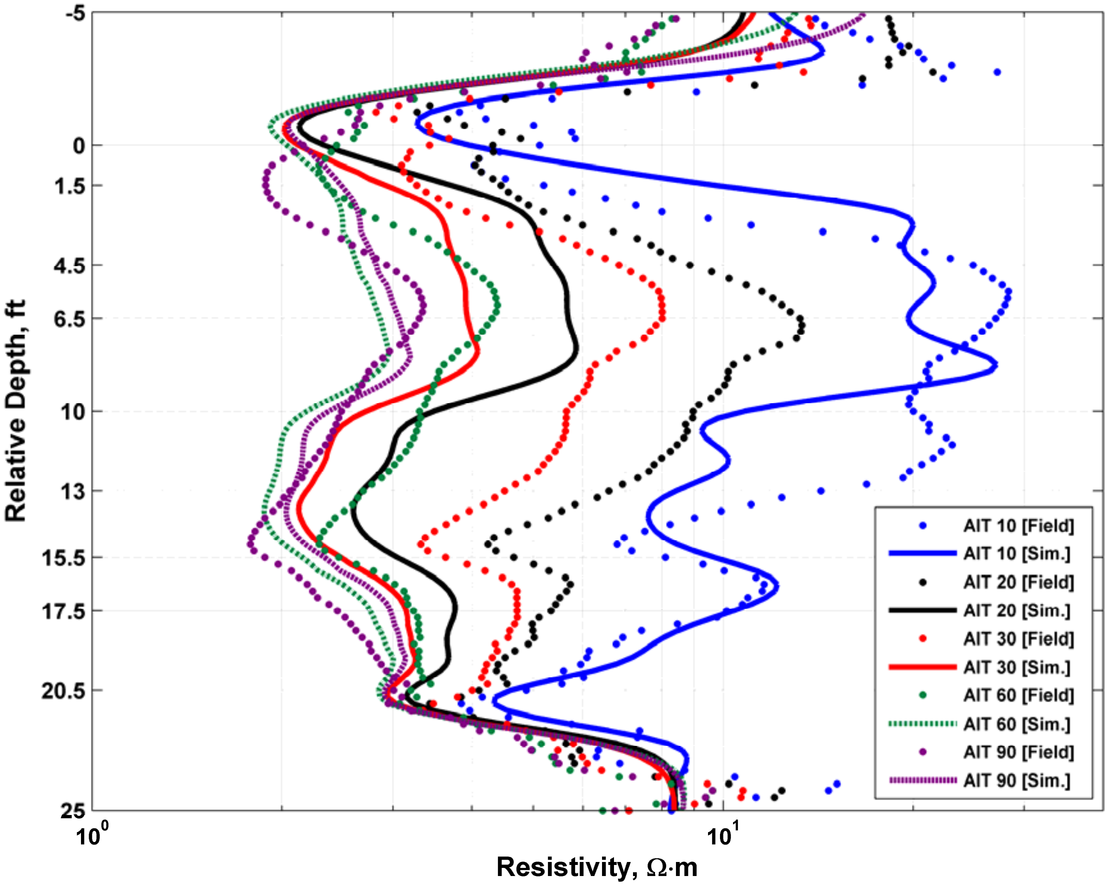

Figure 3.18: Numerical simulation of the array-induction measurements: initial reservoir and fluids properties for the case of a multi-layer heterogeneous formation.

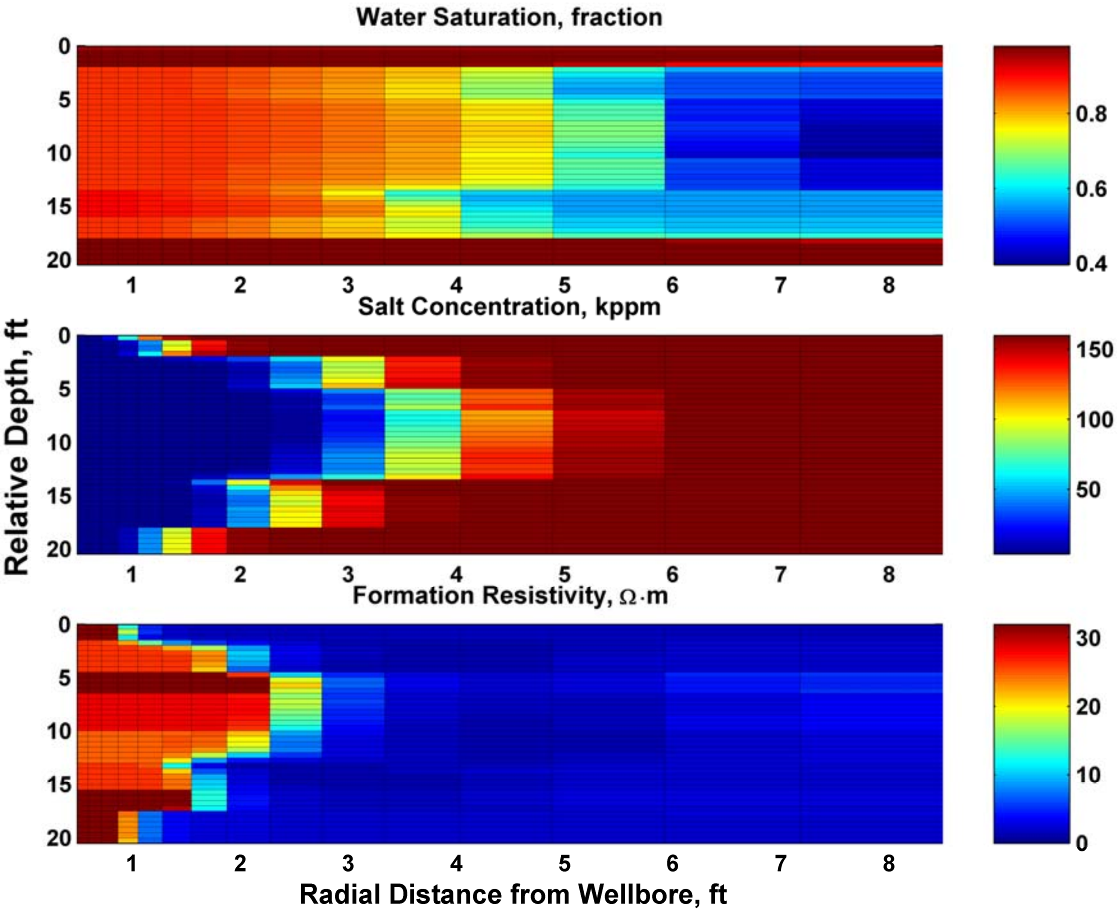

Figure 3.19: Cross-sections of water saturation, salt concentration, and electrical resistivity simulated for the case of a vertically heterogeneous fluid production unit. The time of invasion is five days. Layer permeabilities were manually assigned to reach an acceptable agreement between simulated and measured AIT apparent resistivity logs.

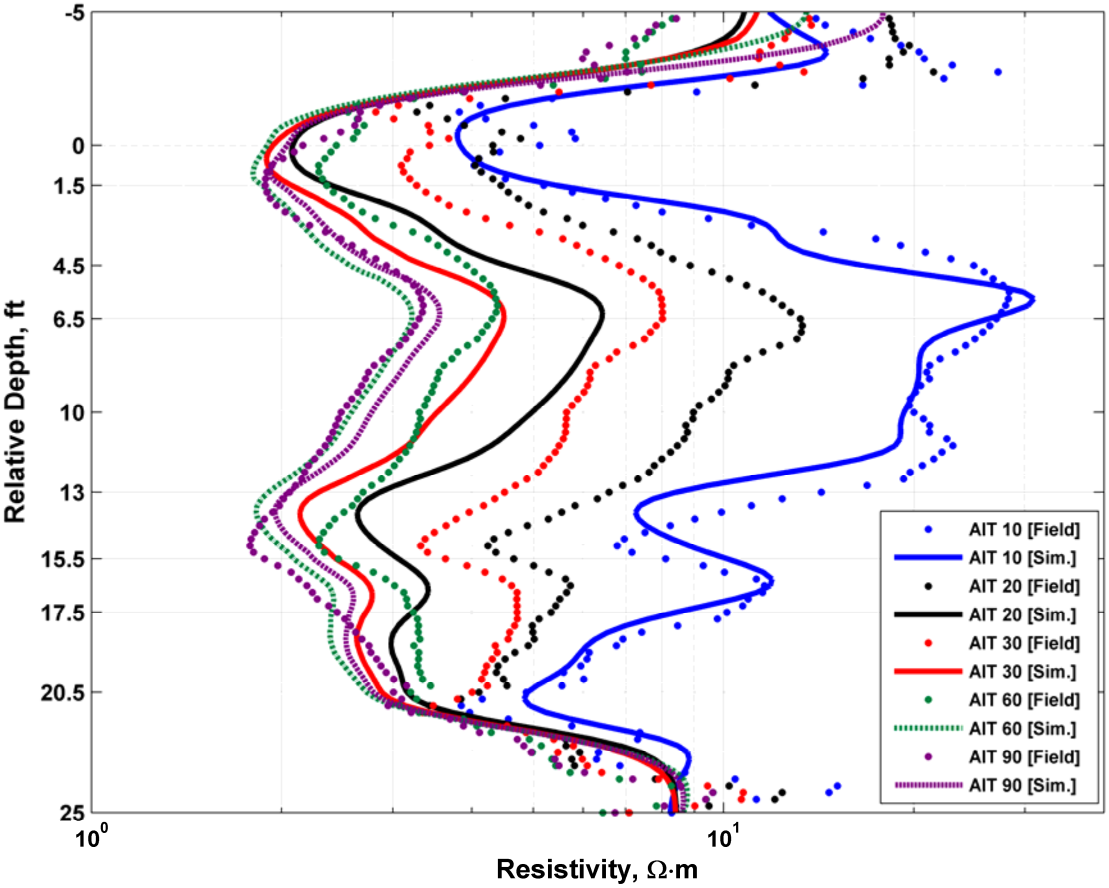

Figure 3.20: Simulation of array-induction measurements: layer permeabilities were manually assigned to reach an acceptable agreement between simulated and measured AIT apparent resistivity logs.

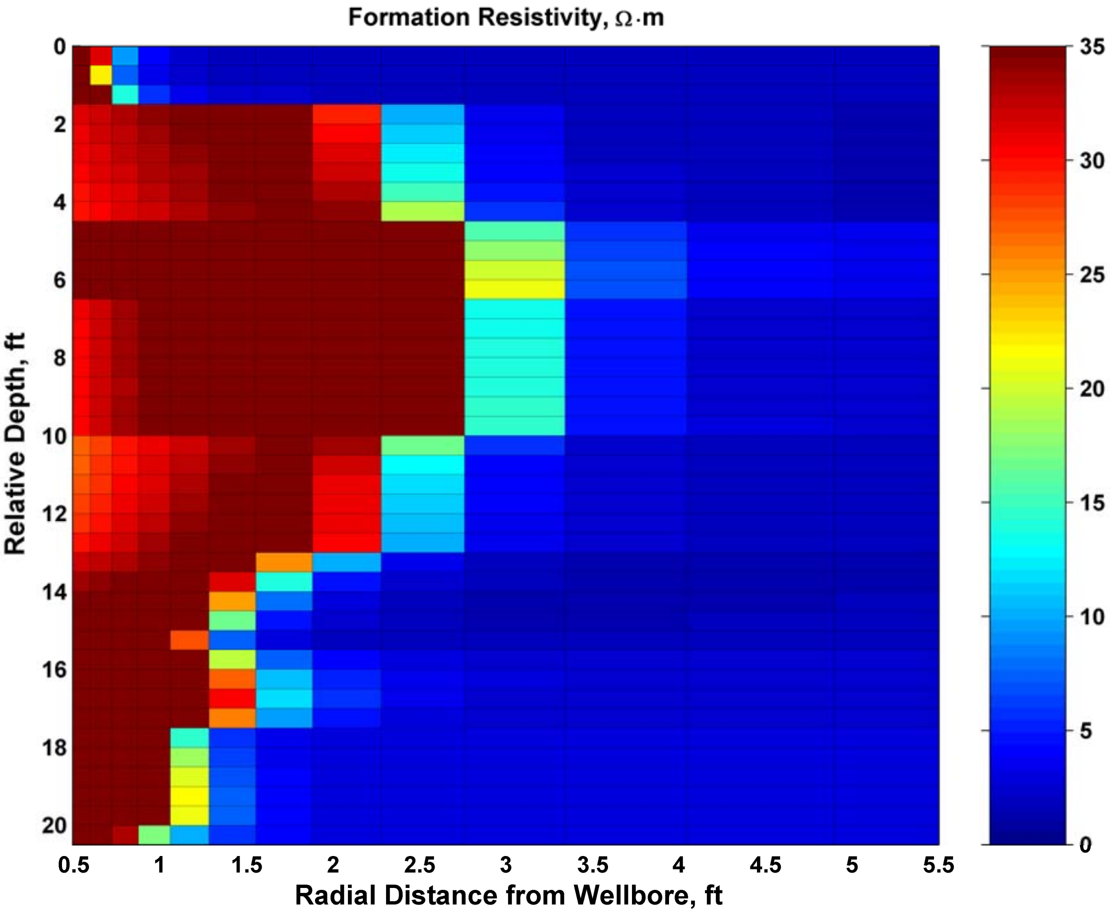

Figure 3.21: Cross-section of electrical resistivity simulated for the vertically heterogeneous fluid production unit model after the inversion of absolute permeability from array-induction logs. The time of invasion is five days.

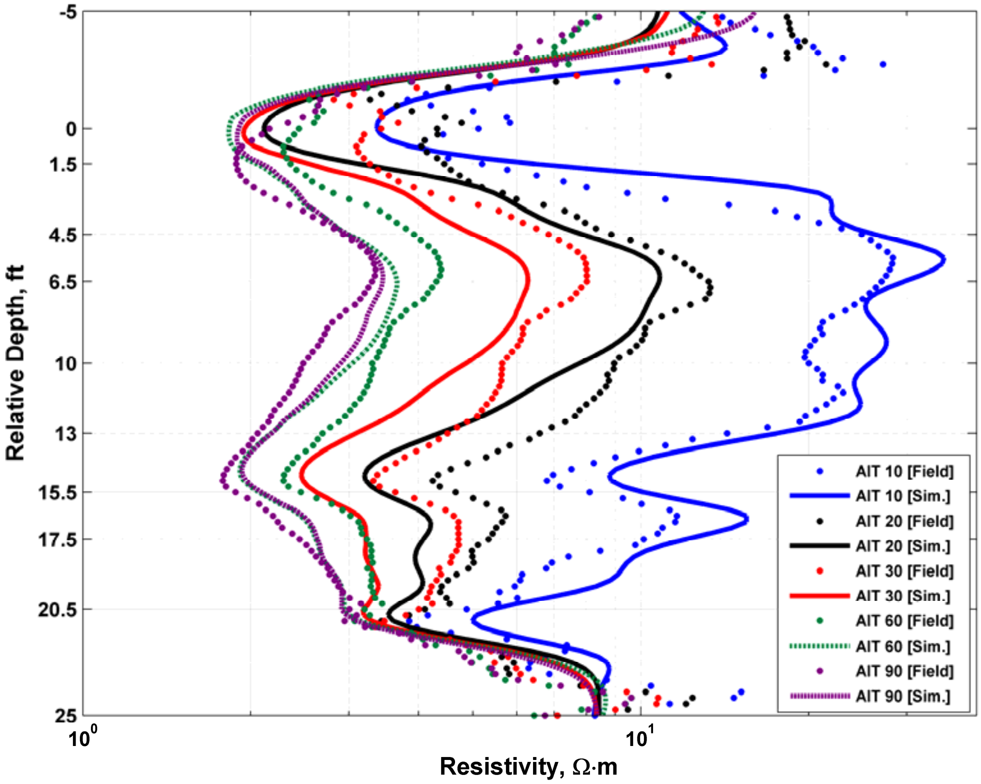

Figure 3.22: Comparison of the measured and simulated array-induction logs yielded by the inversion of absolute permeability for the case of a vertically heterogeneous fluid production unit.

Chapter 4: Effects of Petrophysical Properties on Array-Induction Measurements Acquired in the Presence of Oil-Base Mud-Filtrate Invasion

This chapter quantifies the influence of petrophysical properties on array-induction resistivity measurements acquired in the presence of oil-base mud (OBM) filtrate invasion. To simulate OBM-filtrate invasion, we consider a simple two-component formulation for the oil phase (OBM and reservoir oil) wherein the components are first-contact miscible. Simulations also include the presence of irreducible, capillary-bound, and movable water. The dynamic process of OBM invasion causes the component concentrations to vary with space and time. In addition, the relative mobility of the oil phase varies during the process of invasion given that oil viscosity and oil density are both dependent on component concentrations. This behavior in turn conditions the spatial distribution of electrical resistivity and, consequently, the borehole array-induction measurements. We use an implicit pressure, explicit concentration (IMPEC) reservoir simulator with two-component formation fluids to reproduce the invasion process in axial-symmetric rock formations penetrated by a vertical well. Simulations of the process of OBM-filtrate invasion yield two-dimensional spatial distributions of water and oil saturation that are transformed into spatial distributions of electrical resistivity using Waxman-Smits' formulation. Subsequently, we simulate array-induction measurements with a numerical mode-matching method.

4.1 INTRODUCTION

The array-induction imager tool (AIT) is widely used to measure formation resistivity in the presence of OBM. Resistivity measurements remain influenced by the process of mud-filtrate invasion that takes place under overbalanced drilling conditions. In the case of oil-base muds, invading mud-filtrate is miscible with formation oil. Such a fluid miscibility condition results in changes of bulk fluid density and fluid viscosity, thereby altering the apparent oil phase mobility in the near-wellbore region. Within a capillary transition zone, additional changes in the fluid saturation front due to invasion arise because of the presence of movable water. The fluid saturation front can also be altered because of variations of oil-phase mobility. Thus, it becomes imperative to accurately model the effect of OBM on the invasion process and, subsequently, on AIT measurements acquired some time after the onset of invasion.

Oil-base muds contain a mixture of oil, water, and surfactants necessary to maintain the oil-water mixture as an emulsion (Bourgoyne Jr *et al.*, 1986.; La Vigne *et al.*, 1997), in which oil is the continuous phase and encapsulates the water (Proett *et al.* 2002). The continuous phase dominates the process of invasion and mixes with formation fluids. Proett *et al.* (2002) simulated the process of OBM invasion using Todd and Longstaff's (1972) miscible displacement algorithm in which the OBM was treated as a solvent. In this chapter, we assume that oil is the main component of the OBM and neglect the effect of water and surfactants in the emulsion. Therefore, oil and water phases remain immiscible. This assumption is not restrictive in field applications, especially when the chemical activity of the OBM prevents separation of fluid phases within the mud as the latter invades the formation.

We are interested in quantifying the time-space variability of array-induction resistivity measurements in the presence of OBM-filtrate invasion. La Vigne *et al* (1997) studied several field cases where such variability was attributed not only to invasion, but also to shale fracturing. While performing experiments using OBM invasion on sandstone cores, Yan and Sharma (1989) observed considerable changes of wettability as well as a reduction of permeability. The latter laboratory evidence provides solid footing upon which to analyze the effect of invasion observed on induction resistivity measurements acquired in wells drilled with OBM.

In this chapter, we first analyze the field measurements available to study the process of mud-filtrate invasion in a clastic rock formation. Subsequently, we explain the method adopted to simulate the process of OBM-filtrate invasion and array-induction resistivity measurements. Sensitivity analyses shed insight to the petrophysical and fluid properties affecting the radial length and shape of the fluid invasion front. In addition, they provide a quantitative framework to interpret resistivity measurements. Finally, we use the results of sensitivity analyses to reproduce induction resistivity measurements acquired in a deepwater turbidite reservoir.

4.2 GEOLOGICAL DESCRIPTION

The formation under analysis consists of unconsolidated shaly sands of a turbidite depositional system in the deepwater Gulf of Mexico formed mainly by channel levees. The sedimentary structure includes ripple stratification, clay laminations, and massive intervals with moderate-to-good grain sorting. Based on thin-section interpretation, it is known that cement of clinoptilolite and smectite are present in this system. Quartz concentration is between 85% and 95%, with clay minerals being the remaining solid components of the rock. The latter minerals include illite/smectite, illite/mica, and kaolinite and chlorite in small amounts. In rare cases, it is possible to observe electrically conductive minerals such as pyrite, as well as traces of calcite and dolomite in the rock matrix. Porosity ranges between 20% and 34% while permeability varies from 10 md in low-porosity zones to 2,500 md in high-porosity intervals. Figure 4.1 shows photographs of two core sections displaying both shale-laminated and massive sand intervals.

4.3 PETROPHYSICAL ASSESSMENT

We focus our attention to three depth intervals of the formation penetrated by a cored well. The first interval is at the lower section of the formation and is a 100% water-saturated rock unit that is assumed homogeneous (single layer). This interval is used to calibrate our synthetic base case where we perform sensitivity analyses of resistivity measurements to several petrophysical and fluid properties. The second and third intervals, located in the upper section of the formation, correspond to partially oil-saturated rock units containing movable water. These two intervals will be subsequently used to simulate the process of mud-filtrate invasion and to reproduce field measurements with numerical simulations.

4.3.1 Water Saturation

The formation is mainly composed of shaly sands and this prompts us to invoke Waxman-Smits' (1968) equations to calculate water saturation (S_w). However, since the salt concentration of connate water is very high (>200,000 ppm), Archie's (1942) equation can also be applied to calculate S_w in cases of low values of hydrocarbon saturation. Waxman-Smits' equation is given by

$$\frac{1}{R_t\left(r,z\right)} = {S_w}^{n^*}\left(r,z\right)\frac{\phi^{m^*}\left(z\right)}{a}\left[\frac{1}{R_w}+\frac{BQ_v}{S_w\left(r,z\right)}\right], \tag{4.1}$$

where r is radial distance measured from the wellbore, z is vertical distance with respect to the top of the formation, R_t is true formation resistivity R_w is connate water resistivity, a is the tortuosity factor, m^* and n^* are clay-corrected Archie's cementation and saturation exponents, respectively, Q_v is the volumetric concentration of sodium exchange cations (CEC) associated with clay, and B designates the equivalent conductance of the counterions as a function of connate water resistivity. We use equation (19) of Waxman and Smits' (1968) work to calculate B, whereas m^*, n^* and Q_v are obtained from laboratory measurements. Equation (4.1) is solved iteratively for S_w starting with Archie's S_w as the initial guess. Table 4.1 describes the input parameters used to calculate initial water saturation using Waxman-Smits' model. Such parameters were obtained from laboratory measurements performed on cores and fluid samples withdrawn from the formation under consideration. Appendix A describes in more detail the methodology for the assessment of petrophysical properties.

4.3.2 Porosity and Permeability

We followed the method described by Salazar *et al.* (2006) to calculate porosity and permeability. Porosity is calculated from density and neutron measurements by accounting for the presence of two fluids (oil and water) and two solid components (quartz and clay) in the porous medium. Permeability is calculated via a modified Timur-Tixier equation from porosity and irreducible water saturation. The specific equation for permeability was obtained with calibration of rock-core porosity-permeability measurements, and is given by

$$k = 4.22 \times 10^{6} \frac{\phi^{7.5}}{S_{wir}^{\;0.09}}, \tag{4.2}$$

where k (md) is permeability, ϕ (fraction) is porosity, and S_{wir} (fraction) is irreducible water saturation. The coefficient and the exponents of the above equation were estimated with a multi-linear least-squares regression. Figure 4.2 shows the results obtained from the petrophysical analysis in the water interval. Figure 4.3 describes the results obtained from the petrophysical assessment in the two partially hydrocarbon-saturated zones.

4.4 SIMULATION OF ARRAY-INDUCTION RESISTIVITY MEASUREMENTS

We describe the simulation of array-induction resistivity measurements in two stages. The first stage discusses our reservoir simulation method for OBM-filtrate invasion in the formation. The second stage describes our resistivity simulation technique that uses spatial distributions of water saturation, calculated in the presence of OBM invasion, and transforms them into spatial distributions of electrical resistivity via equation (4.1).

4.4.1 Numerical Simulation of the Process of Mud-Filtrate Invasion with a Compositional Simulator

We use an IMPEC numerical formulation to calculate the spatial distribution of water saturation due to OBM-filtrate invasion. The formulation and the algorithm used in this simulation are similar to those described by Malik *et al*. (2007). We assume azimuthal symmetry in formation properties with respect to the axis of a vertical borehole. Our formulation enforces boundary and source flow-rate conditions on specific depth segments along the wellbore. The outer limits of the reservoir consist of impermeable zones with no-flow boundary conditions. Peng-Robinson (1976) equation of state is used to calculate the fluid compressibility factor and to solve for oil phase density. Since we assume that the OBM is water-free, salt concentration in the water phase is considered constant across the formation and equal to that of connate water.

Malik *et al*. (2007) simulated formation testing and pressure transient measurements using a multi-component formulation in the presence of OBM invasion. They described hydrocarbon phase components in the formation using four pseudo components whereas mud filtrate was modeled with one pseudo component. Increasing the number of pseudo components can lead to longer computation times. In addition, due to the averaging of fluid component properties, we may not observe a significant difference in the fluid saturation front (and, therefore on apparent resistivity measurements) by increasing the number of pseudo components. Thus, in order to keep computational time to a minimum, we use a simpler binary formulation to describe both mud filtrate and formation oil. All components of OBM filtrate and formation oil are lumped into two pseudo components. Appendix C presents the formulation used in the process of multi-component miscible fluid-flow.

Table 4.2 summarizes the geometrical properties for the numerical grid used to simulate the base case. The wellbore radius is equal to 0.49 ft and the external radius is 1000 ft, with the grid consisting of 50 nodes in the radial direction and 60 nodes in the vertical direction. In keeping with the rapid space-time variations of pressure and component concentrations in the near-borehole region, radial nodes are logarithmically spaced from the wellbore toward the outer grid boundary (located 1000 ft away from the axis of the borehole). Along the vertical direction, grid nodes are spaced uniformly.

We simulate the process of OBM-filtrate invasion with flow rates of invasion calculated on the basis of specific formation and mud properties. The calculation of the invasion flow rate is based on the work by Wu *et al*. (2005) concerning WBM-filtrate invasion. At the onset of the mud-filtrate invasion process, the flow rate of filtrate is high due to the overbalance pressure in the wellbore. As the mudcake thickens, the filtrate flow rate gradually decreases with time. Although mudcake eventually becomes impermeable, invasion continues at a slow rate until the casing is set in the wellbore. Since OBM and formation oil are miscible, the invasion process in the presence of OBM differs from that involving WBM. In our work, we use a constant volume-averaged flow rate that was intended to simulate WBM-filtrate invasion as described by Wu *et al*., (2005). Rather than developing a new algorithm to quantify the mud-filtrate invasion process in the presence of OBMs, we use the theoretical WBM algorithm of Wu *et al*.

(2005) and adjust it as necessary to reproduce borehole resistivity measurements and to calculate flow rates of invasion.

We assume that the original formation hydrocarbons consist of components in the range from C_2 to C_{30+}. These hydrocarbons are lumped into one component (FHC_1) using their pseudo properties summarized in Table 4.3. Oil-base mud filtrate is assumed to consist of components from C_{14} to C_{18} that are also lumped into one component (MC_{16}). Moreover, the binary-interaction parameter between the hydrocarbon components is assumed null.

We calculate oil viscosity of the hydrocarbon phase, μ_o, using a quarter-power mixing rule (Todd and Longstaff, 1972) that is widely used in the literature to describe well-mixed fluids (Koval, 1963). The mixing rule is applied to the sum of component concentrations of formation oil (x_{fo}) and OBM (x_{OBM}), given by

$$\mu_o = \left[x_{fo} \cdot \mu_{fo}^{\ 1/4} + x_{OBM} \cdot \mu_{OBM}^{\ 1/4}\right]^4 .$$

In the above expression, component viscosities (μ_{fo}, μ_{OBM}) are initialized to specific values of formation temperature and pressure. Under dynamic drilling conditions, drilling mud mixes with the solid particulate matter and formation fluids when the drill bit penetrates the formation. This can modify the composition and viscosity of the mud. In addition, due to the high cost of OBM compared to WBM, OBM is often recycled in field applications, thereby altering its original composition. Such an adverse situation leads to uncertainty in knowing the exact composition, PVT properties, and viscosity of the OBM. In our simulation model, we take into account uncertainty of mud-filtrate composition by simulating cases of different mud viscosity and by simulating the corresponding impact on AIT measurements.

Relative permeability and capillary pressure are two fundamental properties in the simulation of multiphase fluid flow. Figure 4.4 shows laboratory measurements of oil-water relative permeability and capillary pressure curves, respectively, used for the simulations considered in this chapter. The same figure shows a least-squares fit to the Brooks-Corey (Corey, 1994) relation that is ultimately assumed in our analysis. Table 4.4 summarizes the specific parameters used in conjunction with Brooks-Corey saturation-dependent properties. For completeness, the Appendix describes in detail the Brooks-Corey relationships for capillary pressure and relative permeability Oil-base mud and formation oil are first-contact miscible under reservoir pressure and temperature conditions, whereupon no capillary pressure or relative permeability effects exist within the hydrocarbon phase.

4.4.2 Resistivity Modeling

We simulate array-induction resistivity measurements from the spatial distribution of electrical resistivity. The simulation assumes 2D axial-symmetry, where current loop sources are located at the center of the borehole. We use the Numerical-Mode Matching Method (NMM) to perform the simulation (Chew *et al.*, 1984; Zhang *et al.*, 1999).

In summary, the algorithm is initialized with the fluid-flow simulation of OBM invading porous and permeable media. Inputs for the simulation include rock properties and fluid PVT properties obtained from *a priori* information. One of the main outputs of this process is water saturation, which is converted into electrical resistivity using Waxman-Smits' formulation. Subsequently, we use the spatial distribution of electrical resistivity to simulate the corresponding borehole array-induction resistivity measurements.

4.5 BASE CASE

We designate the rock formation shown in Figure 4.2 as our base case for the simulation of mud-filtrate invasion. The formation under analysis is 100% water saturated. Subsequently, we modify the initial water saturation of the same formation to carry out sensitivity analyses in a partially oil-saturated formation. Table 4.5 summarizes the assumed average petrophysical properties for the formation under consideration.

4.5.1 History Matching of Apparent Resistivity Measurements to Estimate the Flow Rate of OBM

Because the simulation of OBM-filtrate invasion requires knowledge of the flow rate, we invoked the well established concept of WBM-filtrate invasion to estimate the flow rate of invasion. To that end, we used the University of Texas' Formation Evaluation Toolbox (UTFET), which allows one to calculate the flow rate of mud-filtrate invasion based on mudcake, rock, and fluid properties (Alpak *et al.*, 2003; Wu *et al.*, 2005). The process begins with a model that assumes standard mudcake properties for water-base mud (Dewan and Chenevert, 2001). After multiple simulations with varying mudcake properties (permeability, porosity, and maximum thickness), we secured a good match between measured and simulated apparent resistivity measurements. The average flow rate necessary to reproduce the apparent resistivity curves was approximately 0.027 $ft^3/d/ft$. Table 4.6 describes the mudcake properties used to calculate the initial flow rate of mud-filtrate invasion. The same table describes the formation and fluid properties to be used in the analysis of the base case.

Figure 4.5 describes the spatial distributions of water saturation and electrical resistivity calculated after three days of WBM-filtrate invasion. As expected, the low mudcake permeability causes shallow invasion similar to the case of OBM that is subsequently described in this chapter. This procedure is performed to calculate an initial guess of the flow-rate of OBM-filtrate invasion. However, we note that such a low permeability value for mudcake is not common in practical applications.

4.5.2 Simulation of OBM-filtrate Invasion

The calculated average flow rate for the WBM case is used as input to the simulation of OBM-filtrate invasion together with the properties described in the lower section of Table 4.6. Figure 4.6 shows spatial distributions of water saturation and electrical resistivity calculated after three days of invasion. We note the similarity of the spatial distributions of electrical resistivity with those shown in Figure 4.5. Figure 4.7 compares the simulated AIT measurements against field data for the cases of invasion with WBM and OBM.

Figure 4.8 shows the time evolution of the radial distribution of OBM-filtrate saturation into the wet formation. Given that the spatial distribution of formation fluids due to invasion varies with time, formation resisitivity in the near-wellbore region also remains a function of time. Three days after the onset of invasion the radial length of invasion is approximately 0.3 ft. This observation is consistent with previous studies (Proett *et al*. 2002) about the simulation of OBM invasion, which suggested that the radial extent of OBM invasion was shallower than for the case of WBM invasion for the same rock-formation properties.

4.6 SENSITIVITY ANALYSIS

We performed several sensitivity analyses to appraise the effects of several petrophysical and fluid properties on the simulated array-induction resistivity logs. To that end, we slightly modified the base case to study the effect of OBM-filtrate invading a partially oil-saturated formation. In this case, initial water saturation was assumed equal to 42% (hereafter referred to as oil-base-case). Therefore, the formation under consideration is located within a capillary transition zone with presence of movable water together with gravity forces and vertical cross flow. With the intent of emphasizing the spatial variability of array-induction resistivity curves, the average flow rate was increased to 0.1667 ft^3/day/ft, which is approximately six times higher than the one used for the WBM case.

Figure 4.9 shows the calculated spatial distributions of water saturation and electrical resistivity for this new case. We note low water saturation at the top of the formation and high water saturation toward the bottom of the formation due to gravity forces. Since the density of the water phase is higher than the density of the oil phase, water tends to flow toward the lower part of the formation.

Figure 4.10 shows the corresponding simulated AIT measurements. Mud filtrate displaces the movable water in the near-wellbore region thereby causing separation among the array-induction apparent resistivity curves. Figure 4.11 shows the time evolution of the radial distribution of oil saturation and oil viscosity that is miscible with formation oil. Mud filtrate reaches 0.9 ft into the formation due to the increased rate of invasion. Owing to the miscibility between OBM and formation oil, the concentration of OBM varies radially in the formation. The variation of OBM concentration in turn affects both oil-phase density and viscosity. As shown in Figure 4.11, oil-base mud viscosity is higher than formation oil viscosity. The mobility of the oil phase (λ_o) is defined as

$$\lambda_o(S_o, t) = \frac{k_{ro}(S_o)}{\mu_o(t)},$$

where k_{ro} is relative permeability of oil-phase as a function of oil saturation (S_o), and μ_o is oil-phase viscosity that varies spatially with time (t) due to invasion. Therefore, oil-phase mobility also varies spatially in the presence of mud-filtrate invasion. This behavior in turn affects the fluid saturation front, which not only depends on the rate of mud-filtrate invasion, but also on the viscosity contrast between OBM and formation oil.

4.6.1 Sensitivity to the Relationship between Porosity and Permeability

We consolidated this analysis using equation (4.2). To that end, we honored the dependency of permeability on porosity when dealing with extreme perturbations of the two properties. Moreover, for this analysis we kept the ratio of vertical to horizontal permeability equal to 0.30. We remark that for each set of porosity and permeability values, capillary pressure was also modified via Brooks-Corey's equations. Changes in capillary pressure entail changes in the radial distribution of fluid properties. Figure 4.12 shows the corresponding array-induction measurements simulated for three values of porosity and permeability. In high-porosity, high-permeability zones, the effect of gravity forces and cross-flow is remarkable as observed in the right-most track of Figure 4.12. Low-porosity low-permeability rocks entail marked radial variability of electrical resistivity, hence deep invasion profiles. The separation between apparent resistivity curves is largely governed by porosity. Accordingly, Figure 4.13 shows that invasion is relatively shallow for the case of high-porosity and high-permeability rocks.

4.6.2 Sensitivity to Capillary Pressure

For this analysis, we modified the parameters included in Brooks-Corey's equation for capillary pressure in two stages. The first stage consists of modifying the capillary pressure coefficient (P_c^0) to render extreme values of the maximum capillary pressure but keeping the same shape of the base-case capillary pressure curve. We perform the sensitivity for the case of no capillarity (P_c^0=0) and very high capillarity (P_c^0=150 psi·D$^{1/2}$). The effect of this parameter is almost negligible. However, for high values of capillary pressure the variability of resistivity curves is null. In the absence of capillary forces, it becomes easier to displace the water phase, and hence oil saturation increases in the near-wellbore region.

The second stage consists of modifying the capillary pressure exponent (e_p) to produce different shapes of the curves but keeping the same value of capillary-pressure coefficient. This approach is equivalent to either changing the height of the capillary transition zone or changing the grain-size distribution of the rock under analysis. Figure 4.14 shows three capillary pressure curves for three different values of e_p. Figure 4.15 shows the corresponding apparent resistivity curves for each capillary pressure curve. The variation of capillary-pressure exponent leads to a large pressure differential between the oil and water phases and makes it more difficult to displace water from the pore space. Therefore, as the exponent decreases, capillary pressure increases, leading to a decrease in the separation among apparent resistivity curves. Figure 4.16 shows that, for an exponent equal to 2, there is negligible displacement of the water phase by mud filtrate and, consequently, we do not observe separation among apparent resistivity curves.

4.6.3 Sensitivity to Residual Water Saturation

We modified the residual saturation to change the amount of movable water in the transition zone. The base case with S_{wr} = 0.07 was taken as the lower-bound value, whereas S_{wr} = 0.40 was the upper bound, which resulted in only 2% of movable water. Figure 4.17 shows the Brooks-Corey relative permeability and capillary pressure curves for both cases; the two curves are affected by changes of residual water saturation. Figure 4.18 shows the corresponding simulated apparent resistivity curves for three values of S_{wr}. From the plot, we observe that high movable water (low S_{wr}) causes a large variation of array-induction apparent resistivity curves compared to the small variation observed for the case of low movable water (high S_{wr}). Figure 4.19 displays the radial distribution of oil saturation at the end of three days of invasion. Increasing the residual water saturation makes it difficult to displace water from the pores and hence there is no significant separation between the simulated apparent resistivity curves.

4.6.4 Sensitivity to Relative Permeability (Wettability)

In this analysis, we modified the critical water saturation (S_{wcr}: water saturation when the relative permeabilities of wetting and non-wetting phases are the same) by changing the exponents of the Brooks-Corey equation for relative permeability. The critical water saturation of the oil-base case is equal to 59%, which is considered a mixed-wet condition. Figure 4.20 shows extreme cases of relative permeability with low-S_{wcr} indicating a preferentially oil-wet rock, and high-S_{wcr} indicating a preferentially water-wet rock. Figure 4.21 shows the simulated apparent resistivity curves for the three values of wettability, from left to right, oil-, mixed-, and water-wet, respectively. Preferentially oil-wet rocks cause the invading oil to penetrate deeper in the formation, thereby resulting in more variability of the array-induction apparent resistivity curves. Highly water-wet rocks cause water to adhere to the grains, thereby preventing the invading oil from moving freely into the formation and, consequently, the radial length of invasion becomes relatively shallow.

The latter situation is similar to the case of irreducible water saturation. A similar conclusion stems from the radial distribution of oil saturation shown in Figure 4.22. In that figure, the radial length of invasion extends to 1.9 ft into the formation for a value of critical water saturation equal to 0.32. If the wettability of the rock is altered during the process of OBM-filtrate invasion, Archie's saturation exponent is no longer constant in the radial direction, and effectively becomes a function of wettability (Donaldson and Siddiqui, 1989), hence variable with time depending on invasion rate. Such effect is difficult to quantify; it suffices to state that we have found that changes in the wettability state of the rock are the most dominant in controlling the variability of apparent resistivity curves.

4.6.5 Sensitivity to the Rate of Mud-Filtrate Invasion

We perform an additional sensitivity analysis by changing the rate of mud-filtrate invasion associated with the oil base case. Two cases of perturbations of flow rate were considered in which the rates were changed by 50%. Figure 4.23 shows the simulated apparent resistivity curves that resulted from this analysis. We note that as the flow rate increases the variability of the apparent resistivity curves also increases. Figure 4.24 indicates that high invasion rates lead to relatively deep radial invasion. Uncertainty in both the flow rate of invasion and the elapsed time from the onset of drilling can drastically influence apparent resistivity measurements, as the latter are highly sensitive to the time evolution of fluid saturation. Therefore, this sensitivity analysis shows that it is important to quantify both the mud loss and the maximum time of invasion for a given formation in order to assess the impact of mud-filtrate invasion on borehole resistivity measurements.

4.6.6 Sensitivity to OBM Viscosity

In order to quantify the uncertainty of mud-filtrate composition on borehole resistivity measurements, we performed a sensitivity analysis by modifying the value of mud viscosity. Two cases of OBM viscosity were analyzed (0.9 cp and 2.5 cp) and compared to the oil base case. Figure 4.25 shows the radial distribution of oil viscosity resulting from this analysis. Even though we decreased the OBM-filtrate viscosity by 24% and increased it by 40% with respect to the oil base case, there are negligible differences between the simulated apparent resistivity curves for each value of viscosity. Therefore, for the case of low uncertainty (±25%) in the viscosity of mud filtrate, the corresponding impact on simulated apparent array-resistivity measurements will be low in oil-bearing formations. However, if the formation is gas-bearing or heavy oil-saturated, where the viscosity contrast between mud and formation fluids is much higher, uncertainty in OBM viscosity can considerably affect the resistivity measurements.

4.7 REPRODUCING THE FIELD MEASUREMENTS

For the purpose of resistivity matching, we performed multiple simulations of the process of two-phase flow of oil-base mud filtrate invading a partially oil-saturated formation and compared the results to field measurements. As previously explained, the rock is also saturated with movable water whereas both formation and invading oil are fully miscible. The objective is to perform multiple simulations of induction resistivity by modifying the most dominant petrophysical and fluid parameters (as elicited from the sensitivity analysis) on invasion of OBM-filtrate, namely, relative permeability and flow rate of mud filtrate.

4.7.1 Field Data

Figure 4.3 shows the formation under analysis. The lower interval is a 7.5 ft-thick, fairly homogeneous sandstone, and the upper interval is a highly heterogeneous 48.5 ft-thick clastic sequence. Both intervals exhibit high values of porosity and permeability. Previously, we described the algorithm used to perform the petrophysical assessment of field measurements. The lower formation was subdivided into 4 petrophysical layers, whereas the upper formation was subdivided into 12 petrophysical layers. Layer selection was based on observed changes of porosity-permeability and resistivity (Salazar *et al*, 2006). By dividing the formation into several layers, we are honoring the vertical heterogeneities included in the flow units. Table 4.7 shows layer values of petrophysical properties for the two depth intervals. These properties are assumed constant in the radial direction, but distinct for each petrophysical layer. Based on equation (4.2), permeability was averaged within each layer and the ratio of vertical to horizontal permeability (anisotropy) was kept equal to that of the base case (0.3). Additional fluid, formation, and simulation grid properties are described in Tables 4.2 through 4.7.

4.7.2 History Matching

Once the layered model has been defined, we simulate array-induction measurements from the spatial distribution of electrical resistivity. At the end of resistivity modeling, field apparent resistivities are compared to those obtained from the simulation. The initial stage consists of matching the deepest-sensing resistivity curve (R90). This is accomplished by adjusting both porosity and initial water saturation. In the second stage, we attempt to match both the shallow-sensing resistivity curve (R10) and the separation of the intermediate-sensing curves (R20, R30, and R60). In the sensitivity analysis, we found that increasing the flow rate of invasion increased the maximum radial length of invasion. A similar situation occurred when we modified the value of critical water saturation in the relative permeability curves. The variability of the apparent resistivity curves increases when we assume that the rock is preferentially oil wet ($S_{wcr} <$ 50%).

The simulation is initialized with the flow rate and relative permeability curves for the oil-base case, namely, $q_{mf} = 0.1667$ ft^3/day/ft and $S_{wcr} = 59\%$. Subsequently, we change the average flow rate until securing a good match with the R10 curve. For the lower depth interval, the rate varies between 0.4 and 0.9 ft^3/day/ft whereas for the upper depth interval the value is between 0.3 and 0.9 ft^3/day/ft. Such values are 12 to 33 times higher than the ones calculated for the corresponding case of WBM-filtrate invasion. After multiple iterations, we were unable to reproduce the separation of the measured apparent resistivity curves. We realized that it was possible to secure a good match only if we modified the wettability of the rock. Because we did not have core flooding data to quantify the variation of rock wettability due to OBM-filtrate invasion, we implemented the simple approach of modifying the critical water saturation. This modification was performed layer by layer to secure the desired separation of apparent resistivity curves. Such separation also depended on the amount of movable water saturation within each layer. Assuming constant residual water saturation (S_{wr} = 7%), for high values of initial water saturation the invading fluid will move more freely into the formation, thereby causing larger variability of the apparent resistivity curves. In order to secure a good match between measurements and simulations, S_{wcr} was varied between 33% and 40%, with the lower values associated with those layers that exhibited low values of initial water saturation.

Previous studies of alkaline/surfactant/polymer (ASP) flooding validated some simulation models with laboratory measurements and showed that rock wettability depended on both formation and emulsion properties. Under uncertainty on the exact composition of OBM in the dynamic drilling environment, it is difficult to resort to an ASP model to simulate the process of mud-filtrate invasion. By modifying the critical water saturation to honor changes of rock wettability, we have introduced a simpler approach that can be used in conjunction with any reservoir simulator to match the measured apparent resistivities. Results from the simulation of mud-filtrate invasion consist of spatial distributions of water saturation and electrical resistivity, shown in Figures 4.26 and 4.27 for the lower and upper depth formation intervals, respectively. Such distributions were input to the simulation of array-induction resistivity curves. Figures 4.28 and 4.29 show the simulated apparent resistivities (2-foot vertical resolution) after manually changing both flow rate and critical water saturation. The same figures describe the field measurements, layer permeabilities, and average flow rate of mud filtrate. Figures 4.30 and 4.31 compare simulated to measured apparent resistivity curves. For the lower depth interval, the simulated deepest- and shallowest-sensing apparent resistivity curves agree well with field measurements. However, measured and simulated intermediate-sensing curves do not match across the two middle layers, probably due to the transformation of raw conductivity measurements into apparent resistivities. In the field measurements, the R10 curve exhibits higher apparent resistivity values than the R20 curve, which indicates an anomalous behavior. In this case, our simulations show a more realistic variation between R10 and R20 apparent resistivity curves with R10>R20. As shown in Figure 4.31, for the upper depth interval, with the exception of a few layers, most of the simulated apparent resistivity curves agree well with field measurements.

4.8 DISCUSSION AND CONCLUSIONS

We studied the influence of OBM-filtrate invasion on array-induction resistivity measurements using a binary component formulation to describe the miscibility of the oil phase. Numerical simulations indicated that resistivity measurements are highly sensitive to porosity and permeability, rock wettability, and rate of mud-filtrate invasion. Alteration of rock wettability in the near-wellbore region increases the mobility of the water phase and influences the apparent resistivity measurements. Our simulations show that, to properly quantify the influence of the process of OBM-filtrate invasion on borehole resistivity measurements, it is important to quantify the mud loss in the invaded formation as well as the duration of the invasion process.

The well-documented physics of WBM-filtrate invasion can be used to estimate an initial value of flow rate of OBM-filtrate invasion. By performing multiple sensitivity analyses we were able to diagnose which petrophysical and fluid properties entailed the largest change on the spatial distribution of fluid properties resulting from OBM invasion. High rates of invasion cause radially deep invasion profiles. However, relative-permeability and capillary-pressure curves control the shape of the fluid invasion front. Thus, when simulating array-induction resistivity measurements, we found that the variability of apparent resistivity curves with various radial lengths of investigation remained controlled by the rock's relative permeability and capillary pressure. The separation of these curves is relatively large when the rock if preferentially oil wet, whereas the separation is negligible when the rock is preferentially water wet.

We simulated array-induction resistivity measurements using a history-matching approach in a partially oil-saturated turbidite reservoir. The formation consisted of dead oil and was invaded with OBM-filtrate. Simulation results indicated that it was possible to secure a good match with field measurements by simultaneously modifying both critical water saturation and rate of mud-filtrate invasion. However, uncertainty on the value of critical water saturation rendered our history-matching method difficult to adapt for automatic inversion.

Dead oil and OBM-filtrate are fully miscible under reservoir pressure and temperature conditions. In addition, we assumed that OBM did not include a water phase as part of emulsion, thereby neglecting salt mixing between the emulsion and movable water in the formation. Our binary component formulation limits the modeling of partial miscibility between formation gas and OBM as we need additional pseudo-components to accurately reproduce phase behavior effects. In this chapter, we focused our analysis to a high-porosity, high-permeability formation and concluded that flow rate of invasion and relative permeability dominated the radial length of invasion and variability of apparent resistivity curves. However, this conclusion may not hold true in low-porosity, low-permeability formations. As emphasized by the sensitivity analysis, low-porosity rocks entail deep invasion and hence result in significant variability of apparent resistivity curves. At irreducible water saturation conditions, we did not observe changes in the radial distribution of water saturation: the OBM-filtrate mixed with the native oil without entailing separation of apparent resistivity curves with various radial lengths of investigation. On the other hand, we showed that array-induction resistivity measurements can be highly affected by deep invasion (1.5 ft to 2ft) in zones with movable water. The larger the difference between irreducible and initial water saturation, the smoother the radial distribution of water saturation, and hence the larger the variability of apparent resistivity curves with different radial lengths of investigation.

Given the lack of laboratory measurements of wettability, we did not quantify the effect of wettability variations on the saturation exponent. Donaldson and Siddiqui (1989) performed laboratory experiments by flooding crude oil into core samples and measured different values of Archie's saturation exponent, n, for different values of oil saturation. As they injected oil, the rock became strongly oil-wet, thereby increasing the saturation exponent. Based on the comparisons between measurements and simulations, we found that resistivity measurements acquired in the lower-depth interval oil zone were difficult to match. One possible reason for the mismatch could be the processing of field raw conductivity measurements into apparent resistivities. Another reason may be an anomalous radial invasion profile due to the presence of surfactants on the emulsion forming the OBM, which was not studied in this chapter. Including the presence of surfactants in the OBM is still work in progress. History matching with field measurements helped us to diagnose adverse field conditions and led to improved interpretation of apparent resistivity measurements in the presence of invasion.

Table 4.1: Summary of Waxman-Smits' parameters and rock and fluid properties assumed in the calculation of water saturation and porosity.

Variable	Units	Value
Archie's tortuosity factor *a*	-	1.00
Clay corrected *m*, *m**		1.92
Clay corrected *n*, *n**		2.00
Volumetric CEC, Q_v	meq/ml	0.064
Connate water resistivity @ 120 F	Ω·m	0.02
Matrix density	g/cm^3	2.65
Shale density	g/cm^3	2.50
Water density	g/cm^3	1.00
Hydrocarbon density	g/cm^3	0.75

Table 4.2: Summary of geometrical and numerical simulation parameters assumed for all cases of study.

Variable	Units	Value
Wellbore radius (r_w)	ft	0.49
External radius (r_e)	ft	1000
Reservoir thickness	ft	30
Number of nodes – *r*	--	50
Number of nodes – *z*	--	60
Grid cell size – *r*	ft	Variable
Grid cell size – *z*	ft	0.5

Table 4.3: Summary of PVT properties of the assumed in-situ hydrocarbon components and mud filtrate.

Property	Units	FHC_1	MC_{16}
Critical Temperature	^{o}F	854.3	822.4
Critical Pressure	psi	280	245
Acentric Factor	-	0.405	0.7112
Molar Weight	lb-mol	197	222
Viscosity	cp	0.84	1.5

Table 4.4: Summary of relative permeability and capillary pressure parameters used in Brooks-Corey's equations.

Variable	**Value**
Empirical exponent for wetting phase, e_w	2.2
Empirical exponent for non-wetting phase, e_{nw} (water base case and oil base case)	3.0 and 2.0
End point for wetting phase, k^0_{rw}	0.37
End point for non-wetting phase, k^0_{rnw}	0.99
Empirical exponent for pore size distribution, e_p	25
Capillary pressure coefficient, $P_c^0, [psi \cdot D^{1/2}]$	15

Table 4.5: Summary of assumed petrophysical properties for the two cases of study.

Property	**Units**	**Value**
Thickness	ft	30
Effective porosity	fraction	0.27
Water saturation	fraction	1.0
Shale concentration	fraction	0.12
Horizontal permeability	md	325
Vertical permeability	md	100
Formation compressibility	1/psi	1E-8

Table 4.6: Summary of mudcake, fluid, and formation properties assumed in the simulation of the process of mud-filtrate invasion.

Mudcake Parameters for WBM Only		
Variable	**Units**	**Value**
Mudcake reference permeability	md	5.0E-4
Mudcake maximum thickness	inches	0.4
Mudcake reference porosity	fraction	0.50
Mud Solid Fraction	fraction	0.06
Mudcake compressibility exponent	fraction	0.30
Mudcake exponent multiplier	fraction	0.10
Mud hydrostatic pressure	psi	8,000

Formation and Fluid Properties for All Cases of Study		
Variable	**Units**	**Value**
Initial formation pressure	psi	7,750
Mud-filtrate viscosity	cp	1.50
Oil viscosity	cp	0.85
OBM-filtrate density	lb/ft^3	48.07
Oil density	lb/ft^3	46.82
Wellbore radius	ft	0.49
Maximum invasion time	days	3.00
Maximum invasion flow rate	$ft^3/d/ft$	0.027
Temperature	^oF	139
Formation outer boundary	ft	1000
Residual water saturation	fraction	0.07
Residual oil saturation	fraction	0.10

Table 4.7: Summary of average petrophysical properties assumed for the formation under analysis.

Lower Interval			
Thickness	ϕ	S_w	*k*
ft	fraction	fraction	md
1.5	0.260	0.470	198
2.0	0.250	0.220	782
2.0	0.305	0.245	527
2.0	0.273	0.338	250
Upper Interval			
Thickness	ϕ	S_w	*k*
ft	fraction	fraction	md
5.5	0.230	0.230	409
3.5		***shale layer***	
4.0	0.240	0.210	928
2.0	0.275	0.210	628
4.5	0.250	0.215	928
5.5	0.310	0.202	923
3.5		***shale layer***	
5.0	0.250	0.250	1309
2.0		***shale layer***	
6.0	0.280	0.230	1440
2.0	0.290	0.300	989
5.0	0.270	0.250	1153

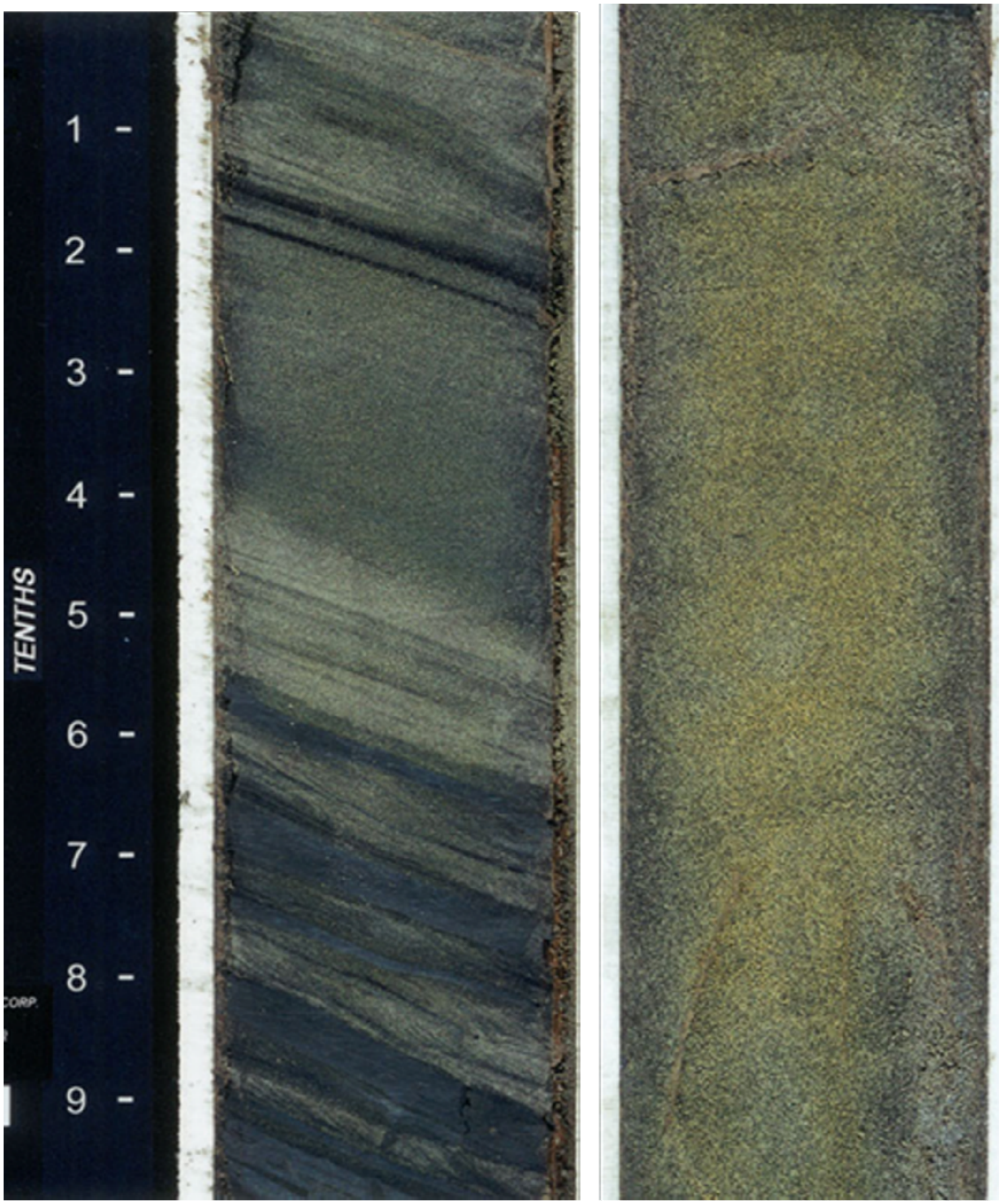

Figure 4.1: Core photographs showing clay-laminated (left panel) and massive (right-most panel) sand intervals. The vertical scale is given in units of 1/10th of foot.

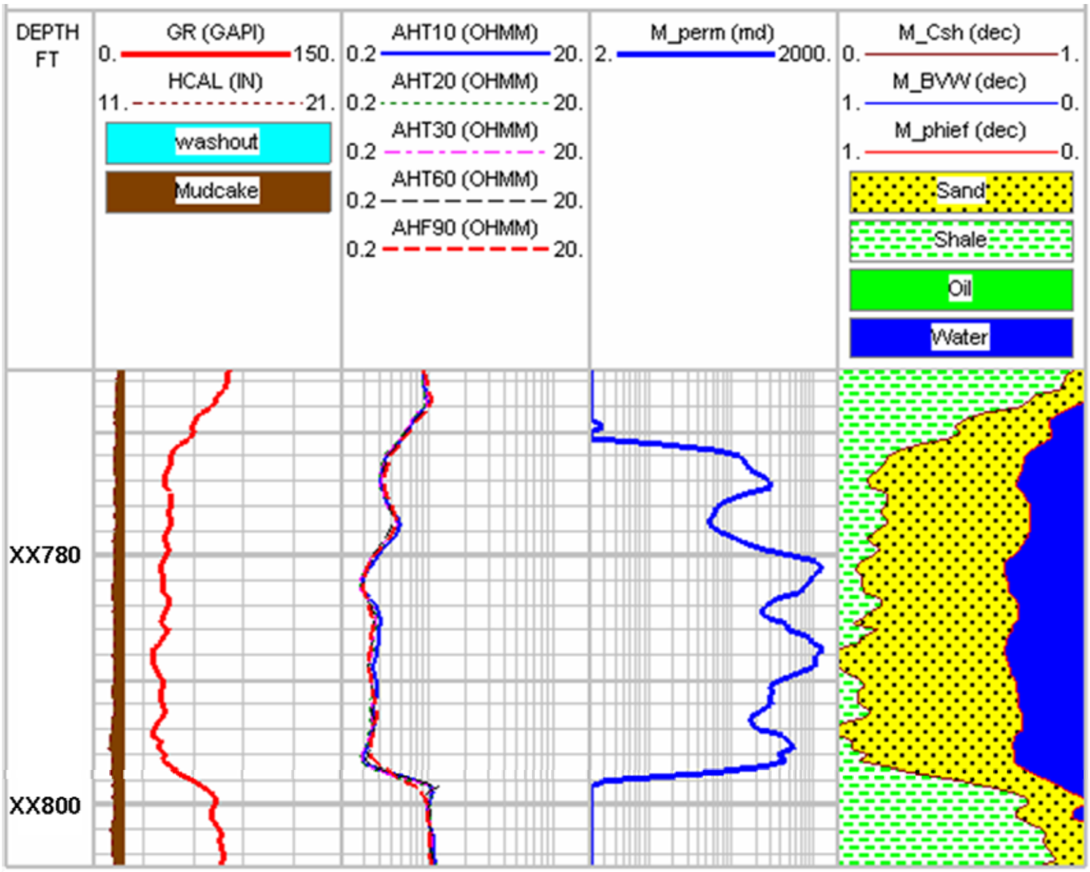

Figure 4.2: Petrophysical assessment within the water zone. Track 1 shows depth. Track 2 displays gamma-ray and caliper logs. Track 3 shows array-induction resistivity measurements (2-foot vertical resolution). Track 4 displays the estimated permeability. Track 5 describes the volumetric analysis with shale concentration, bulk volume water, and effective porosity. This depth interval is regarded as the base case of analysis.

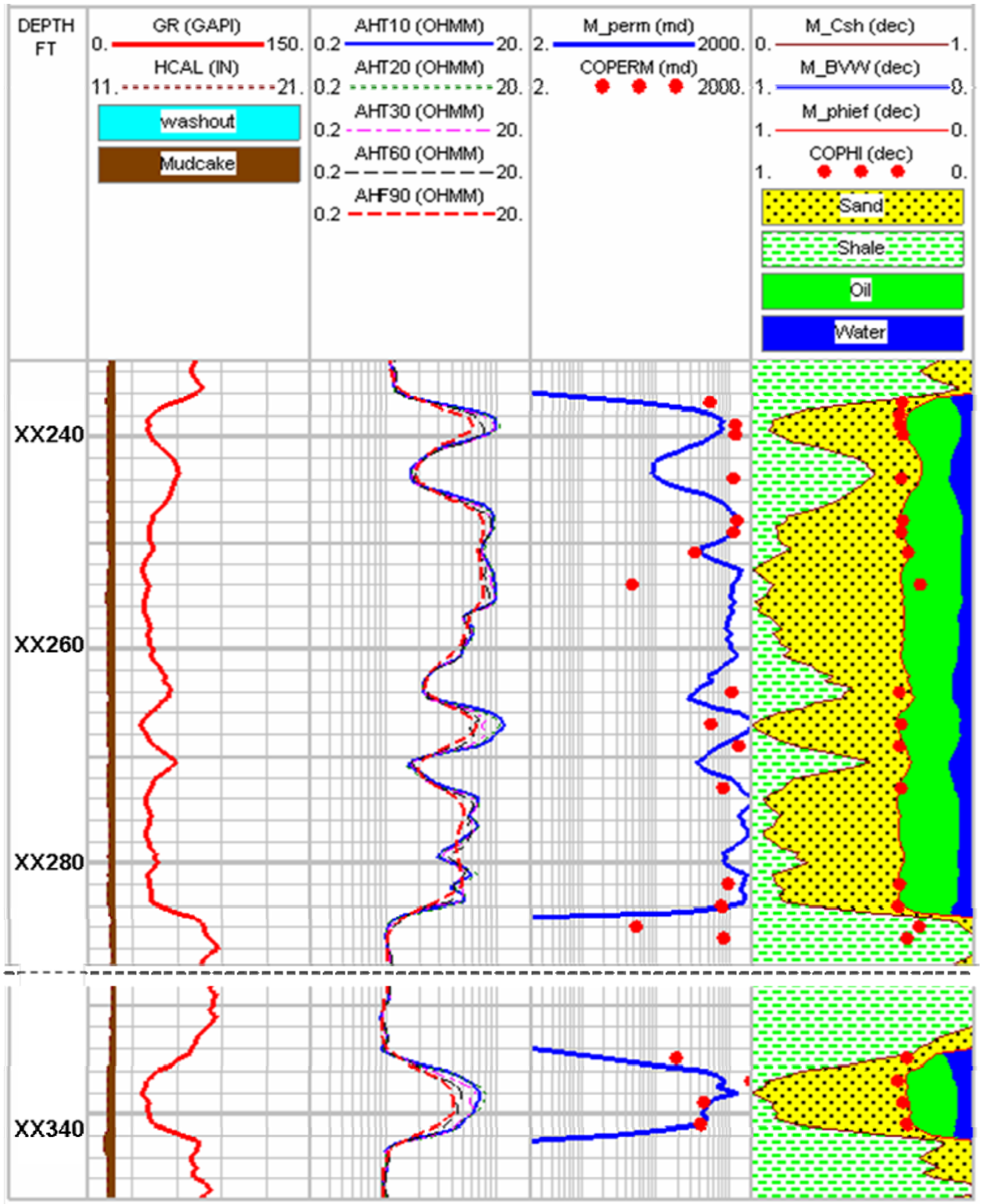

Figure 4.3: Petrophysical assessment of hydrocarbon zones. Track 1 shows depth. Track 2 displays gamma-ray and caliper logs. Track 3 shows array-induction resistivity measurements (2-foot vertical resolution). Track 4 displays log estimated and rock-core permeability. Track 5 describes the volumetric analysis with shale concentration, bulk volume water, and log estimated effective and rock-core porosity. The upper section is vertically heterogeneous while the lower depth interval is a fairly homogenous sand unit.

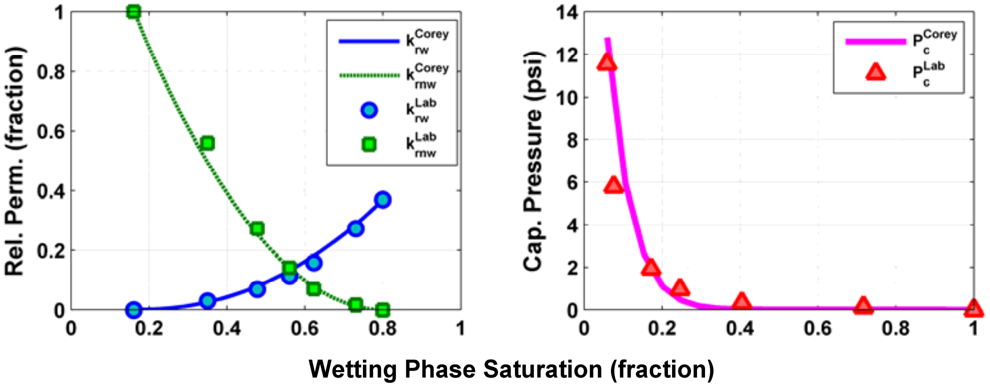

Figure 4.4: Water-oil relative permeability and capillary pressure curves assumed in the simulations of mud-filtrate invasion. Each panel compares Brooks-Corey's model to laboratory core measurements. The superscripts "Corey" and "Lab" designate relative permeability values calculated with the Brooks-Corey equation and measured in the laboratory, respectively.

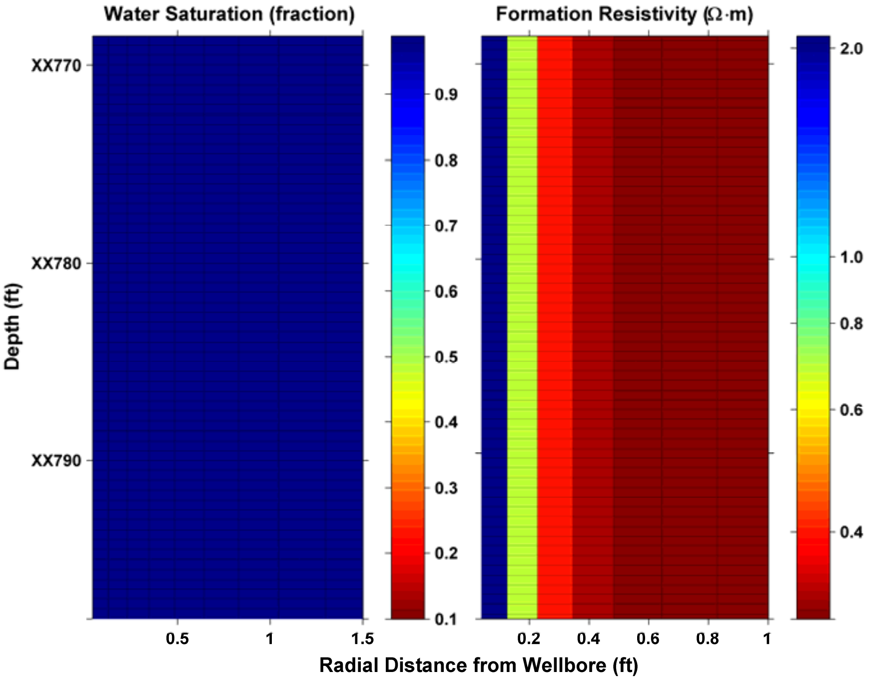

Figure 4.5: Spatial distributions of water saturation (left-hand panel) and electrical resistivity (right-hand panel) calculated after three days of water-base mud-filtrate invasion.

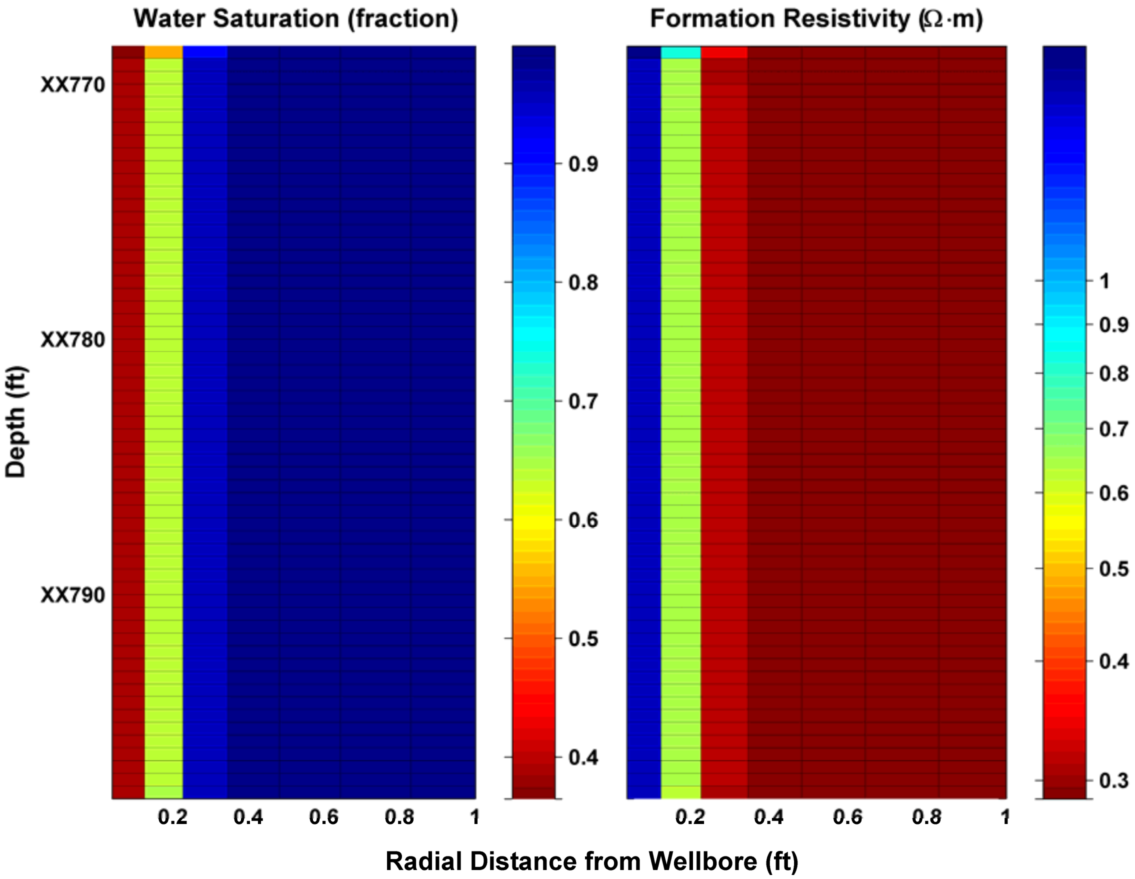

Figure 4.6: Spatial distributions of water saturation (left-hand panel) and electrical resistivity (right-hand panel) calculated after three days of oil-base mud-filtrate invasion into a water zone.

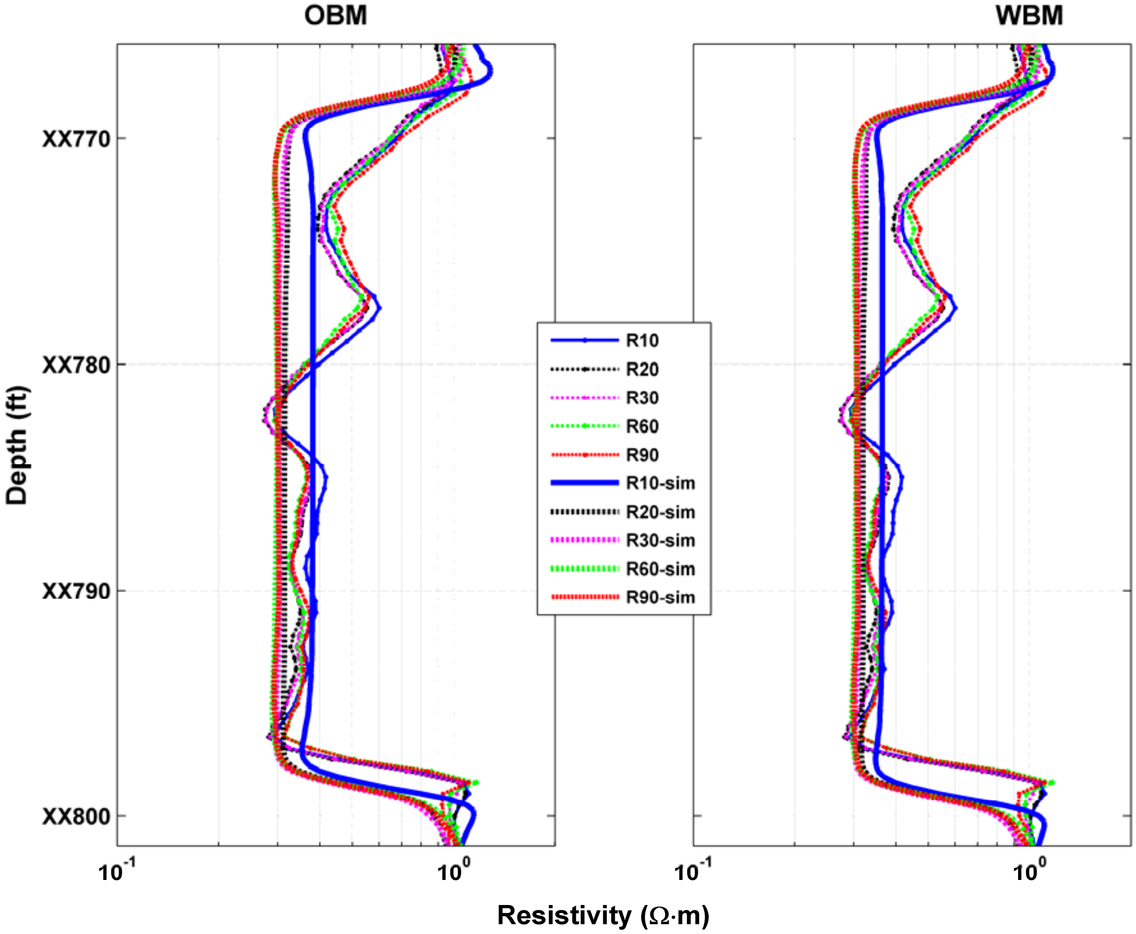

Figure 4.7: Measured and simulated array-induction apparent resistivities after three days of oil-base (right-hand panel) and water-base (left-hand panel) mud-filtrate invasion into a water zone.

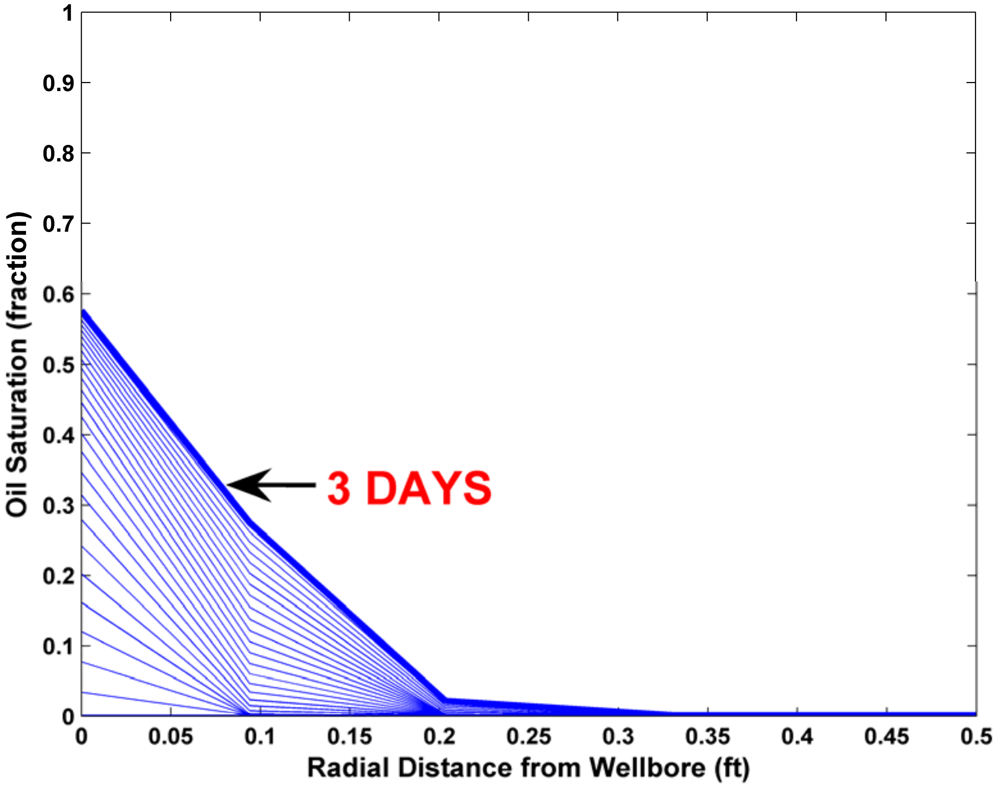

Figure 4.8: Time evolution of the radial distribution of oil saturation in the invaded formation. Twenty five curves are plotted at time intervals of 0.12 days. At the end of three days of invasion, mud-filtrate extends to 0.3 ft into the formation.

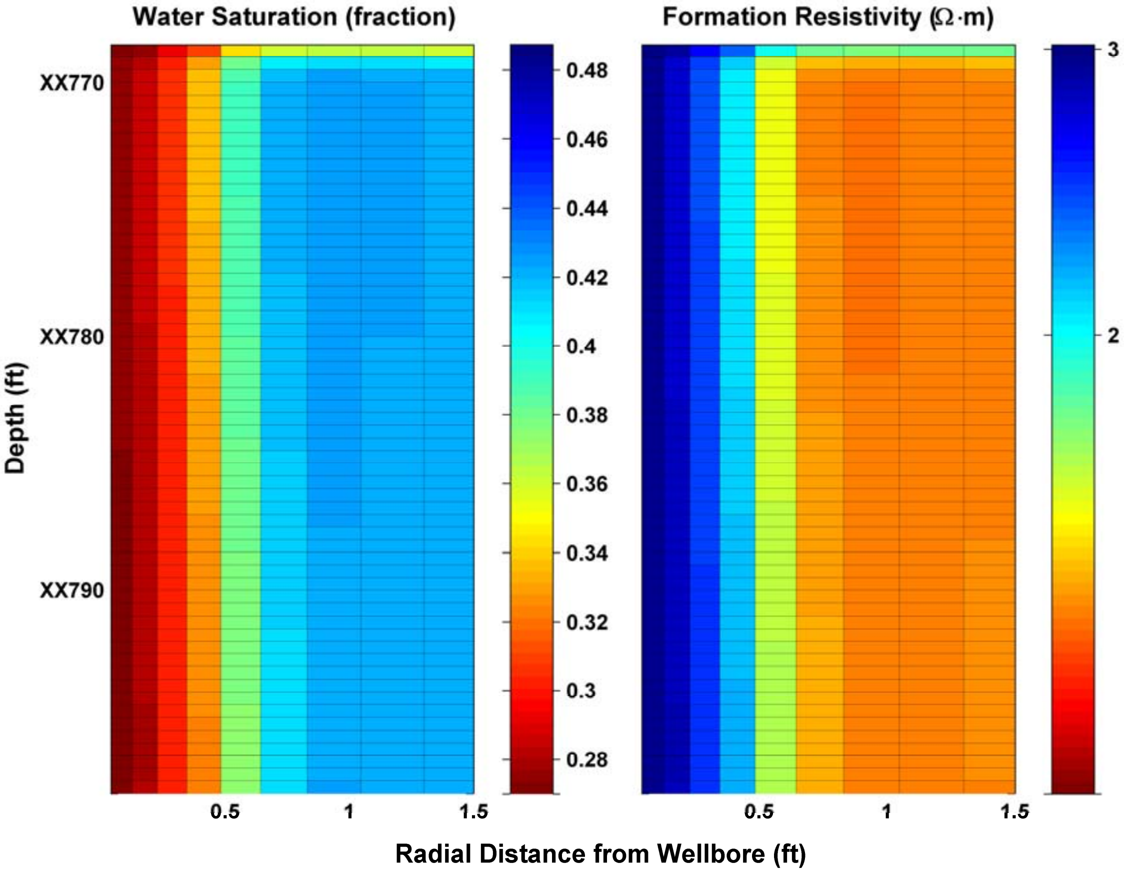

Figure 4.9: Spatial distributions of water saturation (left-hand panel) and electrical resistivity (right-hand panel) calculated after three days of oil-base mud-filtrate invasion into a partially oil-saturated formation.

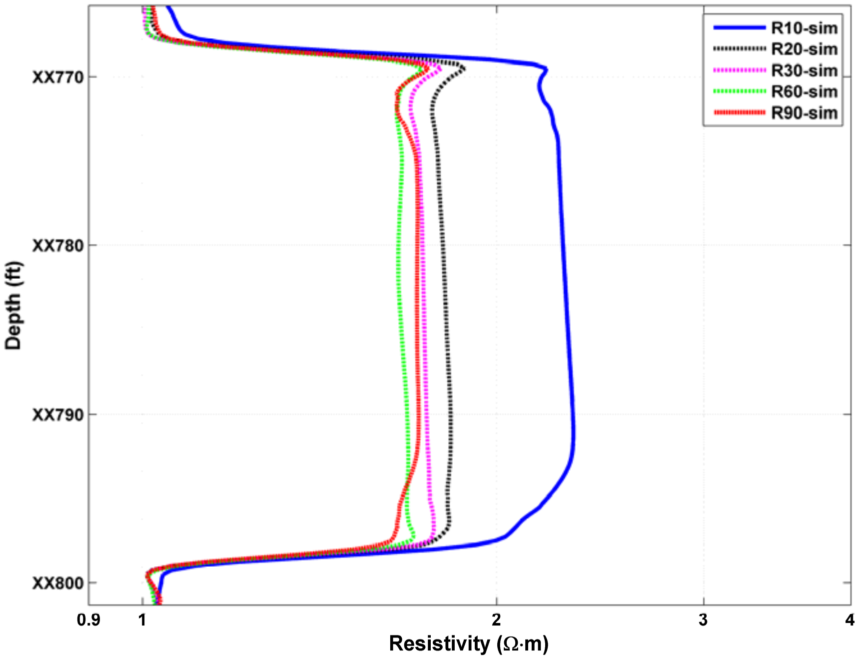

Figure 4.10: Array-induction apparent resistivities simulated after three days of oil-base mud-filtrate invasion into a partially oil-saturated formation.

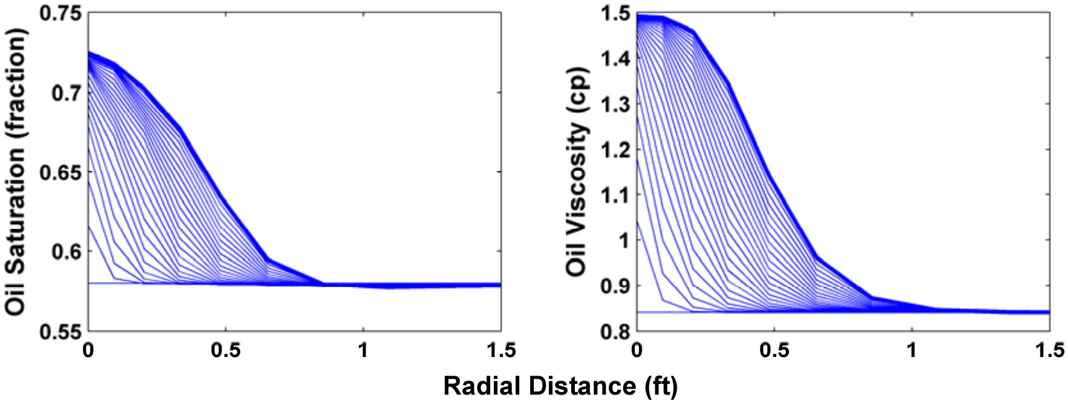

Figure 4.11: Time evolution of the radial distribution of oil saturation and oil viscosity in the invaded formation located within a capillary transition zone. Twenty-five curves are shown at uniform time intervals of 0.12 days spanning three days of mud-filtrate invasion. At the end of invasion, mud filtrate extends to 0.9 ft into the formation.

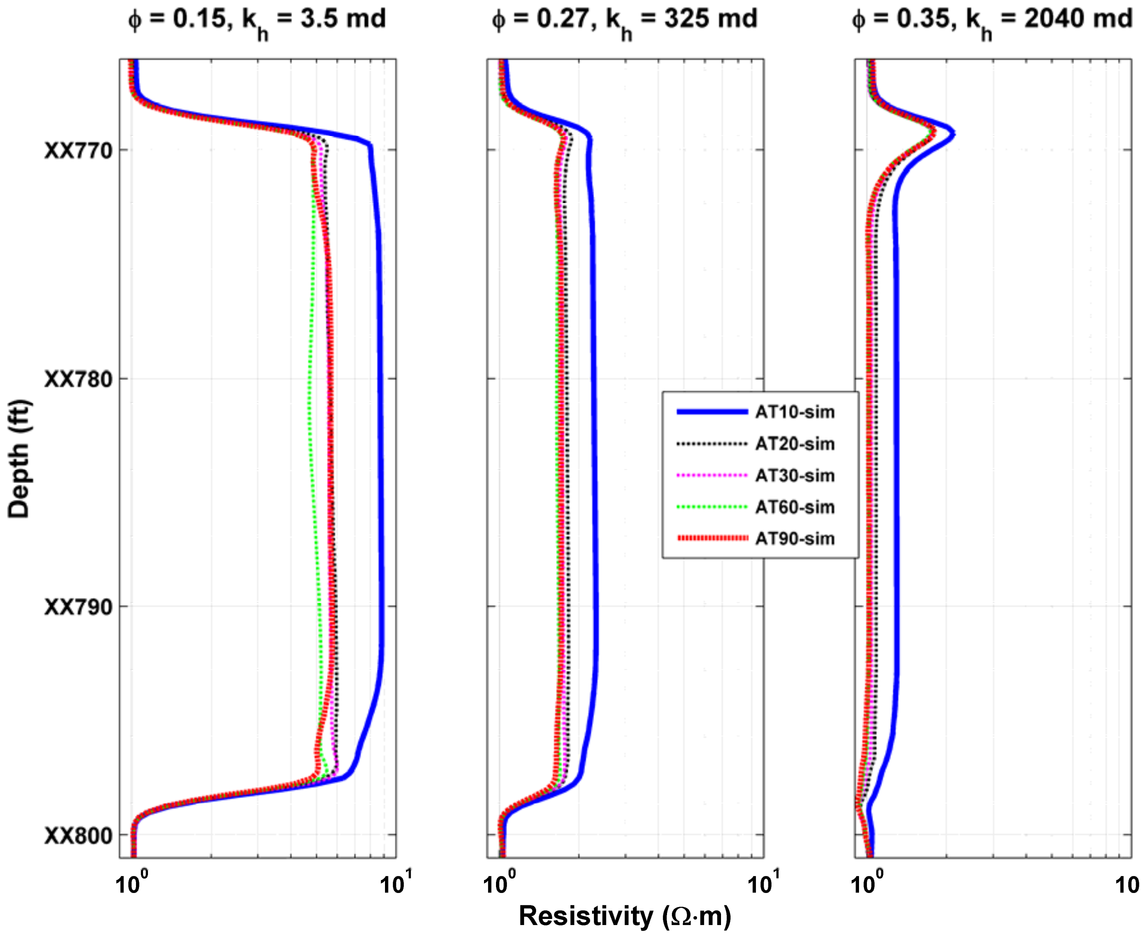

Figure 4.12: Sensitivity to porosity-permeability of array-induction resistivity measurements simulated after three days of oil-base mud-filtrate invasion into a partially oil-saturated formation. The center panel describes the oil base case.

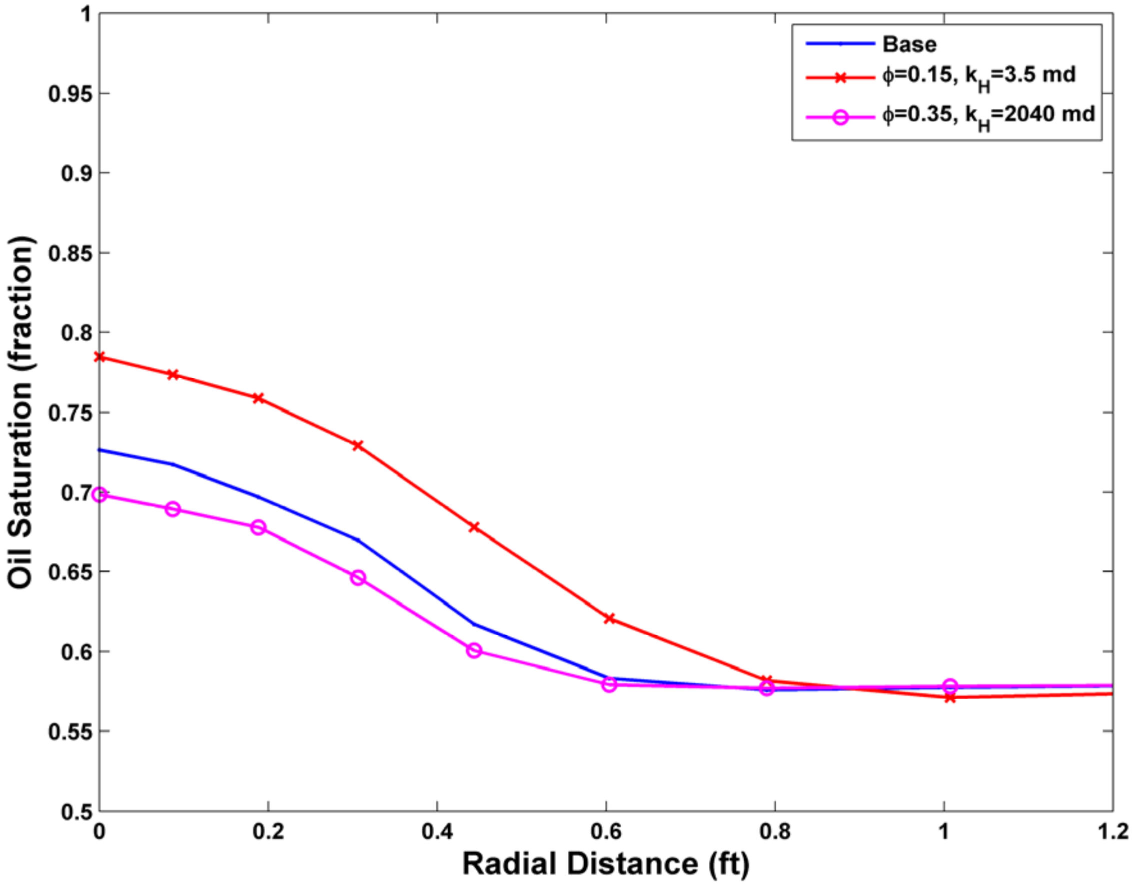

Figure 4.13: Radial distribution of oil saturation at the end of three days of invasion for different cases of formation porosity and permeability. The base case corresponds to a rock with effective porosity (ϕ) equal to 0.25 and horizontal permeability (k_H) equal to 325 md.

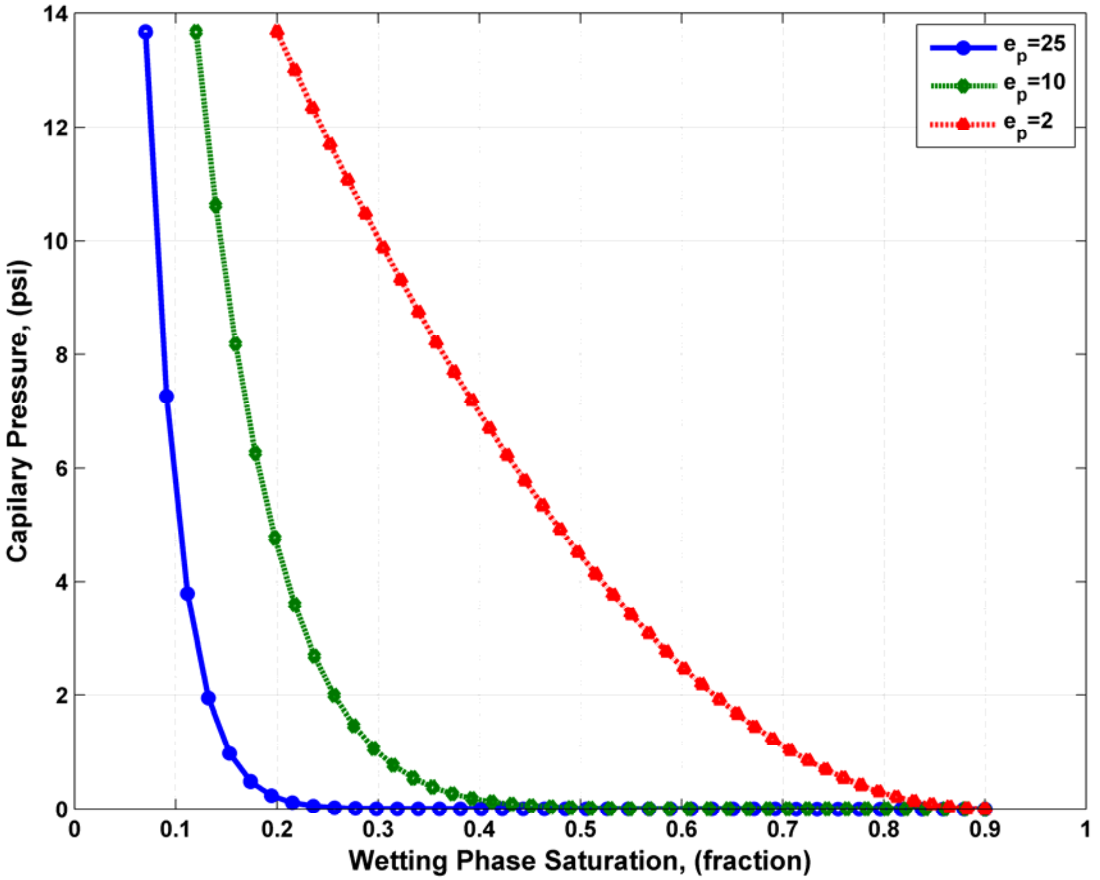

Figure 4.14: Water-oil capillary pressure curves for three different exponents of Brooks-Corey’s equation. Changes in the shape of the curves can also be interpreted as rock-quality (pore size), being the lowest value of e_p the one associated with the poorest rock quality. The blue curve (e_p = 25) corresponds to the oil-base case.

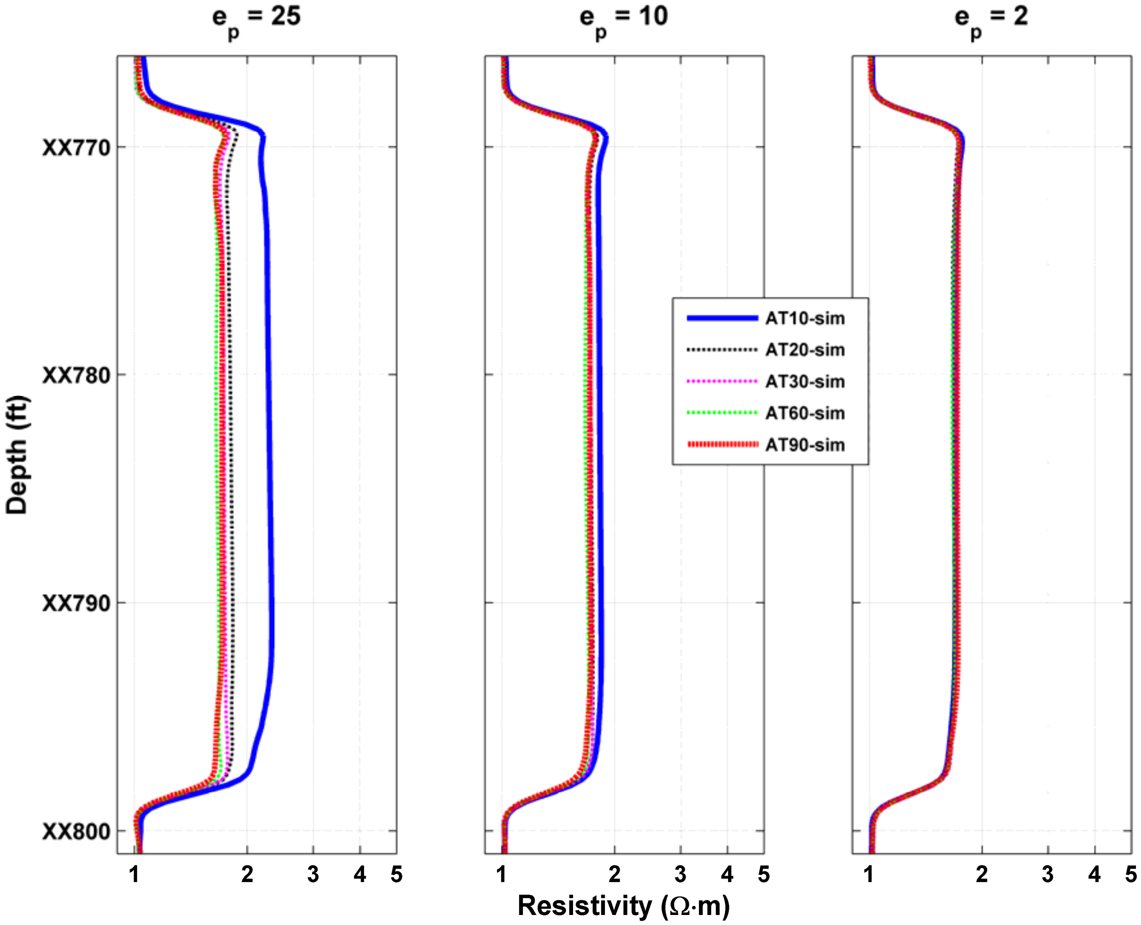

Figure 4.15: Sensitivity of the simulated array-induction resistivity measurements to the shape of capillary pressure curves after three days of oil-base mud-filtrate invasion into a partially oil-saturated formation. The left-most panel describes the oil base case.

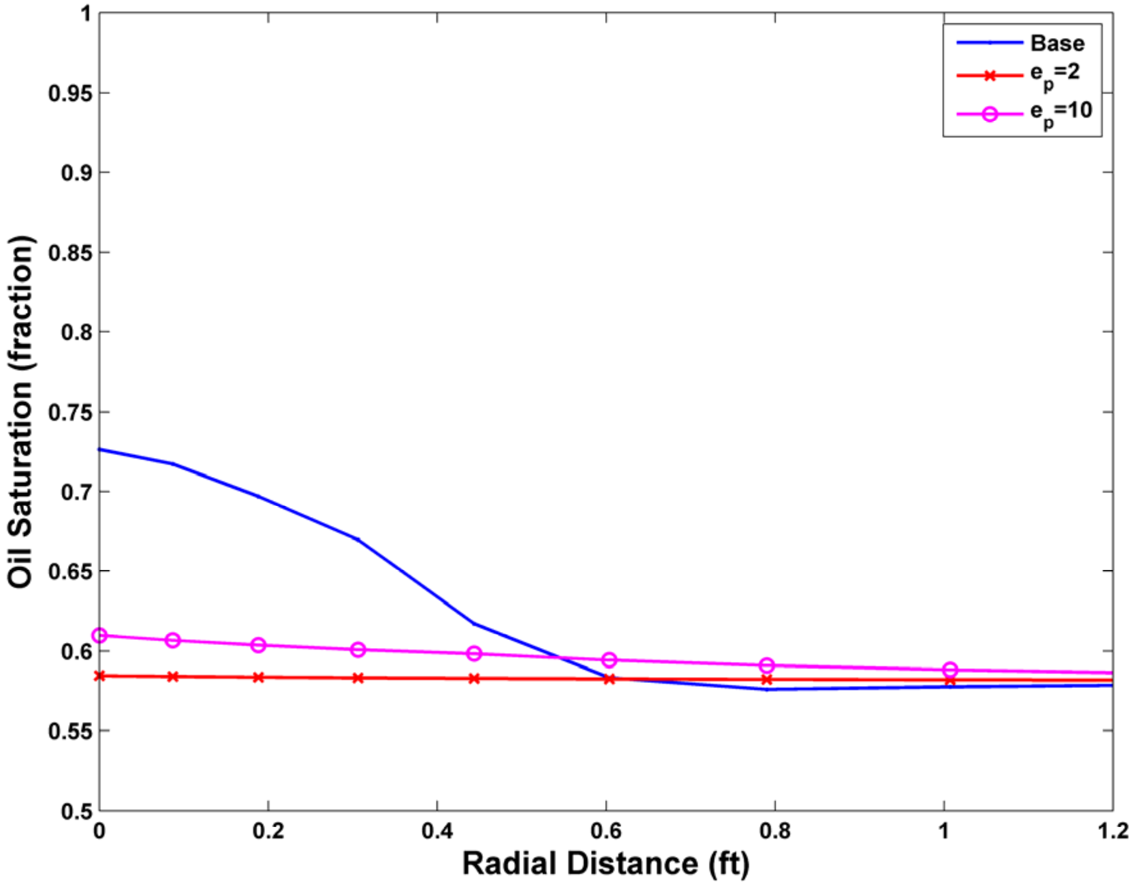

Figure 4.16: Radial distribution of oil saturation at the end of three days of invasion for different values of capillary-pressure exponent.

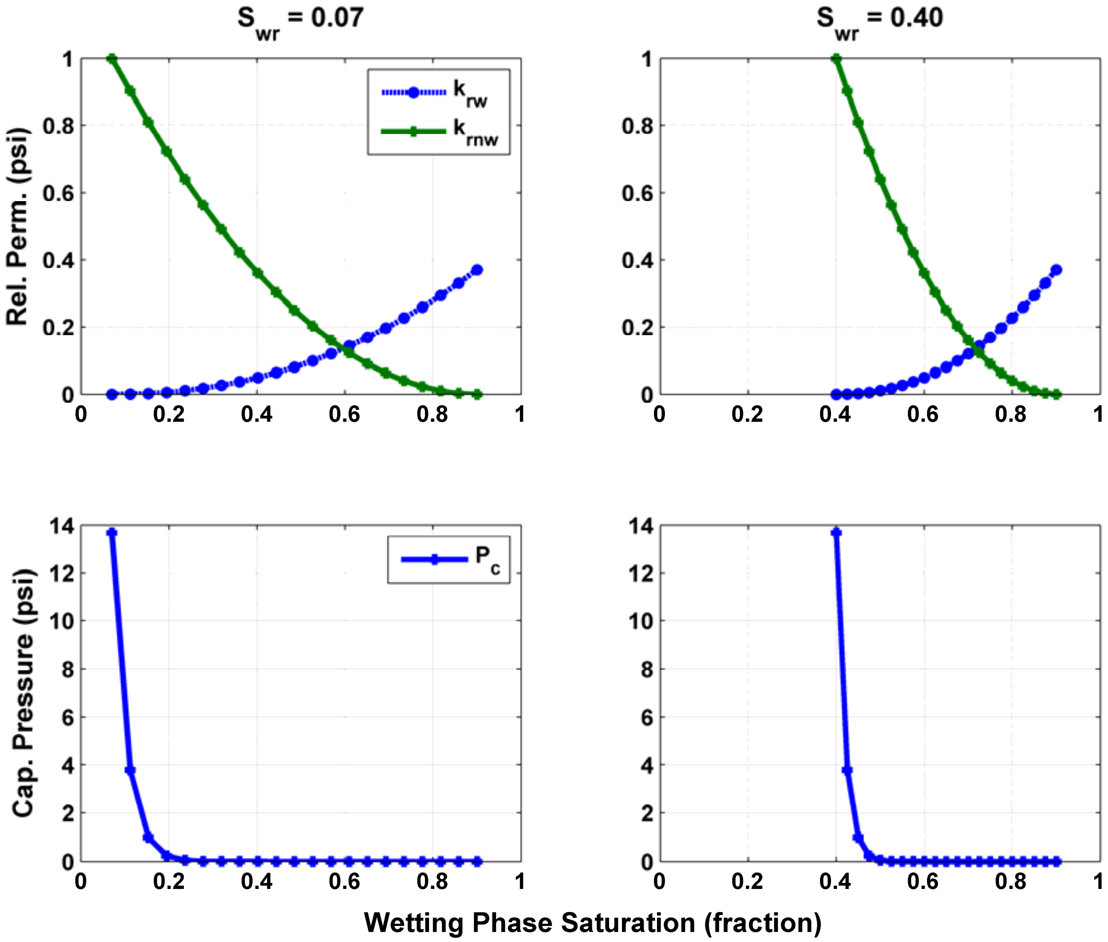

Figure 4.17: Water-oil capillary pressure (P_c) and relative permeability (k_{rw} and k_{rnw}) curves for two different values of residual water saturation. Changes of residual water saturation (S_{wr}) are equivalent to shifting the fluid transition zone toward conditions of irreducible water saturation.

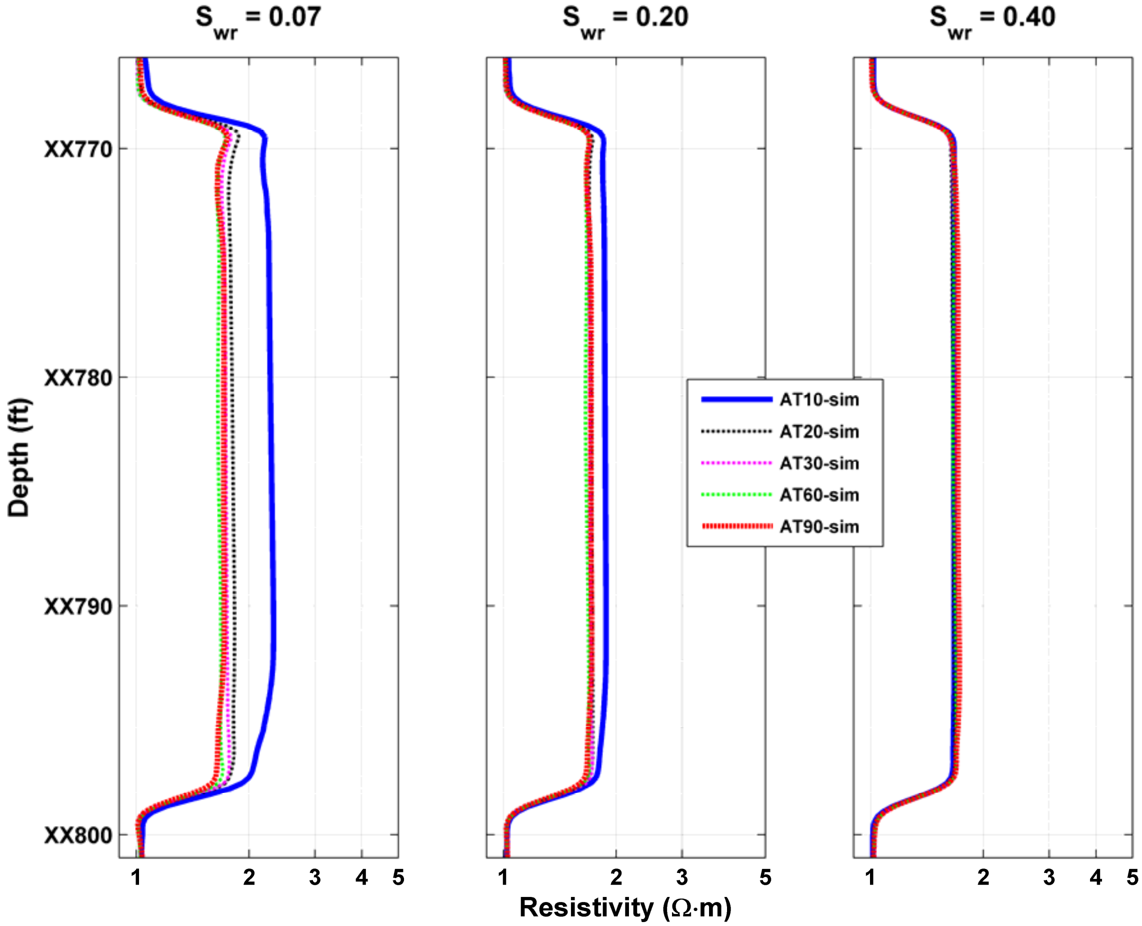

Figure 4.18: Sensitivity to residual water saturation of array-induction resistivity measurements simulated after three days of oil-base mud-filtrate invasion into a partially oil-saturated formation. The left-most panel describes the oil-base case.

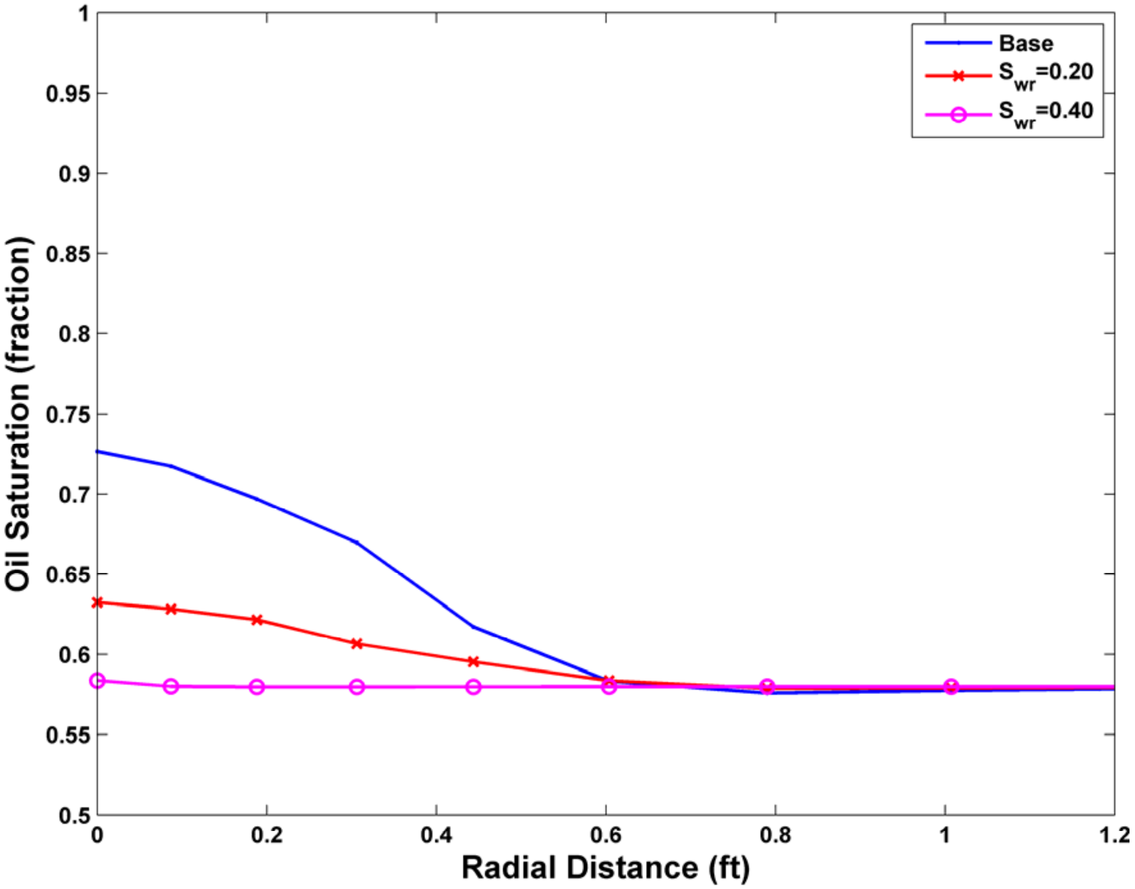

Figure 4.19: Radial distribution of oil saturation at the end of three days of invasion for different cases of residual water saturation.

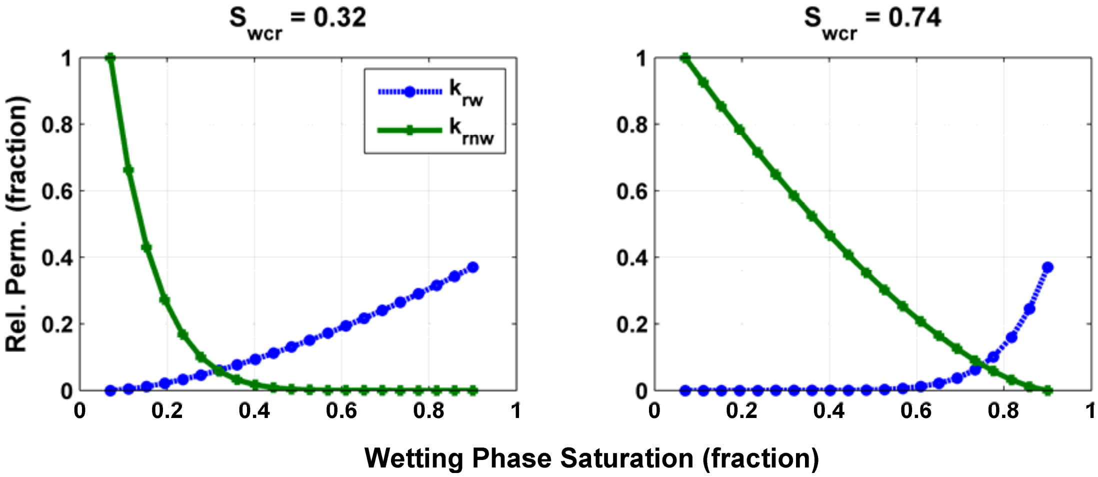

Figure 4.20: Water-oil relative permeability curves obtained by modifying Brooks-Corey's equation exponents. Location of critical water saturation (S_{wcr}) indicates preferential wettability. The left-hand panel corresponds to a strongly oil-wet rock, whereas the right-hand panel represents a strongly water-wet rock.

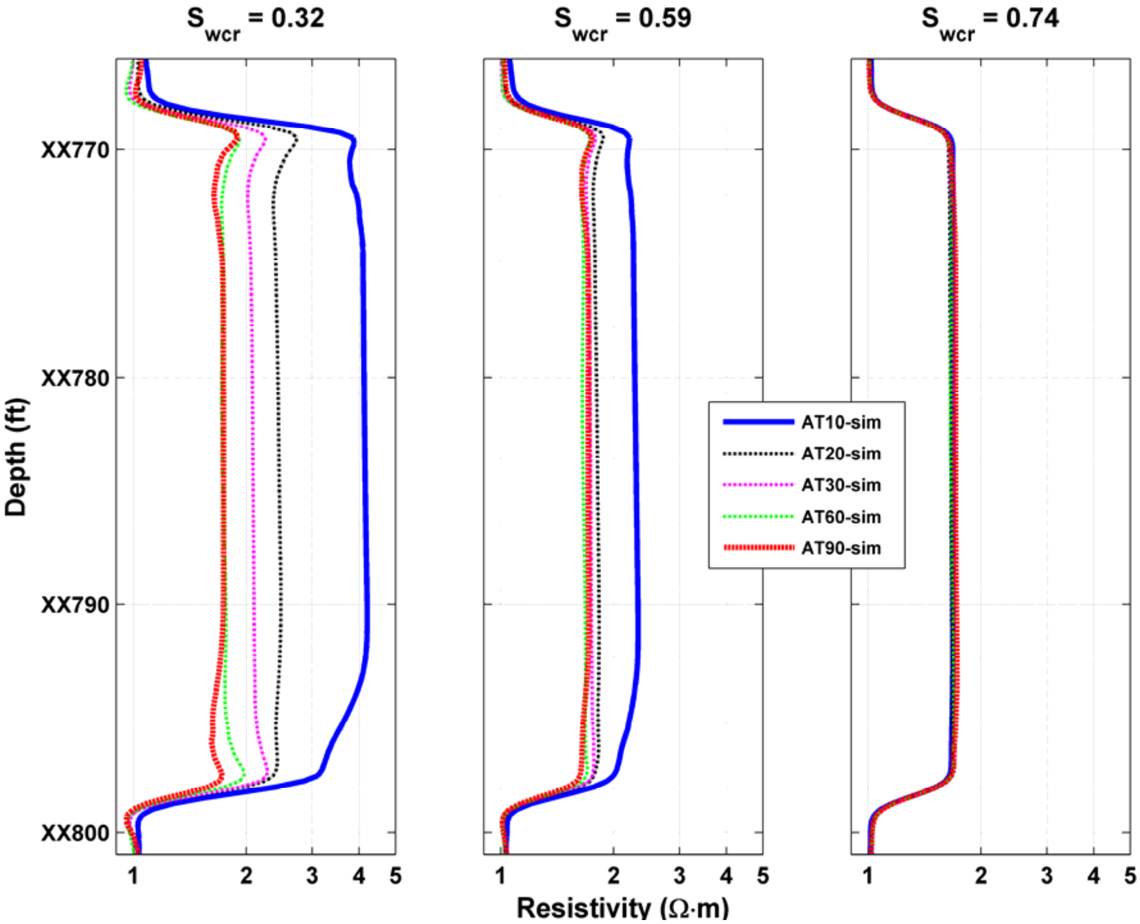

Figure 4.21: Sensitivity to relative permeability of array-induction resistivity measurements simulated after three days of oil-base mud-filtrate invasion into a partially oil-saturated formation. The center panel describes the oil base case.

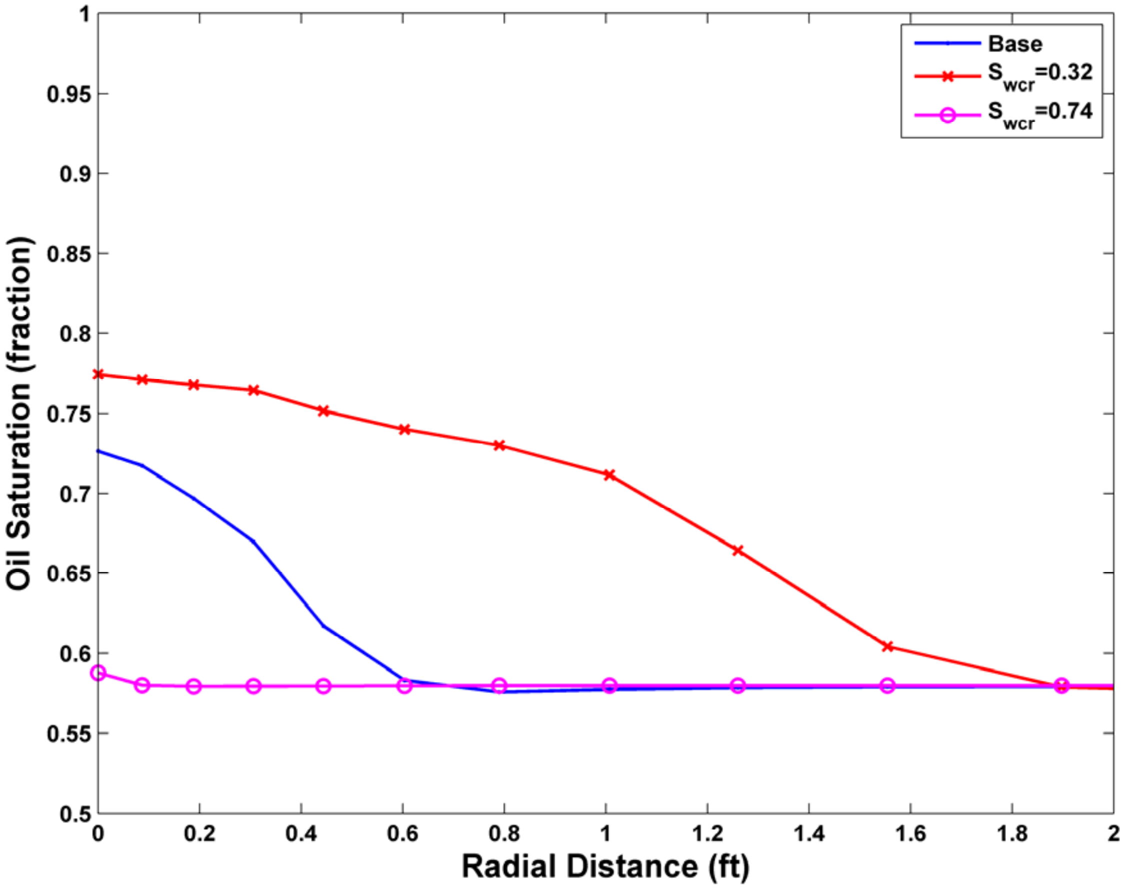

Figure 4.22: Radial distribution of oil saturation at the end of three days of invasion for different cases of critical water saturation. Low values of S_{wcr} cause smooth and deep invasion profiles.

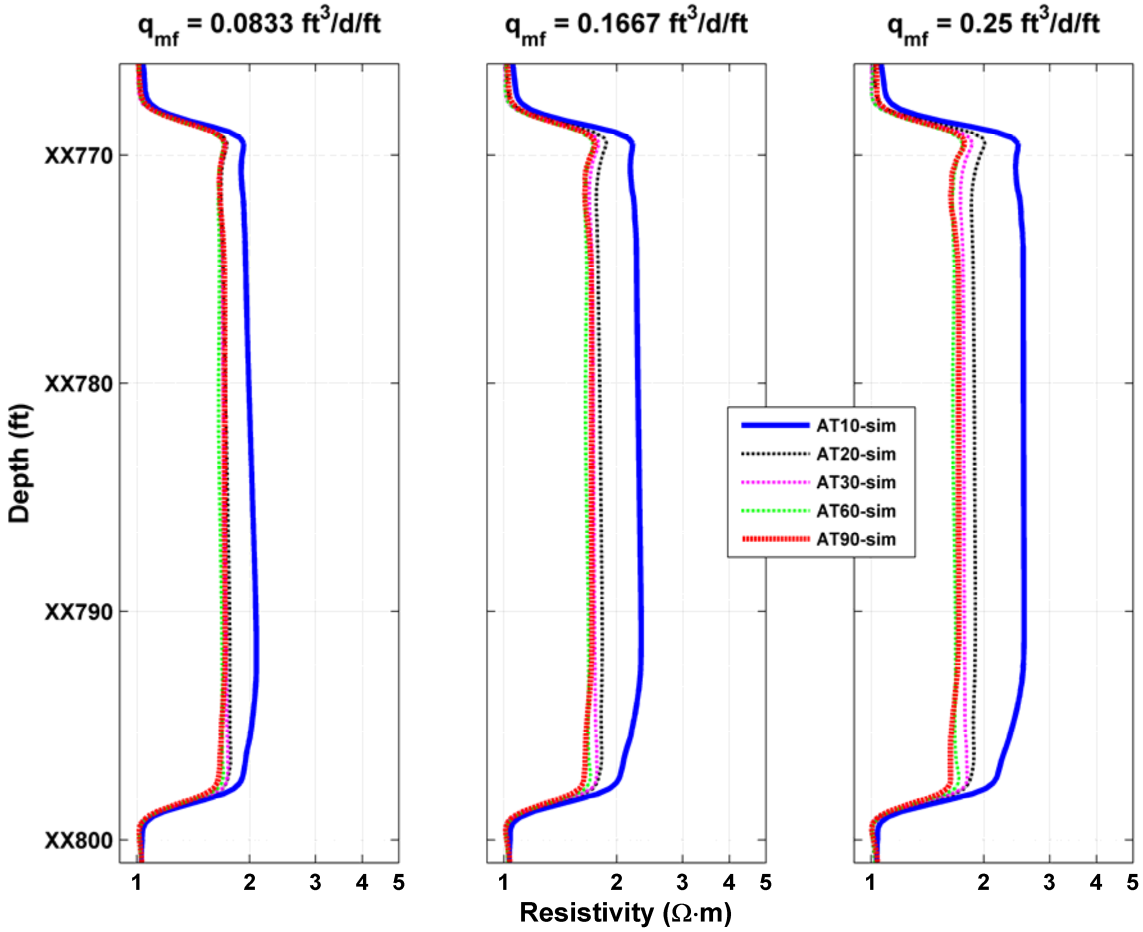

Figure 4.23: Sensitivity to average invasion flow rate of array-induction resistivity measurements simulated after three days of oil-base mud-filtrate invasion into a partially oil-saturated formation. The center panel describes the oil base case.

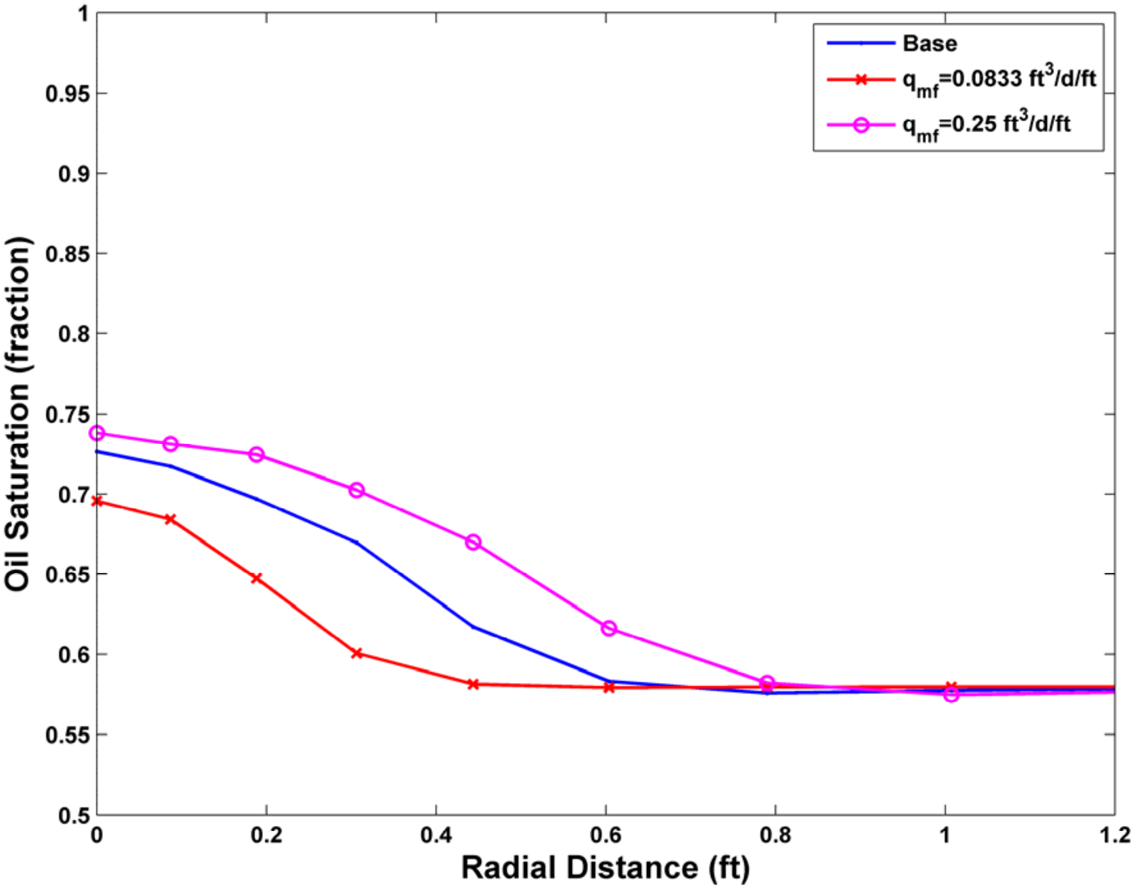

Figure 4.24: Radial distribution of oil saturation at the end of three days of invasion for different values of flow rate of invasion.

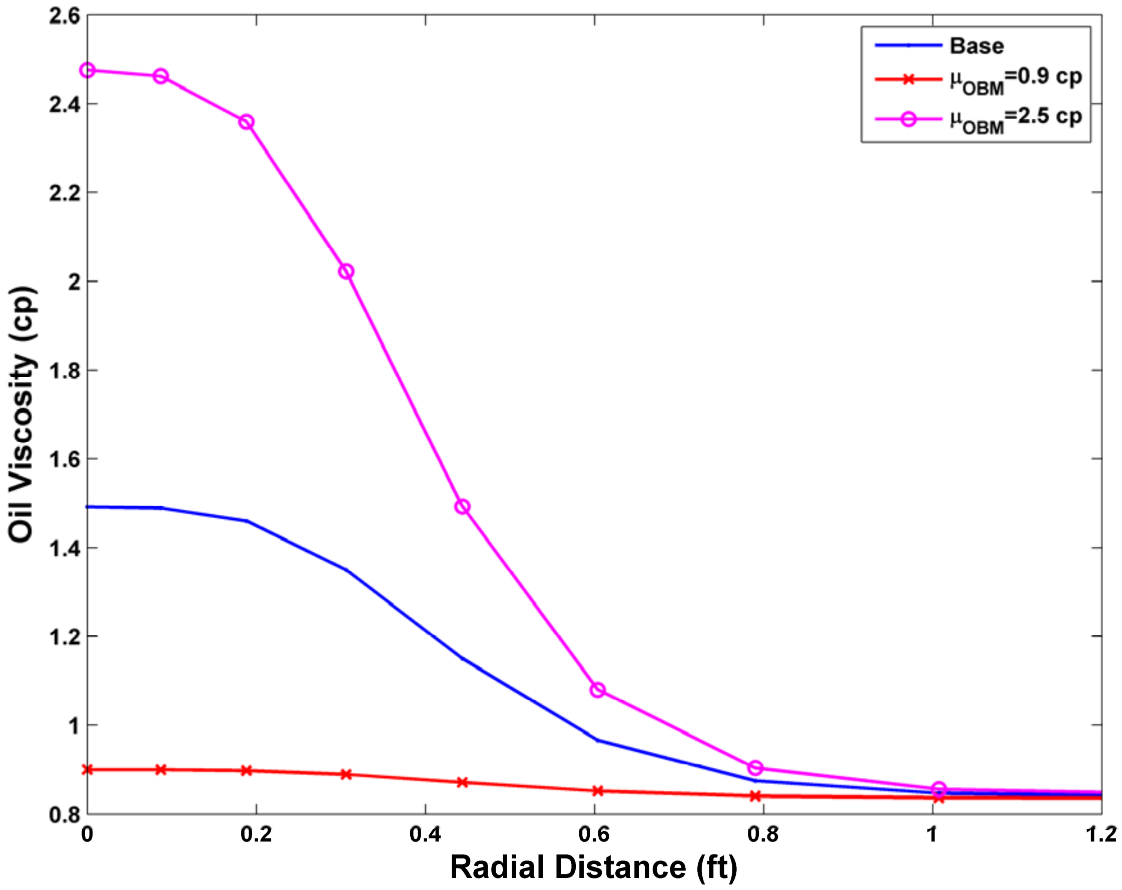

Figure 4.25: Radial distribution of oil viscosity at the end of three days of invasion for different values of filtrate viscosity.

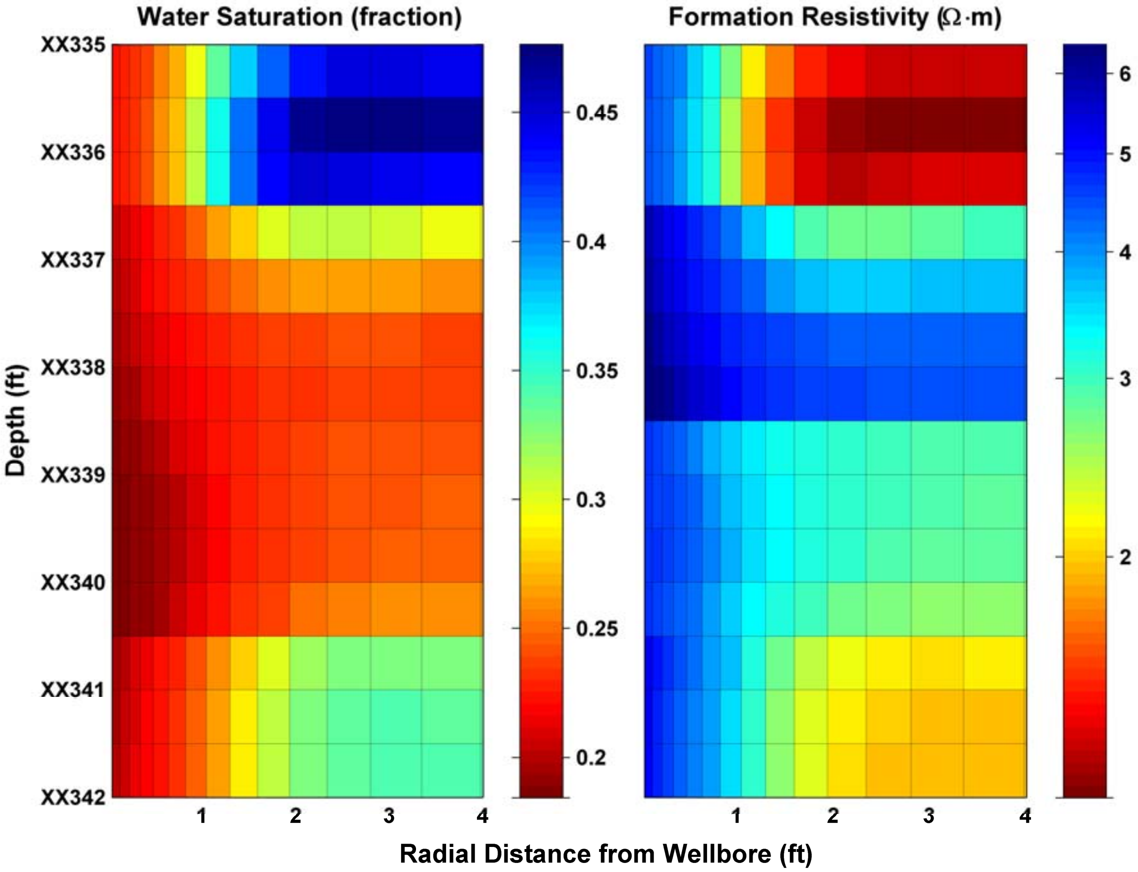

Figure 4.26: Lower depth interval of the oil-zone showing the spatial distributions of water saturation and electrical resistivity calculated after three days of oil-base mud-filtrate invasion. The spatial distributions were calculated after both flow rate of mud-filtrate invasion and relative permeability were adjusted multiple times to fit the available array-induction resistivity measurements.

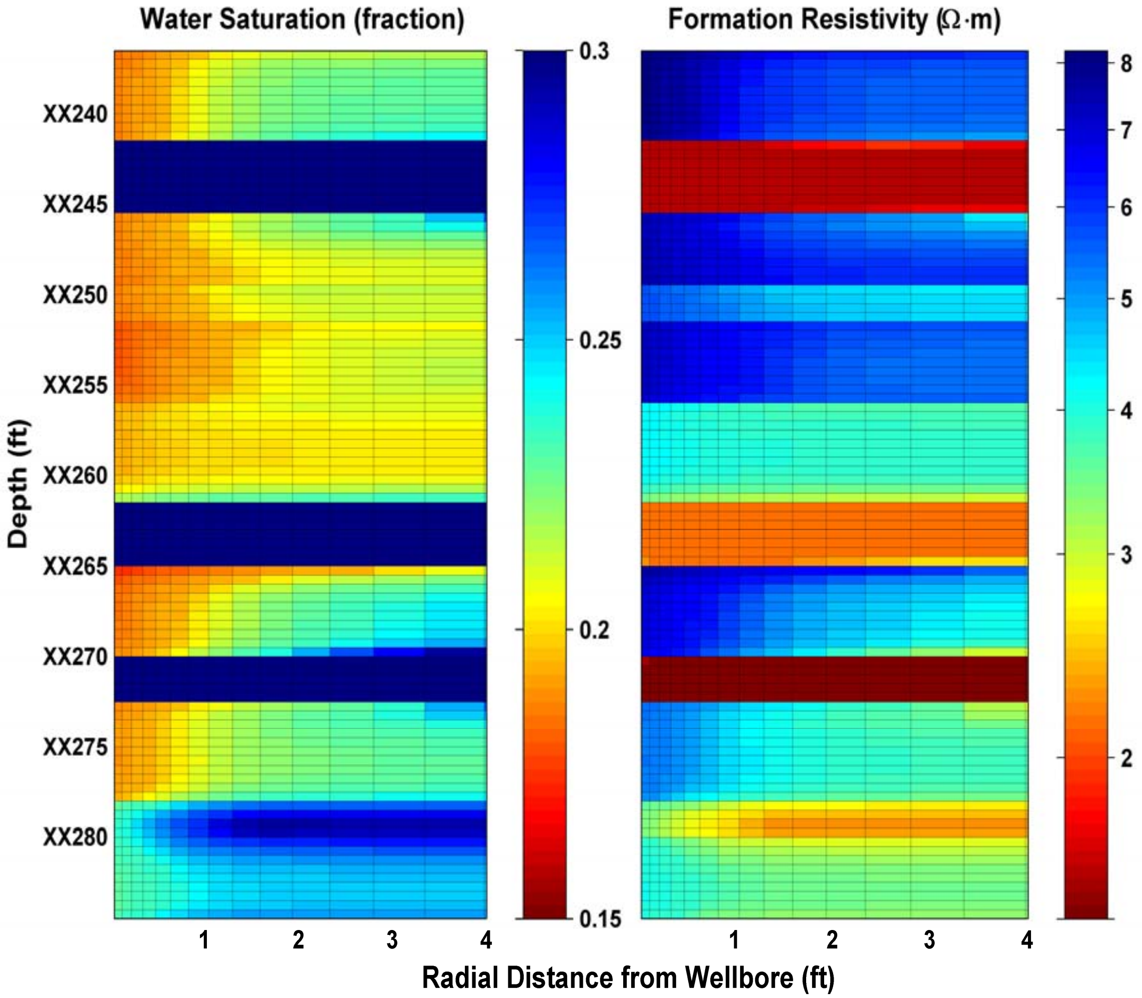

Figure 4.27: Upper depth interval of the oil-zone showing the spatial distributions of water saturation and electrical resistivity calculated after three days of oil-base mud-filtrate invasion. The spatial distributions were calculated after both flow rate of mud-filtrate invasion and relative permeability were adjusted multiple times to fit the available array-induction resistivity measurements.

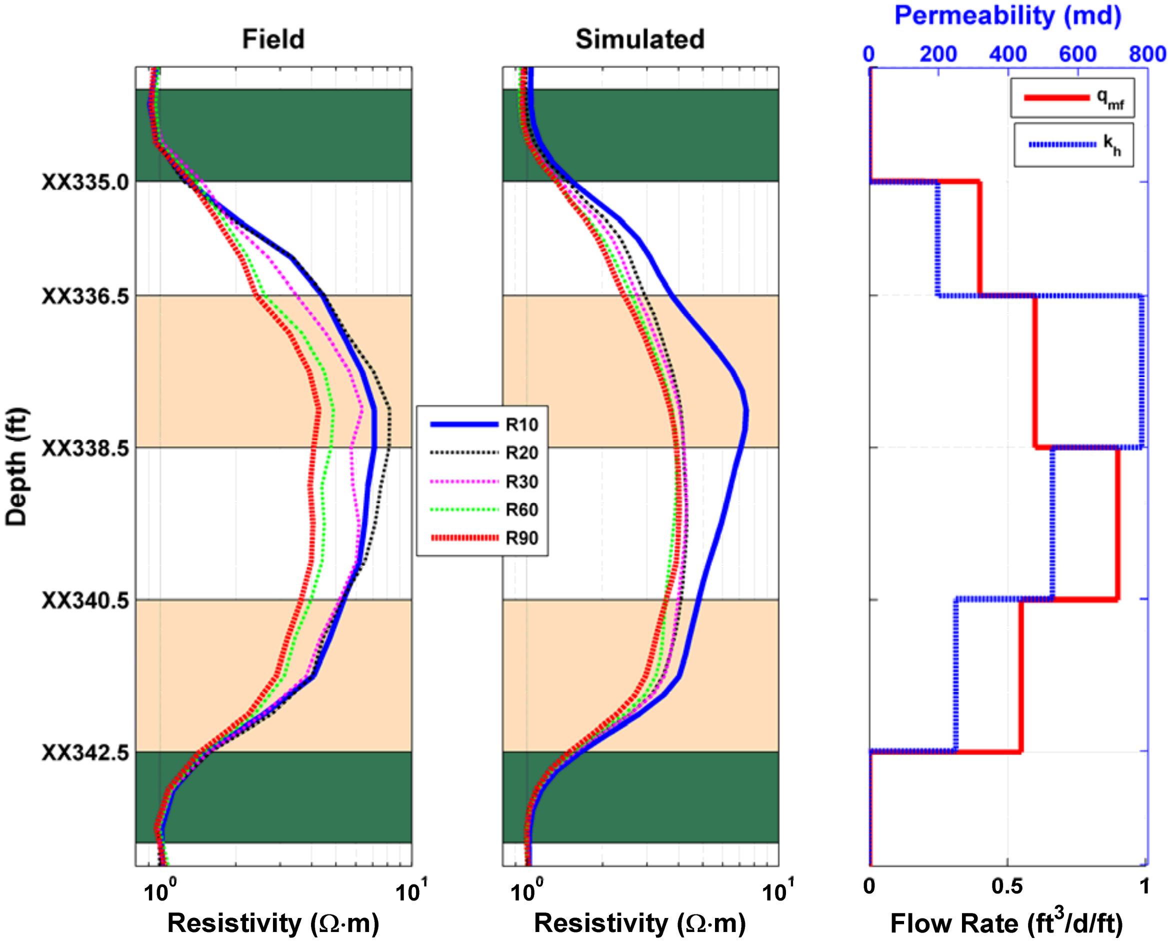

Figure 4.28: Lower depth interval: field (Track 1) 2-foot vertical resolution array-induction resistivity measurements compared to their simulated values after (Track 2) resistivity matching by manually changing both flow rate and relative permeability. The right-most tracks show the matching values of flow rate of mud-filtrate along with the assumed permeability for each layer. Shaded rectangles identify the various layers assumed in the simulation, where green zones identify shales.

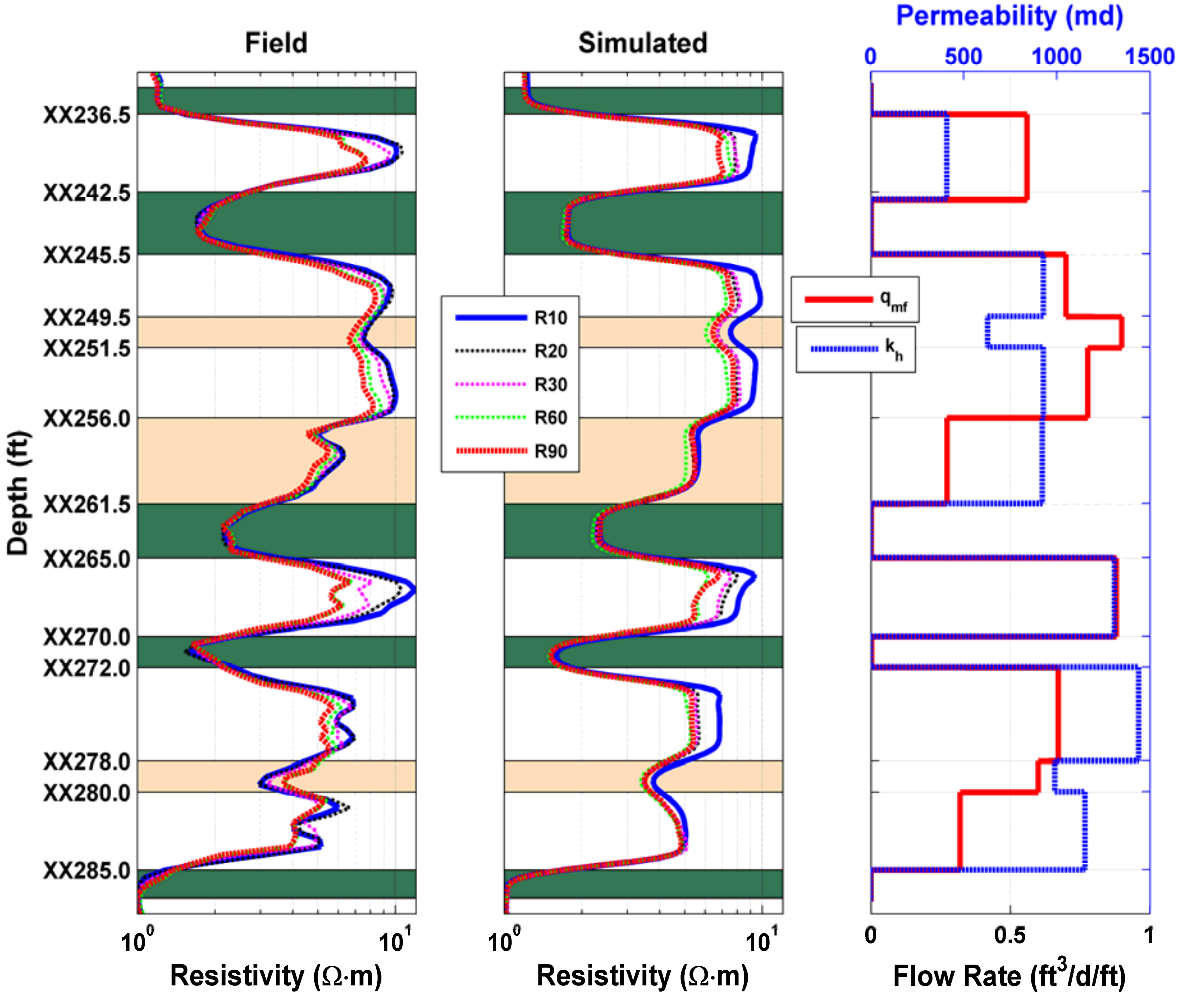

Figure 4.29: Upper depth interval: field (Track 1) 2-foot vertical resolution array-induction resistivity measurements compared to their simulated values after (Track 2) resistivity matching by manually changing both flow rate and relative permeability. The right-most tracks show the matching values of flow rate of mud-filtrate along with the assumed permeability for each layer. Shaded rectangles identify the various layers assumed in the simulation, where green zones identify shales.

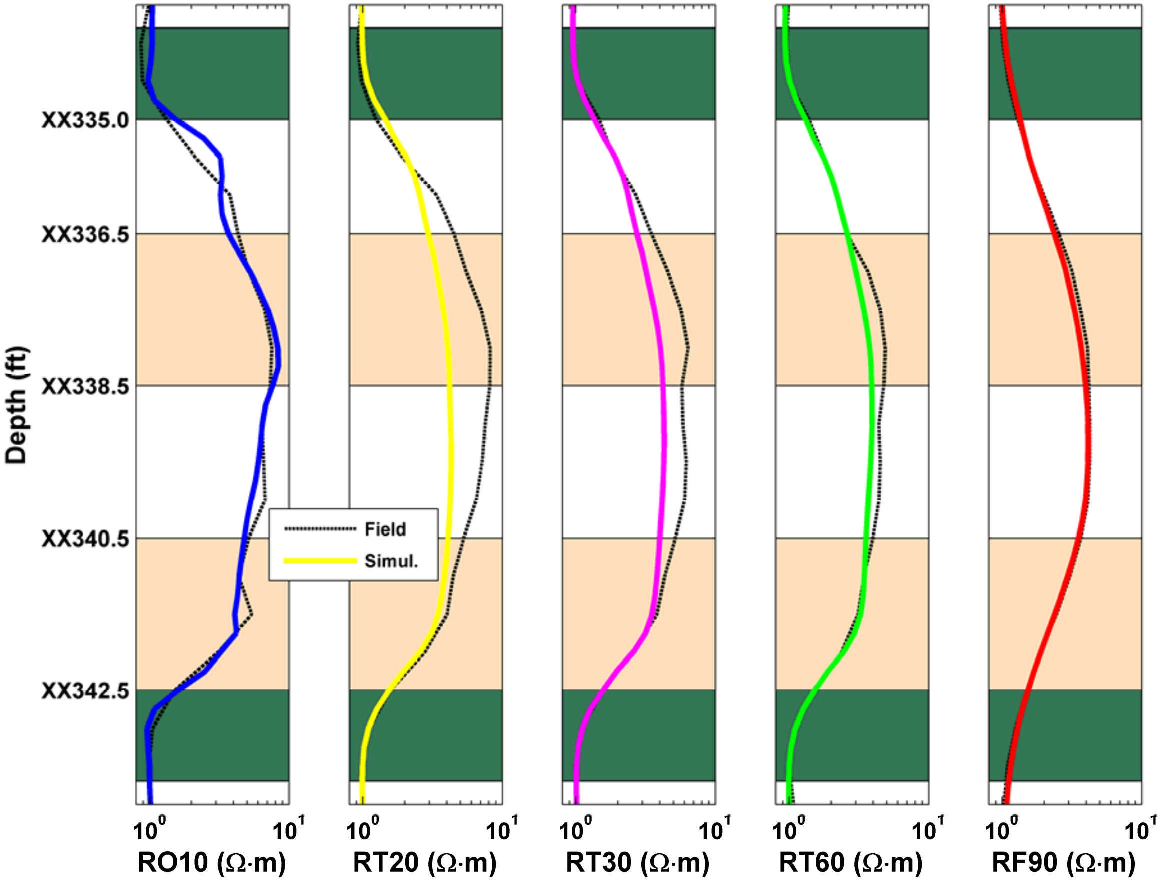

Figure 4.30: Lower depth interval: comparison of field and simulated array-induction resistivity curves after resistivity matching for five radial lengths of investigation. The left-most track shows the 1-foot resolution shallowest-sensing resistivity curves, the right-most-track displays the 4-foot resolution deepest-sensing curves and the three center tracks show the 2-foot resolution intermediate-depth-of-investigation curves. Continuous thick curves identify simulated values and thin dashed curves identify field data.

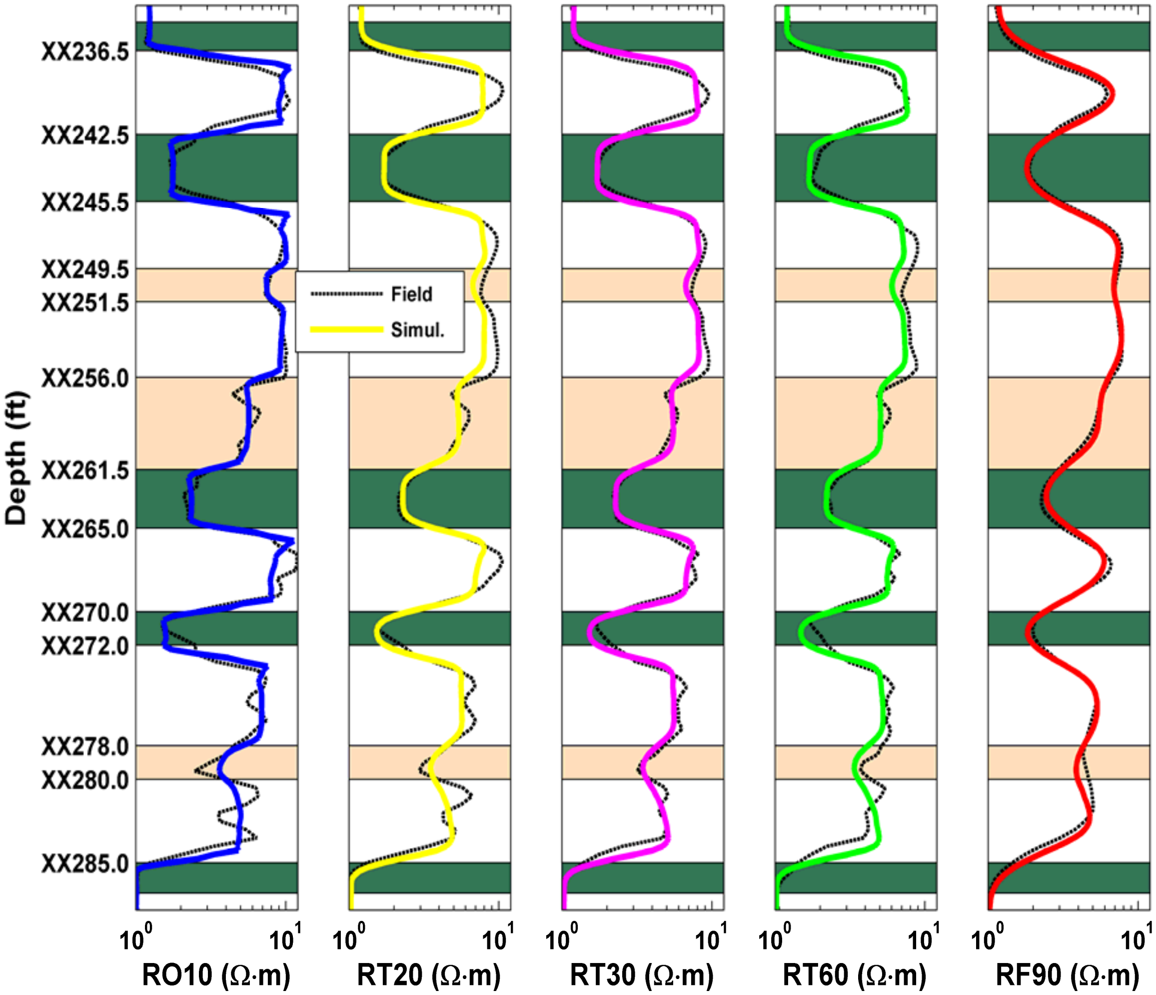

Figure 4.31: Upper depth interval: comparison of field and simulated array-induction resistivity curves after resistivity matching for five radial lengths of investigation. The left-most track shows the 1-foot resolution shallowest-sensing resistivity curves, the right-most-track displays the 4-foot resolution deepest-sensing curves and the three center tracks show the 2-foot resolution intermediate-depth-of-investigation curves. Continuous thick curves identify simulated values and thin dashed curves identify field data.

Chapter 5: Fluid Density and Viscosity Effects on Borehole Resistivity Measurements Acquired in the Presence of Oil-Based Mud and Emulsified Surfactants

The objective of this chapter is to appraise the sensitivity of borehole resistivity measurements to the spatial distribution of fluid saturation resulting from the compositional mixing of oil-base mud (OBM) and in-situ hydrocarbons. Presence of surfactants in the OBM is simulated with a commercial adaptive-implicit compositional formulation that models the flow of three-phase multi-component fluids in porous media. We perform sensitivity analyses on field measurements acquired in a well that penetrates a clastic formation and that includes different values of density and viscosity for mud-filtrate and formation hydrocarbon. These analyses provide evidence of the presence of a high-resistivity region near the borehole wall followed by a low-resistivity annulus close to the non-invaded resistivity region. Such an abnormal annulus is predominantly due to high viscosity contrasts between mud-filtrate and formation oil.

5.1 INTRODUCTION

In general, OBM increases drilling rates and provides better quality boreholes than when drilling with water-base mud (WBM). In oil-base muds, the continuous fluid phase is a mixture of liquid hydrocarbons. This continuous phase dominates the process of invasion and mixes with formation fluids. Water is also present in the form of an emulsion. Chemical emulsifiers/surfactants are added in the mud to prevent water droplets from coalescing and leaving the emulsion (Bourgoyne Jr. *et al.*, 1986) and to ensure that the weighting material is wetted by oil (Skalli *et al.*, 2006). Calcium or magnesium fatty acid soaps are typically used as emulsifiers.

Array-induction resistivity measurements are almost invariably acquired in OBM environments. Such measurements exhibit several radial lengths of investigation, typically from 10 inches to 90 inches and, in some cases, 120 inches. The variability of resistivity curves exhibiting different lengths of investigation is, in most cases, a footprint of mud-filtrate invasion. When array-induction measurements are acquired in the presence of WBM, large separation of resistivity curves and deep invasion can be expected due to monotonic change of formation resistivity. Ideally, we would not expect such a behavior in the presence of OBM. However, in hydrocarbon zones OBM-filtrate can replace native hydrocarbon and movable water, thereby resulting in an invasion front with different resistivity values in the near-wellbore region (La Vigne, *et al*., 1997). Moreover, invading mud filtrate is miscible with native oil. In the mixing process, OBM causes changes of fluid density and fluid viscosity, thereby modifying the apparent oil phase mobility in the invaded zone (Malik *et al*., 2007).

The objective of this chapter is to quantify the effect of fluid properties (density and viscosity) and composition on array-induction measurements acquired in the presence of OBM-filtrate invasion. Special attention is given to the presence of surfactants in the OBM. Previous laboratory experiments with core samples (Van, *et al*., 1988; Yan and Sharma 1989) show that surfactants greatly change the wettability of sandstone cores from a strongly water-wet to an oil-wet condition. Most of these effects were inferred from changes of contact angle that caused a reduction of interfacial tension.

Our study is centered about measurements acquired in a North-Sea well penetrating clastic rock formations. The well was drilled with OBM, whereas resistivity measurements were acquired with the array-induction imager tool (AIT™). We select three depth intervals that exhibit distinct invasion behavior at different depth intervals in the formation. Additionally, we give a detailed background of the method used to simulate the process of OBM-filtrate invasion and the associated array-induction resistivity measurements. A base case with high initial water saturation is used to perform several sensitivity analyses that quantify the influence of formation fluid properties and mud components. A second example allows us to perform sensitivity analyses with a light-hydrocarbon depth interval subject to invasion with OBM that includes an emulsified surfactant. The third example includes a gas-saturated interval close to irreducible water saturation. Finally, we perform the simulation of OBM-filtrate invasion in a long depth interval encompassing a complete capillary transition zone from light oil at the top to water at the bottom.

5.2 GEOLOGICAL DESCRIPTION AND DEPOSITIONAL SYSTEM

The field case considered in this work corresponds to a Paleocene sandstone dome located in the Central North Sea (Martin *et al.*, 2005). The field comprises an average of 60 m of a gas cap with a gas/oil ratio of 871 scf/bbl and 58 m of an oil-saturated column with a gravity of 40^o API followed by an active aquifer (BP, 2003). Preserved Paleocene strata in the North Sea show siliciclastic sediments with minor amounts of coal, tuff, volcaniclastic rocks, marls, and reworked carbonate sediments (Ahmadi *et al.*, 2003). During the early Paleocene, submarine fans developed the faulted basin margins in the west, spread out, and overlapped to form near-continuous sandstone bodies. The specific formation under analysis is predominantly composed of non-calcareous, blocky grey mudstones interbedded with sandy, high-density gravity-flow deposits and minor volcaniclastic rocks. An estimated 35% of net sand volume makes this formation one of the most sand-prone systems of the Paleocene formations in the region. Rock units within the formation consist of alternations of fine- to medium-grained, or in some cases, coarse-grained sandstone with common mudstone and chalk clasts. Porosity (ϕ) ranges between 20% and 28% while permeability (k) varies from 50 md in low-porosity zones to

1,000 md in high-porosity intervals. Figure 5.1 is a plot of core permeability versus core porosity, showing Windland's r_{35} (critical pore-throat radius) curves (Pittman, 1992) along with k/ϕ iso-lines. This plot indicates that the formation consists of high-quality rock units with pore-throat radii above 2 μm and k/ϕ ratios above 200 md/p.u.

5.3 PETROPHYSICAL ANALYSIS OF FIELD MEASUREMENTS

The upper section of the formation corresponds to gas-saturated interbedded sandstones. In the intermediate section, the well penetrates thick sand bodies partially oil-saturated toward a capillary transition zone. The lower depth interval of the formation reaches an active aquifer. Routine core measurements of porosity and permeability are available for the complete hydrocarbon interval as well as for several locations within the water zone. This well provides a textbook example of an ideal hydrocarbon reservoir. It shows a gas cap at the top, followed by an oil column penetrating a capillary transition zone toward the free water-oil contact (WOC).

5.3.1 Water Saturation

Relatively clean sandstones with low water saturation (S_w) at the top and high S_w downward compose the formation. Therefore, we used Archie's (1942) equation to calculate S_w,

$$\frac{1}{R_t(r,z)} = S_w{}^n(r,z)\frac{\phi^m(z)}{a \cdot R_w},$$

where r is radial distance from the wellbore, z is vertical distance with respect to the top of the formation, R_t is true formation resistivity, R_w is connate water resistivity, m and n are Archie's cementation and saturation exponents, respectively, and a is the tortuosity factor. Table 5.1 describes the input parameters used to calculate initial water saturation using Archie's equation. Such parameters were obtained from laboratory measurements performed on core samples and fluid samples withdrawn from the formation.

5.3.2 Shaliness, Porosity, and Permeability

In order to diagnose the type of shale distribution across the formation, we applied Thomas and Stieber's (1975) method to both gamma-ray measurements and computed total porosity. Figure 5.2 shows the Thomas-Stieber cross-plot indicating that dispersed shale is the dominant type of shale distribution in the formation under analysis. Routine core measurements of porosity and permeability are available in the well. Therefore, we calculated core-calibrated curves of porosity and permeability. Effective porosity was calculated from density and neutron measurements by accounting for the presence of two fluids (oil/gas and water) and two minerals (quartz and clay) in the porous medium. Permeability was calculated via a modified Timur-Tixier equation from porosity and irreducible water saturation (Salazar *et al.*, 2006). We specialized the equations for specific intervals of the formation with calibration of porosity-permeability measurements. The coefficient and exponents of the equations were estimated via multi-linear least-squares regression.

5.3.3 Cases of Study

Three different intervals with distinct invasion behavior are chosen from the cored well to perform simulations of the process of OBM-filtrate invasion and to simulate the corresponding resistivity measurements. Each case is considered a single-layer homogeneous formation. Case No. 1 is a 16-ft interval within the oil zone (8600 ft – 8616 ft) and is used to calibrate our synthetic base case. In such interval, variability of array-induction resistivity curves indicates presence of an invasion profile. This variability allows us to perform sensitivity analyses to several fluid and formation properties. By manually matching the simulated apparent resistivity curves to field measurements, we assess the parameters for capillary pressure and relative permeability to be used in the remainder depth intervals along the well. Case No. 2 comprises a depth interval between gas and oil. We observe a 7-ft interval that exhibits invasion (8519.5 ft – 8526.5 ft). The latter is considered a very-light hydrocarbon zone. Case No. 2 is used to perform additional sensitivity analyses in light oil with different values of initial water saturation and presence of emulsifier surfactants in the OBM. Additionally, Case No. 3 corresponds to a gas zone at the top of the formation (8329 ft – 8345 ft) with initial water saturation close to irreducible water saturation. Therefore, when OBM-filtrate invades the formation, all three phases (invading mud, formation water, and gas) are mobile in the near-wellbore region. Mud filtrate is assumed an emulsion of hydrocarbons, water, and surfactants. Table 5.2 summarizes the average petrophysical properties used in the simulations. Figure 5.3 shows well logs (gamma ray, caliper, AIT, density and neutron) for each case where we can diagnose the corresponding invasion behavior.

Finally, we model a very long depth interval (8527 ft – 8806 ft) that includes both the end of the gas zone and the aquifer. The objective is to model the complete capillary transition zone using a simple binary OBM-filtrate invasion model and to study the corresponding effect on array-induction resistivity measurements. Figure 5.4 shows the results obtained from petrophysical analysis. We observe that the water saturation curve resembles a typical capillary pressure curve as a function of depth.

5.4 COMPOSITION OF FLUIDS

With the main objective of performing sensitivity analyses of fluid properties, we assume different compositions of both formation oil and mud filtrate accross different depth intervals in the formation. We also consider presence of irreducible and movable water in these depth zones.

5.4.1 Hydrocarbon Components

Original formation hydrocarbons consist of components in the range from C_1 to C_{18+}. For Case No. 1, we assume only liquid hydrocarbons and lump them into a single component, namely, C_7C_{18}. In Case No. 2, we add a lighter component, C_4C_6, which, in turn is the most abundant in the zone. For the last case (Case No. 3), we include a gaseous component (N_2C_1), which is the leading component in that depth interval. Regarding oil-base mud, we assume that it consists of hydrocarbons in the range of C_{14} to C_{18}, which are lumped into a single MC_{16} component. The binary-interaction parameter between the hydrocarbon pseudo-components is assumed null. Under dynamic drilling conditions, drilling mud mixes with solid particles and formation fluids as the drill bit penetrates the formation. This behavior can further modify the composition of the mud.

5.4.2 Surfactants

Presence of water emulsified with surfactants is also considered in the sensitivity analyses. Common surfactants in the industry are known by the commercial names EZ-MUL™, X-VIS™, and INVERMUL™[6], among others. The viscosity of these surfactants may vary from less than 1 cp to slightly more than 1000 cp. Most of such surfactants act as emulsifiers and oil-wetting agents. They are composed of organic, fatty acid soaps. When the soap forms a mixture with water and oil, soap molecules accumulate at oil/water interfaces with the water-soluble extreme residing in the water phase and the oil-soluble extreme residing in the oil phase (Bourgoyne Jr *et al.*, 1986). In this chapter, we assume a generic surfactant (henceforth referred to as EMUL) composed by stearic acid (La Scala *et al.*, 2004; Lide, 2007), which is a chain of 18 carbon atoms. Table 5.3 summarizes the pseudo-properties of both the lumped hydrocarbon components and the emulsified surfactant (Lide, 2007).

---

[6] Marks of Baroid/Halliburton

5.5 NUMERICAL SIMULATION OF THE PROCESS OF OIL-BASE MUD-FILTRATE INVASION

We approach the simulation of the process of OBM-filtrate invasion with two different simulators. In both cases, we assume axial-symmetrical formation properties with respect to the axis of a vertical borehole. Simulations enforce boundary and source flow-rate conditions on specific depth segments along the wellbore. The outer, lower, and upper limits of the formation consist of impermeable zones with no-flow boundary conditions. We consider simulation cases with both water-free and water-emulsified OBM. Therefore, salt concentration is considered constant across the formation and equal to that of connate water.

5.5.1 UT-FET

In order to construct the base case, we initially use an implicit-pressure explicit-concentration (IMPEC) numerical simulator (Malik *et al*., 2007), implemented with the University of Texas' Formation Evaluation Toolbox (UT-FET) (Wu *et al*., 2005, Ramírez *et al*., 2006). Both mud filtrate and formation oil are described with a binary compositional formulation to ensure minimum computation time. All components of OBM-filtrate and formation oil are lumped into two pseudo-components. The UT-FET is only used to perform the calibration of petrophysical properties to be used as input to the simulation of several sensitivity analyses of fluid properties. We apply the same simulation method to a long depth interval in the case study that considers a capillary transition zone with gas at the top and water at the bottom.

5.5.2 CMG-STARS

A commercial adaptive-implicit formulation simulator, known as STARS[7] (CMG, 2006), is used to perform the sensitivity analysis of fluid properties. The software

---

[7] Mark of Computer Modeling Group

STARS is an advanced three-phase multi-component fluid-flow simulator with the capability of simulating the flow of emulsions and foams in porous media. With this simulator, we are able to treat the OBM-filtrate as a multi-component fluid containing oil and water emulsified within the oil with surfactants. Formation hydrocarbon is also considered a multi-component fluid in which we account for presence of gas. Previous simulation exercises reported by Malik *et al*. (2006) indicated successful benchmarking between UT-FET and CMG-STARS. Hence, for the purposes of this chapter, we perform the sensitivity analyses using the base case previously constructed with the UT-FET. Another advantage of using STARS is the remarkable reduction of computation time.

The geometry used to simulate all the cases of study consists of a finite-differences grid with nodes logarithmically spaced in the radial direction (50 nodes). The wellbore radius is equal to 0.51 ft and the external radius is 2000 ft. A logarithmic radial grid allows us to properly reproduce the rapid space-time variations of pressure and component concentrations in the near-borehole region. Along the vertical direction, grid nodes are uniformly spaced at 0.5 ft intervals.

We use the parametric equations proposed by Brooks and Corey (1964) to define capillary pressure (P_c) and relative permeability (k_{ri}) curves. Laboratory core data were not available for oil-water or gas-liquid systems. Therefore, typical exponents and coefficients for this type of formation were used in the simulation. In selecting the Brooks-Corey parameters, we also accounted for the fact that rock wettability was altered (Yan and Sharma, 1989; Skalli *et al*., 2004) when invading the formation with OBM. Initially, the rock formation under analysis was assumed water-wet. As the OBM invasion started, rock wettability changed to preferentially oil-wet. Hence, the critical value of saturation where relative permeability of oil is equal to that of water is less than

50%. Table 5.4 summarizes the parameters used in the Brooks-Corey model for the simulations of OBM-filtrate invasion considered in this chapter.

5.5.3 Flow Rate of Invasion

In the process of OBM-filtrate invasion, the flow rate (q_{mf}) is a rather uncertain parameter. It depends on both mud properties and formation properties (permeability, porosity, water saturation, capillary pressure, and relative permeability). Our initial estimate of flow rate is based on the approach used by Malik *et al*. (2007). In turn, such an approach is based on the procedure advanced by Wu *et al*. (2005) to simulate water-base mud-filtrate invasion and considers the interplay between mudcake and formation properties to estimate the flow rate of invasion. We simulate array-induction resistivity measurements in a field base case assuming that the formation is invaded with WBM. Once we reproduce the resistivity measurements, we use the average flow rate of WBM invasion as the initial estimate of flow rate of invasion for the simulation of OBM-filtrate invasion. Subsequently, we adjust the rate as needed to reproduce borehole resistivity measurements. This procedures yields physically consistent flow rates of OBM-filtrate invasion. Table 5.5 describes the additional formation and fluid properties necessary to simulate the process of OBM-filtrate invasion.

5.5.4 Simulation of Induction Resistivity Measurements

From the simulation of OBM-filtrate invasion, we obtain spatial distributions (radial and vertical directions) of water saturation. Subsequently, we use Archie's equation to calculate electrical resistivity at each gridblock assuming that electrical resistivity of formation water is not altered during the process of invasion. Finally, we simulate array-induction resistivity measurements from the spatial distribution of electrical resistivity. In order to perform the simulation of resistivity measurements, we assume 2D axial-symmetry of electrical resistivity, where current loop sources are located at the center of the borehole. We use the Numerical-Mode Matching Method (NMM) to simulate electrical resistivity measurements (Chew *et al*., 1984; Zhang *et al*., 1999).

In summary, the algorithm is initialized with the fluid-flow simulation of OBM invading porous media, which is coupled to the NMM code to simulate borehole resistivity measurements.

5.6 FIELD STUDIES

We begin the simulation of mud-filtrate invasion with Case No. 1. The objective is to estimate the initial flow rate of invasion by matching array-induction resistivity measurements. This task was accomplished with the UT-FET. Table 5.2 shows the average petrophysical properties used as inputs to the simulation.

5.6.1 Calibration Case

At the outset, we assumed that the invasion took place with fresh WBM and calculated the flow rate of invasion (Wu *et al*., 2005). Then, we used the calculated initial flow rate as input to the simulation of OBM-filtrate invasion (Malik *et al*., 2007). To that end, we assumed that the formation was saturated with movable and irreducible water and liquid hydrocarbons lumped into the single component C_7C_{18}. On the other hand, OBM-filtrate was described with hydrocarbons in the range of C_{14} to C_{18} lumped into a generic MC_{16} component. This fluid mixture is often referred to as a binary component mixture. Table 5.3 describes the properties of both formation and filtrate fluids. In order to secure a good match between field and simulated resistivity measurements, we modified capillary pressure, relative permeability, and flow rate of invasion, and performed the simulation of invasion several times. While modifying the latter parameters, we accounted for changes of wettability undergone by the rock formation while being invaded with OBM. Table 5.4 describes the Brooks-Corey parameters for capillary pressure and relative permeability used to match resistivity measurements. Figure 5.5 describes the spatial distributions (radial and vertical directions) of water saturation and electrical resistivity calculated after 60 hours of OBM-filtrate invasion. Figure 5.6 compares field with simulated AIT resistivity curves calculated after the simulation of invasion along with the average horizontal permeability and matching flow rate of invasion. Simulated array-induction resistivity measurements agree well with field measurements. The average flow rate necessary to reproduce measured apparent resistivity curves was approximately 0.24 ft^3/d/ft with a radial length of invasion approximately equal to 1.8 ft. This flow rate was used as the initial flow rate (q_{mf}^{o}) of invasion throughout the sensitivity analyses. We remark that the above simulations assumed a single-layer homogeneous formation.

For the sensitivity analyses, we considered presence of surfactants in the OBM. Moreover, gaseous hydrocarbons were included as pseudo-components of formation fluid. Because of such conditions, we also performed the corresponding calibration case with CMG-STARS. Figure 5.7 compares the radial distribution of simulated density, viscosity, water saturation, and electrical resistivity obtained with both FET and STARS. All input properties and parameters were assumed the same for the two simulators, including petrophysical and fluid properties, time of invasion, flow rate, and formation pressure. Results obtained with the two simulators agree well with each other, thereby confirming the reliability of the STARS simulator for the cases under consideration.

5.6.2 Sensitivity Analysis

We used STARS to perform analyses of the sensitivity of the process of invasion to fluid properties for each case based on different assumptions. First, we quantified the sensitivity of apparent resistivity measurements to native oil viscosity and density. Second, we made perturbations of native oil viscosity and capillary pressure while assuming OBM an emulsion that included oil, water, and surfactants. The first two sensitivity analyses were performed for Case No. 1 only. Finally, we moved upward in the formation (Cases No. 2 and No. 3) and performed sensitivity analyses to initial water saturation and flow rate of invasion in multi-component light oil and gas zones subject to invasion with emulsified OBM-filtrate. An additional case of study consisted of simulating a long capillary transition zone using a simple binary formulation for compositional fluid mixing. All the simulations assumed 60 hours of invasion.

5.6.2.1 Sensitivity to Formation Oil Viscosity and Mass Density

We simulated Case No. 1 using a simple binary formulation for compositional fluid mixing. For the base case, viscosity of native oil pseudo-component (C_7C_{18}) was equal to 1.0 cp and mass density was equal to 40.2 lb/ft^3. The OBM-filtrate (MC_{16}) viscosity was equal to 1.5 cp and density equal to 45.7 lb/ft^3. Each perturbation for a given property was performed separately. Formation oil viscosity was changed to 15 and 0.3 cp, respectively, whereas density was modified to 55.5 and 25.5 lb/ft^3, in that order. Figure 5.8 shows radial distributions of electrical resistivity calculated for each perturbation. We observe that resistivity increases close to the borehole wall, while asymptoting toward R_t (initial water saturation conditions) radially deeper into the formation. This behavior is due to the relatively large volume of movable water that is displaced by mud filtrate. Irreducible water saturation was approximately 8% and initial water saturation was approximately 36%. Therefore, the large capillary transition zone causes a radially smooth invasion front. Figure 5.9 shows the corresponding simulated AIT measurements for each perturbation. The most remarkable conclusion of this analysis is that for the case of higher viscosity, mud-filtrate moves faster into the formation, thereby increasing the electrical resistivity in the near-wellbore region. Thus, we observe larger separation of apparent resistivity curves than for the case of no perturbation. Changes of fluid density do not entail a measurable difference on the radial length of invasion. Likewise, array-induction resistivity curves are less affected by gravity in the presence of high-density hydrocarbons than in the presence of low-density hydrocarbons, as indicated by their symmetric behavior within a particular layer.

5.6.2.2 Sensitivity to Formation Oil Viscosity and Capillary Pressure with Emulsified OBM

Case No. 1 was simulated assuming that OBM contained water and emulsifier surfactant (EMUL). We assumed that water and EMUL were two new components of the original OBM. The molar fraction for each component was 0.1 water, 0.4 EMUL, and 0.5 MC_{16}. Viscosities were 1 cp for water and 20 cp for the surfactant. This analysis was performed with simultaneous variations of formation oil viscosity (15 and 0.3 cp) and maximum capillary pressure (7 and 1 psi). The high value of P_c (capillary pressure) was obtained with the Brooks-Corey parameters shown in Table 5.4, whereas the lower value was accomplished with P_c^o (capillary pressure coefficient) equal to 1.2 psi·$D^{1/2}$ and e_p (empirical exponent for pore size distribution) equal to 35. The latter values resulted in a sharper P_c curve that was associated with a rock that exhibited large critical pore-throat radii (>2 μm) and a relatively lower interfacial tension between water and oil than in the base case without surfactants. The objective of performing sensitivity analyses with very low capillary pressure was to quantify the effect of decreasing the interfacial tension because of presence of surfactants in the OBM (Skalli *et al.*, 2006). Figure 5.10 shows radial distributions of water saturation and electrical resistivity associated with each perturbation. Figure 5.11 displays the AIT resistivity measurements simulated from the spatial distributions of electrical resistivity. For the case of high capillary pressure, we observe the same behavior as in the previous example. However, electrical resistivity is slightly higher in this case. Lower capillary pressure causes a remarkable increase of electrical resistivity near the borehole. Such behavior is due to presence of surfactants in the OBM, which reduce the influence of capillary forces due to the reduction of interfacial tension.

5.6.2.3 Sensitivity to Initial Water Saturation and Flow Rate of Invasion with Emulsified OBM

Case No. 2 was the base case for this analysis. We used the same OBM composition as in the previous example. The formation was saturated with very- light hydrocarbon pseudo-components, namely, C_4C_6 and C_7C_{18}, with molar fractions of 0.7 and 0.3, respectively. Initial water saturation (S_{win}) was approximately equal to 23% and Brooks-Corey's parameters for capillary pressure were those that gave lower values of P_c in the previous example. We changed S_{win} to 18% and 28%, and flow rate to 0.96 ($4 \cdot q_{mf}^{o}$) and 0.06 ($q_{mf}^{o}/4$) $ft^3/d/ft$. This case was also simulated assuming a water- and surfactant-free OBM. Figure 5.12 describes the spatial distributions of water saturation and electrical resistivity calculated after 60 hours of OBM-filtrate invasion for base Case No. 2. Water saturation increases above Swin approximately at 1.5 ft radially away from the borehole, which is responsible for the presence of a low-resistivity annulus in the zone. This annulus is more evident in Figure 5.13, where we show radial distributions of water saturation and electrical resistivity separately for each perturbation. With a surfactant-free mud, the annulus vanishes and is similar to the case of very low flow rate of invasion with emulsified OBM. Figure 5.14 shows the corresponding AIT resistivity measurements simulated from the spatial distributions of electrical resistivity. Larger separation of apparent resistivity curves is observed in the cases of high flow rate of invasion and high initial water saturation than in the cases of low S_{win} and low q_{mf}. In general, presence of surfactants causes larger variability of the simulated apparent resistivity curves.

5.6.2.4 Sensitivity to Flow Rate of Invasion with Emulsified OBM Invading a Gas-Bearing Formation

In Case No. 3, fluids saturating the formation consist mainly of gas and very light oil. Mole fractions of gaseous pseudo-components were 0.7 N_2C_1 and 0.3 C4C6. On the other hand, the mole fraction of liquid components was 0.5 for both C_4C_6 and C_7C_{18}, respectively. Case No. 3 was located in the upper depth section of the formation and its initial water saturation (18%) was close to irreducible water saturation (8%). Capillary pressure parameters were the same as those used in the previous example. We changed the flow rate of invasion to 0.96 ($4 \cdot q_{mf}^{o}$) and 2.4 ($10 \cdot q_{mf}^{o}$) ft^3/d/ft. Figure 5.15 shows the spatial distributions of water saturation and electrical resistivity calculated after 60 hours of 10qmfo of mud-filtrate invasion. Presence of a low-resistivity annulus is noteworthy as well as deep invasion due to the exaggerated flow rate. Figure 5.16 shows radial distributions of water saturation and electrical resistivity associated with each perturbation. The higher the flow rate the lower the resistivity in the annulus region and the deeper its radial location away from the wellbore. For the simulation with water- and surfactant-free OBM, the annulus zone was negligible. Figure 5.17 shows the simulated AIT apparent resistivity measurements where we observe large separation of resistivity curves caused by the higher flow rate of invasion. The difference between simulated AIT measurements with and without presence of surfactants was not significant. Such a behavior is due to the low initial water saturation under a low flow rate of invasion; the annulus is relatively shallow, thereby not affecting the array-induction resistivity measurements.

5.6.2.5 Simulation of Invasion in a Capillary Transition Zone

The simulation in the capillary transition zone (8527 ft – 8806 ft) assumed the same conditions as those of the calibration case, that is to say, single OBM-filtrate and native oil pseudo-components (binary formulation), and the same Brooks-Corey parameters for capillary pressure and relative permeability. This example was constructed using 12 petrophysical layers with vertical grids spaced at approximately 1.9 ft intervals. Most of the layers were very thick (>15 ft) with four thin layers (<5 ft) to account for laminated sands and intercalated shales. Figure 5.18 shows the spatial distributions of water saturation and electrical resistivity calculated after 60 hours of mud-filtrate invasion. These distributions show that water saturation increases toward the bottom of the formation within the capillary transition zone. Figure 5.19 shows the corresponding measured and simulated AIT resistivity curves along with curves of layer-by-layer flushed-zone and virgin-zone resistivity obtained from the simulation of OBM-filtrate invasion. We observe separation of apparent resistivity curves in the thicker sands, with the separation more pronounced in the water region at the bottom of the formation.

5.7 DISCUSSION

We studied the influence of several fluid properties on array-induction resistivity measurements in a well drilled with OBM. The formation under analysis included a long hydrocarbon column with a gas cap at the top, followed by a condensate and oil interval in a capillary transition zone with an underlying active aquifer. Detailed petrophysical analysis allowed us to select depth intervals invaded by OBM-filtrate as indicated by the separation of array-induction resistivity curves. An oil interval in the capillary transition zone was used as the calibration case to construct the invasion model. Morever, sensitivity analyses were carried out based on separate perturbations of density and viscosity of native oil and flow rate of mud-filtrate invasion. Additional sensitivity analyses to capillary pressure and initial water saturation allowed us to study the effect of wettability and saturation zones on resistivity measurements acquired across the formation. Both OBM and native oil were initially simulated assuming a single component for each fluid. Subsequently, we treated the OBM as an emulsion by adding water and surfactants. We also modeled multi-components and lighter hydrocarbons as part of native formation fluids.

In the calibration case, we observed that water saturation decreased in the near-wellbore region because of presence of OBM-filtrate invading the formation. The reduction of S_w entailed an increase of electrical resistivity. Sensitivity analyses to native oil viscosity and density indicated that viscosity exerted a measurable control on the spatial distribution of water saturation, thereby affecting the spatial distribution of electrical resistivity. The effect of fluid density on water saturation and resistivity was relatively less significant on the simulated apparent resistivity curves. In the case of large viscosity of native oil, invasion caused a high electrical resistivity zone in the near-wellbore region due to the reduction of fluid mobility of the native oleic phase. Therefore, because mud-filtrate mobility was higher than that of formation fluids, OBM-filtrate penetrated faster into the porous medium. When emulsified surfactants were added to the OBM, we observed a similar behavior. However, when we decreased the capillary pressure, electrical resistivity abruptly increased in the radial zone close to the wellbore. The assumption of low capillary pressure was made in order to quantify the corresponding reduction of interfacial tension between oil and water caused by presence of surfactants in the mud. In low interfacial-tension environments, capillary forces opposing the invasion decrease and, in some cases, cause reduction of residual saturation and increase of relative permeability (Dawe and Grattoni, 1998), thereby allowing the OBM-filtrate to move more freely into the formation (La Vigne *et al*., 1997).

The example of a very light hydrocarbon zone allowed us to perform additional sensitivity analyses to appraise the effect of the flow rate of invasion and saturation zones on the simulated apparent resistivity curves. We assumed low capillary pressure and presence of emulsified OBM (which in general exhibits a larger viscosity than a single-component drilling fluid). When the OBM-filtrate invaded the formation, it rapidly displaced the movable water thereby creating a radial zone with S_w greater than S_{win}. The large viscosity contrast between the light hydrocarbon and the OBM together with the low initial water saturation created the necessary conditions to form a radial water bank. In turn, the latter water bank was responsible for the presence of an electrically conductive annulus in the invaded zone. Such annulus affected the behavior of the AIT resistivity measurements. The corresponding effect on resistivity measurements depended on the magnitude of the flow rate of invasion as well as on initial water saturation. Large values of q_{mf} and S_{win} entailed a significant separation of array-induction resistivity curves. We note that oil saturation abruptly increases in the near-wellbore region, which now becomes an oil-wet rock, whereupon Archie's saturation exponent (n) is no longer constant in the radial direction (Donaldson and Siddiqui, 1989; Dawe and Grattoni, 1998) and this affects the calculation of electrical resistivity. In our analysis, we observed that, when surfactants were not present in the OBM, the resistivity annulus did not ensue. On the other hand, when the formation was gas-bearing, the annulus was more pronounced even within low water-saturation zones. The radial location of the annulus depended on the flow rate of invasion: the larger the flow rate the deeper the radial location of the annulus, thereby causing larger variability of the array-induction resistivity curves. In some cases, the intermediate-sensing resistivity curves were sensitive to the annulus region as indicated by their relatively low values compared to those of the deepest-sensing curves.

Based on the field study and the sensitivity analyses described above, we constructed a final synthetic example of a 16-ft clastic formation with effective porosity equal to 25%, irreducible water saturation equal to 8%, horizontal permeability equal to 446 md, and vertical permeability equal to 223 md. The objective was to perform simulations of invasion of emulsified OBM in the formation at different water saturation conditions. Invasion flow rate was assumed equal to 0.96 ft^3/d/ft ($4q_{mf}^o$). Initially, the top of the formation was assumed in the gas zone (8329 ft, S_{win}=18%), then in an oil zone (8600 ft, S_{win}= 36%), and finally in the aquifer (8770 ft, S_{win}=100%); formation temperature and pressure were modified accordingly. Figure 5.20 shows radial distributions of water saturation and electrical resistivity for each value of S_{win}, where we observe that the higher the initial water saturation, the more discontinuous the radial invasion front. We also observed that the viscosity contrast between emulsified OBM and native hydrocarbon smoothes the radial invasion front. Low native-fluid viscosity together with low S_{win} in gas zones are responsible for an electrically conductive annulus as indicated by the radial distribution of electrical resistivity. Figure 5.21 shows the corresponding simulations of AIT resistivity measurements. We observe the largest relative separation of curves between the deepest-sensing (R90) and the shallowest-sensing (R10) AIT resistivity measurements in the water zone, whereas the smallest curve separation is observed within the partially gas-saturated zone. On the other hand, the partially oil-saturated depth interval with movable water exhibits the most pronounced separation of intermediate-sensing AIT resistivity curves (R20, R30, and R60). The sensitivity analysis shows that, even though AIT resistivity curves in the gas zone do not exhibit large separation among themselves, presence of a resistivity annulus would become more important for AIT measurements acquired in depth zones farther from irreducible water saturation. For completeness, the same simulation example was performed assuming no invasion. Figure 5.22 exhibit the simulated borehole resistivity measurements assuming no invasion. We found no separation of array-induction resistivity curves, thereby confirming that the separation of resistivity curves responded only to invasion and not to processing artifacts associated with the calculation of apparent resistivity.

5.8 CONCLUSIONS

Simulated spatial distributions of water saturation were highly influenced by the assumed properties of OBM and native hydrocarbon components. Such a situation caused high resistivity near the borehole wall, which was governed by:

- capillary forces (in turn modified due to wetting properties of surfactants),
- native and invading fluid viscosity, thereby affecting relative fluid mobility,
- saturation zone (initial water saturation and residual fluid saturation), and
- flow rate of invasion,

We showed that fluid properties of drilling mud and native hydrocarbon affected apparent resistivity measurements under overbalanced drilling conditions. The process of OBM-filtrate with emulsified surfactants caused changes in the spatial distribution of electrical resistivity 10% to 15% larger than when invading with a water- and surfactant-free OBM, thereby causing measurable variability of the simulated AIT resistivity curves. Furthermore, the radial length of invasion decreased in the order of 45% to 55%. A radial water bank ensued when hydrocarbon viscosity was below 0.25 cp together with an absolute difference between S_{win} and S_{wir} less than 25%, giving rise to an electrically conductive annulus in the invaded zone. The latter annulus was more pronounced in gas-bearing than in oil-bearing zones.

For the case of OBM invasion, Archie's cementation exponent varies radially due to alterations of rock wettability and fluid mobility, whereas in water-base mud-filtrate invasion, water resistivity changes radially. In the process of WBM-filtrate invasion, fluid and formation properties are responsible for the separation of AIT resistivity measurements and, in some cases, for the presence of a low-resistivity annulus (George *et al*., 2004) due to differences of salt concentration between mud-filtrate and connate water. Therefore, in either process of invasion, the original electrical properties of the rock are altered in the invaded zone.

Initial water saturation became an exceedingly important parameter to reproduce apparent resistivity measurements in the presence of OBM-filtrate invasion, which allowed us to obtain a more reliable estimate of R_t, thereby improving the assessment of in-place hydrocarbon saturation. Moreover, as in the case of WBM-filtrate invasion, presence of an annulus and large separation of resistivity curves indicated that the invaded formation was porous and permeable, possibly with good production potential.

The formation under analysis was a clastic sequence with high-porosity and high-permeability rock units. We warn that conclusions stemming from this chapter may need to be adjusted for cases of low-porosity, low-permeability formations. Low-porosity rock formations often entail large capillary pressure effects and radially deeper invasion, thereby resulting in significant variability of apparent resistivity curves. However, the assessment method described in this chapter can still be used to appraise the influence of OBM on apparent resistivity curves across invaded low-porosity, low-permeability formations.

Table 5.1: Summary of Archie's parameters and rock and fluid properties used to estimate water saturation and porosity

Variable	Units	Value
Archie's tortuosity factor *a*	-	1.00
Archie's cementation exponent *m*	-	1.89
Archie's saturation exponent *n*	-	1.92
Connate water resistivity @ 240 ^{o}F	Ω·m	0.12
Matrix density	g/cm^3	2.655
Shale density	g/cm^3	2.55
Water density	g/cm^3	1.00
Hydrocarbon density (mix. gas zone)	g/cm^3	0.60
Hydrocarbon density (mix. oil zone)	g/cm^3	0.75

Table 5.2: Summary of assumed petrophysical properties for the cases of study

Property	Units	Case 1	Case 2	Case 3
Thickness	ft	16	6	16
Effective porosity	fraction	0.25	0.27	0.2
Water saturation	fraction	0.363	0.230	0.18
Volumetric shale concentration	fraction	0.04	0.03	0.07
Horizontal Permeability	md	353	434	446
Vertical Permeability	md	180	217	223

Table 5.3**:** Summary of PVT properties of the assumed in-situ hydrocarbon and mud-filtrate components

Property	Units	N_2C_1	C_4C_6	C_7C_{18}	EMUL	MC_{16}
Critical Temperature	^{o}F	-125.7	359.8	656.2	986.7	822.5
Critical Pressure	psi	653.3	498.2	322.2	188.6	240.2
Mass Density	lb/ft^3	1.05	12.06	40.2	59.9	45.7
Molar Weight	lb-mol	16.6	67.73	132.8	284.5	222
Viscosity	cp	0.025	0.105	1.0	20	1.5

Table 5.4: Summary of relative permeability and capillary pressure parameters used in Brooks-Corey's equations

Variable	**Value**
Empirical exponent for wetting phase, e_w	3
Empirical exponent for non-wetting phase, e_{nw}	7
End point for wetting phase, k^o_{rw}	0.80
End point for non-wetting phase, k^o_{rnw}	1
Empirical exponent for pore size distribution, e_p	4
Capillary pressure coefficient, P_c^o, [psi·D$^{1/2}$]	8

Table 5.5: Summary of parameters assumed in the simulation of the process of mud-filtrate invasion

Variable	**Units**	**Value**
Initial formation pressure @ 8616 ft	psi	3,628
Maximum invasion time	hours	60
Initial invasion flow rate	ft^3/d/ft	0.2375
Temperature @ 8616 ft	^{o}F	213
Formation outer boundary	ft	2000
Residual water saturation	fraction	0.08
Residual oil saturation	fraction	0.10

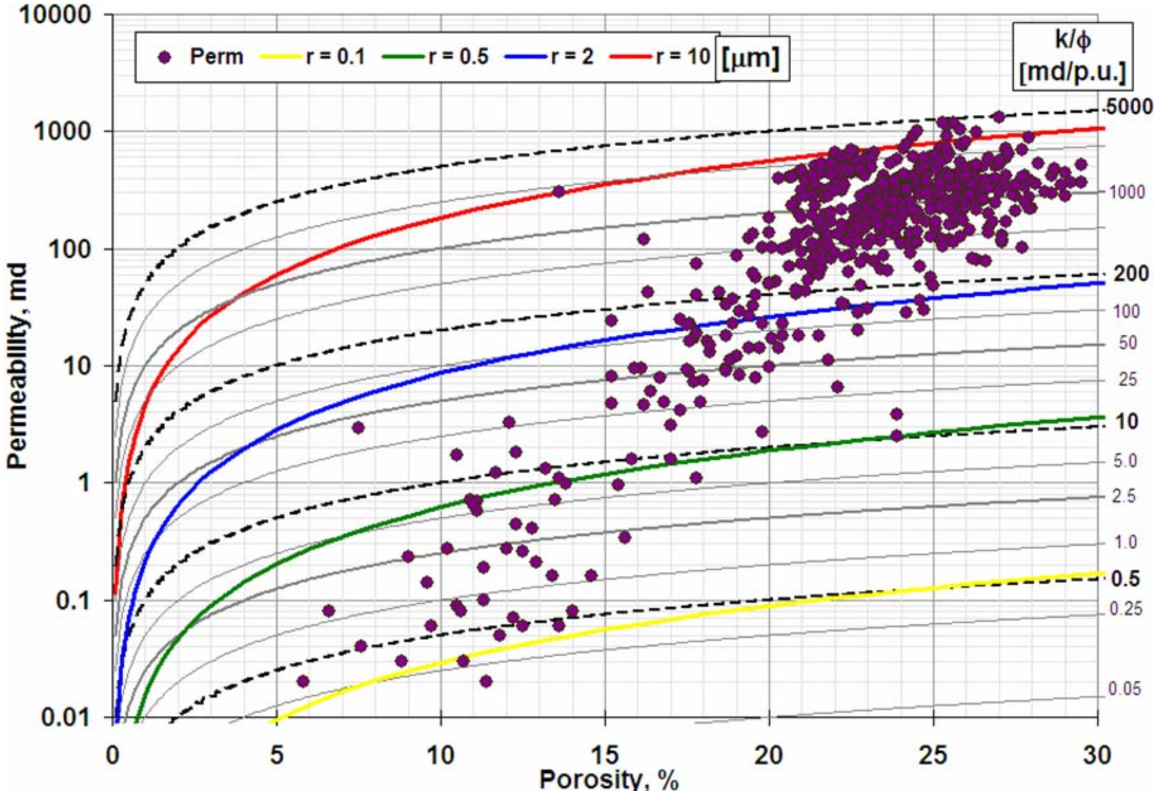

Figure 5.1: Cross-plot of core permeability and porosity along with parametric curves of Winland's critical pore-throat radius, r_{35}, (continuous colored lines) and *k/*□ ratio (grey and dashed-black lines). Most of the samples are located in zones of high porosity and high permeability, which indicates the high flow and storage capacity of the rock units.

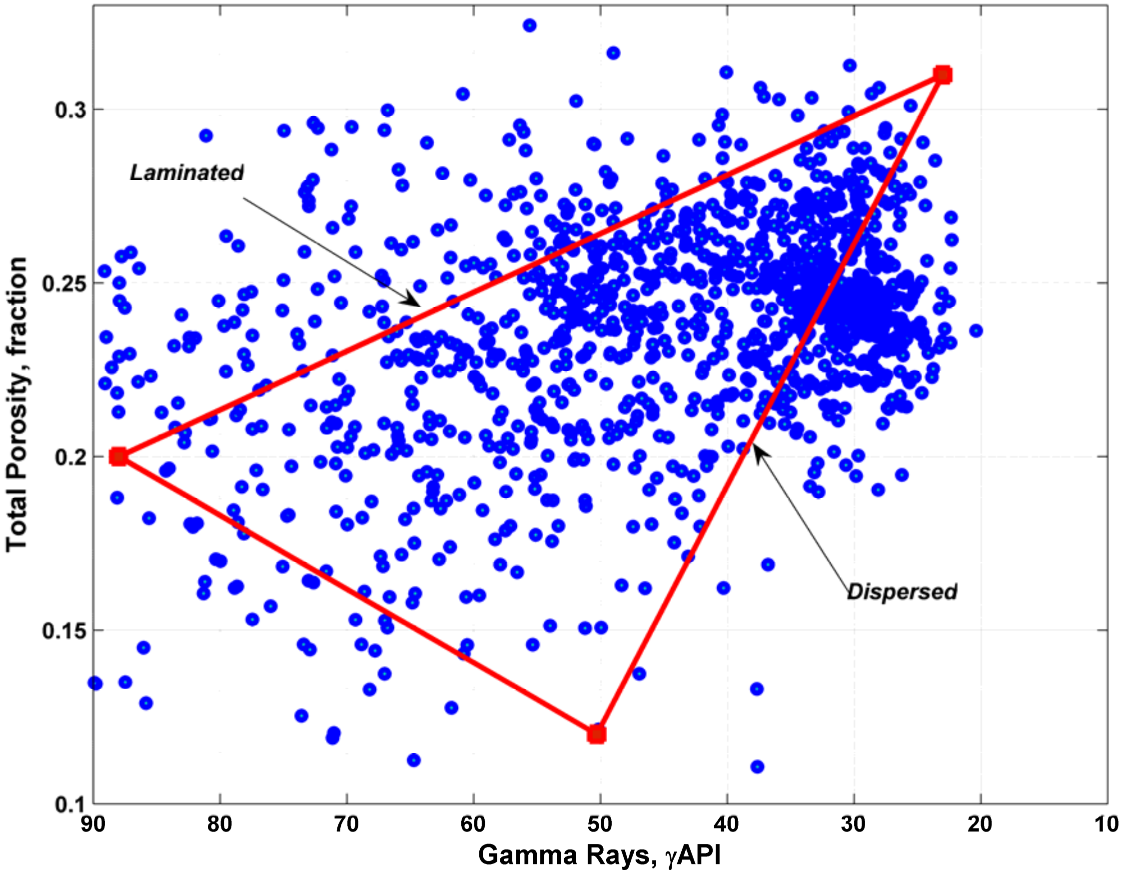

Figure 5.2: Thomas-Stieber cross-plot used to diagnose the type of shale/clay distribution in the formation. Dispersed shale is the dominant type of shale/clay distribution in the sand units.

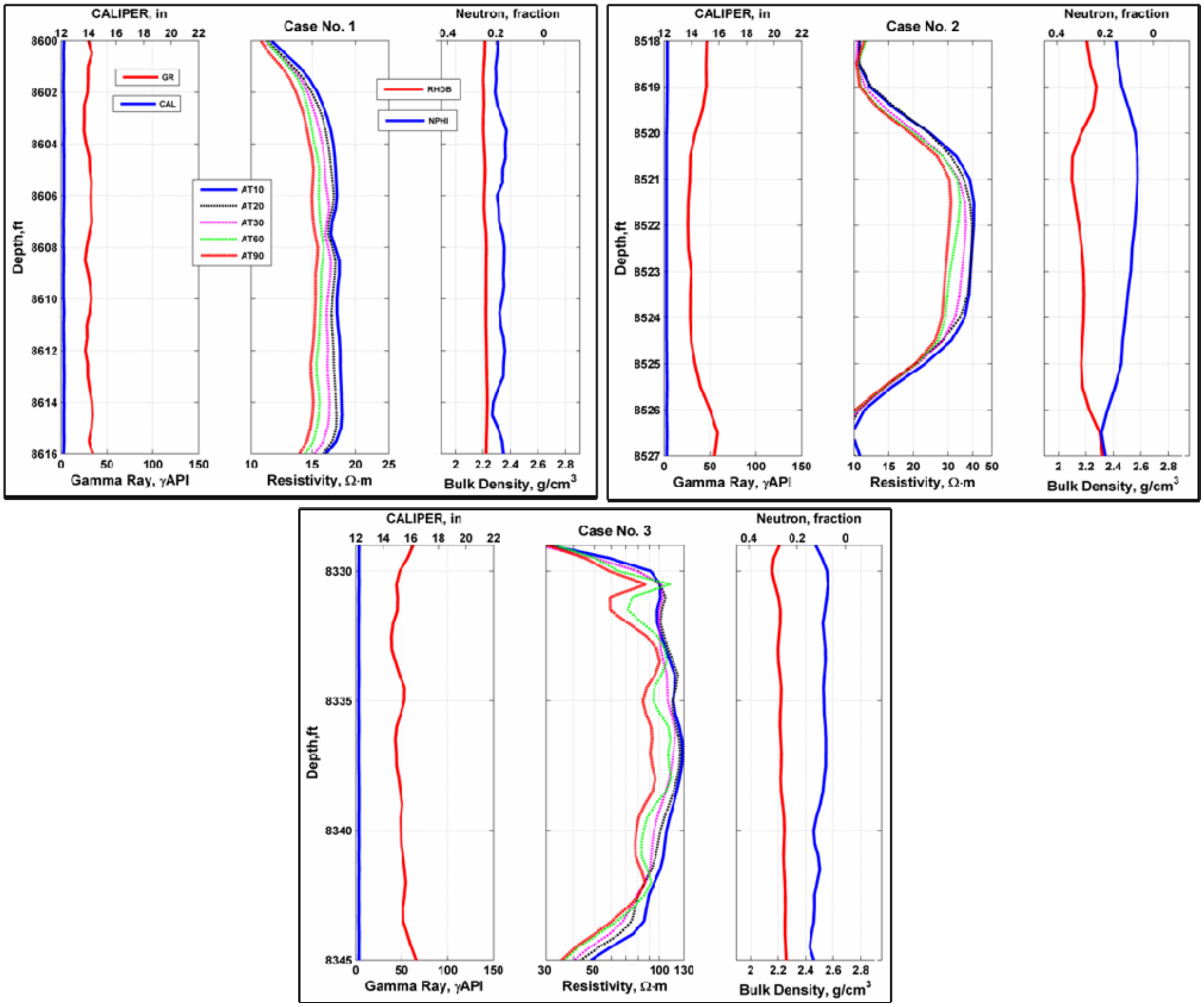

Figure 5.3: Well logs for the three depth intervals used to perform sensitivity analysis of oil-base mud-filtrate invasion to fluid properties. The center panels of each set of logs display 2-foot resolution AIT apparent resistivity curves. Logs were acquired in a partially oil-saturated interval (Case No. 1), a very light hydrocarbon zone (Case No. 2) and a partially gas-saturated sand (Case No. 3). Measurements include 3 fluid-saturation levels of a capillary transition zone

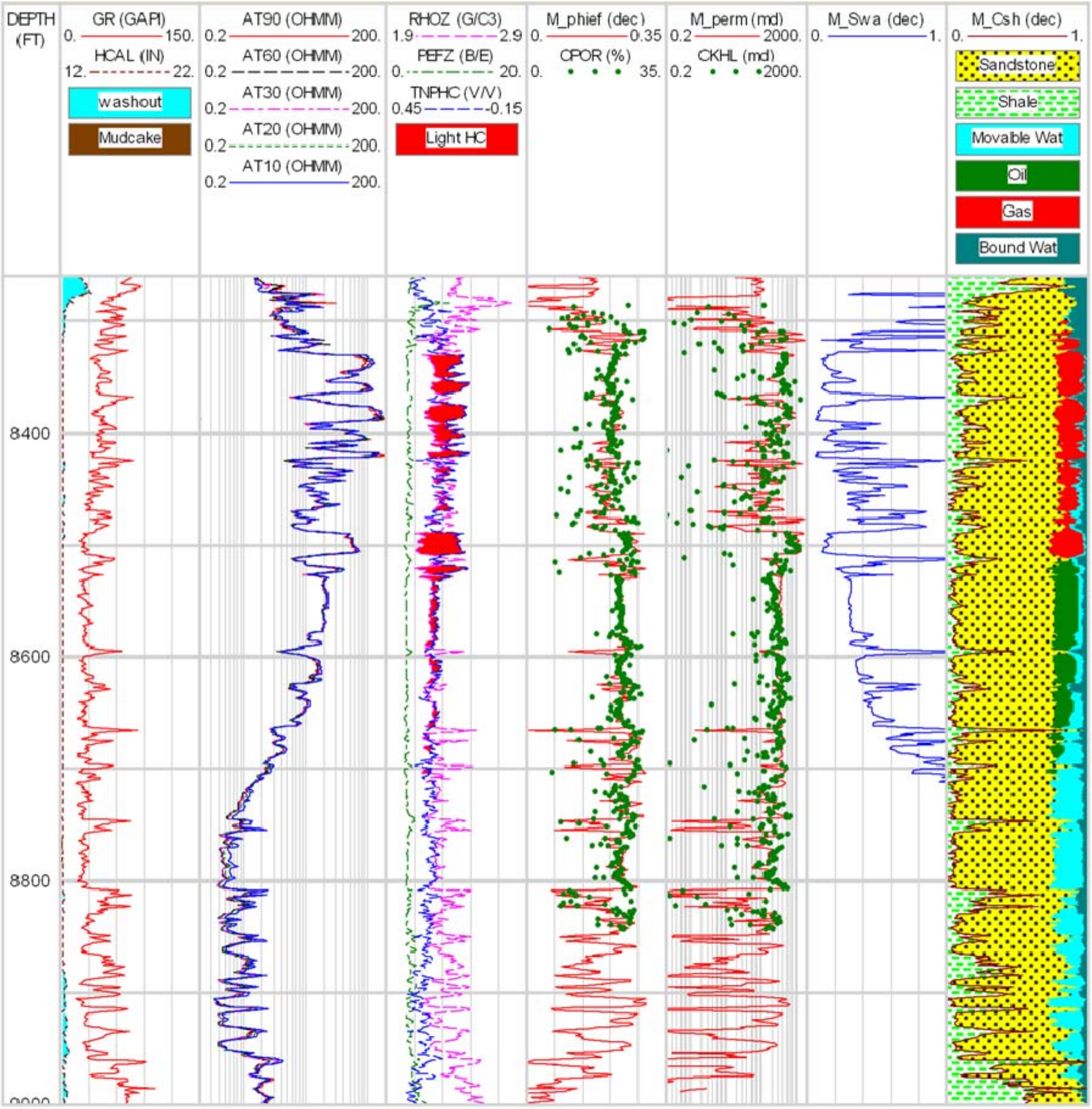

Figure 5.4: Petrophysical Assessment. Track 1: gamma ray and caliper logs. Track 2: array-induction resistivity logs. Track 3: neutron-density logs highlighting light hydrocarbon zones (shown with shading) and photoelectric factor log. Track 5: calculated effective porosity (shown with a continuous line) and core porosity (shown with circles). Track 4: modified Timur-Tixier permeability (shown with a continuous line) and core permeability (shown with circles). Track 6: Archie's water saturation. Tracks 7: volumetric analysis indicating clean sands in the oil and water zones and more heterogeneous sands in the gas zone.

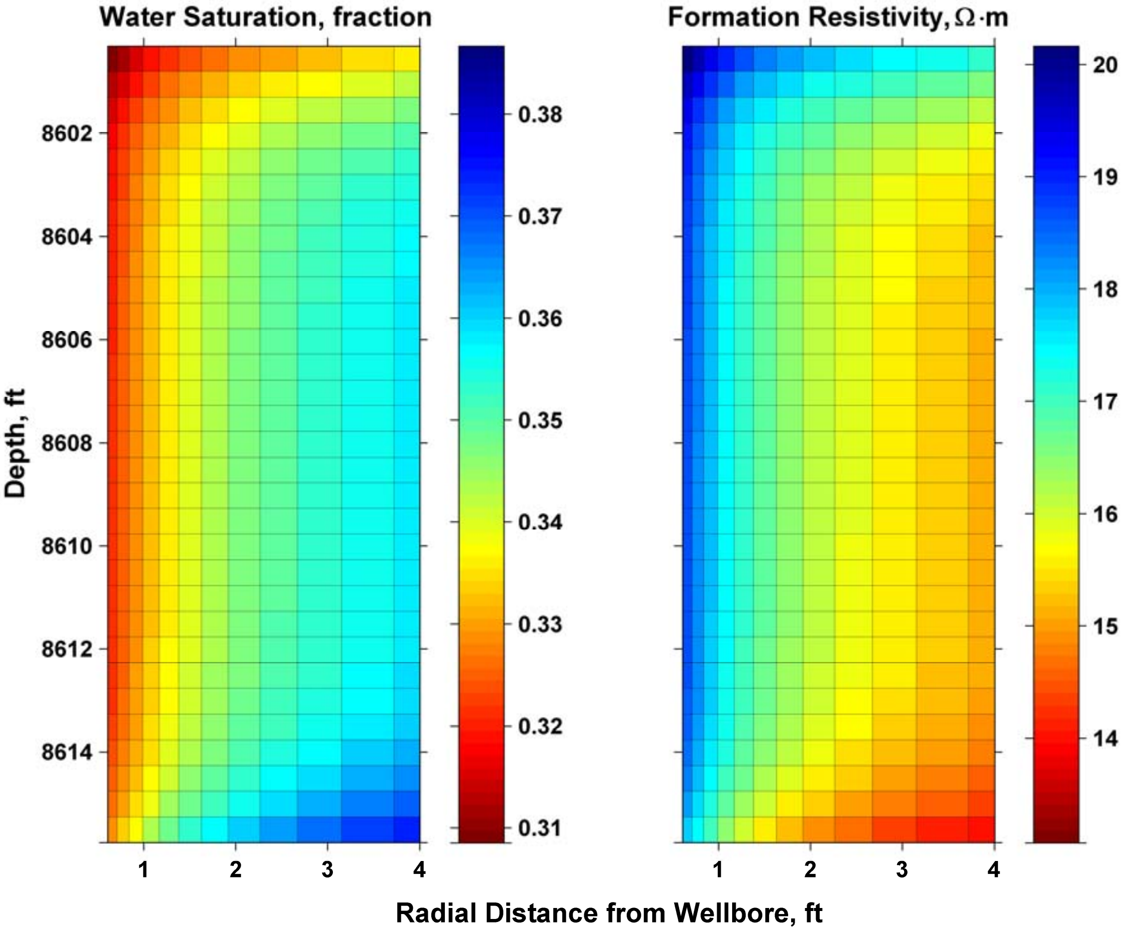

Figure 5.5: Spatial distributions (vertical and radial directions) of water saturation (left-hand panel) and electrical resistivity (right-hand panel) calculated after 60 hours of oil-base mud-filtrate invasion into a partially oil-saturated formation (Case No. 1).

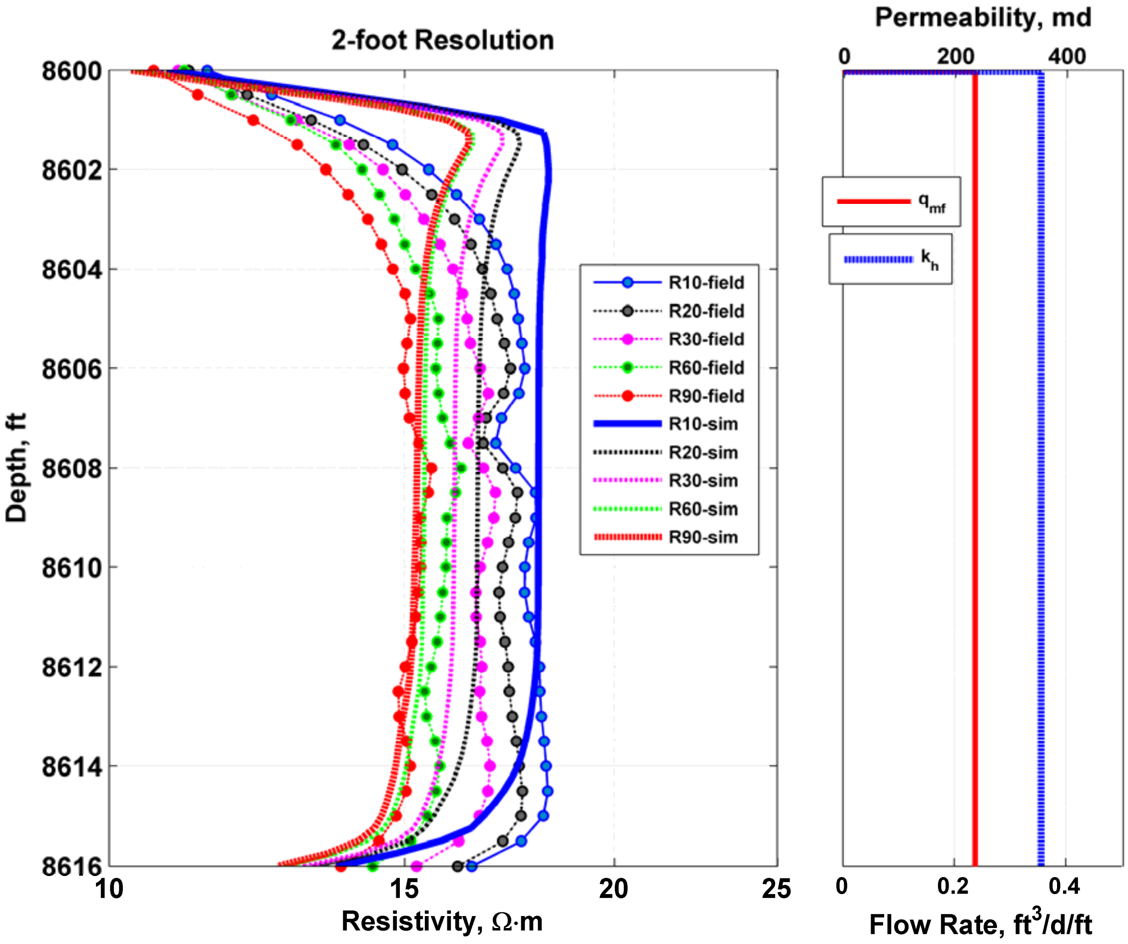

Figure 5.6: The left-hand side panel compares simulated (continuous thick curves) and measured (circles and thin curves) 2-foot array-induction resistivity measurements after 60 hours of oil-base mud-filtrate invasion for Case No. 1. The right-hand side panel describes the assumed average flow rate per foot and the horizontal permeability.

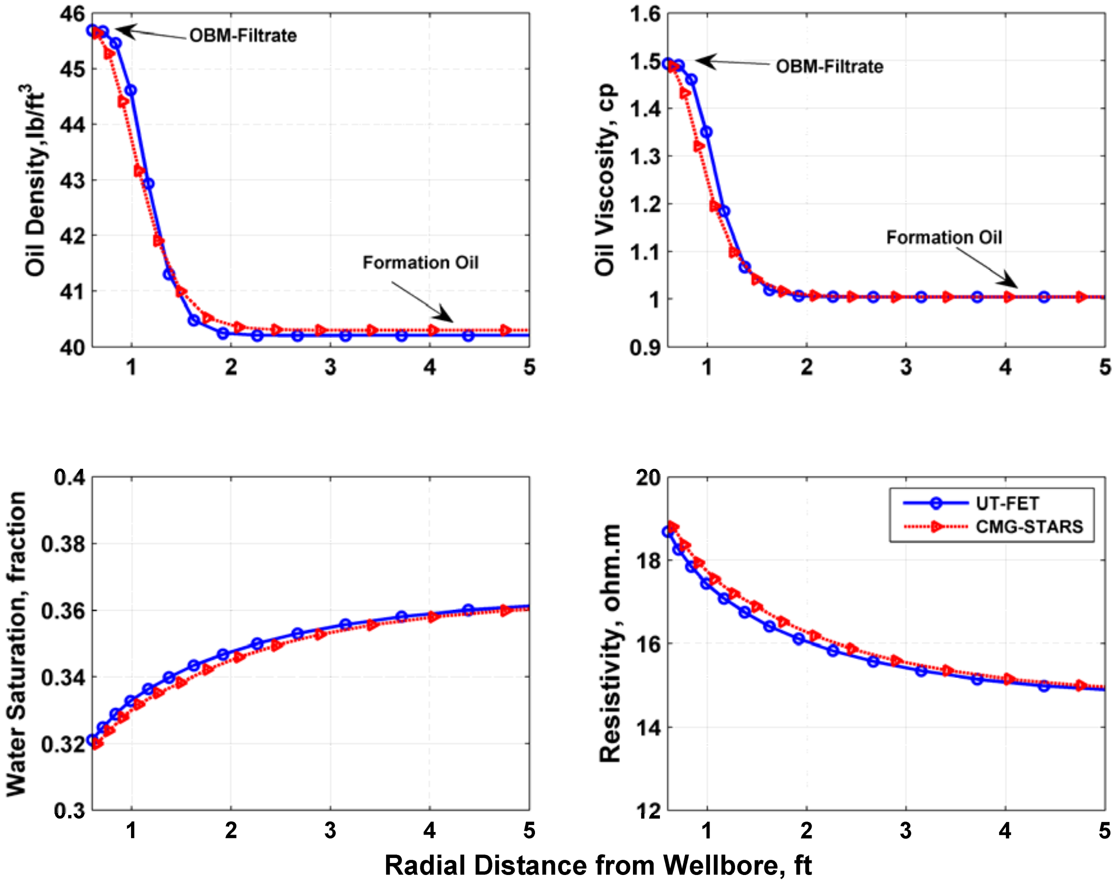

Figure 5.7: Radial distributions (clock-wise) of oil density, oil viscosity, electrical resistivity, and water saturation for the base case (Case No. 1) after 60 hours of invasion. Simulations were performed with the FET and STARS under the same conditions.

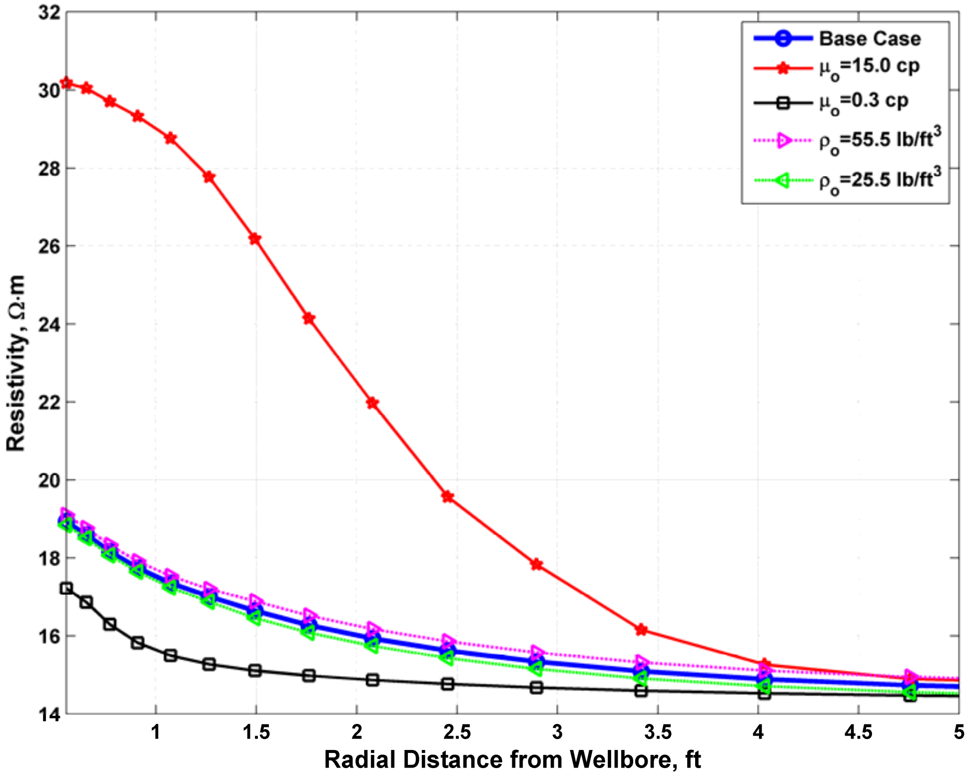

Figure 5.8: Radial distributions of electrical resistivity obtained after 60 hours of invasion for Case No. 1 by performing separate perturbations of formation oil viscosity and density.

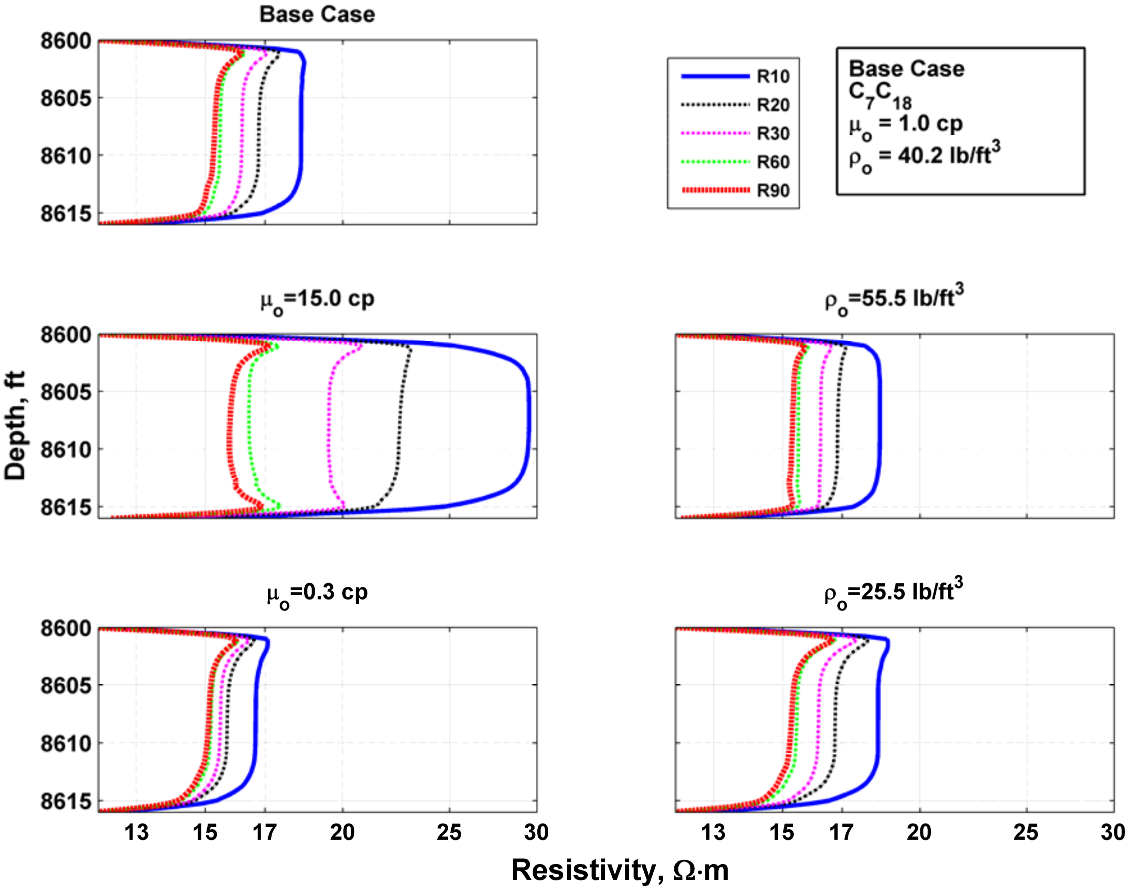

Figure 5.9: Sensitivity analysis of array-induction resistivity measurements to changes of formation oil viscosity and density. Simulated 2-foot AIT resistivity measurements for Case No. 1 are compared to the corresponding measurements simulated from the sensitivity analysis.

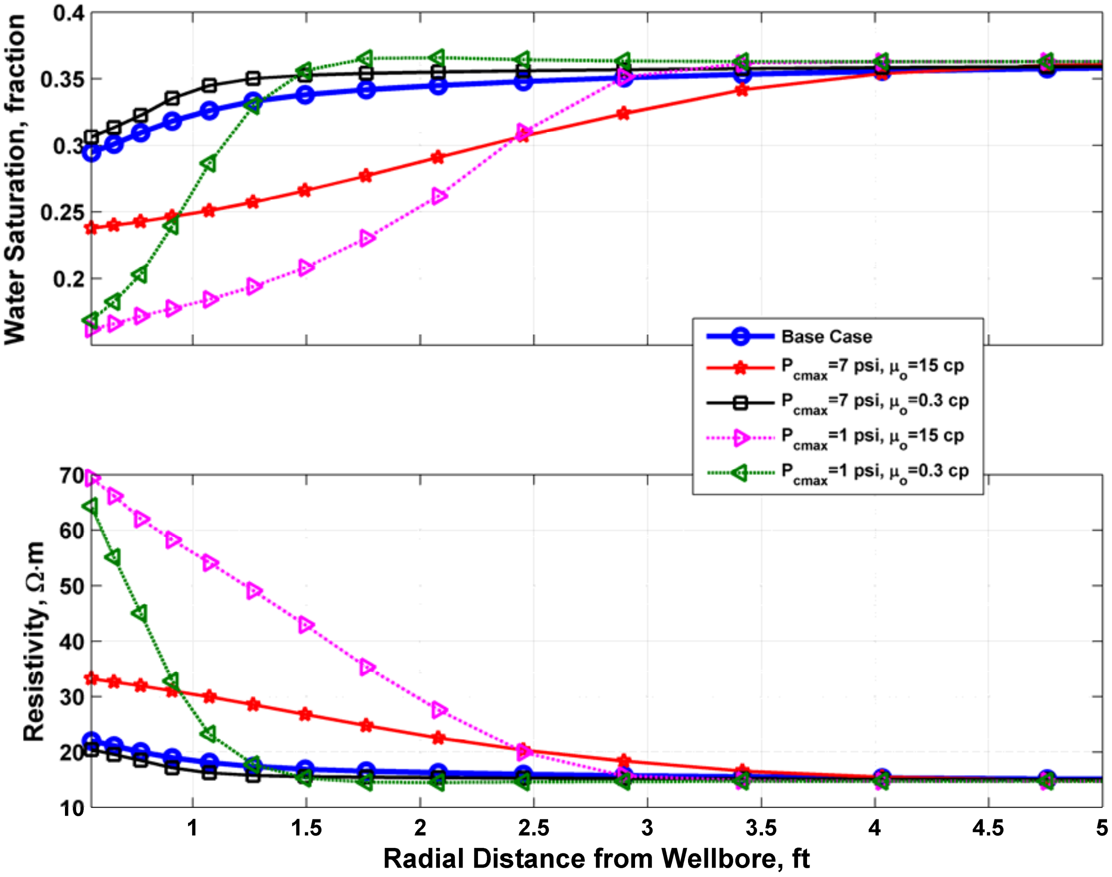

Figure 5.10: Radial distributions of water saturation and electrical resistivity obtained after 60 hours of invasion for Case No. 1. Mud filtrate consists of MC_{16}, EMUL, and water. The radial distributions show simulation results obtained by performing joint perturbations of capillary pressure and native oil viscosity.

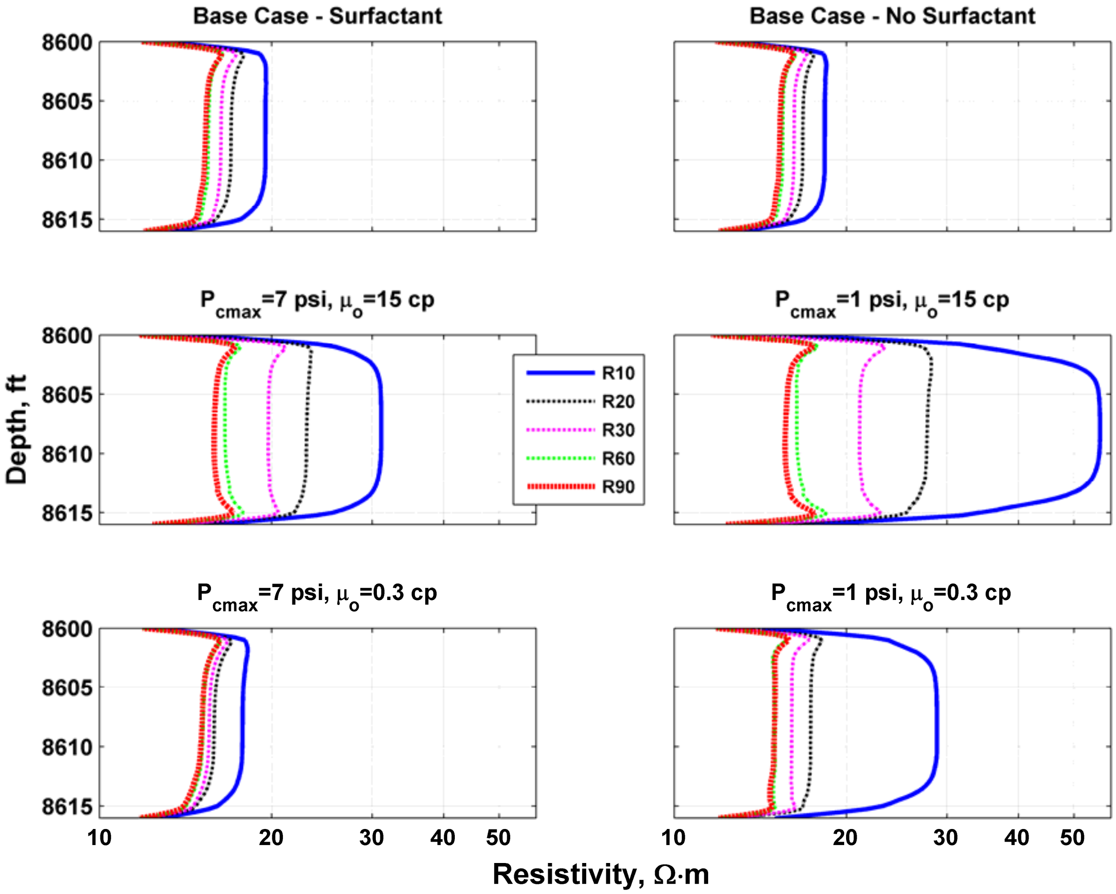

Figure 5.11: Sensitivity analysis of array-induction resistivity measurements to changes of capillary pressure and formation oil viscosity. The base Case No. 1 (with and without presence of surfactants) simulated AIT resistivity measurements are compared to simulations obtained from the sensitivity analysis with a surfactant emulsifying the water present in the OBM.

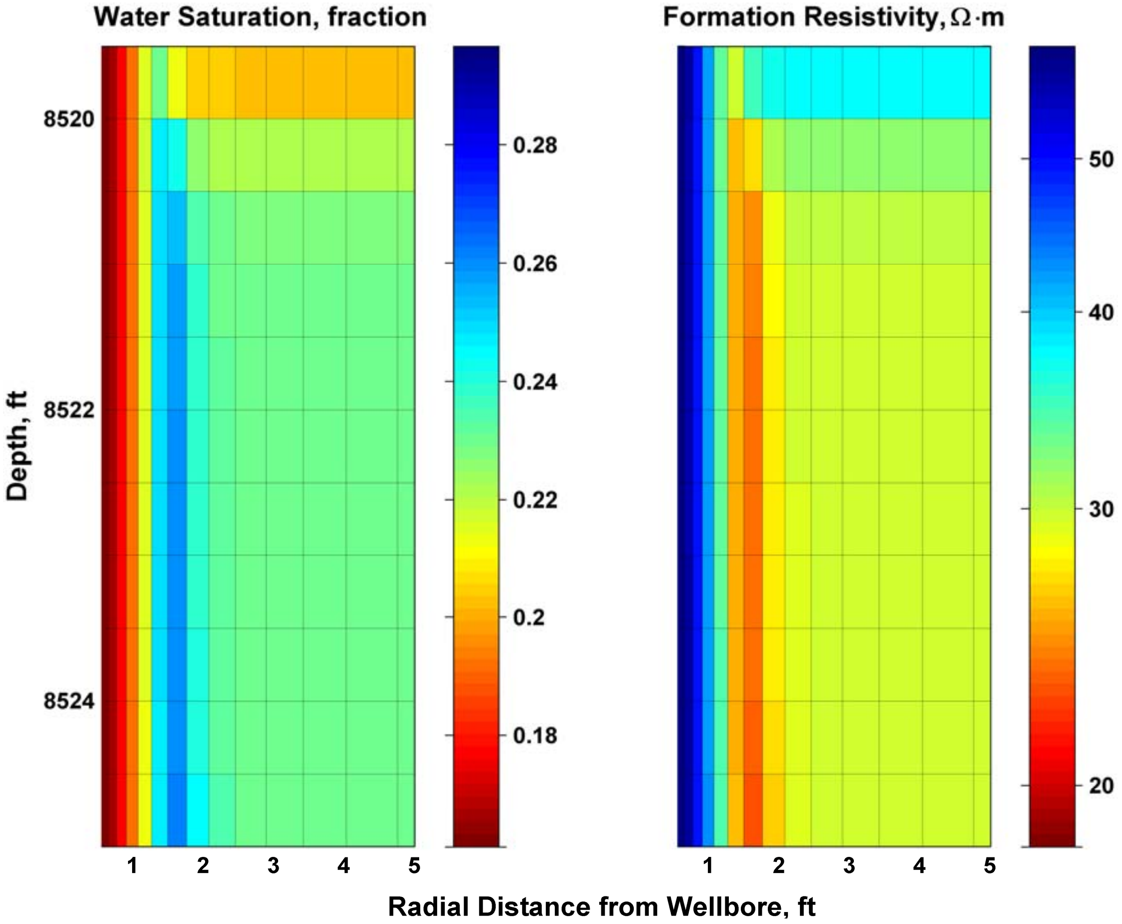

Figure 5.12: Spatial distributions (vertical and radial directions) of water saturation (left-hand panel) and electrical resistivity (right-hand panel) calculated after 60 hours of oil-base mud-filtrate invasion into a partially light oil-saturated formation (Case No. 2). A low-resistivity annulus ensues approximately 1.5 ft away from the borehole.

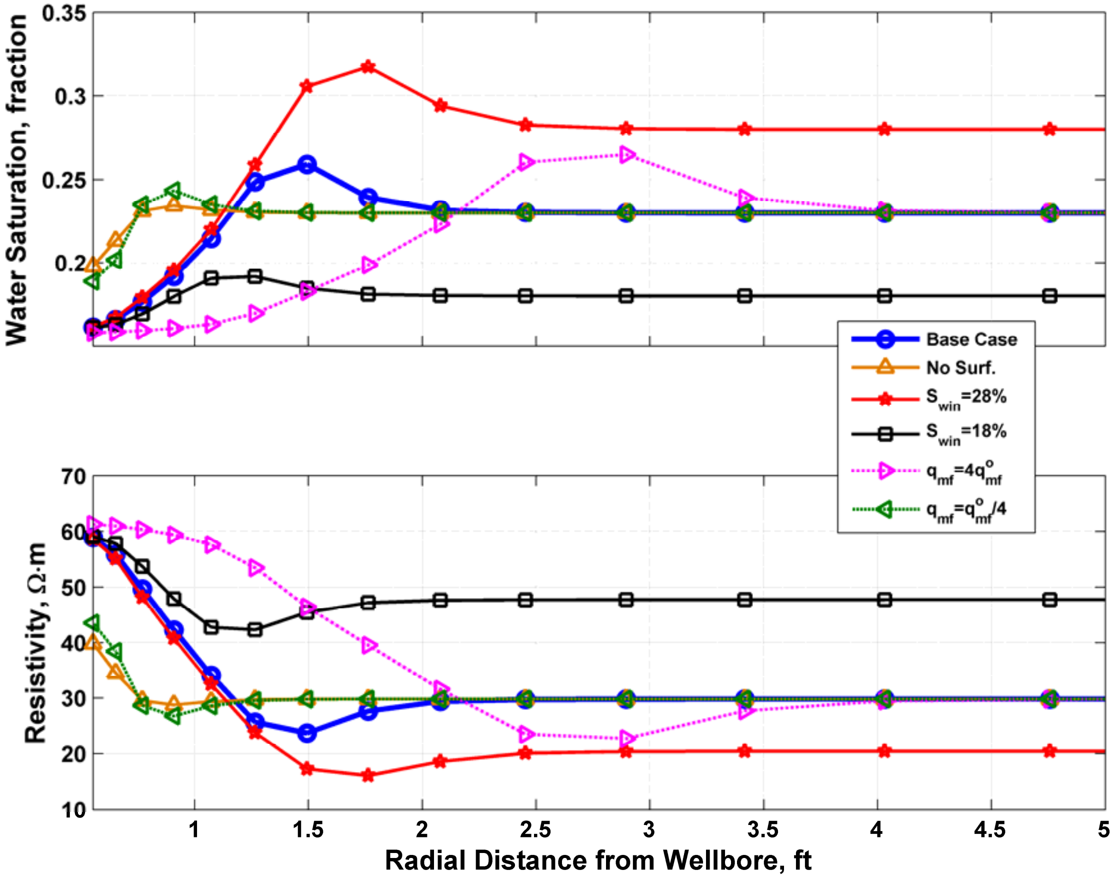

Figure 5.13: Radial distributions of water saturation and electrical resistivity obtained after 60 hours of invasion for Case No. 2. Mud filtrate for the base case consists of MC_{16}, EMUL, and water. The plots show simulations results obtained by performing separate perturbations of initial water saturation and flow rate of invasion. A low-resitivity annulus ensues when the OBM includes surfactants.

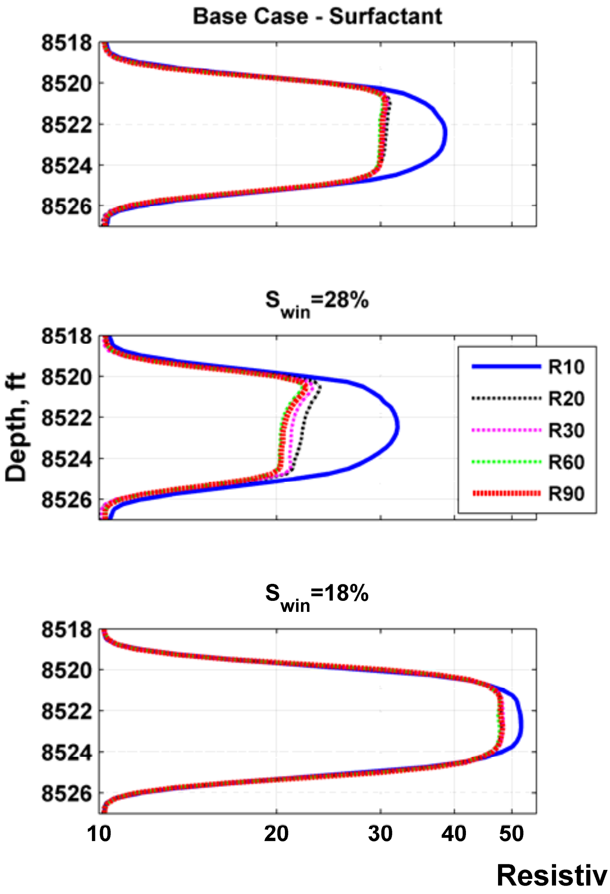

Figure 5.14: Sensitivity analysis of array-induction resistivity measurements to changes of initial water saturation and flow rate of invasion. Simulated AIT resistivity measurements for base Case No. 2 (with and without presence of surfactants) are compared to those obtained from the sensitivity analysis with a surfactant emulsifying the water in the OBM.

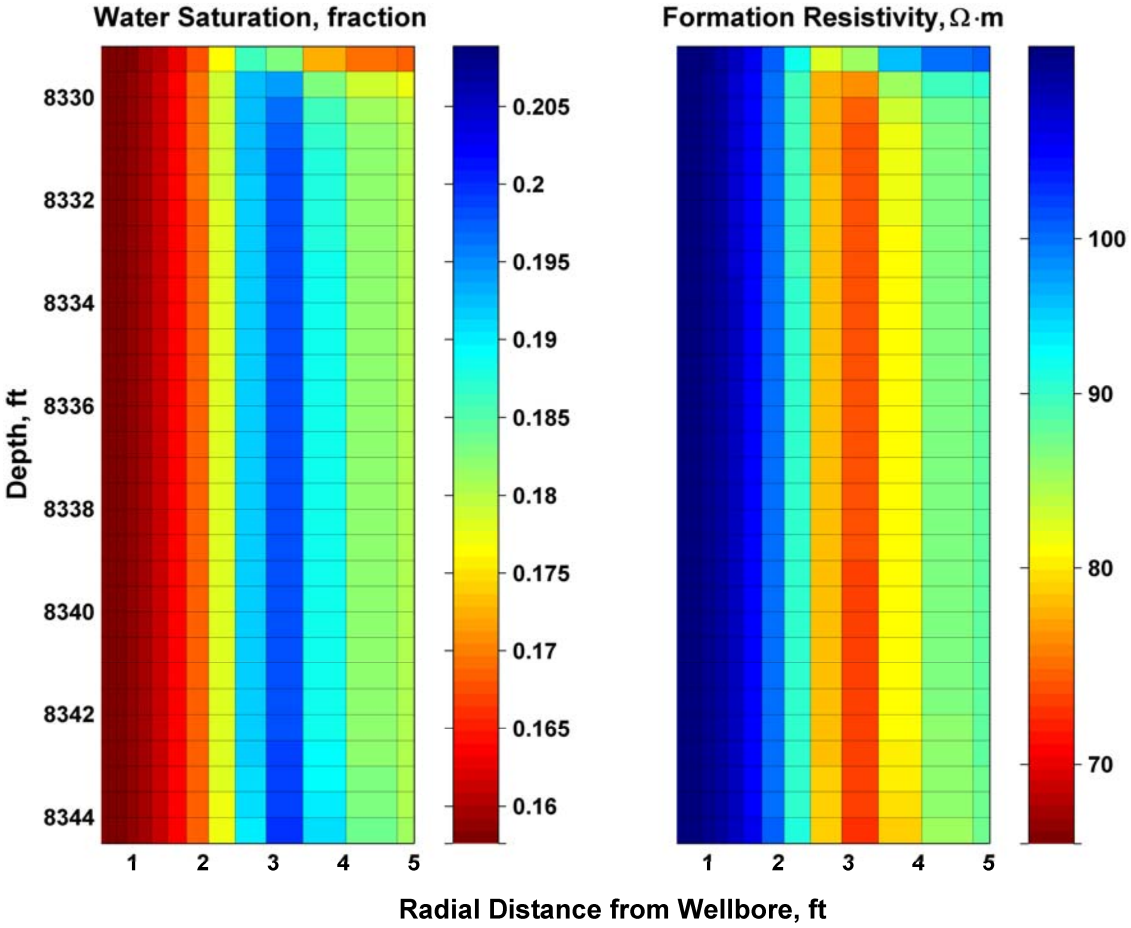

Figure 5.15: Spatial distributions (vertical and radial directions) of water saturation and electrical resistivity calculated after 60 hours of oil-base mud-filtrate invasion into a partially gas-saturated formation (Case No. 3). The flow rate of invasion was exaggerated to emphasize the low-resistivity annulus.

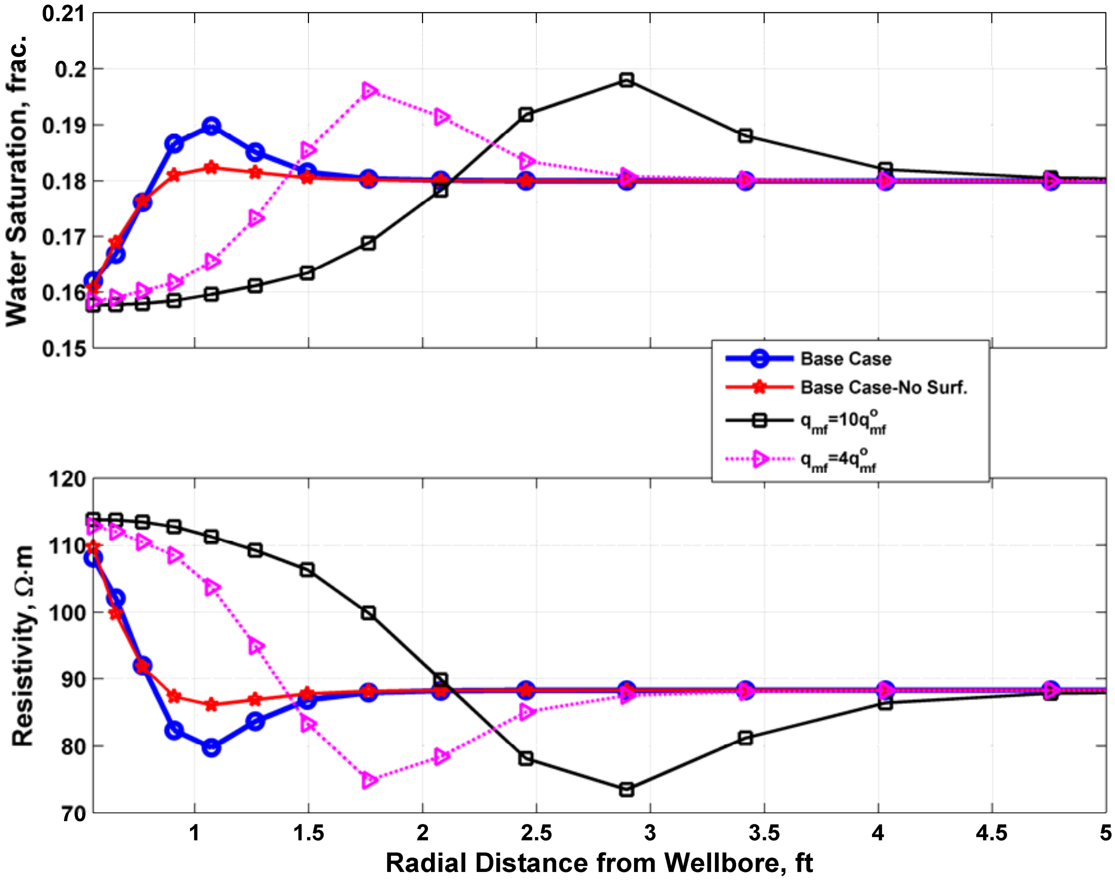

Figure 5.16: Radial distributions of water saturation and electrical resistivity obtained after 60 hours of invasion for Case No. 3. Mud filtrate for the base case consists of MC_{16}, EMUL, and water. The plots show simulation results obtained by performing separate perturbations of the flow rate of invasion. A low-resistivity annulus ensues when the OBM contains surfactants.

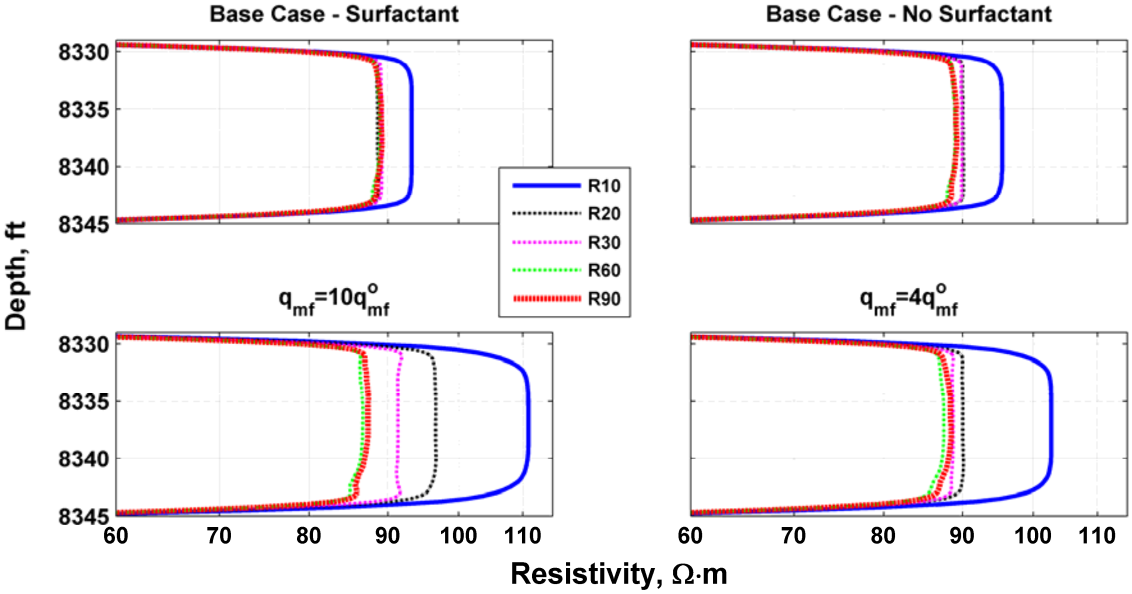

Figure 5.17: Sensitivity analysis of array-induction resistivity measurements to changes of flow rate of invasion. Simulated AIT resistivity measurements are compared to those obtained from the sensitivity analysis with a surfactant emulsifying the water in the OBM.

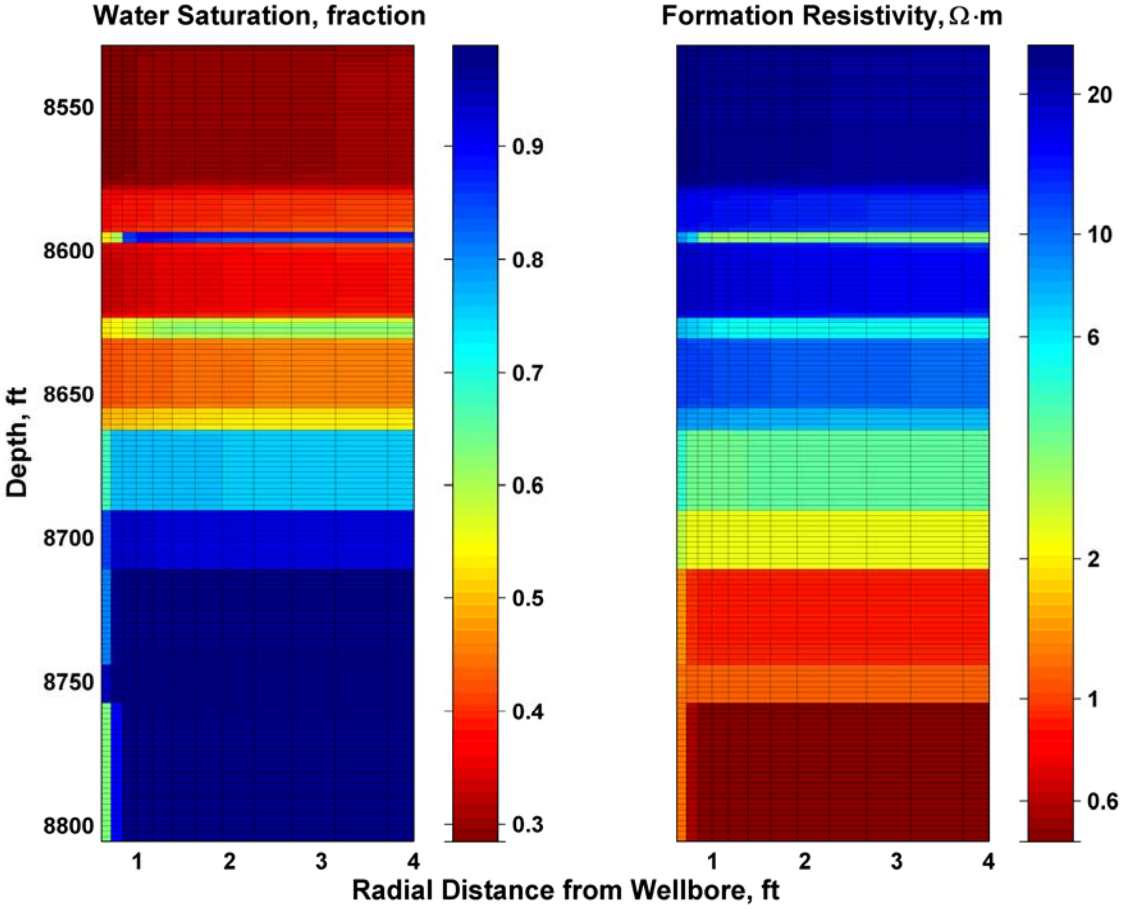

Figure 5.18: Spatial distributions (vertical and radial directions) of water saturation (left-hand panel) and electrical resistivity (right-hand panel) calculated after 60 hours of oil-base mud-filtrate invasion into a formation partially oil-saturated toward the top and fully water-saturated at the base. The spatial distributions of water saturation and electrical resistivity were constructed assuming a subsurface model that emphasizes vertical changes of resistivity within a capillary fluid transition zone toward the free water-oil contact.

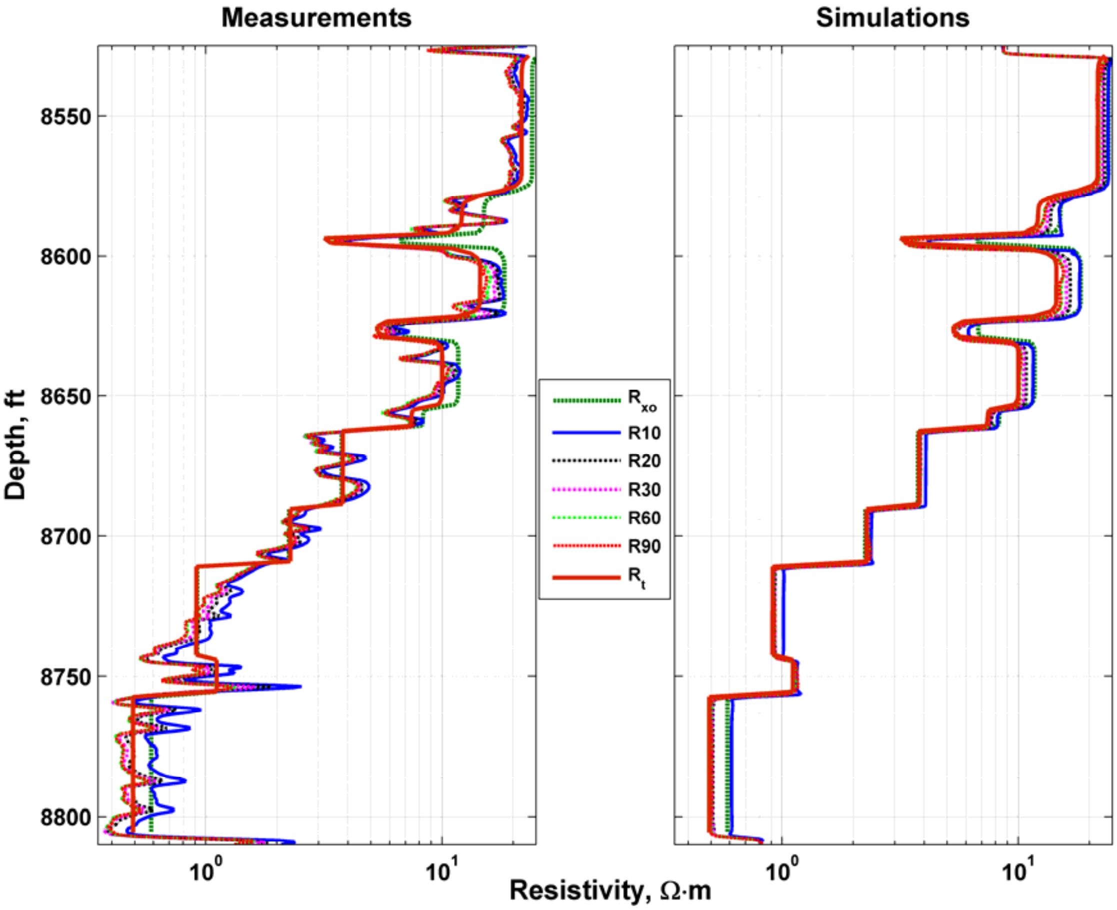

Figure 5.19: Measured 2-foot vertical resolution array-induction resistivity curves compared to their simulated values after resistivity matching performed by manually changing both flow rate of invasion and relative permeability. The panels show layer-dependent values of flushed-zone (R_{xo}) and virgin-zone resistivity (R_t) obtained from the simulation of OBM-filtrate invasion.

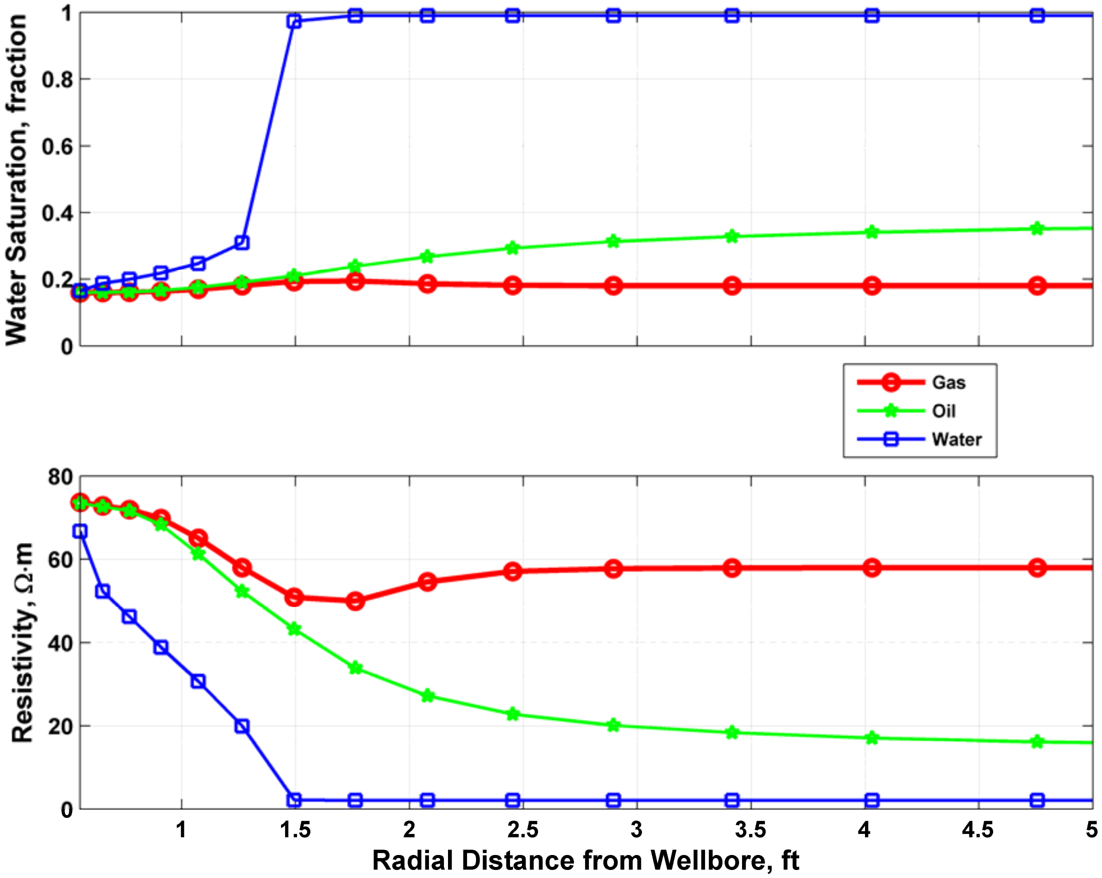

Figure 5.20: Radial distributions of water saturation and electrical resistivity obtained after 60 hours of invasion for three distinct fluids saturating a formation with the same petrophysical properties but different values of initial water saturation. Mud filtrate for the base case consists of MC_{16}, EMUL, and water. The plots show simulation results obtained by performing separate perturbations of the flow rate of invasion. A low-resistivity annulus ensues when the OBM includes surfactants and invades a formation with a low-viscosity saturating fluid.

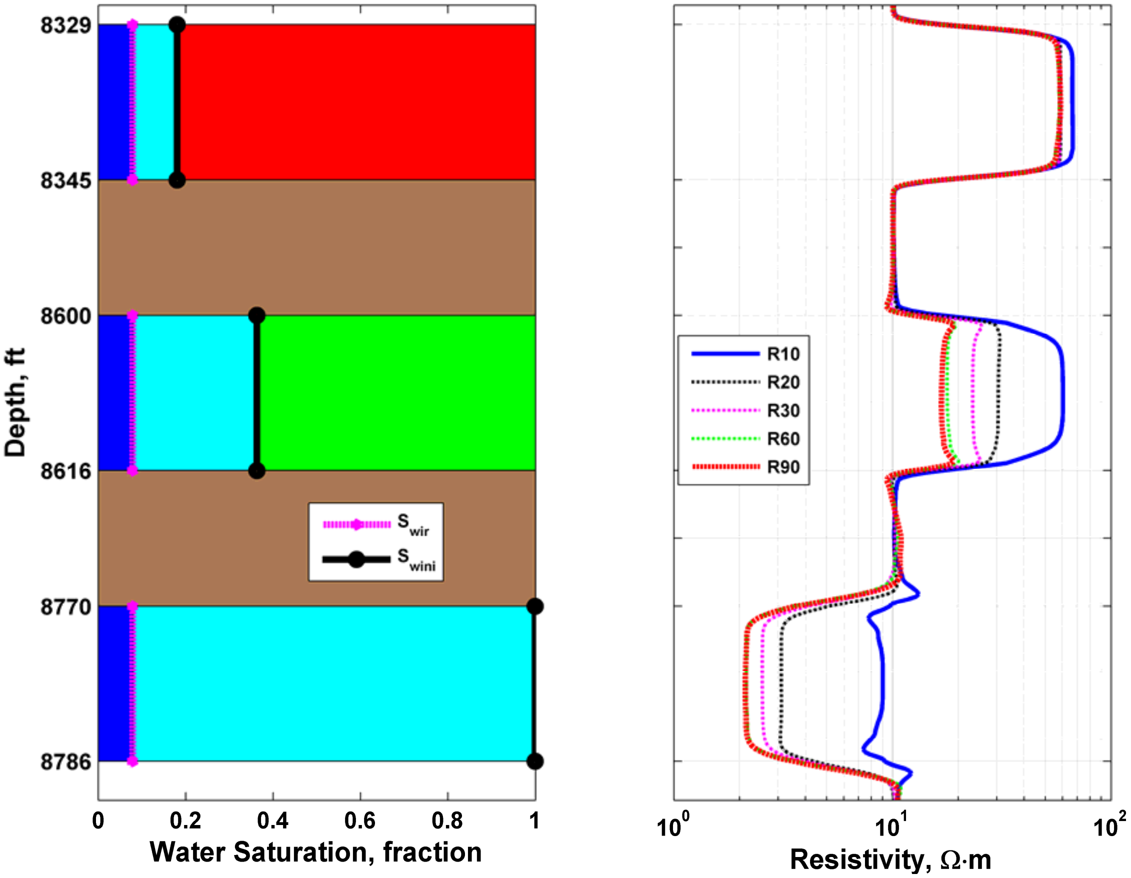

Figure 5.21: Simulated array-induction resistivity measurements across three distinct fluid zones in a clastic formation. The assumed OBM-filtrate includes an emulsifying surfactant. In the right-hand panel, brown blocks identify shale layers, whereas dark blue, light blue, green, and red identify irreducible water, movable water, oil, and gas zones, respectively.

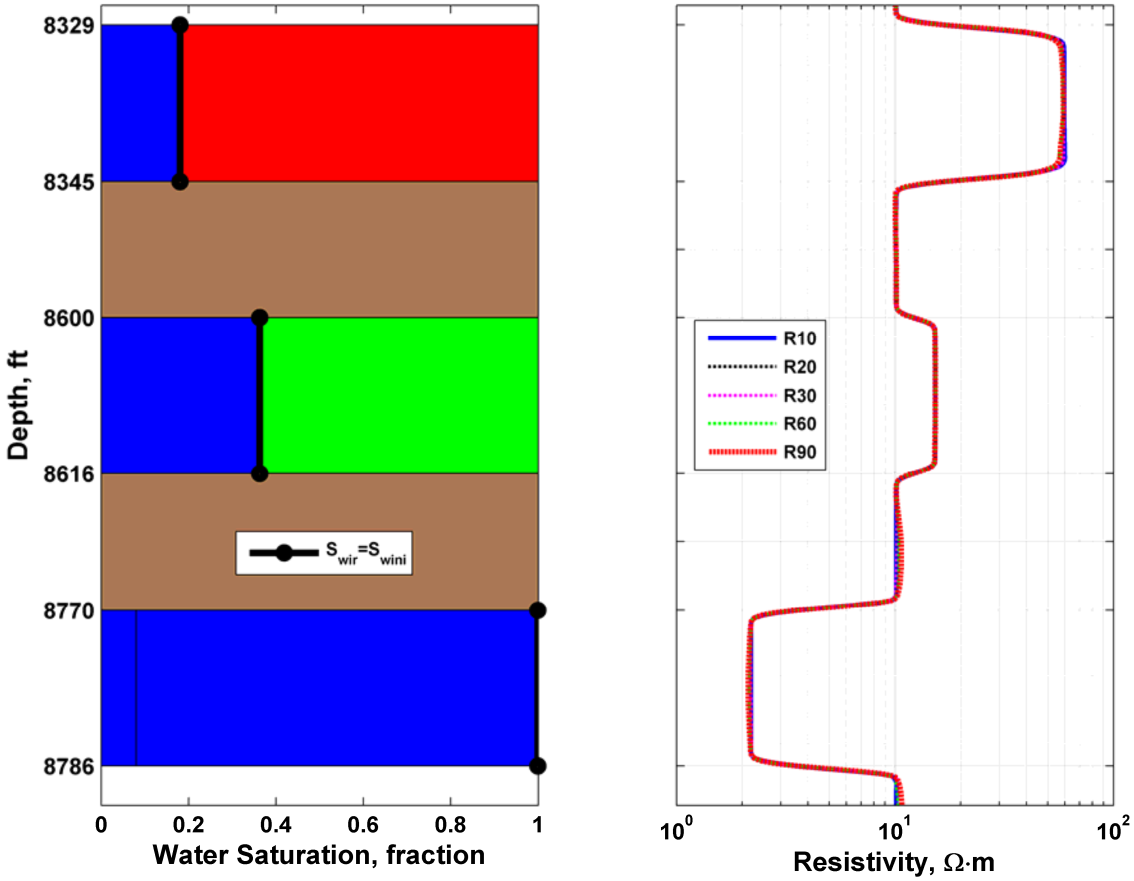

Figure 5.22: Simulated array-induction resistivity measurements across three distinct fluid zones in a clastic formation. This case assumes no invasion and irreducible water saturation conditions.

Chapter 6: Quantitative Comparison of the Processes of Oil- and Water-Base Mud-Filtrate Invasion and their Corresponding Effects on Borehole Resistivity Measurements

This chapter studies the effect of mud-filtrate on porous and permeable rocks assuming one-dimensional (1D) radial distributions of fluid saturation. Subsequently, borehole resististivity measurements acquired in the presence of oil-base mud (OBM) and water-base mud (WBM) are simulated from the radial distributions of electrical resistivity. In order to quantify the effect of mud-filtrate invasion on well logs it is necessary to accurately describe the time-dependent flow rate of invasion. In this chapter, we develop an algorithm to calculate a time-dependent flow rate of OBM-filtrate invasion by adapting the available formulation of the physics of WBM-filtrate invasion. This approach includes the dynamically coupled effects of mudcake growth and multi-phase filtrate invasion. In turn, the flow rate is calculated from both mud and formation properties. Numerical simulations are performed with a commercial adaptive-implicit compositional formulation that allows one to consider additional components of mud-filtrate and native fluids, including surfactants in the case of OBM and salt in the case of WBM.

6.1 INTRODUCTION

During the process of drilling wells for hydrocarbon production, the drilling fluid sustains a higher pressure than that of formation fluids (pore pressure), thereby resulting in radial pressure overbalance. In porous and permeable rocks, overbalance pressure is responsible for mud filtrate invading the rock near the wellbore. Solids contained in the mud deposit in the borehole wall thereby developing a mudcake, which decreases the volume of mud filtrate radially displacing in-situ fluids (water or hydrocarbons) away from the borehole wall (Dewan and Chenevert 1993 and 2001). Both mud and rock properties control the dynamic growth of mudcake and the time evolution of the process of invasion (Wu et al., 2004). The interplay between mud and formation properties occurs with both OBM and WBM, whereby the spatial distributions of fluids within the invaded formation affect measurements acquired with well-logging instruments, particularly resistivity measurements (La Vigne et al., 1997; George et al., 2004; Wu et al., 2004).

Borehole induction resistivity measurements are commonly acquired in the presence of OBM and fresh WBM. In the case of OBM, invading mud filtrate is miscible with formation oil. Such a fluid miscibility condition results in changes of fluid density and fluid viscosity, thereby altering the apparent oil-phase mobility in the near-wellbore region (Malik et al., 2007; Salazar et al., 2007). On the other hand, WBM-filtrate invasion accounts for the effect of salt mixing between mud filtrate and connate water, which often gives rise to a large resistivity contrast between the near-wellbore region and the undisturbed (virgin) zone (George et al., 2004). Therefore, it becomes imperative to accurately model the effect of OBM and WBM on the invasion process and, subsequently, on borehole resistivity measurements acquired some time after the onset of invasion.

Dewan and Chenevert (2001) performed laboratory experiments with WBM to study both mudcake buildup and mud-filtrate invasion. Wu et al. (2004 and 2005) numerically implemented the same theory and performed sensitivity analyses of both mudcake and rock properties to the time evolution of the flow rate of invasion and mudcake buildup. Warner and Rathmell (1997) performed laboratory experiments on rock-core samples invaded with OBM filtrate to determine the mechanism controlling the rate of filtration. They concluded that mudcake controls the pressure gradient between the mud and the rock sample, thereby controlling the radial length of invasion.

The objective of this chapter is to quantitatively compare the processes of OBM- and WBM-filtrate invasion. For that purpose, and without loss of generality, we focus our attention exclusively to the case of radial variations of fluid saturation and fluid properties while keeping porosity, permeability, relative permeability, and capillary pressure constant. Even though this approach does not account for the effect of gravity and permeability anisotropy it provides adequate physical reference to compare the effect of two types of muds on the time evolution of the process of invasion. To that end, we implement a 1D simulation method similar to that advanced by Wu et al. (2005) into a commercial multi-phase and multi-component reservoir simulator. This simulation method calculates the time evolution of the flow rate of mud-filtrate invasion and mudcake thickness for both OBM- and WBM-filtrate invasion and accounts for the effects of capillary pressure and relative permeability. The simulation of OBM-filtrate invasion also considers the mixing between invading and native oil when the latter is present (Malik et al., 2007) or else assumes immiscible fluid displacement in the presence of a water-bearing rock formation. Initially, OBM is considered as a single-component hydrocarbon and, subsequently, as an emulsion formed by oil, surfactants, and water (Bourgoyne Jr. et al., 1986) invading an oil-bearing sand. Alteration of wettability due to presence of surfactants in the OBM (Van, et al., 1988; Yan and Sharma, 1989) is simulated by changing both capillary pressure and relative permeability in response to changes of component concentration (Carlson, 2003). On the other hand, the immiscible fluid-displacement process associated with WBM-filtrate invading hydrocarbon-bearing sands includes the effect of salt mixing between filtrate and connate water.

For the purpose of illustration, the study focuses on a synthetic clastic formation invaded with either OBM or WBM filtrate for a set of assumed petrophysical and fluid properties. Comparative sensitivity analyses to mud and rock petrophysical properties for both OBM and WBM invasion allow us to quantify the influence of parameters affecting the time-dependent flow rate of invasion. We calculate radial distributions of water saturation assuming either transient, constant, or step flow rates to account for the effect of spurt loss at the onset of invasion. Finally, we simulate array-induction resistivity measurements from the radial distributions of resistivity in the presence of OBM- and WBM-filtrate invasion at different native fluid saturation conditions. The objective is to assess the influence of fluid and petrophysical properties on array-induction resistivity measurements for the two types of invasion processes. For the case of OBM filtrate invading the formation we assume cases of 100% water-saturated, partially oil-saturated, and partially gas-saturated conditions. In the case of WBM filtrate invading the formation we consider partially oil-saturated and partially gas-saturated conditions. Simulations of borehole induction resistivity measurements reveal different variability of apparent resistivity curves with multiple radial lengths of investigation for each case. These analyses shed insight to the petrophysical and fluid properties affecting the radial distribution of fluids in the near-wellbore region and provide a general quantitative framework for the interpretation of borehole electrical resistivity measurements.

6.2 NUMERICAL SIMULATION OF THE PROCESS OF MUD-FILTRATE INVASION

We approach the simulation of the process of mud-filtrate by assuming cylindrical coordinates with the origin at the center of a vertical borehole. Simulations enforce boundary source conditions on the wellbore with constant pressure to calculate the flow rate at each time step while simulating the process of invasion. Remaining vertical limits of the formation consist of impermeable zones with no-flow boundary conditions. The geometry used to simulate all the cases of study consists of a finite-differences grid with 51 nodes logarithmically spaced in the radial direction. Since the simulation is 1D, we assume a reservoir thickness equal to 1 foot. Moreover, we assume a wellbore with radius equal to 0.477 ft and a reservoir with external radius equal to 2000 ft. Figure 6.1 shows the 1D cylindrical grid used for the simulations considered in this chapter.

Simulations are performed with a commercial adaptive-implicit formulation simulator, known as STARS[8] (CMG, 2006). Because STARS is a three-phase multi-component fluid-flow simulator, the same software allows us to simulate invasion with both OBM and WBM filtrate into either water- or hydrocarbon-bearing rock formations. We assume that WBM filtrate and connate water constitute the aqueous phase and that they may include salt components. On the other hand, the OBM-filtrate is considered as a component of the oleic phase. Initially, the OBM consists of a single oil component with hydrocarbons in the range of C_{14} to C_{18} lumped into a single component, namely, MC_{16}. Subsequently, OBM is described as an emulsion of oil, surfactant, and water forming an oil phase. We assume a generic surfactant composed of a chain of 18 carbon atoms (La Scala *et al*., 2004; Lide, 2007), henceforth referred to as EMUL (Salazar *et al*., 2007). For the case of native oil, the latter is formed by hydrocarbons with pseudo-components in the range from C_1 to C_{18+}. Initially, we assume a single-phase native hydrocarbon lumped into a single-component, namely C_7C_{18}. For completeness, we also consider the case of an additional lighter hydrocarbon lumped into the pseudo-component C_4C_6 and a gas-bearing formation with the single component CH_4 invaded with WBM filtrate. Table 6.1 summarizes the critical properties of the surfactant and hydrocarbon pseudo-components assumed in the simulations of mud-filtrate invasion considered in this chapter.

6.3 CALCULATION OF THE FLOW RATE OF INVASION

In the process of OBM-filtrate invasion, the magnitude and time evolution of the flow rate of invasion (q_{mf}) remains uncertain. In general, static filtration governs the

---

[8] Mark of Computer Modeling Group

initial mudcake growth while the role of dynamic filtration is to limit the growth itself (Chin, 1995; Dewan and Chenevert, 2001). In this chapter, we assume that mudcake reaches a limiting thickness and that mudcake growth is dynamically coupled to the invasion model such that the growth rate is linked to the invasion front that continuously penetrates the rock formation displacing *in-situ* fluids.

The time evolution of both thickness of mudcake (h_{mc}) and flow rate of invasion depend on both mud properties and formation properties, such as permeability (k), porosity (ϕ), water saturation (S_w), capillary pressure (P_c), and relative permeability (k_{ri}). In turn, capillary pressure is a function of water saturation and is given by

$$P_c(S_w) = P_{nw} - P_w \, , \tag{6.1}$$

where P is pressure and the subscripts w and nw refer to wetting (water) and non-wetting (oil or gas) fluid phases, respectively. Dewan and Chenevert (2001) performed laboratory experiments of WBM filtrate invasion on rock samples and used Darcy's equation to describe the flow rate of invasion, namely,

$$q_{mf}\left(t\right) = \frac{k_{mc}(t)A}{\mu_{mf}}\left[\frac{P_m - P_{mc}(t)}{h_{mc}(t)}\right], \tag{6.2}$$

where t is time of invasion, k_{mc} is permeability of mudcake, A is the core's cross-sectional area, μ_{mf} is viscosity of filtrate, h_{mc} is thickness of mudcake, P_m is mud pressure, and P_{mc} is pressure across the mudcake. Permeability (k_{mc}) and porosity (ϕ_{mc}) of mudcake are given by (Dewan and Chenevert, 1993)

$$k_{mc}(t) = \frac{k_{mc0}}{P_{mc}^{\nu}(t)} \, , \tag{6.3}$$

and

$$\phi_{mc}(t) = \frac{\phi_{mc0}}{P_{mc}^{\delta \cdot \nu}(t)}, \tag{6.4}$$

respectively, where k_{mc0} is reference mudcake permeability defined at 1 psi differential pressure, ν is a "compressibility" exponent in the range of 0.4 to 0.9, ϕ_{mc0} is reference mudcake porosity, and δ is a multiplier in the range 0.1-0.2 based on porosity-permeability cross-plots for shaly sands. We calculate the flow rate of invasion assuming the radial 1D geometry described in Figure 6.1.

The flow rate of mud-filtrate invasion is calculated using the method advanced by Wu *et al*. (2005) that enforces mass balance for the total flow rate through the entire 1D model. Therefore, the inlet filtrate flow rate is dynamically coupled to the fluid flow in the invaded formation by the expression (Wu *et al*., 2005)

$$q_{mf}(t) = \frac{2\pi h\left[P_m - P_{mc}(t)\right]}{\displaystyle\sum_{i=2}^{N-1} \frac{\ln(r_{i+1}) - \ln(r_i)}{\left(\frac{k_{nw}}{\mu_{nw}}\right)_i \left(\frac{P_{c,i}(t) - P_{c,i+1}(t)}{P_{w,i}(t) - P_{w,i+1}(t)}\right) + \left(\frac{k_{nw}}{\mu_{nw}} + \frac{k_w}{\mu_w}\right)_i} + \frac{\mu_{mf}}{k_{mc}(t)} \ln\left(\frac{r_w}{r_{mc}(t)}\right)}, \tag{6.5}$$

where h is formation thickness, $P_{mc}(t) = P_{w,1}$ (t), r is radial distance away from the wellbore center, N is the number of radial gridblocks, k and μ are the permeability and viscosity of the fluid phases, respectively, r_w is wellbore radius, and r_{mc} is mudcake radius. If we assume that solid particles in the mud do not enter the formation, the time evolution of mudcake radius is given by (Chin, 1995; Wu *et al*, 2005)

$$\frac{dr_{mc}}{dt} = \frac{f_s}{(1 - f_s)[1 - \phi_{mc}(t)]} \frac{q_{mf}(t)}{2\pi h \cdot r_{mc}(t)}, \tag{6.6}$$

where f_s is mud solid fraction. The maximum flow rate of invasion occurs at $t = 0$, where $h_{mc} = 0$ ($h_{mc} = r_w - r_{mc}$) and hence $r_{mc} = r_w$. As mudcake builds up, h_{mc} monotonically increases and the flow rate decreases until reaching steady-state behavior once the mudcake has been completely formed. Equation (6.6) can be integrated numerically for each time step. However, for constant mudcake properties, equation (6.6) can be analytically solved and r_{mc} becomes a function of $\sqrt{t}$ (Wu *et al*., 2005).

The algorithm described above was implemented with an interface between MATLAB®[9] and STARS. Simulations begin by assuming constant pressure exerted by the mud at the borehole wall, which is in overbalance with the formation pore pressure. From STARS we obtain values of relative permeability, capillary pressure, and oil pressure as a function of water saturation at each gridblock and for each time step. In MATLAB®, equation (6.1) is used to calculate water pressure and equations (6.3) to (6.6) are solved at each time step to obtain both flow rate of invasion and mudcake thickness. We compared flow rates for WBM calculated with this method to those obtained with the University of Texas' Formation Evaluation Toolbox (UT-FET) (Ramírez *et al*., 2006). Results indicated a good agreement between the two calculations for times of invasion larger than 1 hour. At early times, the agreement varies between 80% and 90%, thereby confirming the reliability of our method.

6.4 CASES OF STUDY

We assess the flow rate of oil-base and water-base mud-filtrate invasion on a radially homogeneous synthetic clastic rock with porosity equal to 25%, permeability equal to 30 md, and irreducible water saturation equal to 8%. The assumed connate water in the formation has a high salt concentration (*[NaCl]*), equal to 160,000 ppm, which allows the use of Archie's (1942) equation to calculate resistivity from water saturation. We classify the base cases of study as follows:

---

[9] Mark of The MathWorks

- **Base Case OBM**, where the rock is assumed 100% water-saturated with null irreducible hydrocarbon saturation.
- **Base Case WBM**, with initial water saturation (S_{win}) of the rock equal to 30% and residual oil saturation equal to 10%.

The objective of the above assumptions is to compare the time evolution of flow rate of oil invading movable water to that of water invading movable oil assuming immiscible fluid-flow displacement. Simulations of mud-filtrate invasion begin by assuming typical properties of WBM (Dewan and Chenevert, 2001; Wu *et al.*, 2005) and OBM with null or low water saturation (Warner Jr. and Rathmell, 1997). For all the cases of study, the overbalance pressure is fixed at 350 psi. Moreover, we assume that (1) OBM consists of the lumped pseudo-component MC_{16}, (2) the WBM is fresh with salinity equal to 3,000 ppm, and (3) native oil consists of the lumped pseudo-component C_7C_{18}. Table 6.2 summarizes the mudcake and additional formation properties assumed in the simulation of mud-filtrate invasion.

6.4.1 Sensitivity Analysis

We apply the method described above to calculate the flow rate of invasion with OBM and WBM for the base case. Subsequently, we perform perturbations to the petrophysical properties of both rock and mudcake to assess their effect on the flow rate of invasion. The first step of the analysis consists of performing perturbations to formation properties (P_c, k_{ri}, k, ϕ, and S_{win}) whereas the last two step of analysis consider perturbations to mudcake petrophysical properties (k_{mc} and ϕ_{mc}).

6.4.1.1 Effect of Capillary Pressure and Relative Permeability

We assume a sandstone lithology represented by three rock types with different petrophysical properties as described in Table 6.3. Rock No. 1 represents a good-quality rock with large pore throat sizes, whereas Rock No. 3 corresponds to poor-quality tight rock. Rock No. 2 is a medium-quality rock and describes the base case that serves as reference in the sensitivity analysis. Capillary pressure curves are calculated using the Brooks-Corey (1966) model wherein we perform simultaneous changes of porosity-permeability (Leverett, 1941), irreducible water saturation, and values of exponents and coefficients involved in the equation. Moreover, we use the Brooks-Corey equations in their parametric form to calculate saturation-dependent relative permeability (Delshad and Pope, 1989). Relative permeability curves are modified by altering the values of residual fluid-saturation (wetting and non-wetting phases), end points, and exponents involved in the Brooks-Corey equation. Figure 6.2 describes the water-oil capillary pressure and relative permeability curves associated with the three rock types assumed in the analysis.

Figure 6.3 shows the calculated flow rate of invasion and mudcake thickness for the rocks under consideration. The shapes of the simulated curves are very similar for both cases OBM and WBM. Rock No. 1 (best quality) entails a very short spurt-loss[10] duration (<1 s) compared to the poorest-quality rock with a spurt-loss duration greater than 50 seconds. Moreover, mudcake thickens faster for the cases of Rocks No. 1 and No. 2 than for Rock No. 3. Finally, we observe that WBM entails higher flow rates of invasion and shorter mudcake buildup times than OBM.

6.4.1.2 Effect of Absolute Permeability and Porosity

We performed simulations for three values of absolute permeability, namely, 10 md, 30 md (Base Case), and 100 md. Capillary pressure and remaining petrophysical properties were kept the same as those of the base case. Figure 6.4 shows the effect of

---

[10] The instantaneous constant rate immediately after the onset of invasion.

permeability on both flow rate of invasion and mudcake thickness. As in the previous analysis, large permeability is an indication of a good-quality rock, and hence the results of this case are similar to those obtained in the previous case. In general, the flow rate of invasion for WBM filtrate is larger than that of OBM, while the time of mudcake buildup is shorter for WBM than for OBM. Additionally, we observe that the higher the permeability the shorter the spurt-loss time for both OBM and WBM. Individual perturbations of interconnected porosity (20%, 25%, and 30%) do not entail appreciable changes on the shape and magnitude of the flow rate of invasion. However, porosity does affect the radial length of invasion.

6.4.1.3 Effect of Initial Water Saturation

The importance of this analysis lies in the fact that initial water saturation (S_{win}) affects the values of capillary pressure at early times in the simulation. Since the OBM case is 100% water-saturated and the initial water saturation for the WBM case is equal to 30%, the analysis is slightly different in the two cases. Figure 6.5 displays the results from this sensitivity analysis. Variations of S_{win} only entail changes on both the maximum flow rate and the time of spurt loss (t_{SL}). When the rock is partially oil-saturated, low values of S_{win} are responsible for a larger maximum flow rate and shorter time of spurt loss compared to large values of S_{win}. Such behavior is identical for both OBM and WBM. Nonetheless, when oil invades a wet rock (Base Case OBM), the flow rate exhibits an anomalous behavior, similar to the case when the same formation exhibits S_{win} ≈25%. The latter situation can be due to the lack of miscibility of OBM with native fluids, with presence of water slowing down the process of invasion.

6.4.1.4 Effect of Mudcake Permeability and Porosity

Variations of mudcake properties entail amplitude and time variations of the flow rate of invasion and mudcake. We made independent perturbations of mudcake permeability (k_{mc}) and porosity (ϕ_{mc}) while keeping the maximum mudcake thickness constant. Figure 6.6 shows the results of this sensitivity analysis for three orders of magnitude of k_{mc}. The maximum flow rate remains constant regardless of the values of mudcake permeability. However, we observe that for large values of k_{mc} mudcake forms relatively fast and the flow rate of invasion reaches steady-state conditions faster than for low values of k_{mc}. Even though mudcake forms rapidly, the flow rate of invasion is larger and the time of spurt loss longer than for the case of low mudcake permeability. Therefore, the total volume (V_t) of invading fluid, $V_t = \int q(t) \cdot dt$, increases with increasing mudcake permeability. The effect of mudcake porosity on the flow rate of invasion and mudcake thickness is less obvious than that due to mudcake permeability. Figure 6.7 shows the time evolution of both flow rate of invasion and mudcake thickness for three values of mudcake porosity. Large values of ϕ_{mc} entail faster mudcake buildup and, in turn, slightly lower values of V_t than for low values of mudcake porosity. Additional mudcake properties affecting the flow rate of invasion are mud solid fraction, maximum mudcake thickness, and mudcake compressibility exponent. For muds containing a large solid fraction, mudcake builds up more rapidly due to the increasing speed of solid deposition (Wu et al., 2005), whereupon the total volume of invading fluid decreases. All the observations made for this analysis are equally valid for both OBM and WBM.

Tables 6.4 and 6.5 summarize the sensitivity analyses performed in this section for OBM and WBM, respectively. Such tables compare the duration of spurt loss, maximum rate of mud-filtrate invasion, and total volume of invading mud filtrate after 3 days of invasion. In general, the total volume of invading mud filtrate is larger for WBM than for OBM. The latter behavior implies that the process of OBM invasion into a rock formation subject to immiscible flow ($S_{win}=1$) is slower than for the case of WBM. In the following section we perform a more in-depth analysis of this latter behavior.

6.5 EFFECT OF THE FLOW RATE OF INVASION ON THE RADIAL DISTRIBUTIONS OF WATER SATURATION

Knowledge of the flow rate of invasion is necessary to assess the radial distribution of water saturation as a function of time. Simulations of mud-filtrate invasion can be performed using a time-variable flow rate $[q_{mf}(t)]$ as shown in Figures 6.3-6.7, with an average equivalent constant flow rate (q_{mfave}) (Wu *et al.*, 2004), or with an average equivalent step rate (q_{mfstep}) to account for the effect of instantaneous fluid loss at the onset of invasion (spurt loss). Such equivalent rates can be calculated with the equations

$$q_{mfave} = \frac{1}{t_2 - t_1} \int_{t_1}^{t_2} q(t) \cdot dt \,, \tag{6.7}$$

and

$$q_{mfstep} = \begin{cases} q_{mf}^{\max}, & t < t_{SL} \\ \dfrac{1}{t_2 - t_{SL}} \displaystyle\int_{t_{SL}}^{t_2} q(t) \cdot dt, & t \geq t_{SL} \end{cases}, \tag{6.8}$$

where $q_{mf}^{\max}$ is the maximum flow rate of invasion, and t_1 and t_2 are starting and ending times of invasion, respectively. The value of t_{SL} is assumed as the time when the flow rate reaches 90% of its maximum value and begins to monotonically decrease. In so doing, the time-dependent flow rate and those described by equations (6.7) and (6.8) account for approximately the same volume of accumulated invading fluid (water or oil) during the same period of time. Figure 6.8 shows the results of calculating the various flow rates of mud-filtrate invasion for the Base Case with both OBM and WBM. Additionally, we show the flow rate of invasion for the case of single-component OBM invading a partially oil-saturated (with pseudo-component C_7C_{18}) Base Case and the same case with surfactant (EMUL) and water emulsified in the OBM. In the case of emulsified OBM, molar fractions for each component in mud filtrate are equal to 0.1, 0.4, and 0.5 for water, EMUL, and MC_{16}, respectively. Surfactants contained in the OBM reduce the interfacial tension between oil and water (Skalli *et al*., 2006) and hence make the rock preferentially oil-wet (Van *et al*., 1988; Yan and Sharma 1989). As shown in Figure 6.9, such effects are accounted for by decreasing the capillary pressure (Salazar *et al*., 2007) and by changing the value of critical water saturation and end points on the relative permeability curves (Carlson, 2003). We observe that presence of surfactants in the OBM entail lower values of $q_{mf}^{\max}$ and steeper slopes in the time variations (compared to the cases of WBM or OBM with no surfactants) after the instantaneous rate has taken place. Table 6.1 describes the properties for each fluid component assumed in the simulation.

6.5.1 Effect of the Flow Rate of Invasion on Water Saturation

We simulated the processes of OBM- and WBM-filtrate invasion assuming the different modalities of flow rate described above, namely, constant, step, and time-variable. Figure 6.10 shows radial distributions of water saturation for the Base Case OBM (S_{win} = 100%) whereas Figures 6.11 and 6.12 show radial distributions of water saturation and salt concentration for the Base Case WBM (S_{win} = 30%), respectively. Such radial distributions were calculated with the previously defined flow rates after 0.5 hours, 2.35 hours, 1 day, and 3 days of mud-filtrate invasion, in that order. We observe that invasion with a constant or step rate yields the same radial distributions (S_w and *[NaCl]*) since the duration of the instantaneous rate is too fast to account for a large volume of invading fluid. The instantaneous fluid loss is 27 and 22 seconds for the OBM and WBM cases, respectively. When invading with a time-variable flow rate, we do observe a difference of 15% for the case of OBM (more oil) and 8% for the case of WBM (more water) in the shape of the radial distributions at late times (after 1 day of invasion). However, the total volume of fluids invading the formation is the same for constant, step, and variable rates, which causes the maximum radial length of invasion to be approximately the same for all cases. Based on this behavior, in the remaining examples of mud-filtrate invasion described below we assume a time-variable flow rate of invasion.

6.5.2 Effect of the Flow Rate of Invasion on the Radial Length of Invasion

Comparison of Figures 6.10 and 6.11 indicates that WBM filtrate entails radially deeper invasion than OBM filtrate. After 3 days of invasion, OBM-filtrate penetrates 2.65 ft radially into the formation whereas WBM-filtrate penetrates 3.68 ft, which is 39% deeper than for the case of OBM. At early times in the invasion process (< 12 hours) WBM filtrate penetrates 15% to 20% radially deeper than in the case of OBM filtrate. We emphasize that in performing this comparison we considered both cases as immiscible fluid-flow displacement. The same conclusion holds when considering mixing between OBM filtrate and native oil as is shown in the next section.

6.6 EFFECT OF THE FLOW RATE OF INVASION ON THE RADIAL DISTRIBUTIONS OF ELECTRICAL RESISTIVITY

We calculate radial distributions of electrical resistivity from the radial distributions of water saturation obtained from the numerical simulation of mud-filtrate invasion. Because we assume shale-free sandstones with high salt concentration in the connate water (160,000 ppm), Archie's (1942) equation is a good approximation to calculate resistivity, namely,

$$\frac{1}{R_t(r)} = S_w{}^n(r) \cdot \frac{\phi^m}{a \cdot R_w(r)},$$

where R_t is true formation resistivity, R_w is connate water resistivity, $m=2$ and $n=2$ are Archie's cementation and saturation exponents, respectively, and $a=1$ is the tortuosity factor. For the case of OBM-filtrate invasion, R_w is assumed radially constant in the formation. On the other hand, when WBM filtrate invades the rock, it mixes with formation water, whereby salt concentration fluctuates radially between that of mud-filtrate (3,000 ppm) and that of connate water. Moreover, R_w can be calculated as a function of temperature (T) and salt concentration using the equation advanced by Bigelow (1992) and Hallemburg (1998),

$$R_W(r) = \left[0.0123 + \frac{3647.5}{\left([NaCl]\right)^{0.955}} \right] \cdot \left[\frac{81.77}{T + 6.77} \right],$$

where $[NaCl]$ is salt concentration in parts per million (ppm) and T is formation temperature in ^{o}F.

6.6.1 Modeling of Borehole Resistivity Measurements

Calculated radial distributions of electrical resistivity are used to simulate array-induction resistivity measurements (AIT[11]). The objective is to quantify the relative variability of apparent resistivity measurements that exhibit multiple radial lengths of investigation (R10, R20, R30, R60, and R90). We emphasize that although the invasion modeling entails only radial variations of electrical resistivity the simulation of borehole resistivity measurements does include the presence of the borehole. We assume a vertically homogeneous formation to avoid shoulder bed effects, and focus our attention to the variations of apparent resistivity for the various radial lengths of investigation. The

---

[11] Mark of Schlumberger

simulation of AIT is performed with the Numerical-Mode Matching Method (NMM) (Chew *et al*., 1984; Zhang *et al*., 1999).

6.6.1.1 Resistivity Modeling in the Presence of OBM: Water and Oil

We modeled four different cases of OBM-filtrate invading Rock No. 2 (Base Case) assuming immiscible, binary, and multi-component fluid-flow, namely,

Case (a): Single-component (MC_{16}) OBM invading a 100% water-saturated rock formation (immiscible fluid displacement). Native fluid is only water.

Case (b): Single-component (MC_{16}) OBM invading a 70% partially oil-saturated rock formation (binary miscible fluid-flow). Native fluids are water (irreducible and movable) and single-component oil (C_7C_{18}).

Case (c): Multi-component OBM (MC_{16}, EMUL, and water) invading a 70% partially oil-saturated rock formation. Native fluids are water (irreducible and movable) and single-component oil (C_7C_{18}).

Case (d): Multi-component OBM (MC_{16}, EMUL, and water) invading a 70% partially oil-saturated rock formation. Native fluids are water (irreducible and movable), and multi-component oil (C_4C_6 and C_7C_{18}) constituting a very light fluid.

We used the time-dependent flow rates described in Figure 6.8 to simulate the radial distribution of water saturation shown in Figure 6.13 after 3 days of OBM-filtrate invasion for the cases of study described above. Figure 6.14 shows the corresponding radial distributions of electrical resistivity for each case. We observe that Case (a) exhibits the largest difference between flushed- and virgin-zone resistivities due to the large amount of movable water displaced by the OBM filtrate thereby entailing a radial length of invasion equal to 2.65 ft. By contrast, the radial length of invasion is approximately equal to 2 ft for Cases (b) and (c), and 2.25 ft for Case (d). However, the low amount of movable water together with the mixing between OBM filtrate and native oil is responsible for the relatively small difference between flushed- and virgin-zone resistivities for the partially oil-saturated cases. Moreover, presence of surfactants causes a large viscosity contrast between filtrate and native oil, which results in a water bank near the wellbore. Such a water bank is responsible for the presence of a low resistivity annulus in the invaded zone. The annulus is only remarkable for Case (d) because that case involves the largest viscosity contrast between native oil and OBM. Figure 6.15 shows the corresponding simulated AIT measurements for Case (a), whereas Figure 6.16 compares the simulated AIT resistivity measurements for Cases (b), (c), and (d). In similarity with the corresponding radial distributions of electrical resistivity, Case (a) exhibits the largest variability of apparent resistivity for all the cases, where the relative difference between R10 and R90 is approximately one order of magnitude. Presence of surfactants in the OBM (Cases (c) and (d)) entails higher resistivity values in the flushed-zone than for the case of single-component OBM, as indicated by the shallowest-sensing apparent resistivity curves. Even though initial water saturation is constant in Cases (b), (c), and (d), presence of different components in both OBM (surfactants) and formation oil (light hydrocarbons) causes different resistivity readings in the invaded zone as indicated by the shallow- and intermediate-sensing apparent resistivity curves (R20, R30, and R60). Moreover, the reading of R60 below R90 in Case (d) is due to the presence of the annulus observed on the radial distribution of electrical resistivity.

6.6.1.2 Resistivity Modeling in the Presence of OBM: Water and Gas

For completeness, we modeled two additional cases of OBM-filtrate invading Rock No. 2 (Base Case) partially gas-saturated assuming a binary miscible fluid-flow, namely,

Case (e): Movable water, single-component (MC_{16}) OBM invading a 70% partially gas-saturated rock formation. Native fluids are water (irreducible and movable) and single-component gas (CH_4).

Case (f): Irreducible water, single-component (MC_{16}) OBM invading a 70% partially gas-saturated rock. Native fluids are irreducible water and single component gas (CH_4).

We calculated the radial distribution of water saturation using time-dependent flow rates of OBM-filtrate invasion. Such distributions are shown in Figure 6.17 after 3 days of OBM-filtrate invasion for Cases (e) and (f) and compared to the partially oil-saturated Case (b). Water saturation in the movable water case shows variability up to 2.3 ft in the formation, which is consistent with Case (b). The bottom panels of Figure 6.17 show the radial distributions of gas and oil saturation, where we observe that the gas is fully flushed in the movable water case and partially removed in the irreducible water case. Between the radial distances of 0.75 ft and 2.3 ft, the three phases (water, oil, and gas) coexist. Figure 6.18 shows the corresponding radial distributions of electrical resistivity for each case. We observe that the electrical resistivity for Case (e) is approximately equal to 4.5 Ω·m near the borehole wall and slowly decreases to 3.4 Ω·m around 0.75 ft, while exhibiting another reduction below 3.4 Ω·m between the radial distances of 1.6 ft and 2.3 ft. Irreducible water saturation is only altered near the borehole wall due to the effect of overbalance pressure and remains constant away from the borehole. We observe that Case (b) exhibits the largest difference between flushed- and virgin-zone resistivities monotonically decreasing from 6.2 Ω·m on the borehole wall to 3.4 Ω·m in the virgin zone with a radial length of invasion less than 2 ft. Figure 6.19 compares the simulated array-induction resistivity curves for Cases (e) and (f). The case with movable water entails radial variability of apparent resistivity curves with a difference of only 0.3 Ω·m between shallowest- and deepest-sensing curves with marginal variability between the intermediate- and deepest-sensing curves. Even though water saturation in the case of irreducible water is practically constant in the radial direction, the reduction of resistivity near the wellbore causes variations of the apparent resistivity curves in the order of 0.15 Ω·m between shallowest- and deepest-sensing curves. The latter situation is consistent with previously published field cases that report R10 reading higher than R90 in zones remaining at irreducible water saturation (La Vigne *et al*., 1997). As expected, Figure 6.19 also indicates a complete overlap between the shallowest- and deepest-sensing curves for Case (f).

6.6.1.3 Resistivity Modeling in the Presence of WBM

We modeled two different cases of WBM filtrate invading Rock No. 2 (Base Case) assuming immiscible fluid-flow displacement, namely,

- WBM-filtrate invading a 70% partially gas-saturated rock formation. Native fluids are water (irreducible and movable) and single-component gas (CH_4).
- WBM-filtrate invading a 70% partially oil-saturated rock formation. Native fluids are water (irreducible and movable) and single-component oil (C_7C_{18}).

We calculate time-dependent WBM-filtrate flow rates of invasion for each case to simulate invasion with fresh WBM-filtrate into Rock No. 2 (Base Case) during 3 days. Figure 6.20 shows that, at early times, the flow-rate for the gas case is two orders of magnitude larger than that associated with the oil case. Furthermore, the relatively high mobility of formation fluid causes the spurt-loss time to become negligible for the case of native gas. As indicated in Table 6.2, the salt concentration of mud-filtrate is equal to 3,000 ppm, whereas the salt concentration of connate water is approximately 160,000 ppm. The latter situation is responsible for a large salinity contrast in the radial direction, which in turn has a strong effect on the radial distribution of electrical resistivity. Figures 6.21 and 6.22 show the radial distributions of water saturation and salt concentration for each case obtained after 3 days of WBM-filtrate invasion. Radial distributions of water saturation indicate that the movable gas is completely removed by mud filtrate in the near-wellbore region. By contrast, movable oil is partially removed by mud filtrate and the radial distributions are smoother than those simulated for the gas case. This behavior indicates that oil moves slower than gas during the process of invasion and the effects of capillary pressure in the water-oil system are more remarkable than in the water-gas system. We use radial distribution of water saturation and salt concentration to calculate the radial distributions of electrical resistivity after 3 days of WBM-filtrate invasion. Figure 6.23 compares radial distributions of electrical resistivity calculated for the gas- and oil-bearing formations. The latter radial distributions indicate that the invasion front penetrates radially deeper into the formation than in the case of OBM filtrate even though the petrophysical properties remain identical. The large contrast of salt concentration causes a large difference between flushed- and virgin-zone resistivities, whereupon a low resistivity annulus ensues in the invaded zone. The annulus associated with the gas case exhibits a lower resistivity than for the case of native oil. Moreover, the radial distributions of electrical resistivity calculated for the gas case show constant resistivity in the flushed zone due to full displacement of free gas by mud filtrate, which is not observed in the oil case. Finally, we simulated the corresponding array-induction resistivity measurements described in Figure 6.24. Simulated apparent resistivities exhibit a large separation between the deepest- and shallowest-sensing curves in response to the large resistivity contrast between flushed and invaded zones. In addition, presence of the resistivity annulus has a strong effect on the R20 R30, and R60 curves, which read lower resistivity values than R90 in both cases of native gas and native oil. The latter behavior is more emphasized in the gas case than in the oil case.

6.7 SUMMARY AND CONCLUSIONS

We adapted the well-known physics of water-base mud-filtrate invasion to calculate the flow rate of oil-base mud-filtrate invasion using a commercial implicit compositional simulator. Our method considered the interplay between mud and formation properties to calculate a time-dependent flow rate that accounted for mudcake buildup, capillary pressure, and relative permeability. From the various cases considered in the sensitivity analysis we observed that flow rates associated with WBM-filtrate invasion are 20%-40% higher than those associated with OBM-filtrate invasion. We conclude that rock formations that exhibit large pore throats and low capillary pressure entail high flow rates and rapid spurt loss. On the other hand, rock formations that exhibit small pore throats and large capillary pressure entailed instantaneous flow rates of invasion 100 to 200 times larger than those associated with best quality rocks thereby slowing down the process of mudcake buildup and entailing radially deeper invasion. Furthermore, mudcake permeability remained as the main parameter controlling the process of mudcake buildup and hence the total volume of fluid invading the formation. It was observed that the maximum flow rate of invasion was not affected by changes of mudcake permeability.

Simulations showed that using an integrated average flow rate of invasion is equivalent to assuming an average step rate that accounts for fluid spurt losses. The high constant flow rate of invasion (spurt loss) observed at the onset of invasion lasted between 1/4 and 550 seconds, which is negligible compared to the total time of invasion. Nonetheless, when using a time-dependent flow rate of invasion we found a difference of 15% (OBM) and 8% (WBM) on the corresponding radial profiles of fluid saturation compared to assuming either constant or step rates. Radial distributions of fluid saturation indicated that WBM entailed radial lengths of invasion 15%-20% (early times) larger and approximately 40% (late times) radially deeper than those associated with OBM-filtrate invasion. This behavior is the result of large flow rates of invasion associated with WBM compared to those associated with OBM and it indicates that mixing between OBM filtrate and native oil slows down the process of invasion. In turn, the variability of fluid saturation in the invaded zone significantly affected the radial distribution of electrical resistivity.

Array-induction resistivity measurements simulated from the radial distributions of electrical resistivity are largely affected by the invading fluids near the wellbore. In the case of OBM-filtrate invading a wet zone, we observed a large separation between apparent resistivity curves, similar to that observed for the case of WBM filtrate invading a movable hydrocarbon-saturated zone. Alterations of wettability due to presence of surfactants in the mud increased the contrast between flushed- and virgin-zone resistivities for the cases of OBM-filtrate invading a partially oil-saturated rock formation. Presence of surfactants in the OBM altered both the shape of the flow rate of invasion as well as the radial distributions of electrical resistivity, thereby affecting the response of array-induction resistivity measurements. The large viscosity contrast between native oil and emulsified OBM resulted in a water bank, which formed a low resistivity annulus in the invaded zone. Such an annulus was remarkable when native oil consisted of very light liquid hydrocarbon components (μ_o<0.25 cp). Both capillary pressure and relative permeability governed the shape and contrast of the radial distribution of electrical resistivity in the invaded zone. Simulations of both OBM-WBM-filtrate invasion into gas-bearing formations indicated that the effect of capillary pressure on the radial distributions of electrical resistivity was more remarkable in oil-bearing than in gas-bearing formations.

Sensitivity analyses to mud and rock properties described in this chapter shed insight to the character of fluid distributions near the wellbore resulted from OBM- and WBM-filtrate invasion. Simulation of the process of invasion for three different rock types confirmed the reliability of our simulation method to assess the effect of invasion on borehole resistivity measurements. These simulations can be used to improve the petrophysical interpretation of other logging measurements, including those acquired with nuclear and sonic tools.

Table 6.1: Summary of assumed PVT properties for both in-situ hydrocarbon components and mud filtrate.

Property	**Units**	**C_7C_{18}**	**C_4C_6**	**CH_4**	**EMUL**	**MC_{16}**
Critical Temperature	^oF	656.2	359.8	-125.7	986.7	822.5
Critical Pressure	psi	322.2	498.2	653.3	188.6	240.2
Mass Density	lb/ft^3	40.2	12.06	1.05	59.9	45.7
Molar Weight	lb-mol	132.8	67.73	16.6	284.5	222
Viscosity	cp	1.0	0.105	0.025	20	1.5

Table 6.2: Summary of mudcake, fluid, and formation properties assumed in the simulation of the process of mud-filtrate invasion.

Variable	**Units**	**Value**
Mudcake reference permeability	md	0.03
Mudcake maximum thickness	inches	0.40
Mudcake reference porosity	fraction	0.25
Mud solid fraction	fraction	0.06
Mudcake compressibility exponent	fraction	0.40
Mudcake exponent multiplier	fraction	0.10
Filtrate salt concentration (WBM)	ppm	3,000
Formation salt concentration	ppm	160,000
Mud hydrostatic pressure	psi	4,000
Initial formation pressure	psi	3,650
Wellbore radius	ft	0.477
Formation outer boundary	ft	2000
Maximum invasion time	days	3.00
Formation and fluid temperature	^oF	213
Residual hydrocarbon saturation (oil or gas)	fraction	0.10

Table 6.3: Summary of petrophysical properties of the rock types considered in the sensitivity analysis of capillary pressure and relative permeability.

Property	**Units**	**Rock 1**	**Rock 2**	**Rock 3**
Irreducible water saturation	fraction	0.04	0.08	0.15
Effective porosity	fraction	0.30	0.25	0.15
Absolute Permeability	md	300	30	3

Table 6.4: Results of the sensitivity analysis of the flow rate of invasion of OBM-filtrate invading a 1-foot-thick clastic formation. Time of spurt loss (t_{SL}), maximum flow rate of invasion (q_{mf}^{max}), and the total volume of mud-filtrate (V_t) injected after 3 days of invasion for all cases are compared to the base case (BC).

Sensitivity to	*Value*	t_{SL} *[s]*	q_{mf}^{max} *[ft^3/d] @ t → 0*	V_t *[ft^3] (3 days)*
Rock Type	1	1/4	156.4	1.819
	2 (BC)	27	15.7	1.752
	3	55	1.6	1.258
k [md]	100	3	52.3	1.802
	10	137	5.2	1.623
S_{win} *[fraction]*	0.60	217	6.6	1.685
	0.30	22	20.8	1.774
	0.15	5	40.3	1.797
k_{mc} *[md]*	0.300	217	15.7	9.630
	0.060	43	15.7	2.796
	0.010	9	15.7	0.994
	0.003	3	15.7	0.550
ϕ_{mc} *[md]*	0.50	17	15.7	1.595
	0.15	27	15.7	1.819

Table 6.5: Results of the sensitivity analysis of the flow rate of WBM-filtrate invading a 1-foot-thick clastic formation. Time of spurt loss (t_{SL}), maximum flow rate of invasion (q_{mf}^{max}), and total volume of mud-filtrate (V_t) injected after 3 days of invasion for all cases are compared to the base case (BC).

Sensitivity to	*Value*	t_{SL} *[s]*	q_{mf}^{max} *[ft³/d] @ t → 0*	V_t *[ft³] (3 days)*
Rock Type	1	1/2	134.4	2.39
	2 (BC)	22	20.8	2.31
	3	55	3.3	1.80
k *[md]*	100	2	67.9	2.38
	10	109	6.7	2.12
S_{win} *[fraction]*	0.60	217	6.2	2.14
	0.08	3	52.7	2.35
k_{mc} *[md]*	0.300	172	20.8	13.48
	0.060	43	20.8	3.85
	0.010	7	20.8	1.22
	0.003	2	20.8	0.68
ϕ_{mc} *[md]*	0.50	14	20.8	2.14
	0.15	22	20.8	2.37

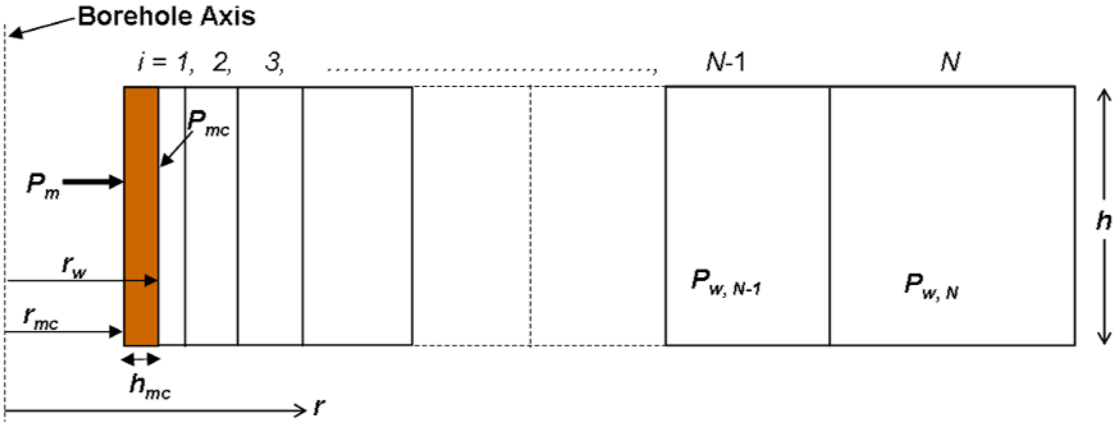

Figure 6.1: Finite-difference radial grid used in the numerical simulations. The shaded region in the borehole wall corresponds to mudcake formed during the process of mud-filtrate invasion. Variable N designates the number of gridblocks, P_m, P_w, and P_{mc} are mud, water, and pressure across the mudcake, respectively, r_w and r_{mc} are wellbore and mudcake radius, respectively, and h_{mc} is mudcake thickness.

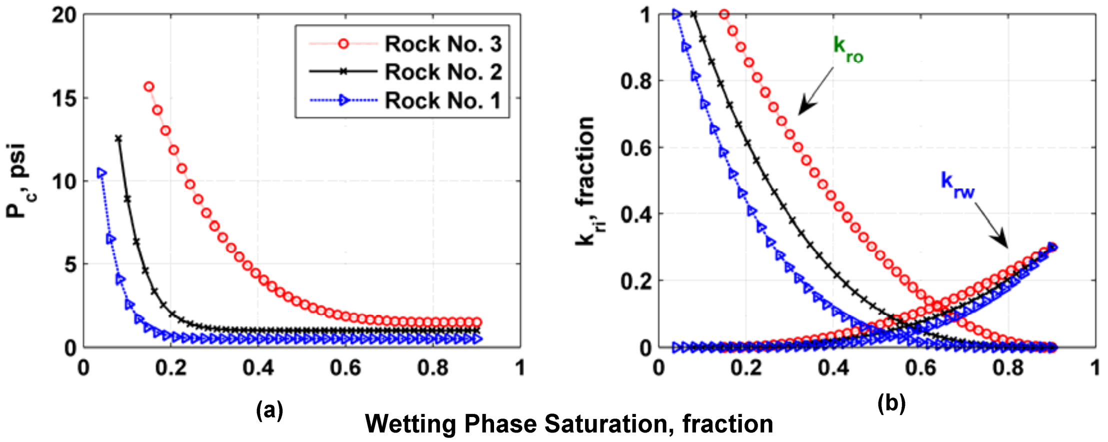

Figure 6.2: Water-oil capillary pressure (panel (a)) and relative permeability (panel (b)) curves assumed for the three different rock types in the simulations of mud-filtrate invasion. Rock No. 2 corresponds to the base case. Different entry pressures are assumed for each rock whereas residual non-wetting phase saturation is assumed equal to zero when the formation is 100% water-saturated. Variables k_{ro} and k_{rw} designate the relative permeabilities of oil and water, respectively.

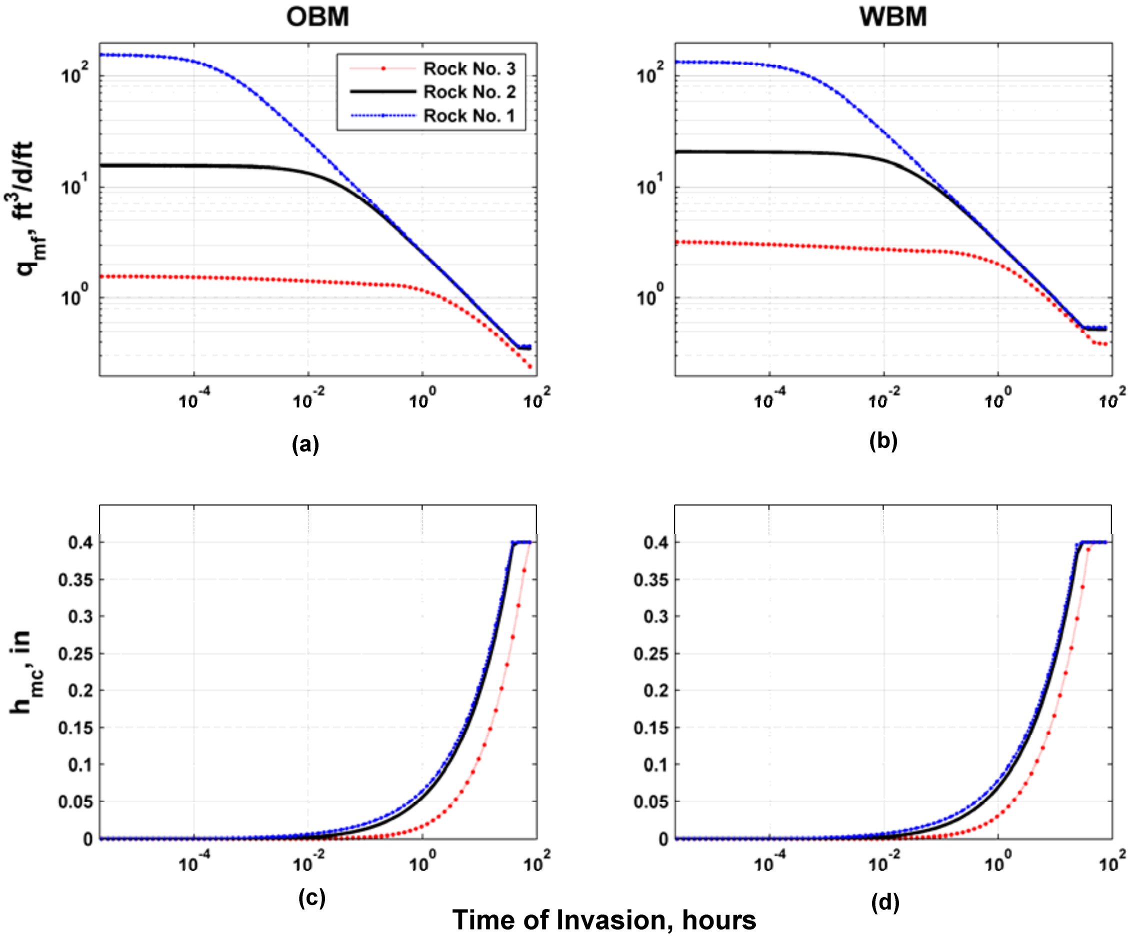

Figure 6.3: Sensitivity of the processes of OBM- and WBM-filtrate invasion to capillary pressure and relative permeability. Black solid curves identify the base cases (Rock No. 2). Panels (a) and (b) describe the time evolution of the flow rate of invasion whereas panels (c) and (d) describe the mudcake thickness as a function of time of invasion.

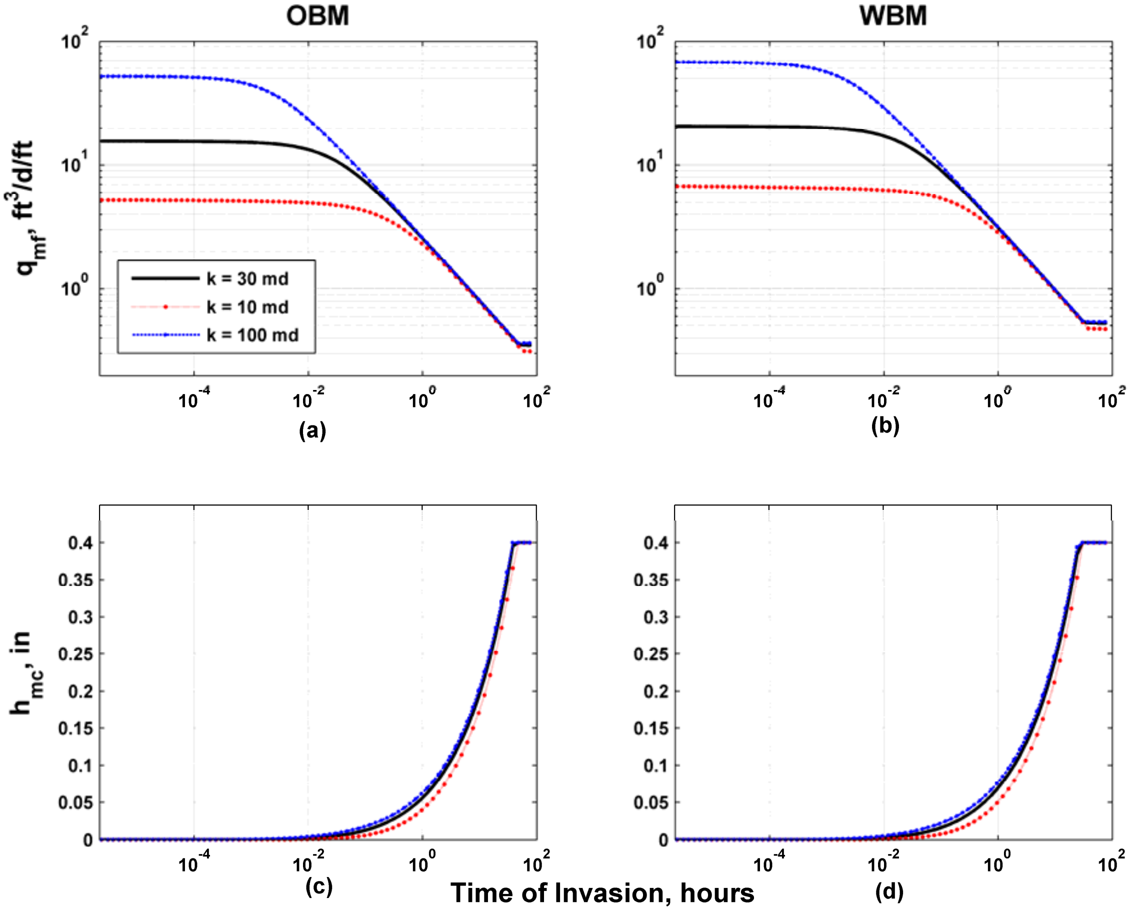

Figure 6.4: Sensitivity of the processes of OBM- and WBM-filtrate invasion to formation permeability (k). Black solid curves identify the base cases (k=30 md). Panels (a) and (b) describe the time evolution of the flow rate of invasion whereas panels (c) and (d) describe the mudcake thickness as a function of time of invasion.

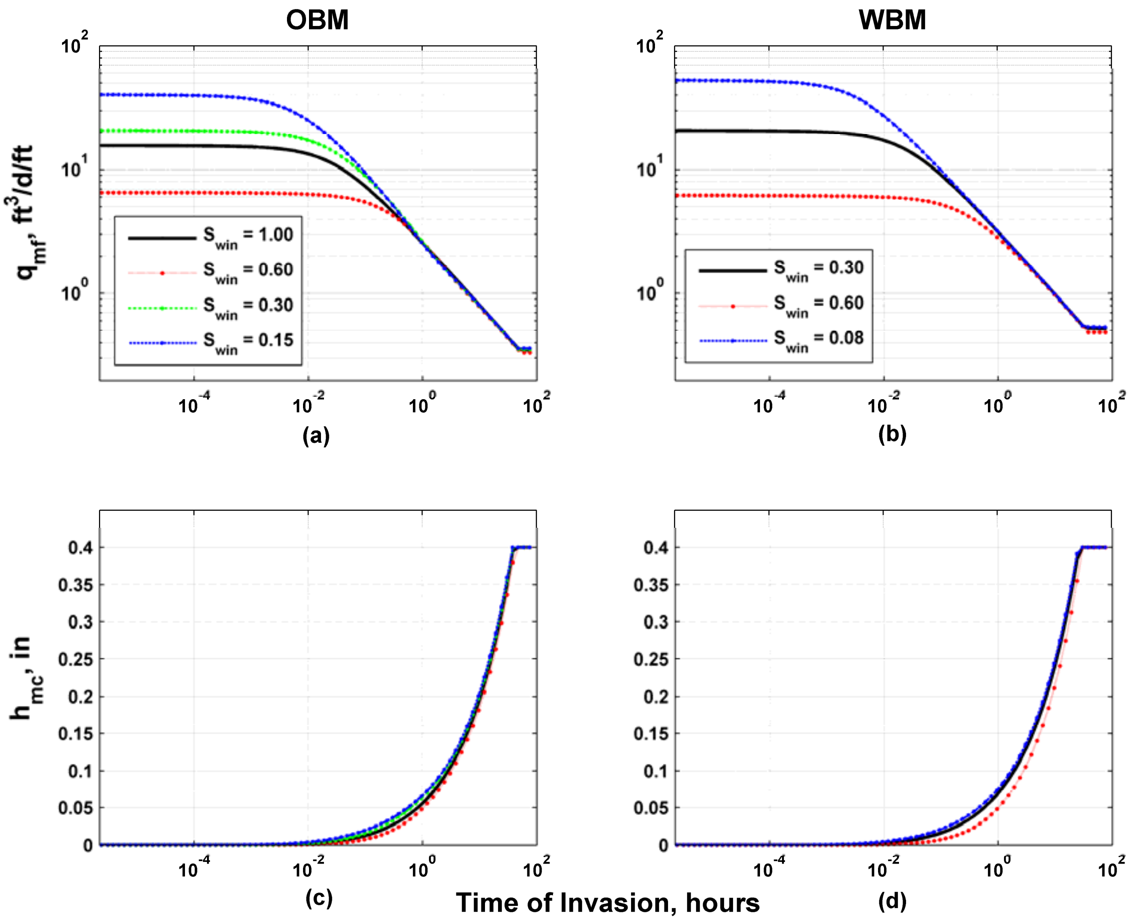

Figure 6.5: Sensitivity of the processes of OBM- and WBM-filtrate invasion to initial water saturation (S_{win}). Black solid curves identify the base cases (S_{win}=1.0 for OBM and S_{win}=0.3 for WBM). Panels (a) and (b) describe the time evolution of the flow rate of invasion whereas panels (c) and (d) describe the mudcake thickness as a function of time of invasion.

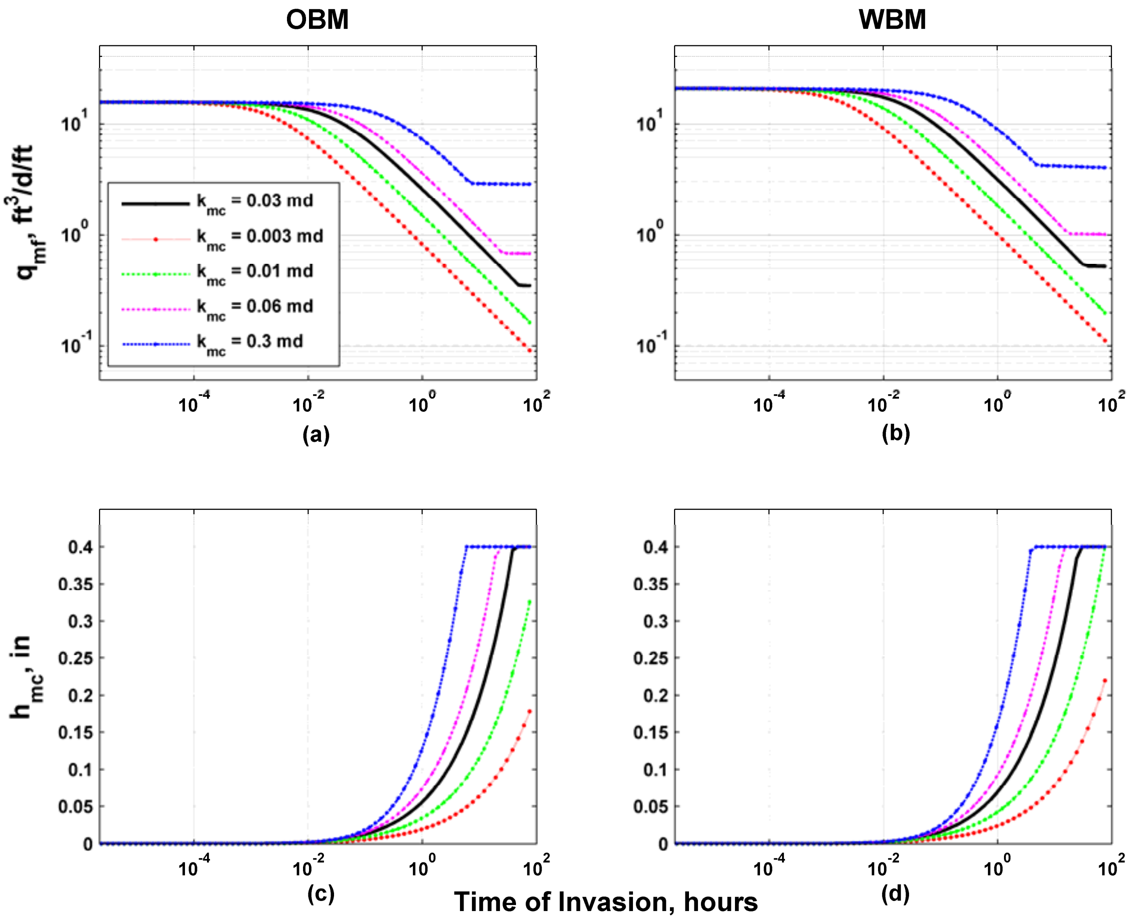

Figure 6.6: Sensitivity of the processes of OBM- and WBM-filtrate invasion to mudcake permeability (k_{mc}). Black solid curves identify the base cases (k_{mc}=0.03 md). Panels (a) and (b) describe the time evolution of the flow rate of invasion whereas panels (c) and (d) describe the mudcake thickness as a function of time of invasion.

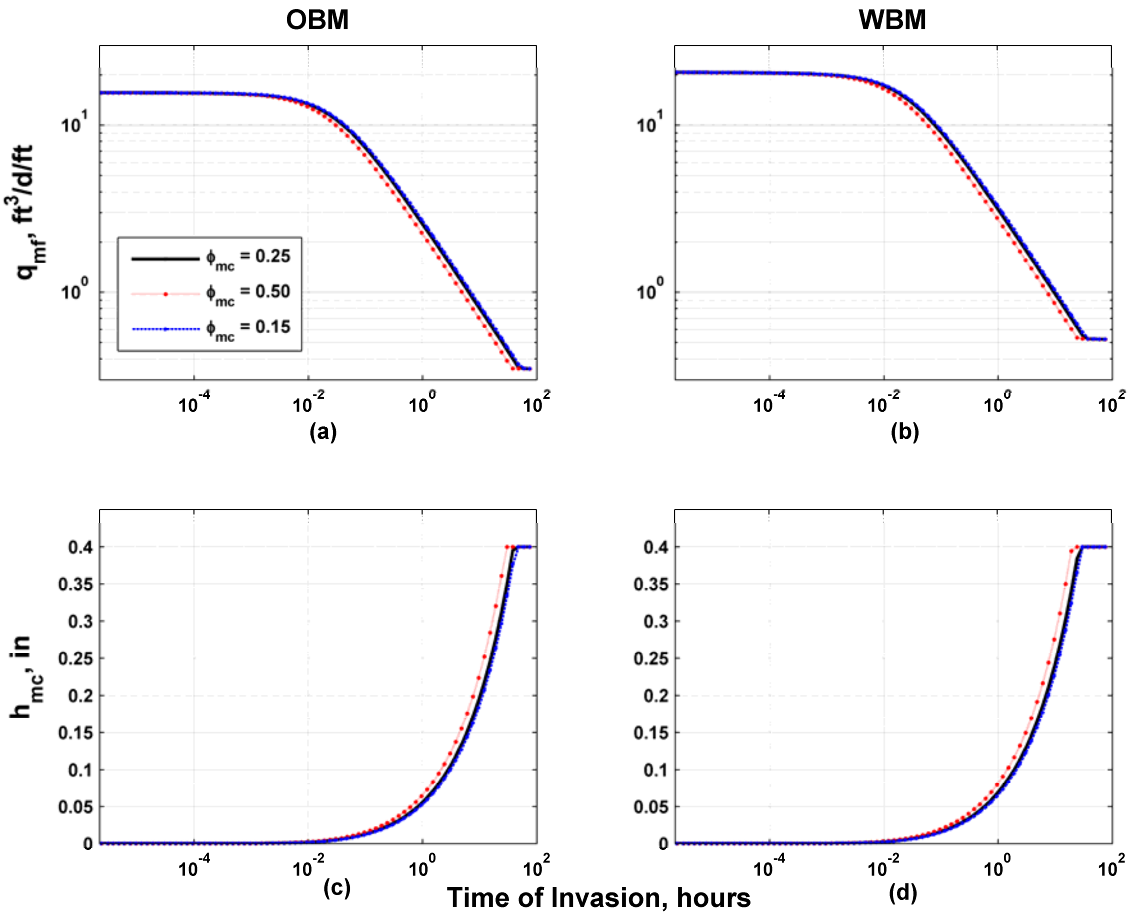

Figure 6.7: Sensitivity of the processes of OBM- and WBM-filtrate invasion to mudcake permeability (ϕ_{mc}). Black solid curves identify the base cases (ϕ_{mc} =0.25). Panels (a) and (b) describe the time evolution of the flow rate of invasion whereas panels (c) and (d) describe the mudcake thickness as a function of time of invasion.

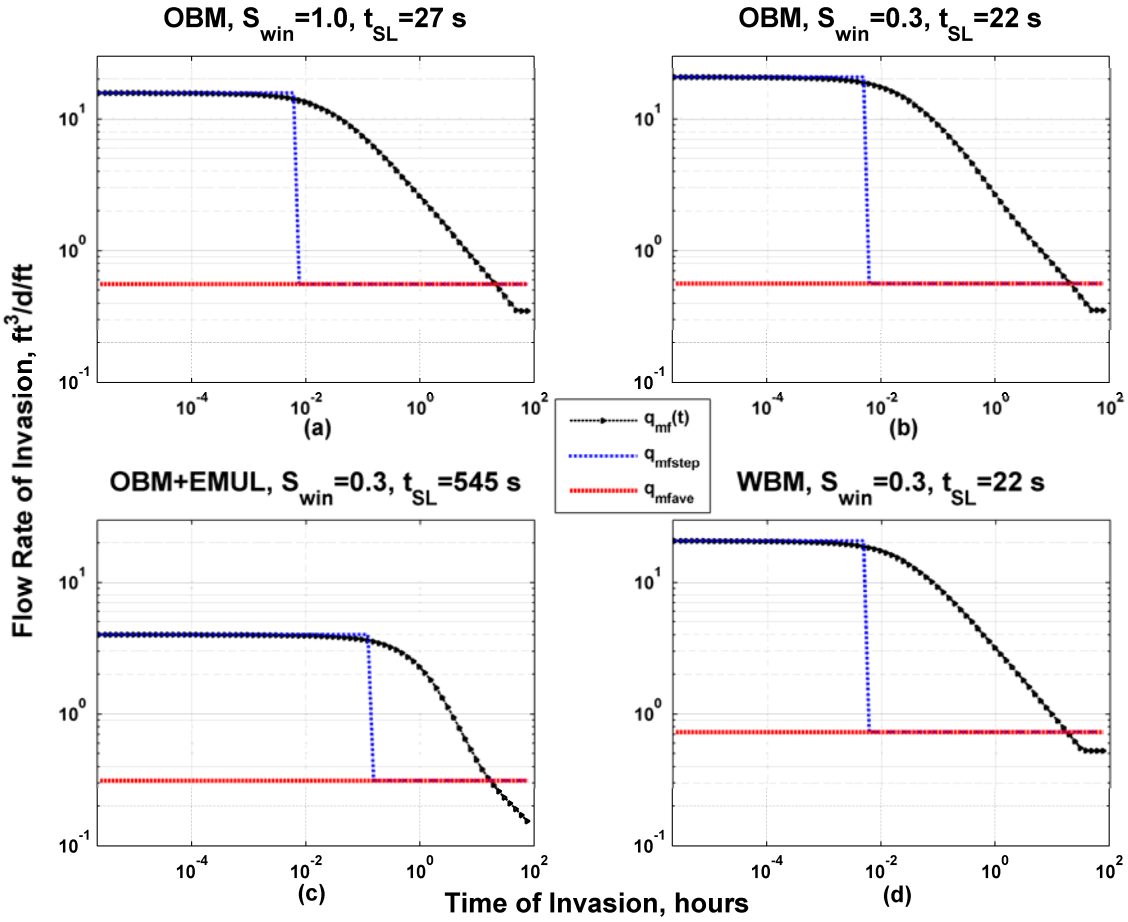

Figure 6.8: Calculated flow rate invasion as a function of time ($q_{mf}(t)$, shown in black triangles) for the various cases of OBM- and WBM-filtrate invasion. Constant (q_{mfave}, shown in red) and step (q_{mfstep}, shown in blue) rates were calculated as average values over 3 days of mud-filtrate invasion. Panel (a) describes the Base Case OBM (100% water-saturated), panel (b) describes the same case with 30% water and 70% oil. Panel (c) describes the Base Case with initial water saturation (S_{win}) equal to 30% with invading fluid formed by water and surfactant emulsified within MC_{16}. Finally, panel (c) describes the Base Case WBM with S_{win} = 30%. In each panel, t_{SL} designates the duration of the spurt loss.

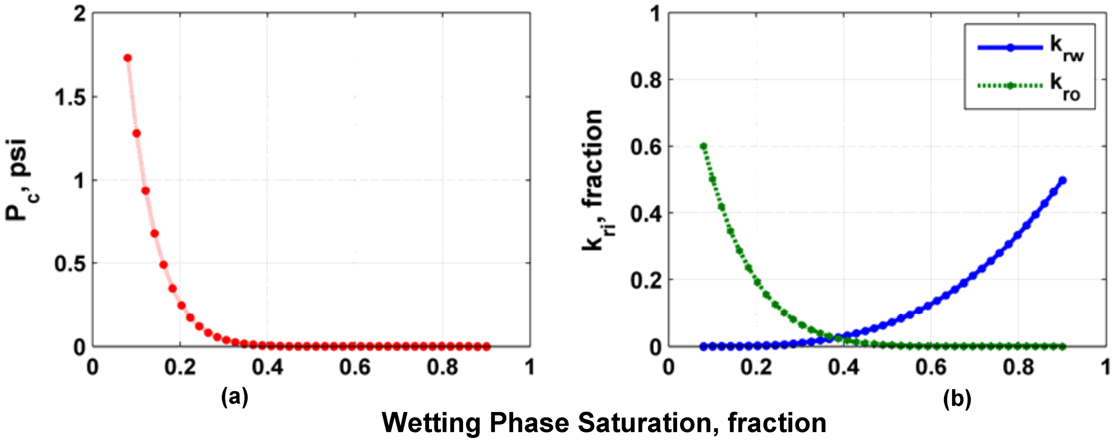

Figure 6.9: Water-oil capillary pressure (a) and relative permeability (b) curves assumed in the simulations of mud-filtrate invasion with water and surfactants emulsified in the OBM. Notice that capillary pressure decreases, the end points of relative permeability change, and critical water saturation is less than 50% compared to the base case shown in Figure 2.

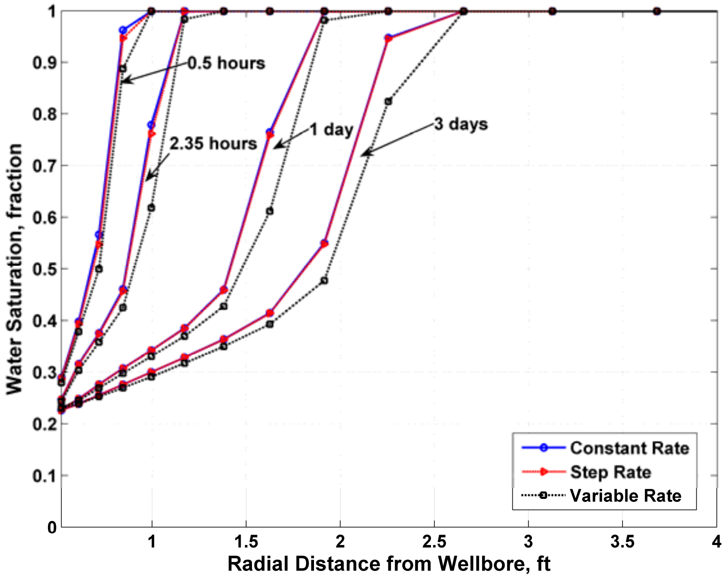

Figure 6.10: Comparison of radial distributions of water saturation simulated for the case of OBM-filtrate invading a wet formation (Base Case OBM) after 0.5 hours, 2.35 hours, 1 day, and 3 days of mud-filtrate invasion, respectively. Radial distributions were simulated assuming constant, step, and variable flow rates.

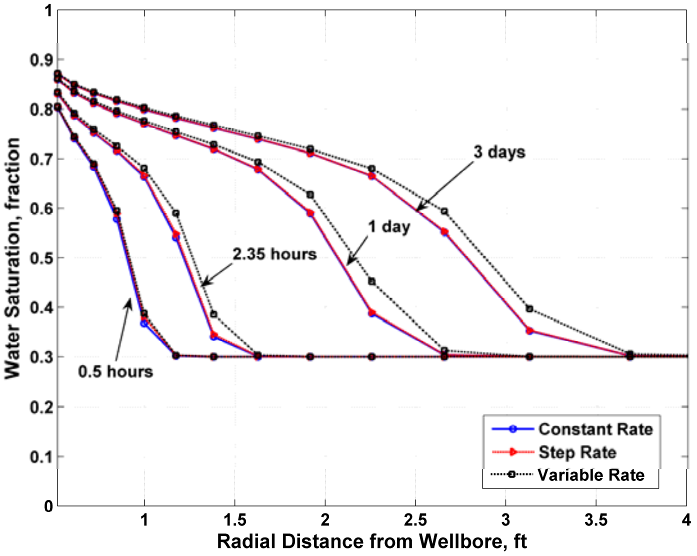

Figure 6.11: Comparison of radial distributions of water saturation simulated for the case of WBM-filtrate invading a formation with S_{win}=30% (Base Case WBM) after 0.5 hours, 2.35 hours, 1 day, and 3 days of mud-filtrate invasion, respectively. Radial distributions were simulated assuming constant, step, and variable flow rates.

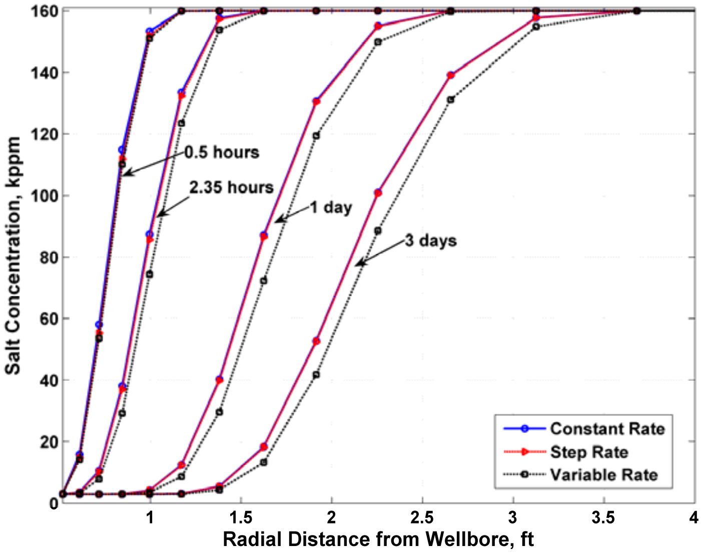

Figure 6.12: Comparison of radial distributions of salt concentration simulated for the case of WBM-filtrate invading a formation with S_{win}=30% (Base Case WBM) after 0.5 hours, 2.35 hours, 1 day, and 3 days of mud-filtrate invasion, respectively. Radial distributions were simulated assuming constant, step, and variable flow rates.

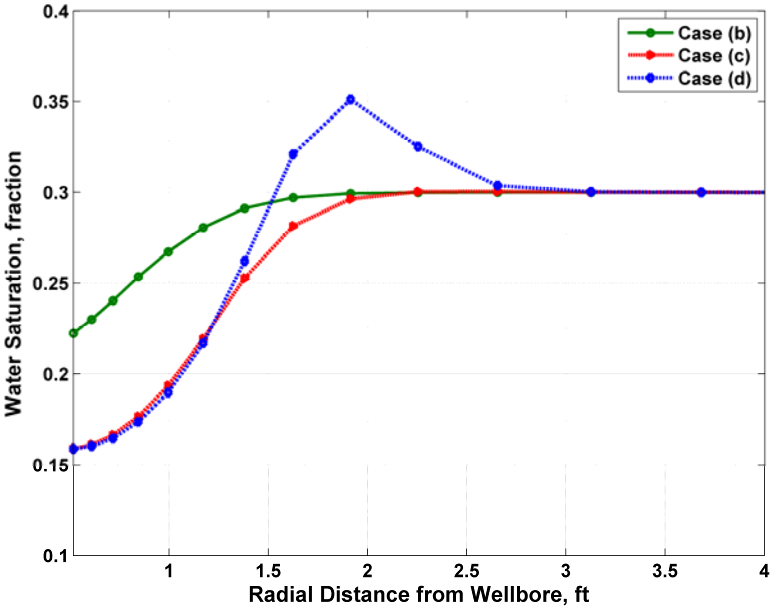

Figure 6.13: Radial distributions of water saturation simulated after 3 days of OBM-filtrate invasion for Cases (b), (c), and (d). Radial distributions were simulated with a time-dependent flow rate for each case. Figure 10 shows the results for Case (a). The cases were desigined for the modeling of borehole resistivity measurements in the presence of OBM.

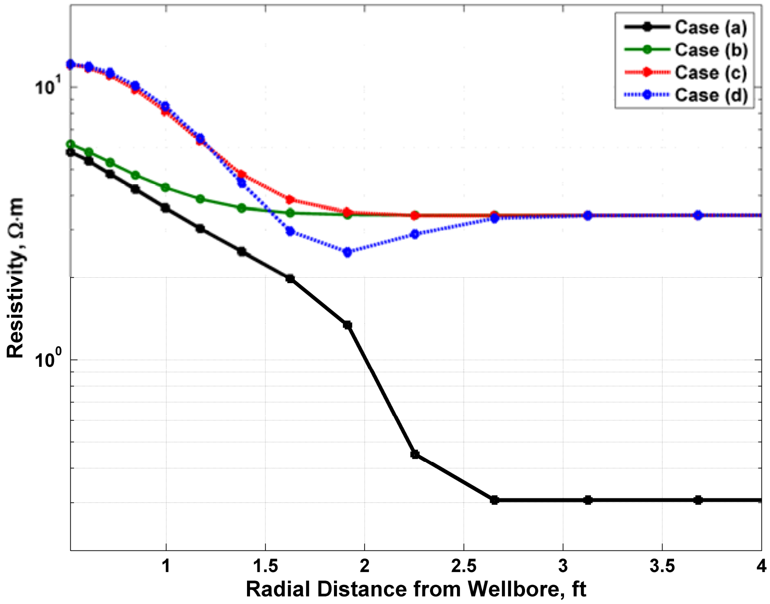

Figure 6.14: Radial distributions of electrical resistivity calculated after 3 days of OBM-filtrate invasion for Cases (a), (b), (c), and (d).

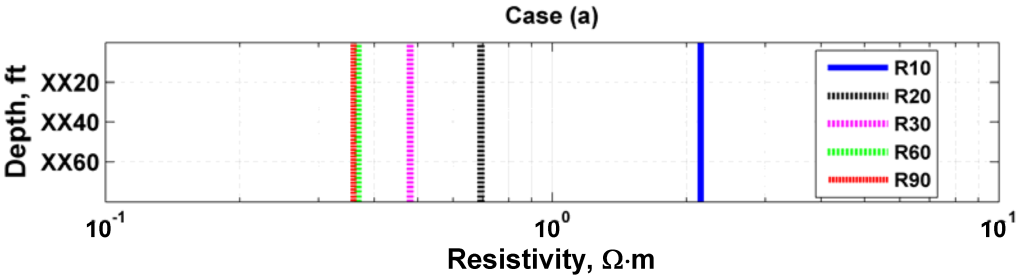

Figure 6.15: Two-foot vertical resolution array-induction resistivity measurements simulated after 3 days of OBM-filtrate invasion for Case (a).

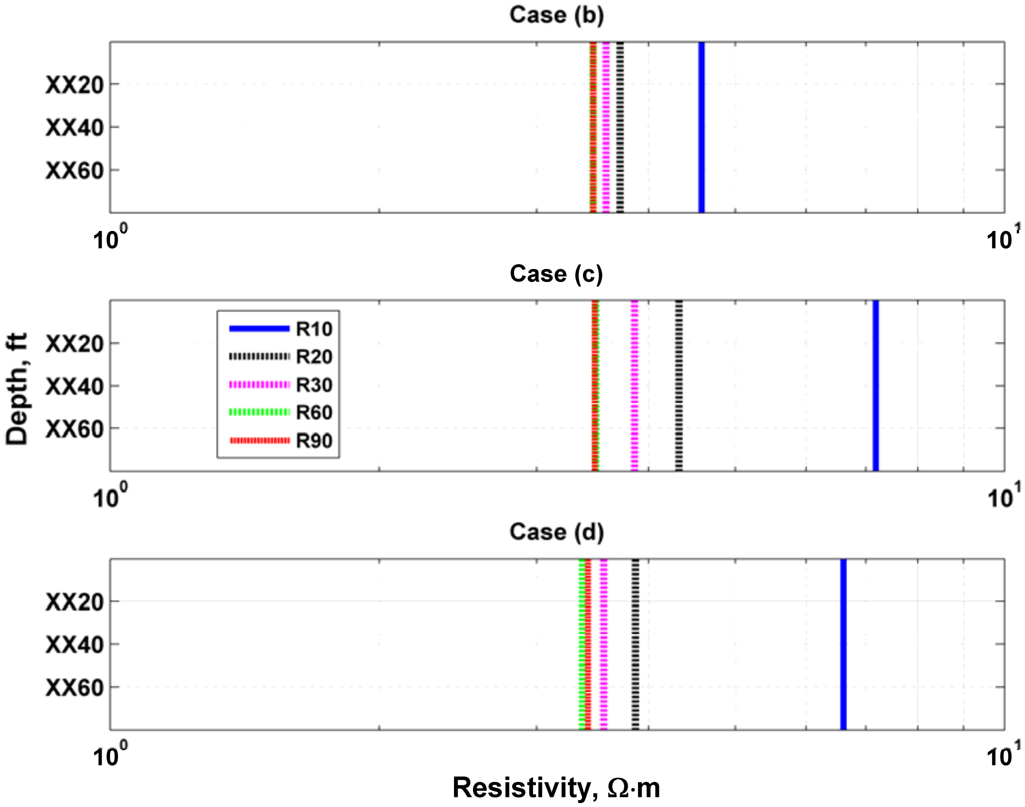

Figure 6.16: Two-foot vertical resolution array-induction resistivity measurements simulated after 3 days of OBM-filtrate invasion for Cases (b), (c), and (d).

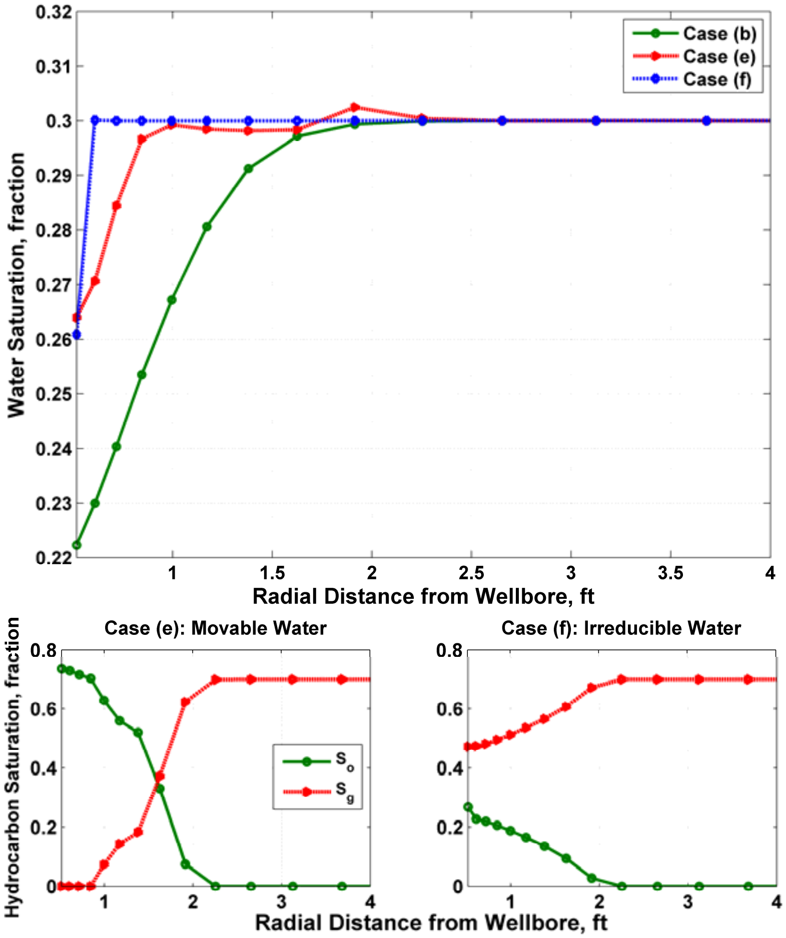

Figure 6.17: Top panel: radial distributions of water saturation simulated after 3 days of OBM-filtrate invasion for Cases (b), (e), and (f). The overbalance pressure reduces the capillary-bound saturation in the irreducible water Case (f) without entailing deep invasion. Bottom panels: radial distributions of oil (S_o) and gas (S_g) saturation for Cases (e) and (f), respectively, indicating that the radial length of invasion is approximately 2.3 ft. The cases were designed for the modeling of borehole resistivity measurements in the presence of OBM.

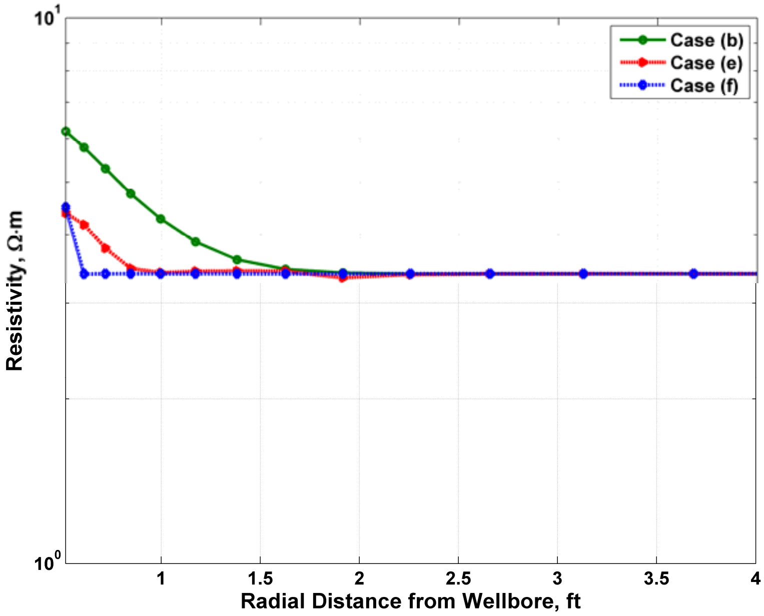

Figure 6.18: Radial distributions of electrical resistivity calculated after 3 days of OBM-filtrate invasion for Cases (b), (e), and (f).

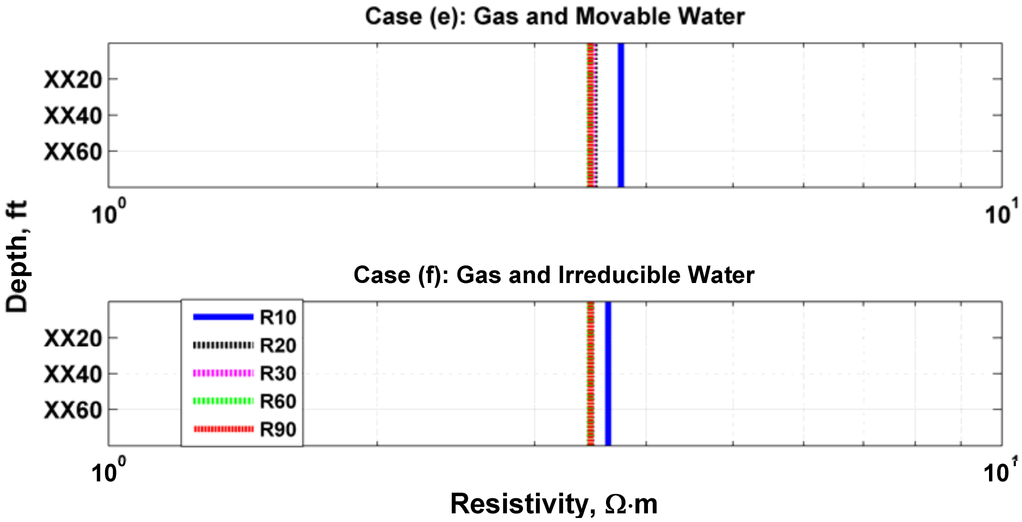

Figure 6.19: Two-foot vertical resolution array-induction resistivity measurements simulated after 3 days of OBM filtrate invading a partially gas-saturate rock formation.

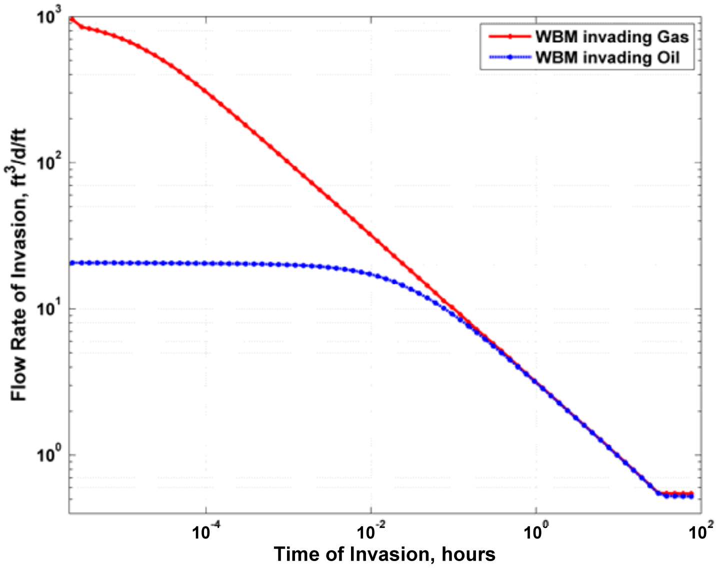

Figure 6.20: Simulated flow rate of invasion as a function of time for the case of WBM-filtrate invading both gas- and oil-bearing rock formations. The maximum time of invasion is 3 days.

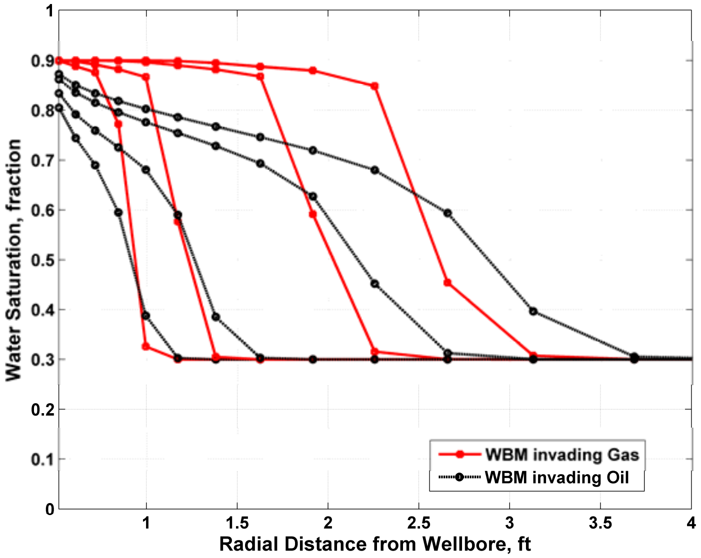

Figure 6.21: Comparison of radial distributions of water saturation simulated for the case of WBM filtrate invading a formation with S_{win}=30% (Base Case WBM) after 0.5 hours, 2.35 hours, 1 day, and 3 days of mud-filtrate invasion, respectively. Radial distributions were simulated by assuming a time-dependent flow rate of invasion into both gas- and oil-bearing rock formations with the same petrophysical conditions.

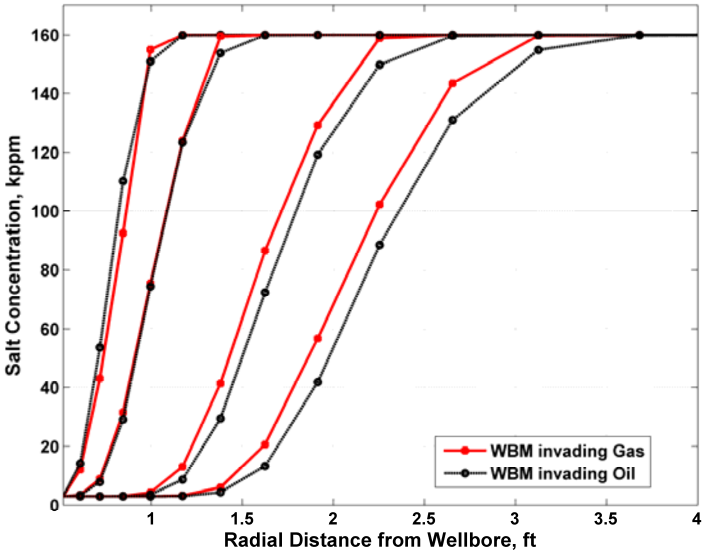

Figure 6.22: Comparison of radial distributions of salt concentration simulated for the case of WBM filtrate invading a formation with S_{win}=30% (Base Case WBM) after 0.5 hours, 2.35 hours, 1 day, and 3 days of mud-filtrate invasion, respectively. Radial distributions were simulated by assuming a time-dependent flow rate of invasion into both gas- and oil-bearing rock formations with the same petrophysical conditions.

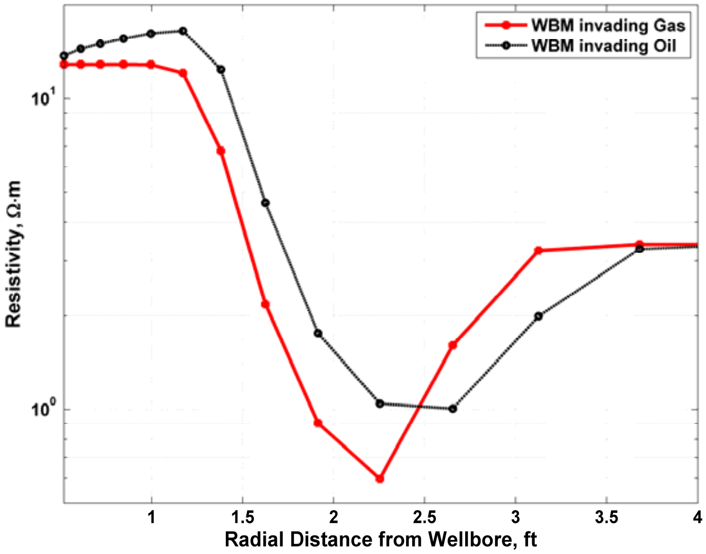

Figure 6.23: Radial distributions of electrical resistivity calculated after 3 days of WBM-filtrate invasion into both partially gas- and oil-saturated sandstone formations.

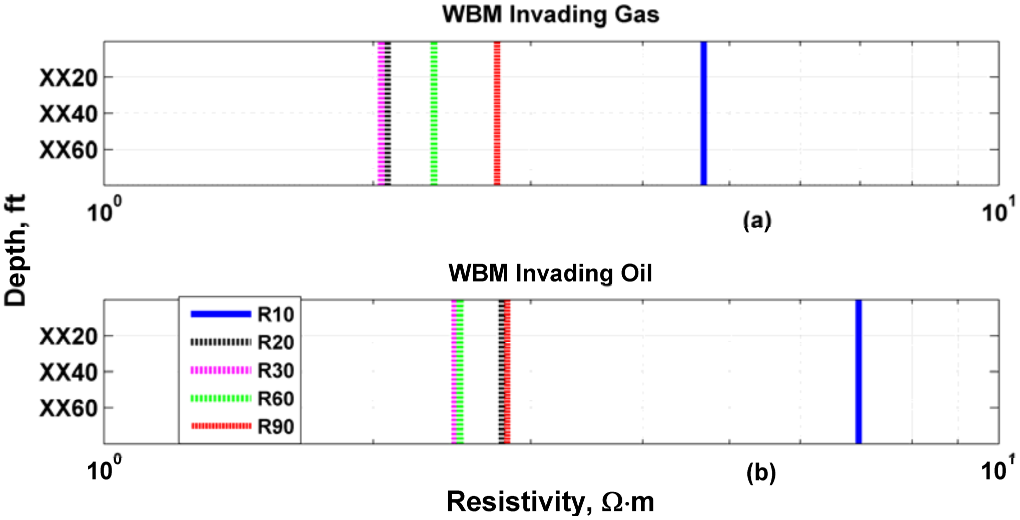

Figure 6.24: Two-foot vertical resolution array-induction resistivity measurements simulated after 3 days of WBM-filtrate invasion for both gas- and oil-bearing formations represented by panels (a) and (b), respectively.

Chapter 7: Summary, Conclusions, and Recommendations

This chapter summarizes the results stemming from this dissertation. We also list the main conclusions and provide recommendations for future research work.

7.1 SUMMARY

The focus of this dissertation was the integration of borehole EM, geological, and laboratory measurements to estimate petrophysical properties. In so doing, we incorporated the physics of WBM- and OBM-filtrate invasion to the simulation and inversion of borehole EM measurements.

In the first stage, we successfully applied a new combined inversion method to estimate connate water resistivity and Archie's cementation exponent to a data set acquired in a clastic formation exhibiting high permeability and connate water with moderately high salt concentration. Values of R_w and m yielded by the inversion were consistent with those obtained via a traditional interpretation method, thereby confirming the reliability of the estimation. The method described in this dissertation is an efficient and rigorous alternative to conventional interpretation techniques to perform petrophysical analysis of exploratory and appraisal wells wherein rock-core measurements may not be available.

The second stage considered a challenging field example of tight-gas sands, where we calculated absolute permeabilities of rock formations from inversion of borehole array-induction measurements. The estimation was based on the simulation of the process of WBM-filtrate invasion. This approach required detailed knowledge of borehole environmental variables, including overbalance pressure, temperature, mud properties, and time of invasion. Accurate simulation of the process of mud-filtrate invasion also required knowledge of fluid and rock properties such as porosity, permeability, relative permeability, capillary pressure, initial water saturation, salt concentration of connate water, and hydrocarbon density and viscosity, among others. Some of these properties were available from laboratory measurements, while others were estimated from basic petrophysical analysis of well logs. Permeability values yielded by the inversion of array-induction resistivity measurements were higher than those calculated with standard petrophysical formulas. However, these results were in the same range of rock-core permeabilities for porosity values larger than 10%. We remark that the method tested in this work to estimate permeability was based on the use of apparent resistivity curves yielded by the processing of AIT induction measurements. It is likely that the resolution and accuracy of the estimated values of permeability would improve with the use of "raw" voltages instead of processed apparent resistivity curves. Likewise, it is possible that the resolution and accuracy of the estimated values of permeability would improve with the use of micro-resistivity measurements in addition to AIT measurements.

We also quantified the influence of OBM-filtrate invasion on array-induction resistivity measurements using a binary component formulation to describe the miscibility of the oil phase. A history-matching approach allowed us to simulate array-induction resistivity measurements acquired in a partially oil-saturated turbidite reservoir. The formation consisted of dead oil and was invaded with OBM-filtrate. Simulation results indicated that it was possible to secure a good match with field measurements by simultaneously modifying both critical water saturation and rate of mud-filtrate invasion. Low-porosity rocks entailed radially deep invasion, hence resulting in significant variability of apparent resistivity curves. In addition, we studied the influence of several fluid properties on array-induction resistivity measurements in a well drilled with emulsified OBM. The formation under analysis included a long hydrocarbon column with a gas cap at the top, followed by a condensate and oil interval in a capillary transition zone with an underlying active aquifer. Detailed petrophysical analysis allowed us to select depth intervals invaded by OBM-filtrate as indicated by the separation of array-induction resistivity curves. An oil interval in the capillary transition zone was used as the calibration case to construct the invasion model. Moreover, sensitivity analyses were carried out based on separate perturbations of density and viscosity of native oil and flow rate of mud-filtrate invasion. Additional sensitivity analyses to capillary pressure and initial water saturation allowed us to study the effect of wettability and saturation zones on resistivity measurements acquired across the formation. Both OBM and native oil were initially simulated assuming a single component for each fluid. At the outset, we treated the OBM as an emulsion by adding water and surfactants and modeled multi-components and lighter hydrocarbons as part of native formation fluids.

Finally, we quantitatively compared the effect of the processes of WBM- and OBM-filtrate invasion on borehole resistivity measurements. We adapted the well-known physics of water-base mud-filtrate invasion to calculate the flow rate of oil-base mud-filtrate invasion using a commercial implicit compositional simulator. This approach included the dynamically coupled effects of mudcake growth and multi-phase filtrate invasion. Furthermore, we compared simulations of radial distributions of water saturation using transient, constant, and a step flow rate that accounted for the effect of spurt loss. Simulations indicated that the three assumptions of time-dependent flow rate of invasion entailed the same radial length of invasion with similar radial profiles of fluid saturation. The latter result justifies the use of a time-dependent flow rate of invasion and contradicts the common belief that the spurt loss has a dominant effect on invasion. We also found that, in general, flow rates of WBM-filtrate invasion are higher than those associated with OBM-filtrate invasion due to viscosity contrasts between OBM-filtrate and native fluids, which slow down the process of invasion. Such a conclusion was validated by the marginal variability of array-induction resistivity measurements observed in the simulations of OBM invasion compared to those of WBM invasion.

7.2 CONCLUSIONS

7.2.1 Combined simulation and inversion of SP and resistivity logs for the estimation of connate water resistivity and Archie's cementation exponent

i. The combined inversion of resistivity and SP measurements is a reliable method to estimate R_w and m in water-bearing formations. Results obtained from the inversion were consistent with those obtained from Pickett's plots. The difference between the estimates obtained with the two methods was of the order of 10%.

ii. The combined inversion method is highly recommended in zones where NaCl is the most abundant solution component and where connate salt concentration does not change in short depth intervals. This method of inversion works very well in high-permeability, thick formations and when connate water exhibits medium to high concentration of NaCl.

iii. In depth zones where the most abundant salt components are different from NaCl (e.g., $CaCl_2$, KCl, etc.) equation 2.6 is not valid. In addition, when the salt concentration of mud-filtrate and connate water are similar, the deflection of the SP curve is marginal and, therefore, the inversion method is not recommended.

iv. In low-permeability formations ($k < 5$ md) the electrokinetic components of the SP may become important for the total contribution to *SSP* and hence could be needed in the formulation before applying the inversion method introduced in this dissertation.

v. In the absence of water zones, resistivity inversion can still be used to estimate R_{xo} and R_t for the refined calculation of initial water saturation. This calculation method can be useful in the petrophysical assessment of exploratory and appraisal wells that are devoid of core samples and laboratory measurements.

7.2.2 Estimation of permeability from borehole array induction measurements: application to the petrophysical appraisal of tight-gas sands

i. Sensitivity analyses considered in this research indicated that absolute permeability had the largest effect on the measured array resistivity curves, especially on the shallow-reading curves. This observation provided a solid physical background for the estimation of permeability.

ii. By progressively increasing the number of individual flow sub-units within a single production zone, we were able to further refine the assumed values of porosity, capillary pressure and relative permeability.

iii. For the tight-gas sand reservoir under analysis, salt mixing between WBM-filtrate and connate water, and relative permeability had the largest influence on the spatial distribution of electrical resistivity resulting from invasion.

iv. Rocks with high critical water saturation (strongly water wet) were associated with piston-like invasion fronts and hence did not entail appreciable variations of the intermediate array-induction apparent resistivity curves.

v. Rocks with low critical water saturation were associated with spatially smooth distributions of electrical resistivity. Variations on the shape of the spatial distribution of electrical resistivity only occurred with a substantial change of relative permeability.

7.2.3 Effects of petrophysical properties on array-induction measurements acquired in the presence of oil-base mud-filtrate invasion

i. Numerical simulations of EM measurements indicated that resistivity measurements are highly sensitive to porosity and permeability, rock wettability, and rate of OBM-filtrate invasion. Alteration of rock wettability in the near-wellbore region increases the mobility of the water phase and influences the apparent resistivity measurements.

ii. Simulations show that, to properly quantify the influence of the process of OBM-filtrate invasion on borehole resistivity measurements, it is important to quantify the mud loss in the invaded formation as well as the duration of the invasion process.

iii. Multiple sensitivity analyses showed that high flow rates of OBM-filtrate entail radially deep invasion profiles.

iv. We found that the variability of apparent resistivity curves with various radial lengths of investigation was controlled by the rock's relative permeability and capillary pressure. The separation of these curves is relatively large when the rock is preferentially oil wet, whereas the separation is negligible when the rock is preferentially water wet.

v. We showed that array-induction resistivity measurements can be highly affected by deep invasion (1.5 ft to 2ft) in zones with movable water. The greater the differences between irreducible and initial water saturation, the smoother the radial distribution of water saturation, hence the larger the variability of apparent resistivity curves with different radial lengths of investigation.

7.2.4 Fluid density and viscosity effects on borehole resistivity measurements acquired in the presence of oil-base mud and emulsified surfactants

i. Simulated spatial distributions of water saturation were highly influenced by the assumed properties of OBM and native hydrocarbon components. Such a situation caused high resistivity values near the borehole wall, which were governed by capillary forces, native and invading fluid viscosities, saturation zone, and flow rate of invasion,

ii. The process of OBM-filtrate with emulsified surfactants caused changes in the spatial distribution of electrical resistivity 10% to 15% larger than when invading with a water- and surfactant-free OBM, thereby causing measurable variability of the simulated AIT resistivity curves.

iii. A radial water bank ensued when hydrocarbon viscosity was below 0.25 cp together with an absolute difference between S_{win} and S_{wir} less than 25%, giving rise to an electrically conductive annulus in the invaded zone.

iv. Initial water saturation became an exceedingly important parameter to reproduce apparent resistivity measurements in the presence of OBM-filtrate invasion, which allowed us to secure a more reliable estimate of true formation resistivity.

v. As in the case of WBM-filtrate invasion, presence of an annulus and large separation of resistivity curves indicated that the invaded formation was porous and permeable, possibly with good production potential.

7.2.5 Quantitative comparison of the processes of oil- and water-base mud-filtrate invasion and their corresponding effects on borehole resistivity measurements

i. Simulations showed that using an integrated average flow rate of invasion was equivalent to assuming an average step rate that accounted for spurt losses. The high spurt loss observed at the onset of invasion lasted between

1/4 and 550 seconds, which was negligible compared to the total time of invasion.

ii. Radial distributions of fluid saturation indicated that WBM entailed radial lengths of invasion 15%-20% (early times) larger and approximately 40% (late times) radially deeper than those associated with OBM-filtrate invasion.

iii. In the case of OBM-filtrate invading a wet zone, we observed a large separation between apparent resistivity curves, similar to those observed for the case of WBM filtrate invading a movable hydrocarbon-saturated zone. Moreover, in the cases of OBM-filtrate invading a partially oil-saturated rock formation, alterations of wettability due to presence of surfactants in the mud increased the contrast between flushed- and virgin-zone resistivities.

iv. Flow rates associated with WBM-filtrate invasion are 20%-40% higher than those associated with OBM-filtrate invasion. We conclude that rock formations that exhibit large pore throats and low capillary pressure entail high flow rates and rapid spurt loss. On the other hand, rock formations that exhibit small pore throats and large capillary pressure entailed instantaneous flow rates of invasion 100 to 200 times larger than those associated with best quality rocks thereby slowing down the process of mudcake buildup and causing radially deeper invasion.

v. Mudcake permeability remained as the main parameter controlling the process of mudcake buildup and hence the total volume of fluid invading the formation. Likewise, both capillary pressure and relative permeability governed the shape and contrast of the radial distribution of electrical resistivity in the invaded zone.

7.3 RECOMMENDATIONS

The following is an itemized list of possible research avenues that expand the technical topics considered in this dissertation:

i. Introduction of a new numerical formulation to apply the combined inversion of SP and resistivity to estimate R_w and m in formations with salt components other than NaCl (e.g., $CaCl_2$, KCl, etc.).

ii. Inclusion of the effect of the electrokinetic components of the SP in low-permeability formations ($k < 5$ md) to perform a more reliable estimation of R_w in such type of rocks.

iii. Inclusion of "raw" voltages instead of processed apparent resistivity curves. This will improve the resolution and accuracy of the values of permeability estimated from inversion of array-induction resistivity measurements.

iv. Improvement of the resolution and accuracy of the estimated values of permeability by including the use of micro-resistivity measurements in addition to array-induction resistivity measurements.

v. Consideration of laboratory measurements of rock-core samples to quantify the effect of wettability alteration on capillary pressure and relative permeability curves and radial variability of Archie's saturation exponent as a result of OBM-filtrate invasion.

vi. Simulation of array-induction resistivity measurements acquired in low-porosity and low-permeability formations, such as tight-gas sands, in the presence of emulsified OBM.

vii. Simulation of nuclear and acoustic measurements acquired in the presence of OBM-filtrate invasion.
viii. Extension of simulations and inversion methods considered in this dissertation to measurements acquired in deviated and horizontal wells.

Appendix A: Petrophysical Assessment

This Appendix details the calculations and conventions included on the estimation of petrophysical properties from well logs used to define initial simulation models.

A.1 VOLUMETRIC SHALE CONCENTRATION

The Gamma Ray log is used to compute a shale index (I_{sh}) using a linear relationship, namely

$$I_{sh} = \frac{GR\text{-}GR_{\min}}{GR_{\max}\text{-}GR_{\min}},$$

where GR_{min} and GR_{max} are the minimum and maximum values of GR, respectively in the zone of interest. Three different models are used to estimate the volumetric shale concentration (C_{sh}) as a function of I_{sh} (Bigelow, 1992). These models are linear, Clavier, and Stieber, respectively. The following equations describe such models:

$$C_{sh}^{Linear} = I_{sh}, \tag{A.1}$$

$$C_{sh}^{Clavier} = 1.7 - \left[3.38 - \left(I_{sh}+0.7\right)^2\right]^{1/2}, \tag{A.2}$$

and

$$C_{sh}^{Stieber} = \frac{I_{sh}}{3.0 - 2.0 \times I_{sh}}, \tag{A.3}$$

respectively.

A.2 POROSITY AND WATER SATURATION

The porosity and saturation models explained in this section assume dispersed shale distribution. Therefore, once C_{sh} has been calculated with equations (A.1), (A.1), or (A.3), neutron and density porosity logs are corrected for shaliness using the equations

$$\phi_N{}^{sh} = \phi_N - C_{sh}\phi_{Nsh},$$

and

$$\phi_D{}^{sh} = \phi_D - C_{sh}\phi_{Dsh},$$

where ϕ_{Nsh} and ϕ_{Dsh} are the readings of neutron and density porosity logs in a pure shale interval, respectively and $\phi_N{}^{sh}$ and $\phi_D{}^{sh}$ are shale-corrected neutron and density porosity, in that order. We compute an initial guess of non-shale porosity (ϕ_o) from $\phi_N{}^{sh}$ and density $\phi_D{}^{sh}$ values via the equations

$$\phi_o = \frac{1}{2}\left(\phi_N{}^{sh} + \phi_D{}^{sh}\right),$$

and

$$\phi_o = \sqrt{\frac{1}{2}\left[\left(\phi_N{}^{sh}\right)^2 + \left(\phi_D{}^{sh}\right)^2\right]}$$

for oil and gas, respectively. Subsequently, the calculation of non-shale porosity is improved with a dual-fluid dual-mineral nonlinear model given by

$$\hat{\rho}_b = \phi\left[\sqrt[n]{\frac{R_{wxo}a}{\phi^m R_{xo}}}\left(\rho_1 - \rho_2\right) + \rho_2\right] + \left(1 - \phi - C_{sh}\right)\rho_{ma} + C_{sh}\rho_{sh}, \qquad \text{(A.4)}$$

where $\hat{\rho}_b$ is modeled bulk density, ρ_{ma} is matrix (quartz) density, ρ_{sh} is shale density, ρ_1 is mud-filtrate (fresh water) density, ρ_2 is density of the gas-mud-filtrate mixture estimated from log interpretation charts (Schlumberger, 1991), R_{wxo} is invaded-zone water resistivity, R_{xo} is invaded-zone resistivity, and C_{sh} is volumetric shale concentration.

Equation (A.4) is solved by minimizing the difference between measured bulk density (ρ_b) and bulk density computed with the initial guess of porosity, i.e.,

$$\min_{(\phi^j)} \sum_j \left(\rho_b{}^j - \hat{\rho}_b{}^j \right)^2, \qquad \phi \in [0,1]. \tag{A.5}$$

The minimum of equation (A.5) yields the estimate of non-shale porosity. Archie's (1942) equation is used to compute the initial guess of water saturation, given by,

$$S_w{}^n = \frac{R_w}{R_t} \frac{a}{\phi^m}, \tag{A.6}$$

where ϕ is non-shale porosity, R_w is connate water resistivity, R_t is true formation resistivity, a is the tortuosity factor, and m and n are the cementation and saturation exponents, respectively.

A.3 PERMEABILITY

The generalized Timur-Tixier equation (Balan *et al*, 1995) reproduces the interplay between porosity, permeability, and irreducible water saturation of rock-core measurements. Accordingly, the relationship between permeability (k, [md]), porosity (ϕ, [fraction]), and irreducible water saturation (S_{wir}, [fraction]) is given by

$$k = A \frac{\phi^B}{S_{wir}{}^C}, \tag{A.7}$$

where A, B, and C are constants to be determined from multilinear regression analysis.

A.4 WATER SATURATION IN SHALY SANDS

In the presence of shaly sands, the dual-water (D-W) model (Clavier *et al*, 1984) and the Waxman-Smits (1968) equations can be independently used to calculate water saturation and to recompute effective porosity from equation (A.4). The following equations are used to apply the D-W model (Dewan, 1983):

$$\phi_{tsh} = \delta\phi_{Dsh} + (1-\delta)\phi_{Nsh},$$

$$\phi_t = \phi + C_{sh}\phi_{tsh},$$

$$S_b = C_{sh}\frac{\phi_{tsh}}{\phi_t}, \text{ and}$$

$$R_b = R_{sh}\phi_{tsh}{}^{m},$$

where ϕ_{tsh} is total shale porosity, δ is a weighing parameter between 0.5 and 0.9, ϕ_t is total porosity, S_b is the clay-bound water saturation, R_{sh} is shale resistivity, and R_b is clay-bound water resistivity. It follows that in the D-W model, the calculated true formation resistivity ($\hat{R}_t$) is given by

$$\frac{1}{\hat{R}_t} = S_w^n \frac{\phi_t^m}{aR_w} - S_w \frac{\phi_t^m}{aR_w} S_b \left(1 - \frac{R_w}{R_b}\right), \tag{A.8}$$

and the Waxman-Smits equations is represented by

$$\frac{1}{\hat{R}_t} = S_w{}^{n*} \frac{\phi^{m*}}{a}\left[\frac{1}{R_w} + \frac{BQ_v}{S_w}\right], \tag{A.9}$$

where *m** and *n** are clay-corrected Archie's cementation and saturation exponents, respectively, Q_v is volumetric concentration of sodium exchange cations (CEC) associated with clay, and *B* designates the equivalent conductance of the counterions as a function of connate water resistivity. We use equation (19) of Waxman and Smits' (1968) work to calculate *B*, whereas m^*, n^* and Q_v are obtained from laboratory measurements.

Both D-W and Waxman-Smits are nonlinear equations. Therefore, S_w can be calculated by minimizing the difference between the measured true formation resistivity and the true formation resistivity computed with equations (A.8) or (A.9), where the initial guess is obtained from Archie's equation (A.6), i.e.,

$$\underset{\left(S_w^{\,j}\right)}{\min} \sum_j \left(\frac{1}{R_t^j} - \frac{1}{\hat{R}_t^j} \right)^2, \qquad S_w \in [0,1].$$

where R_t are the field measurements of the assumed true formation resistivity. The above equation is solved iteratively using a Newton method that includes analytical derivatives of equations (A.8) and (A.9).

Appendix B: Numerical Simulation of WBM-Filtrate Invasion

The process of water-base mud-filtrate invading a partially hydrocarbon-saturated formation is simulated with the physics of two-phase multi-component fluid flow.

B.1 PHYSICS OF MULTI-PHASE IMMICIBLE FLUID-FLOW

The problem of immiscible fluid-flow is modeled as convective transport of aqueous and hydrocarbon phases, and components of water, hydrocarbon, and salt concentration (Alpak *et al*., 2003). Isothermal convective miscible transport is assumed for the salt component while diffusion between mud-filtrate and connate water is neglected. Disregarding chemical reactions, rock/fluid mass transfer, and diffusive/dispersive transport, the mass balance equation for the i^{th} fluid phase is given by

$$\frac{\partial\left(\rho_i \phi S_i\right)}{\partial t} + \nabla \cdot \left(\rho_i \overline{\mathbf{v}}_i\right) = -q_{vi}, \quad i = 1,2. \tag{B.1}$$

where t, ρ_i, S_i, $\overline{\mathbf{v}}_i$, and q_v designate time, mass density of the i^{th} phase, saturation of the i^{th} phase, Darcy's velocity vector, and source/sink term, respectively. Simulation of mud-filtrate invasion is performed assuming axi-symmetrical cylindrical flow and permeability anisotropy. A two-dimensional finite-difference grid is constructed with logarithmically spaced radial nodes that include shorter radial steps in the near wellbore region. Rock properties are considered constant in the radial direction. Upper, lower, and external boundaries of the formation consist of no-flow conditions. A constant flow rate is imposed at the borehole wall for each numerical layer as a fixed source condition at each time step. In equation (B.1), the fluid velocity is described by Darcy's law, namely,

$$\overline{\mathbf{v}}_i = -\frac{k_{ri}}{\mu_i} \overline{\overline{\mathbf{k}}} \cdot \left(\nabla p_i - \gamma_i \nabla h_z\right), \quad i = 1,2,$$

where $\overline{\overline{\mathbf{k}}}$ is the formation absolute permeability tensor, h_z is the vertical location of the reservoir with respect to a given reference level, and k_{ri}, μ_i, p_i, and γ_i, are relative permeability, viscosity, pressure, and specific gravity of the i^{th} phase, respectively. In the case of simultaneous flow of oleic and aqueous phases, we assume that both fluids and rock compressibilities are constant over the pressure range of interest. On the other hand, for the two-phase flow of gaseous and aqueous phases, gas compressibility is treated as a function of the PVT properties of gas at each time step. Fluid pressure is related to capillary pressure (P_c) and saturation of wetting (S_w) and non-wetting (S_{nw}) phases by the following equations,

$$P_c(S_w) = P_{nw} - P_w \, ,$$

and

$$S_w + S_{nw} = 1 \, .$$

where P is pressure and the subscripts w and nw refer to wetting (water) and non-wetting (oil or gas) fluid phases, respectively

Finally, we simulate the advective transport of the salt component after obtaining a converged solution at each time step and by assessing the interblock flows. The spatial distributions of salt concentration (C_w) are updated upon solving a mass conservation equation, as follows:

$$\frac{\partial\left(\rho_w \phi S_w C_w\right)}{\partial t} + \nabla \cdot \left(\rho_w \bar{\mathbf{v}}_w C_w\right) = -C_{mf} q_{mf} \, . \tag{B.2}$$

In the above equation, C_w, is the salt concentration of connate water and C_{mf} and q_{mf} represent the salt concentration and the flow rate of the invading mud-filtrate at a given time step, respectively. Modeling of multi-phase and multi-component fluid-flow is performed with commercial finite-difference reservoir simulators. The main outputs of the simulation are the spatial distributions of water saturation and salt concentration, which are transformed into electrical resistivity using the method described in Chapter 3.

Appendix C: Numerical Simulation of OBM-Filtrate Invasion

We use an IMPEC numerical formulation to calculate the spatial distribution of water saturation due to OBM-filtrate invasion.

C.1 PHYSICS OF MULTI-COMPONENT MISCIBLE FLUID-FLOW

The formulation and the algorithm used in the simulation of OBM-filtrate invasion are similar to those described by Malik *et al.* (2007). We assume azimuthal symmetry in formation properties with respect to the axis of a vertical borehole. The general formulation assumes n_c hydrocarbon components and one water component in the aqueous phase. There are n_p phases with negligible mass fluxes between water and other phases. We assume that there are no chemical reactions between the OBM and native hydrocarbon and that space-time variations of temperature are negligible. The evolution of fluid pressure and component concentration for multi-phase flow in porous media is governed by Darcy's law. In turn, the partial differential equation for pressure is given by

$$\left(V_p c_f - \frac{\partial V_t}{\partial P}\right)\frac{\partial P}{\partial t} + V_b \sum_{i=1}^{n_c+1} \overline{V}_{ti} \nabla \cdot \sum_{j=1}^{n_p}\left(\xi_j x_{ij} \overline{\mathbf{v}}_j\right) - \sum_{i=1}^{n_c+1} \overline{V}_{ti} q_i = 0, \tag{C.1}$$

where t is time, V_p, V_b, V_t, are pore, bulk, and total (fluid) volume, respectively, c_f is formation compressibility, ξ_j is molar density of the j^{th} phase, x_{ij} is mole fraction of the i^{th} component in the j^{th} phase, q_i is molar flow rate of the i^{th} component, and $\overline{V}_{ti}$ is the partial derivative of V_t with respect to molar concentration of component i. Moreover, the net change of the i^{th} component is expressed in mol with a mass conservation equation, namely,

$$\frac{\partial N_i}{\partial t} + V_b \sum_{j=1}^{n_p} \nabla \cdot \left(\xi_j x_{ij} \overline{\mathbf{v}}_j\right) - q_i = 0, \quad i = 1, ..., n_c + 1, \tag{C.2}$$

and the number of moles (N_i) of the i^{th} component per unit pore volume is given by

$$N_i = \sum_{j=1}^{n_p} \xi_j x_{ij} S_j \,,$$

where S_j designates the saturation of phase j. In the previous equation, we use the Peng-Robinson equation-of-state to calculate molar density from the compressibility factor (Z_j), viz.,

$$\xi_j = \frac{P}{Z_j RT} \,, \tag{C.3}$$

where R is the universal gas constant. Both molar density and molecular weight (M_i) allow us to calculate the mass density,

$$\rho_i = \xi_j \sum_{i=1}^{n_c} x_{ij} M_i \,. \tag{C.4}$$

The above equation indicates that mass density depends on both component concentration and formation pressure. Oil viscosity (μ_o) is calculated by enforcing a quarter-power mixing rule (Todd and Longstaff, 1972) applied to the sum of concentrations of the i^{th} component in the oil phase (x_{io}), namely,

$$\mu_o = \left[\sum_{i=1}^{n_c} x_{io} \mu_i^{1/4} \right]^4 . \tag{C.5}$$

Mass conservation is enforced with the volume constraint given by

$$\sum_{j=1} \frac{N_j}{\xi_j} = 1, \; j = 1, 2 \,, \tag{C.6}$$

where 1 and 2 represent water and oil phases, respectively.

This formulation enforces boundary and source flow-rate conditions on the borehole wall. The outer limits of the reservoir consist of impermeable zones with no-flow boundary conditions. We solve equations (C.1) and (C.2) via finite-difference discretization in cylindrical coordinates. Equations (C.3) to (C.6) are solved at each time step with concomitant updates of fluid properties based on flash calculations. Petrophysical properties remain constant in the radial direction. The main outputs of the simulation are the spatial distributions of oil saturation and water saturation. Salt concentration in the water phase remains constant.

Acronyms and Nomenclature

Acronyms

1D : one-dimensional

2D : two-dimensional

AIT : Array-induction imager tool

BC : Base Case

CMG : Computer Modeling Group

DBIM : distorted Born iterative method

EM : Electromagnetic

IMPEC : implicit pressure explicit concentration

NMM : numerical-mode matching method

OBM : oil-base mud

PVT : pressure-volume-temperature

STARS : Steam, thermal, and advanced processes reservoir simulator

SVD : singular-value decomposition

T : transpose of a matrix

UT-FET : The University of Texas' Formation Evaluation Tool Box

WBM : water-base mud

Nomenclature

a : Archie's tortuosity coeficient [ ]

B : equivalent conductance of counterions [$\mathrm{cm}^2/(\Omega\cdot\mathrm{meq})$]

c_f : formation compressibility [psi^{-1}]

C_{sh} : volumetric shale concentration [fraction]

C_w : salt concentration [ppm]

$\bar{\mathbf{d}}$: vector of numerically simulated measurements [arbitrary]

$\bar{\mathbf{d}}^o$: vector of field measurements [arbitrary]

E_φ : azimuthal component of electric field [V/m]

$\bar{\mathbf{e}}$: vector of data residuals [arbitrary]

e_{nw} : empirical exponent for non-wetting-phase relative permeability [ ]

e_p : empirical exponent for capillary pressure [ ]

e_w : empirical exponent for wetting-phase relative permeability [ ]

f_s : mud solid fraction [ ]

$G(r,z;r_s,z_s)$: Green's function [ ]

GR : gamma ray [γAPI]

GR_{max} : maximum value of gamma ray (pure shale) [γAPI]

GR_{min} : minimum value of gamma ray in (cleanest sand) [γAPI]

$H(z)$: Heaviside function [ ]

h_{mc} : mudcake thickness [inches]

I : electric-current intensity [A]

K	:	induction tool constant	[V·Ω·m]
$\overline{\overline{\mathbf{k}}}$	:	permeability tensor	[md]
k	:	formation absolute permeability	[md]
k_{mc}	:	mudcake permeability	[md]
k_{nw}	:	non wetting-phase permeability	[ ]
k_{rnw}	:	non-wetting-phase relative permeability	[ ]
k_{rnw} (k_{ro})	:	non-wetting-phase (oil) relative permeability	[ ]
k_{rnw}^{0}	:	non-wetting-phase relative permeability end point	[ ]
k_{rw}	:	wetting-phase relative permeability	[ ]
k_{rw}^{0}	:	wetting-phase relative permeability end point	[ ]
k_{w}	:	wetting-phase permeability	[md]
m	:	Archie's cementation exponent	[ ]
m^{*}	:	clay-corrected Archie's cementation exponent	[ ]
M_{i}	:	molecular weight of component *i*	[lb/lb-mol]
[NaCl]	:	equivalent salt concentration	[ppm]
N_{i}	:	number of moles of component *i*	[ ]
n	:	Archie's saturation exponent	[ ]
n^{*}	:	clay-corrected Archie's saturation exponent	[ ]
P_{c}	:	capillary pressure	[psi]
P_{c}^{0}	:	coefficient for capillary pressure equation	[psi·Darcy$^{1/2}$]
P_{cmax}	:	maximum capillary pressure	[psi]
P_{m}	:	mud hydrostatic pressure	[psi]

P_{mc} : mudcake pressure [psi]

P_{nw} : non-wetting phase pressure [psi]

P_w : wetting-phase pressure [psi]

Q_v : volumetric concentration of sodium exchange cations [meq/ml]

q_{mf} : flow rate of invasion [ft^3/d]

q_{mfave} : average flow rate of invasion [ft^3/d]

q_{mf}^{max} : maximum flow rate of invasion [ft^3/d]

q_{mfstep} : step flow rate of invasion [ft^3/d]

R : Universal gas constant [psi·ft/lb-mol/^oF]

R10 : 10-inch radial length of investigation apparent resistivity [Ω·m]

R20 : 20-inch radial length of investigation apparent resistivity [Ω·m]

R30 : 30-inch radial length of investigation apparent resistivity [Ω·m]

R60 : 60-inch radial length of investigation apparent resistivity [Ω·m]

R90 : 10-inch radial length of investigation apparent resistivity [Ω·m]

R_b : clay-bound water resistivity [Ω·m]

R_{mfe} : equivalent mud-filtrate resistivity [Ω·m]

R_{shbot} : bottom-shoulder resistity [Ω·m]

R_{shtop} : top-shoulder resistity [Ω·m]

$\widehat{R}_t$: calculated true formation resistivity [Ω·m]

R_t : true formation resistivity [Ω·m]

R_w : connate water resistivity [Ω·m]

R_{we} : equivalent water resistity [Ω·m]

R_{wxo} : invaded-zone water resistivity [Ω·m]

R_{xo} : invaded-zone resistivity [Ω·m]

r : radial distance from the center of the wellbore [ft]

r_{inv} : radial length of invasion [ft]

r_{mc} : mudcake radius [ft]

r_s : radius of an electrical source current loop [m]

r_T : radius of an electrical transmitter [m]

r_w : wellbore radius [ft]

S_b : clay-bound water saturation [fraction]

S_N : normalized water saturation [fraction]

S_o : oil saturation [fraction]

SSP : static spontaneous potential [mV]

S_w : water saturation [fraction]

S_{wcr} : critical water saturation [fraction]

S_{win} : initial water saturation [fraction]

S_{wir} (S_{wr}) : irreducible (residual) water saturation [fraction]

T : temperature [^{o}F]

T_F : formation temperature [^{o}F]

t : time of invasion [hours], [days]

t_{SL} : time of spurt loss [s]

$\bar{\bar{\mathbf{U}}}$: unitary matrix formed by eigenvectors [arbitrary]

V : current potential [A]

V_b : bulk volume [ft^3]

V_p : pore volume [ft^3]

V_T : total volume of fluid injected [ft^3]

V_t : total volume of fluid [ft^3]

$\bar{\bar{\mathbf{V}}}$: unitary matrix formed by eigenvectors [arbitrary]

$\bar{\mathbf{v}}$: Darcy's fluid velocity [ft/s]

$\bar{\mathbf{x}}$: vector of unknown model parameters [arbitrary]

x_{fo} : component concentration of formation oil [fraction]

x_{OBM} : component concentration of oil-base mud [fraction]

z : vertical distance with respect to the top of formation [ft]

Z_j : compressibility factor of phase j [ ]

z_S : vertical location of an electrical source current loop [m]

z_T : vertical location of an electrical transmitter [m]

Greek Symbols

β : Constant used to calculate the regularization parameter [ ]

χ^2 : target data misfit [arbitrary]

δ : mudcake exponent multiplier [ ]

weighing parameter in the dual-water model [ ]

$\delta(r-r_s)$: Dirac’s delta function [m^{-1}]

ε_{SSP} : total potential difference across dipole layers [mV]

ϕ : formation effective porosity [fraction]

ϕ_D^{sh} : shale-corrected density porosity [fraction]

ϕ_{Dsh} : density porosity in a pure shale interval [fraction]

ϕ_{mc} : mudcake porosity [fraction]

ϕ_N^{sh} : shale-corrected neutron porosity [fraction]

ϕ_{Nsh} : neutron porosity in a pure shale interval [fraction]

ϕ_o : initial guess of effective porosity [fraction]

ϕ_t : total porosity [fraction]

ϕ_{tsh} : shale total porosity [fraction]

γ_i : specific gravity of phase *i* [ ]

λ^2 : regularization (stabilization) parameter [ ]

λ_o : oil mobility [md/cp]

μ : viscosity [cp]

or Lagrange multiplier [ ]

μ_{fo} or μ_o : formation oil viscosity [cp]

μ_{mf} : mud-filtrate viscosity [cp]

μ_{OBM} : oil-base mud-filtrate viscosity [cp]

μ_0 : magnetic permeability of vacuum [H/m]

ν : mudcake compressibility exponent [ ]

ρ_1, ρ_2 : fluid density [g/cm^3]

ρ_b : bulk density [g/cm^3]

ρ_{ma} : matrix density [g/cm^3]

ρ_{sh} : shale density [g/cm^3]

σ : electrical conductivity [S/m]

σ^0 : background conductivity [S/m]

σ_a : apparent conductivity [S/m]

σ_{mud} : borehole conductivity [S/m]

σ_{mud} : mud conductivity [S/m]

σ_t : virgin-zone conductivity [S/m]

σ_{xo} : invaded-zone conductivity [S/m]

$\overline{\overline{\mathbf{\Sigma}}}$: diagonal matrix formed by singular values [arbitrary]

ω : angular frequency [rad/s]

ξ : molar density [mol/ft^3]

References

Ahmadi, M., Sawyers, M., Kenyon-Roberts, S., Stanworth, B., Kugler, K., Kristensen, J., and Fugelli, E., 2003, in "*The Millenium Atlas: Petroleum Geology of the Central and Northern North Sea*," Ch. 14., The Geological Society of London.

Alpak, F.O., Dussan V., E.B., Habashy, T.M., and Torres-Verdín, C., 2003, "Numerical simulation of mud filtrate invasion in horizontal wells and sensitivity analysis of array induction tools," *Petrophysics*, v. 44, no. 6, pp. 396-411.

Alpak, F.O., Habashy, T.M., Torres-Verdín, C., and Dussan V., E.B., 2004, Joint inversion of pressure and time-lapse electromagnetic logging measurements: *Petrophysics*, v. 45, no. 3, May-June, pp. 251-267.

Alpak, F.O., Torres-Verdín, C., and Habashy, T.M., 2006, Petrophysical inversion of borehole array-induction logs: Part I – Numerical examples: *Geophysics*, v. 71, no. 4, July-August, pp. F101-F119.

Archie, G.E., 1942, "The electrical resistivity log as an aid in determining some reservoir characteristics," *Petroleum Transactions*, *AIME*, v. 146, pp. 54-62.

Arps J.J., 1953, The effect of temperature on the density and electrical resistivity of sodium chloride solutions: *Transactions AIME*, v. 198, pp. 327-330.

Balan, B., Mohagheh, S., and Armeri, S., 1995, "State-of-the-art in permeability determination from well log data: Part 1- A comparative study, model development," paper SPE 30978 presented at the SPE Eastern Regional Conference and Exhibition, Morgantown, West Virginia, September 17-21, 10 p.

Bigelow, E., 1992, "*Introduction to Wireline Log Analysis*," Western Atlas International, Inc., Houston, Texas.

Bourgoyne Jr., A.T., Millheim, K.K., Chenevert, M.E., and Young Jr., F.S., 1986, "*Applied Drilling Engineering*," SPE Textbook Series, v. 2, Richardson, Texas.

BP, 2003, The UK upstream asset portfolio, BP Exploration, Farburn Industrial Estate, Dyce, Aberdeen, U.K. http://www.bp.com/liveassets/bp_internet/globalbp/STAGING/global_assets/downloads/U/uk_asset_andrew.pdf

Brooks, R.H. and Corey, A.T., 1966, "Properties of porous media affecting fluid flow," *J. Irrig. Drain. Div.*, v. 92, no. IR2, pp. 61-88.

Carlson, M.R., 2003, "*Practical Reservoir Simulation*," PennWell, Tulsa, Oklahoma.

Chew, W.C. and Liu, Q.H., 1994, “Inversion of induction tool measurements using the distorted Born iterative method and CG-FFHT,” IEEE *Trans. Geosciences and Remote Sensing*, v. 32, no. 4, pp. 878-884.

Chew, W.C., Barone, S., Anderson, B., and Henessy, C, 1984, “Diffraction of axisymmetric waves in a borehole by bed boundary discontinuities,” *Geophysics*, v. 49, no. 10, pp. 1586-1595.

Clavier, C., Coates, G. Dumanoir, J., 1984, “Theoretical and experimental bases for the dual-water model for interpretation of shaly-sands,” *SPE Journal*, v. 24, no. 2 pp. 153-168.

Chin, W.C., 1995, “*Formation Invasion with Applications tTo Measurement-While-Drilling, Time-Lapse Analysis, and Formation Damage*,” Gulf Publishing Company, Houston, Texas.

CMG, 2006, “*STARS User’s Guide: Advanced Process and Thermal Reservoir Simulator*,” Computer Modeling Group Ltd., Calgary, Alberta, Canada.

Corey, A.T., 1994, *Mechanics of Immiscible Fluids in Porous Media*: Water Resource Publications, Highland Ranch, Colorado.

Dawe, R.A. and Grattoni, C.A., 1998, “The visualization of the pore-scale physics of hydrocarbon recovery from reservoirs,” *first break*, v. 16, no. 11, pp. 371-386.

Delshad, M, Pope, G.A., and Sepehrnoori, K., 1996, A compositional simulator for modelling surfactant enhanced aquifer remediation: *Journal of Contaminant Hydrogeology*, v. 23, pp. 303-327.

Delshad, M. and Pope, G.A., 1989, “Comparison of the three-phase oil relative permeability models,” *J. Transport in Porous Media*, v. 4, no. 1, pp. 59-83.

Dewan, J.T. and Chenevert, M.E., 1993, “Mudcake buildup and invasion in low permeability formations; application to permeability determination by measurement while drilling,” presented at SPWLA/CWLS Symposium, Calgary, Alberta June 13-14.

Dewan, J.T. and Chenevert, M.E., 2001, A model for filtration of water-base mud during drilling: determination of mudcake parameters: *Petrophysics*, v. 42, no. 3, May-June, pp. 237-250.

Dewan, J.T., 1983, “*Essentials of Modern Open-Hole Log Interpretation*,” PennWell Publishing Company, Tulsa, OK

Doll, H.G., 1949, “The S.P. log: theoretical analysis and principles of interpretation,” *Transactions AIME*, v. 179, pp. 146-185.

Donaldson, E.C., and Siddiqui, T.K., 1989, "Relationship between the Archie saturation exponent and wettability," *SPE Formation Evaluation*, v. 4, no. 3, pp. 359-362.

Druskin, V. Knizhnerman, L., and Lee, P., 1999, New spectral Lanczos decomposition method for induction modeling in arbitrary 3D geometry: *Geophysics*, v. 64, no. 3, pp. 701-706.

Finley, R.J., 1984, Geology and engineering characteristics of selected low-permeability sandstones: A National Survey: University of Texas at Austin, Bureau of Economic Geology, Report of Investigation no. 138, pp. 59-60.

George, B.K., Torres-Verdín, C., Delshad, M., Sigal, R., Zouioueche, F., and Anderson, B., 2004, "Assessment of in-situ hydrocarbon saturation in the presence of deep invasion and highly saline connate water," *Petrophysics*, v. 45, no 2, pp. 141-156.

Gunter, G.W., Finneran, J.M., Hartmann, D.J. and Miller, J.D., 1997, Early determination of reservoir flow units using an integrated petrophysical method: paper SPE 38679 *in* SPE Annual Technical Conference and Exhibition, Proceedings: Society of Petroleum Engineers, pp. 373-380.

Habashy, T.M. and Abubakar, A., 2004, "A general framework for constrained minimization for the inversion of electromagnetic measurements," *Progress in Electromagnetic Research*, PIER 46, pp. 265-312.

Hallemburg, J.K., 1971, "A resume of spontaneous potential measurements," paper U presented at the 12th Annual Logging Symposium: Society of Professional Well Log Analysts, El Paso, TX, May 2-5, 16 p.

Hallenburg, J.K., 1998, *Standard Methods of Geophysical Formation Evaluation*: Lewis Publishers, Boca Raton, Florida.

Haro, C. F., 2004, The perfect permeability transform using logs and core: paper SPE 89516 *in* SPE Annual Technical Conference and Exhibition, Proceedings: Society of Petroleum Engineers, 17 p.

Koval, E.J., 1963, "A method for predicting the performance of unstable miscible displacement in heterogeneous media," *SPE Journal*, v. 3, no. 2, pp. 145-154.

La Scala, J.J., Sands, J.M., Orlicki, J.A., Robinette, E.J., and Palmese, G.R., 2004, "Fatty acid-based monomers as styrene replacements for liquid molding resins," *Polymer*, v. 45, no. 22, pp. 7729-7737.

LaVigne, J., Barber, T., and Bratton, T., 1997, "Strange invasion profiles: what multiarray induction logs can tell us about how oil-based mud affects the invasion process and wellbore stability", paper B presented at the 38th Annual Logging

Symposium: Society of Professional Well Log Analysts, Houston, TX, June 15-18, 12 p.

Leverett, M.C., 1941, “Capillary behavior in porous solids,” *Transactions AIME*, v. 142, pp. 152-169.

Lide, D.R., ed., 2007, “Physical constants of organic compounds", in “*CRC Handbook of Chemistry and Physics*,” Internet Version, (87th Edition) Taylor and Francis, Boca Raton, FL.

Luffel, D.L., Howard, W.E., and Hunt, E.R., 1991, “Travis Peak core permeability and porosity relationships at reservoir stress,” *SPE Formation Evaluation*, v. 6, n. 3, pp. 310-318.

Malik, M., Salazar, J.M., Torres-Verdín, C., Wang, G.L., Lee, H.J., and Sepehrnoori, K., 2007, “Influence of petrophysical and fluid properties on array-induction measurements acquired in the presence of oil-base mud-filtrate invasion,” paper AAA presented at the 48th Annual Logging Symposium: Society of Petrophysicist and Well Log Analysts, Austin, TX, June 3-6, 16 p.

Malik, M., Torres-Verdín, C., and Sepehrnoori, K., 2006, “Robust and efficient simulation of formation-tester measurements with a rigorous compositional simulation code,” paper SPE 102151 presented at the SPE Annual Technical Conference and Exhibition, San Antonio, Texas, September 24-27, 12 p.

Malik, M., Torres-Verdín, C., and Sepehrnoori, K., 2007, “Axially symmetric compositional simulation of formation-tester measurements,” *Journal of Petroleum Science and Engineering*, v. 59, no. 3-4, pp. 333-349.

Martin, A.J., Robertson, D., Wreford, J. and Lindsay, A., “High-accuracy oriented perforating extends the sand-free production life of Andrew Field,” paper SPE 93639 presented at the 2005 Offshore Europe, Aberdeen, Scotland, U.K., September 6-9, 7 p.

McGowen, M.K., and Harris, D.W., 1984, Cotton Valley (Upper Cretaceous) and Hosston (Lower Cretaceous) depositional systems and their influence on salt tectonics in the East Texas Basin: University of Texas at Austin, Bureau of Economic Geology, Geological Circular 84-5, 41 pp.

Newsham, K.E. and Rushing, J.A., 2002, Laboratory and field observations of an apparent sub capillary-equilibrium water saturation distribution in a tight-gas sand reservoir: paper SPE 75710 presented at the SPE Gas Technology Symposium, Calgary, Alberta, Canada, April 30-May 2, 11 p.

Peng, D. Y., and Robinson, J. D., 1976, “A new two-constant equation of state,” *Industrial and Engineering Chemistry Fundamentals*, v. 15, pp. 59-64

Pickett, G.R., 1966, "A review of current techniques for determination of water saturation from logs," *Journal of Petroleum Technology*, v. 18, no. 11, pp. 1425-1433.

Pirson, S.J., 1963, "*Handbook of Well Log Analysis: For Oil and Gas Formation Evaluation*," Prentice-Hall, Inc., Englewood Cliffs, NJ.

Pittman, E.D., 1992, "Relationship of porosity and permeability to various parameters derived from mercury injection capillary pressure curve for sandstones," AAPG Bulletin, v. 76, no 2, pp. 191-198.

Proett, M.A., Chin, W., Wu, J., and Manohar, M., 2002, "Sample quality prediction with integrated oil and water-based mud invasion modeling," paper SPE 77964 presented at the SPE Asia Pacific Oil and Gas Conference and Exhibition, Melbourne, Australia, October, 8-10, 14 p.

Ramakrishnan, T.S. and Wilkinson, D.J., 1999, Water-cut and fractional flow from array-induction measurements: *SPE Formation Evaluation*, v. 2, no. 1, February, pp. 85-94.

Ramírez, T. R., Torres-Verdín, C., Lee, H-J, and Wang, G. L., 2006, Interactive assessment of the sensitivity of well logs to static and dynamic petrophysical properties of rock formations," presented at the American Association of Petroleum Geologists International Conference and Exhibition, Perth, Australia, November 5-8.

S.A. Holditch Associates, 1988, Special Core Analysis Report, Staged Field Experiment #2: Core Laboratories, Irving, TX.

Salazar J.M., Malik, M., Torres-Verdín, C., Wang G.L., and Duan H., 2007, "Fluid density and viscosity effects on borehole resistivity measurements acquired in the presence of oil-based mud and emulsified surfactants," paper SPE 109946 presented at the SPE Annual Technical Conference and Exhibition, Anaheim, California, November 11-14, 16 p.

Salazar, J.M., Torres-Verdín, C., Alpak, F.O., Habashy, T.M., and Klein, J.D., 2006, "Estimation of permeability from borehole array induction measurements: application to the petrophysical appraisal of tight-gas sands," *Petrophysics*, v. 47, no. 6, pp. 527-544.

Salazar, J.M., Torres-Verdín, C., and Sigal, R., 2005, "Assessment of permeability from well logs based on core calibration and simulation of mud-filtrate invasion," *Petrophysics*, v. 46, no. 6, pp. 434-451.

Schlumberger, 1991, "*Log Interpretation Charts*," Schlumberger Educational Services, U.S.A.

Segesman, F., 1962, "New SP correction charts", *Geophysics*, v. 27, no. 6, pp. 815-828.

Semmelbeck, M.E. and Holditch, S.A., 1988, The effect of mud-filtrate invasion on the interpretation of induction logs: *SPE Formation Evaluation*, June, pp. 386-392.

Semmelbeck, M.E., Dewan, J.T., and Holditch, S.A., 1995, Invasion-based method for estimating permeability from logs, SPE 30581 *in* SPE Annual Technical Conference and Exhibition, Proceedings: Society of Petroleum Engineers, pp. 517-531.

Skalli, L., Buckley, J.S., Zhang, Y., and Morrow, N.R., 2006, "Surface and core wetting effects of surfactants in oil-based drilling fluids," *Journal of Petroleum Science & Engineering*, v. 52, no. 1-4, pp. 253-360.

Thomas, E.C. and Stieber S.J., 1975, "The distribution of shale in sandstones and its effects upon porosity," paper T presented at the SPWLA 16th Annual Logging Symposium, New Orleans, Louisiana, June 4-7.

Tobola, D.P. and Holditch, S.A., 1991, Determination of reservoir permeability from repeated induction logging: *SPE Formation Evaluation*, March, pp. 20-26.

Todd, M. R., and Longstaff, W. J., 1972, "The development, testing, and application of a numerical simulator for predicting miscible flood performance," *Journal of Petroleum Technology*, v. 24, no. 7, pp. 874-882.

Torres-Verdín, C., Alpak, F.O., and Habashy, T.M., 2006, Petrophysical inversion of borehole array-induction logs: Part II – Numerical examples: *Geophysics*, v. 71, no. 5, September-October, pp. G261-G268.

Van, J-N., Menezes, J.L., and Sharma, M.M., 1988, "Wettability alteration due to interactions with oil-based muds and mud components," paper SPE 18162 presented at the SPE Annual Technical Conference and Exhibition, Houston, Texas, October 2-5, pp. 557-570.

Warner Jr., H.R. and Rathmell, J.J., 1997, "Mechanisms controlling filtration at the core bit for oil-based muds," *SPE Drilling & Completion*, v. 12, no 2, June, pp. 111-118.

Waxman, M.H. and Smits, L.J.M., 1968, "Electrical conductivities in oil-bearing shaly sands," *Transactions* AIME, v. 243, Part II, pp. 107-122.

Worthington, A.E., Hedges, J.H., and Pallatt, N, 1990, SCA Guidelines for sample preparation and porosity measurements of electrical resistivity samples: Part I – Guidelines for preparation of brine and determination of brine resistivity for use in electrical resistivity measurements: *The Log Analyst*, v. 31, no. 1, January-February, pp. 20-28.

Wu, J, Torres-Verdín, C., Sepehrnoori, K., and Delshad, M., 2004, Numerical simulation of mud-filtrate invasion in deviated wells: *SPE Reservoir Evaluation and Engineering*, v. 7, no. 2, April, pp. 143-154.

Wu, J, Torres-Verdín, C., Sepehrnoori, K., and Proett, M.A., 2005, "The Influence of water-base mud properties and petrophysical parameters on mudcake growth, filtrate invasion, and formation pressure," Petrophysics, v. 46, no. 1, pp. 14-32.

Wyllie, M.R.J. and Southwick, P.F., 1954, "An experimental investigation of the S.P. and resistivity phenomena in dirty sands," *Journal of Petroleum Technology*, v. 6, no. 2, pp. 44-57.

Yan, J. and Sharma M.M., 1989, "Wettability alteration and restoration for cores contaminated with oil-based muds," *Journal of Petroleum Science & Engineering*, v. 2, no. 2, pp. 63-76.

Yao, C.Y. and Hoditch, S.A., 1996, Reservoir permeability estimation from time-lapse log data: *SPE Formation Evaluation*, June, pp. 69-74.

Zhang, G.J. and Wang, G.L., 1997, "Application of vector potential theory to spontaneous potential calculation," *Radio Science*, v. 32, no. 3, pp. 899-905.

Zhang, G.J. and Wang, G.L., 1999, "A new approach to SP-vector potential approach," *IEEE Transactions on Geoscience and Remote Sensing*, v. 37, no. 4, pp. 2092-2098.

Zhang, G.J., 1984, "*Electrical Logging*," Petroleum Industry Press, Beijing, China.

Zhang, G.J., Wang, G.L., and Wang, H.M, 1999, "Application of novel basis functions in a hybrid method simulation of the response of induction logging in axisymmetrical stratified media," *Radio Science*, v. 34, no. 1, pp. 19-26.

Vita

Jesús Mauricio Salazar Luna was born in Porlamar, Margarita Island, Venezuela, on September 16, 1974, the fifth son of Mr. Erasmo Salazar and Mrs. Maximiliana Luna de Salazar. He received a B.Sc. degree in Physics (with honors) from Universidad Central de Venezuela in 1998 and a M.Sc. degree in Petroleum Engineering from The University of Texas at Austin in 2004. He worked 5 years for PDVSA (Maracaibo, Venezuela) as a petrophysicist and well-log analyst. Jesus was a Research and Teaching Assistant with the Department of Petroleum and Geosystems Engineering of The University of Texas at Austin between May 2003 and December 2007. In the summers of 2004 through 2006 he was an intern with ConocoPhillips and Occidental Oil and Gas. Upon completion of his Doctoral degree Jesús will join ConocoPhillps to work in petrophysics. He is recipient of the 2006 Best Paper Award by *Petrophysics*.

Permanent address: Calle Cocheima # 9-49

La Asunción, Nueva Esparta 6311
Venezuela

This dissertation was typed by the author.